

**Colloidal synthesis and characterization of molybdenum
and tungsten-based phosphide electrocatalysts for
hydrogen evolution reaction**

Siyabonga Siphonkabinde

Student number: 564058

A thesis submitted to the Faculty of Science, School of
Chemistry at the University of the Witwatersrand, in partial
fulfilment of the requirements for the degree of

Doctor of Philosophy

Supervisor: Prof. Nosipho Moloto

Johannesburg 2021

Declaration

I proclaim that the work reported in this thesis is my own and was independently studied. It is being submitted for the degree of Doctor of Philosophy to the School of Chemistry, Faculty of Science at Wits University, Johannesburg. It has not been submitted to any institution previously for examination.

Candidate name: Siyabonga Sipho Nkabinde



Signature.....

Date.....October 2021.....

Supervisor name: Prof. Nosipho Moloto



Signature.....

Date.....October 2021.....

Dedication

TO MY WIFE, PARENTS AND MY SIBLINGS, THIS IS FOR YOU.

Abstract

The production of hydrogen gas via hydrogen evolution reaction (HER) in acidic media has become an important area of research in light of the increasing demand for sustainable and environmentally friendly sources of energy. However, its large-scale production is currently being hindered by the lack of inexpensive and highly efficient non-noble electrocatalysts. Transition metal phosphides (TMPs) have transpired as favourable catalysts that can be prepared from cheap and readily available sources. Up to now, TMPs have been commonly prepared using solid-state and solid-gas reactions, which rely on the use of high temperatures and hence generate inhomogeneity in the prepared materials. Inhomogeneous materials are unattractive as catalysts because the correlation between a catalyst and its structural features cannot be systematically studied. For this reason, colloidal synthesis has emerged as a powerful method in the synthesis of TMPs as it allows for control over the resulting physical features (i.e. size, morphology, crystal phase, crystallinity etc.). The ability to tailor these physical properties provides room for improving the catalytic activity. By using the colloidal synthesis method, we have successfully prepared molybdenum and tungsten-based phosphide nanoparticles and studied the effect of their physical features on HER activity.

In chapter 3, we report a facile colloidal synthesis method to produce an amorphous phase of molybdenum phosphide (MoP) by using trioctylphosphine (TOP) as a phosphorus source, molybdenum pentachloride (MoCl_5) as a metal source and 1-octadecene (1-ODE) as a solvent/reducing agent. The use of the forementioned precursors promoted the formation of very small, shape controlled and well dispersed amorphous molybdenum phosphide (MoP) nanoparticles. Annealing ($800\text{ }^\circ\text{C}$) of the amorphous MoP nanoparticles resulted in the formation of a crystalline MoP phase with a slightly bigger size but retained its dispersity and morphology upon exposure to high temperature. The amorphous and crystalline MoP phases were compared as HER electrocatalysts. HER results indicated that the amorphous MoP phase exhibited enhanced catalytic activity in hydrogen evolution reaction compared to the crystalline MoP phase. The high activity displayed by the amorphous MoP was attributed to the small sizes and the high density of unsaturated active sites characteristic of nanoparticles lacking long range crystalline order.

Motivated by the need to expand the use of metal chloride salts to prepare other TMPs catalysts, we employed the colloidal synthesis method to prepare two different phases of tungsten phosphide by using TOP, tungsten hexachloride (WCl_6) and 1-octadecene. The two different phases of tungsten phosphide were obtained by simply varying the W:P precursor ratio, with ratios of 1:1 and 1:20 resulting to the formation of WP (orthorhombic) and α - WP_2 (monoclinic) phases, respectively. The phosphorus rich α - WP_2 displayed superior catalytic activity over the phosphorus poor WP in HER. Specifically, α - WP_2 catalyst displayed a low overpotential of -271 mV at $J = 10 \text{ mA}\cdot\text{cm}^{-2}$, higher electrochemically active surface area, low charge transfer resistance and excellent long-term stability. Theoretical calculations done using density functional theory (DFT) revealed that the high activity of α - WP_2 was due to high conductivity, low hydrogen adsorption energy, low energy barrier to H-H formation and long M-P bond length.

Having determined that amorphous MoP nanoparticles were more active as HER catalysts, we proposed that by combining the sort after properties in amorphous structures and tailoring the electronic properties through doping, the catalytic activity of MoP could be significantly enhanced. In chapter 5, we report on the colloidal synthesis of tungsten-doped molybdenum phosphide nanoparticles for use as electrocatalysts in HER. The synthesis of tungsten-doped molybdenum phosphide (WMoP) was done by introducing 10 mol % of the dopant precursor (i.e. tungsten hexachloride) into a mixture of TOP, molybdenum pentachloride (MoCl_5) and 1-octadecene. XRD and XPS analysis were used to confirm the successful incorporation of the tungsten (W) dopant into the crystal structure of MoP. A comparative study was conducted between pure MoP (amorphous vs. crystalline) and W-doped MoP (amorphous vs. crystalline) electrocatalysts in HER. The HER results revealed that the amorphous W-doped MoP catalyst exhibited the highest activity requiring a very low overpotential of -145 mV and a low Tafel slope of $65.85 \text{ mV}\cdot\text{dec}^{-1}$. In addition to high conductivity, increased density of electrochemically active sites and excellent long-term stability, the synergistic effect between the W and Mo metals were responsible for the enhanced activity of amorphous W-doped MoP catalyst.

Encouraged by the promising catalytic activity displayed by α - WP_2 , we hypothesized that its catalytic activity can be enhanced further through doping. Hence, in chapter 6, we report a facile colloidal synthesis method to prepare molybdenum-doped α - WP_2 nanoparticles for use as HER catalysts. Molybdenum-doped α - WP_2 was prepared by adding various amounts (2.5, 5

and 10 mol %) of the molybdenum pentachloride salt into a mixture of TOP, WCl_6 and 1-octadecene to produce $Mo/\alpha-WP_2$ with different dopant concentrations. Comparative analysis of $\alpha-WP_2$, $Mo(2.5\%)/\alpha-WP_2$, $Mo(5\%)/\alpha-WP_2$ and $Mo(10\%)/\alpha-WP_2$ as electrocatalysts for HER clearly indicated that doping modifies their properties and an increase in the dopant concentration result to improved catalytic activity. $Mo(10\%)/\alpha-WP_2$ possessed the best HER catalytic activity, requiring only -165 mV to generate current density of $10 \text{ mA}\cdot\text{cm}^{-2}$ and the Tafel slope was $71.65 \text{ mV}\cdot\text{dec}^{-1}$. Experimental results revealed that the improved catalytic activity of the molybdenum doped tungsten phosphide resulted from superior electronic conductivity, high density of electrochemically active sites and an increased electron density around the W atoms.

Acknowledgements

- ❖ I would like to thank my supervisor Professor Nosipho Moloto for guidance throughout the course of this project. No words could ever explain how grateful I am for your contributions towards my success as a researcher.
- ❖ To my wife Lebogang Nkabinde, thank you for being there for me in times when I needed you the most. You have been by my side through thick and thin, and for that I will forever be grateful. Ngiyabonga!
- ❖ To my family, Duduzile, Zandile, Mzwakhe and Phindile Mgaga, your emotional and financial support throughout the course of my studies has kept me going even at times where I wanted to give up.
- ❖ My gratitude goes to the Microscopy and Microanalysis Unit (MMU) staff, specifically Dr Z. Tetana, Dr C. Linganiso, Dr M. Maubane-Nkadimeng and Prof. A. Ziegler for all the assistance provided throughout this study.
- ❖ To the Nano-WEBS and the CATMAT group, the meetings have contributed so much to me as student. Sharing my work with you and getting constructive criticism back has made me a better researcher and presenter.
- ❖ To my friends, Xolani, Ella, Prince and Zakes, you guys kept me sane during times where I thought it was not possible to get here. Thank you for putting a smile on my face throughout the course of my research.

Publications

- ❖ **S.S. Nkabinde**, Z.B. Ndala, N.P. Shumbula, T. Kolokoto, O. Nchoe, G.N. Ngubeni, K.P. Mubiayi, N. Moloto, Delineating the role of crystallinity in the electrocatalytic activity of colloiddally synthesized MoP nanocrystals, *New Journal Chemistry* 44 (2020) 14041-14049. {Contribution: I did all the synthetic and electrochemical characterization work, wrote and corrected the manuscript and conducted the majority of the characterization including XRD, TEM and EDS. HRTEM and XPS analysis were ran externally at NMISA but I did the interpretation. Mr Z.B. Ndala helped with the running of electrochemical experiments and data processing. Mr N.P. Shumbula, Ms T. Kolokoto, Mr O. Nchoe and Ms G.N. Ngubeni helped with brainstorming of ideas and discussion of results. Prof. N. Moloto and Dr K.P. Mubiayi conceptualized the project and helped with correcting the manuscript }.
- ❖ **S.S. Nkabinde**, Z.B. Ndala, N.P. Shumbula, T. Kolokoto, O. Nchoe, G.N. Ngubeni, K.P. Mubiayi, N. Moloto, Phase-dependant electrocatalytic activity of colloiddally synthesized WP and α -WP₂ electrocatalysts for hydrogen evolution reaction, *New Journal of Chemistry* 45 (2021) 15594-15606. {Contribution: I did all the synthetic and electrochemical characterization work, wrote and corrected the manuscript and conducted the majority of the characterization including XRD, TEM and EDS. XPS analysis were ran externally at NMISA but I did the interpretation. Prof. R. Maphanga, Prof. K. Ozoemena and Dr P. Mwonga conducted the DFT calculations and helped with the writing and correction of the manuscript. Mr S. Mpelane helped running HRTEM analysis of the samples. Mr Z.B. Ndala helped with the running of electrochemical experiments and data processing. Mr N.P. Shumbula, Ms T. Kolokoto, Mr O. Nchoe and Ms G.N. Ngubeni helped with brainstorming of ideas and discussion of results. Prof. N. Moloto and Dr K.P. Mubiayi conceptualized the project and helped with correcting the manuscript }.

Manuscript under review

- ❖ **S.S. Nkabinde**, N.P. Shumbula, Z.B. Ndala, T. Kolokoto, O. Akinbami, V. Mashindi, O. Nchoe, G.N. Ngubeni, K.P. Mubiayi, N. Moloto, Fine-tuning the electronic properties of α -WP₂ electrocatalyst via Mo-doping for efficient hydrogen evolution in acidic media,

International Journal of Hydrogen Energy (Under Review). Manuscript ID: HE-D-21-04366.

Manuscript to be submitted

- ❖ **S.S. Nkabinde**, Z.B. Ndala, N.P. Shumbula, T. Kolokoto, O. Nchoe, G.N. Ngubeni, K.P. Mubiayi, N. Moloto, The synergistic effect of W dopant on colloiddally synthesized molybdenum phosphide electrocatalyst in hydrogen evolution reaction. “To be submitted”

Presentations

1. Oral presentation at the Catalysis Organometallics and Materials (CATOMAT) seminar held at the School of Chemistry, University of the Witwatersrand on the 14 March 2019
Title: In, Mo and W nanoparticles for hydrogen evolution reaction.
2. Poster presentation at the 70th Annual Meeting of the International Society of Electrochemistry conference in Durban on the 4 - 9 August 2019
Title: MoP and α -WP₂ nanoparticles as non-noble electrocatalysts for hydrogen evolution reaction.
3. Poster presentation at the 10th Cross Faculty Postgraduate Symposium held at New Commerce Building West Campus, University of the Witwatersrand on the 3 - 4 September 2019
Title: Tungsten phosphide (WP) and Tungsten diphosphide (α -WP₂) as electrocatalysts for hydrogen evolution reaction.
4. Virtual poster presentation at the SACI Young STEM Poster Symposium 2020, hosted by the University of Johannesburg on the 17th of November 2020
Title: MoP and α -WP₂ particles as non-noble electrocatalysts for hydrogen evolution reaction.

Table of Contents

Declaration.....	i
Dedication	ii
Abstract.....	iii
Acknowledgements	vi
Publications	vii
Presentations	ix
List of figures.....	xiv
Chapter 2	xiv
List of Tables	xviii
Chapter 3	xviii
Chapter 4	xviii
Chapter 5	xviii
Chapter 6	xviii
List of abbreviations	xix
Synopsis.....	1
1. Brief description of the thesis.....	1
Chapter 1	3
General background	3
1. Problem statement	3
2. Motivation and rationale	3
3. Aim and Objectives.....	4
4. References	5
Chapter 2	6
Literature review	6
1. Colloidal synthesis of nanoparticles.....	6

2.	Electrochemical water splitting	8
3.	Transition metal phosphides (TMPs)	12
4.	Synthesis of transition metal phosphides (TMPs).....	14
4.1.	Gas-solid phase reaction.....	14
4.2.	Solid-state reduction.....	15
4.3.	Electrodeposition.....	16
4.4.	Colloidal synthesis method.....	17
5.	Performance parameters for HER	22
5.1.	Overpotential (η).....	22
5.2.	Tafel slope and exchange current density.....	23
5.3.	Stability.....	25
6.	Enhancing electrocatalytic performance of TMPs	26
6.1.	Tuning M:P stoichiometric ratio.....	26
6.2.	Elemental alloying or doping	27
6.3.	Introduction of conducting carbon support	27
6.4.	Crystallinity tailoring.....	28
7.	References	29
Chapter 3		42
Delineating the role of crystallinity in the electrocatalytic activity of colloiddally synthesized MoP nanocrystals.....		42
1.	Introduction	42
2.	Experimental	44
2.1	Chemicals and Materials	44
2.2	Synthesis of amorphous molybdenum phosphide nanocrystals	44
2.3	Electrochemical measurements and preparation of working electrode.....	44
2.4	Materials characterization.....	45
3.	Results and discussion.....	46
3.1.	Structural and electronic characterization	46
3.2.	Hydrogen evolution reaction	50
4.	Conclusion.....	54
5.	References	54

6.	Supporting information	60
Chapter 4		63
Phase-dependant electrocatalytic activity of colloiddally synthesized WP and α-WP₂ electrocatalysts in hydrogen evolution reaction		63
1.	Introduction	63
2.	Experimental	64
2.1.	Chemicals and materials	64
2.2.	Synthesis of WP and WP ₂	65
2.3.	Materials characterization.....	65
2.4.	Electrochemical measurements and preparation of working electrode	66
2.5.	Theoretical calculations	66
3.	Results and discussion.....	67
3.1.	Structural and electronic characterisation.....	67
3.2.	Electrocatalytic HER	72
3.3.	DFT calculations.....	78
4.	Conclusion.....	80
5.	References	80
6.	Supporting Information	86
Chapter 5		91
The synergistic effect of W dopant on colloiddally synthesized molybdenum phosphide electrocatalyst in hydrogen evolution reaction.....		91
1.	Introduction	91
2.	Experimental	92
2.1.	Chemicals and Materials	92
2.2.	Synthesis of pure A-MoP and W-doped MoP (A-WMoP).....	93
2.3.	Electrochemical Measurements and Preparation of Working Electrode.....	93
2.4.	Materials Characterization.....	94
3.	Results and discussion.....	95
3.1.	Compositional, morphological and structural characterization	95
3.2.	Hydrogen Evolution Reaction (HER).....	98
4.	Conclusion.....	104

5.	References	105
Chapter 6		111
Fine-tuning the electronic properties of α-WP₂ electrocatalyst via Mo-doping for efficient hydrogen evolution in acidic media		111
1.	Introduction	111
2.	Experimental	112
2.1.	Chemicals and materials	112
2.2.	Synthesis of pristine α -WP ₂ and Mo-doped α -WP ₂ (Mo/ α -WP ₂)	113
2.3.	Electrochemical measurements and preparation of working electrode	113
3.	Results and discussion.....	115
3.1.	Structural characterization.....	115
3.2.	HER Performance Evaluation	118
4.	Conclusion.....	124
5.	References	125
6.	Supporting Information	130
Chapter 7		136
General conclusions and future work		136
1.	Conclusions	136
2.	Future work	137

List of figures

Chapter 2

Fig. 1: Graphical representation of hydrogen evolution reaction (HER) and oxygen evolution reaction (OER) via water electrolysis. ⁴⁰	9
Fig. 2: The two mechanisms of HER on the electrocatalyst surface.	10
Fig. 4: Various crystal structures of metal-rich phosphides. ⁸⁴ (phosphorus = green, metal = brown)	13
Fig. 3: (a) Triangular prism and (b) tetrakaidecahedral structures of metal phosphides. ⁸⁴	13
Fig. 5: Schematic illustration of a typical solid-state reduction reaction setup.	15
Fig. 6: Illustration of the electrodeposition method conducted using a conventional three-electrode system.	17
Fig. 7: A graph showing the relationship between the Gibbs free energy versus the radius of the clusters.	19
Fig. 8: Graphical representation of the LaMer and Dineger's nucleation mechanism. ¹¹¹	20
Fig. 9: General schematic representation of the colloidal synthesis method.	21
Fig. 10: Linear sweep voltammetry demonstrating catalysts with different catalytic performance based on overpotential required to generate $10 \text{ mA}\cdot\text{cm}^{-2}$	23
Fig. 11: (a) A plot of overpotential vs $\log \text{current density} $ (b) Tafel slopes of two catalyst exhibiting different activity as extrapolated from the linear region of the overpotential vs $\log \text{current density} $ plot.	24
Fig. 12: Linear scan voltammetry curves of a catalyst before and after 1000 potential cycles.	25
Fig. 1: X-ray diffraction patterns of (a) A-MoP and (b) C-MoP nanocrystals.	46
Fig. 2: TEM images of (a) A-MoP, (b) HRTEM image of A-MoP and (insert c) the corresponding SAED pattern, (d) TEM images of C-MoP, (e) HRTEM image of C-MoP and (insert f) corresponding SAED pattern.	47
Fig. 3: (a) HAADF-STEM image and elemental mapping of amorphous A-MoP, and (b) HAADF-STEM image and elemental mapping of crystalline C-MoP nanocrystals.	48
Fig. 4: XPS survey spectrum of (a) A-MoP and corresponding high-resolution spectra: (b) P 2p, (c) Mo 3d; survey spectrum of (d) C-MoP and corresponding high-resolution spectra: (e) P 2p and (f) Mo 3d.	49
Fig. 5: LSV polarization curves of (a) A-MoP and C-MoP together with Pt/C, bare GCE and Vulcan as controls ($0.5 \text{ M H}_2\text{SO}_4$; scan rate 1 mVs^{-1}). (b) Tafel slope plots of A-MoP, C-MoP	

and Pt/C. (c) LSV curves of A-MoP and C-MoP before and after 1000 potential cycles. (d) Nyquist plots of A-MoP and C-MoP nanocrystals.	51
Fig. 6: Schematic diagram illustrating the structural transformation of MoP upon annealing.....	51
<i>Table 1: Comparison of catalytic activity of non-noble metal electrocatalysts in 0.5 M H₂SO₄.</i> .	53
Fig. S2: EDX spectroscopy of (a) amorphous A-MoP and (b) crystalline C-MoP(2 h) nanocrystals.	60
Fig. S1: The size distributions of (a) A-MoP and (b) C-MoP nanocrystals as determined from TEM images (N = 100).	60
61	
Fig. S4: XRD pattern of long term stored amorphous C-MoP.	61
Fig. S3: XRD pattern of long term stored amorphous A-MoP.	61
62	
Fig. S6: High resolution spectra of C 1s of C-MoP.	62
Fig. S5: High resolution spectra of C 1s of A-MoP.	62
Fig. 1: XRD patterns of (a) tungsten monophosphide (WP, orthorhombic) and (b) tungsten diphosphide (α -WP ₂ , monoclinic) nanoparticles.	68
Fig. 2: TEM image of (a) WP, (b) HRTEM image of WP and (inset (c) and (d)) magnified region showing lattice fringes and corresponding SAED pattern for WP. TEM image of (e) α -WP ₂ , (f) HRTEM image of α -WP ₂ and (inset (g) and (h)) magnified region showing lattice fringes and corresponding SAED pattern for α -WP ₂	69
Fig. 3: XPS survey spectrum of (a) WP and corresponding high-resolution spectra: (b) P 2p, (c) W 4f; survey spectrum of (d) α -WP ₂ and corresponding high-resolution spectra: (e) P 2p and (f) W 4f.	71
Fig. 4: (a) LSV polarization curves of Pt/c, α -WP ₂ , WP, Vulcan and GCE at a scan rate of 2 mV/s; (b) corresponding Tafel plots for Pt/c, α -WP ₂ and WP; (c) and (d) the C _{dl} of WP and α -WP ₂ ; (e) Nyquist plots of WP and α -WP ₂ catalysts; (f) LSV curves of WP and α -WP ₂ before and after 1000 potential cycles and (insert (g)) chronoamperometry measurements of WP and α -WP ₂ at constant applied potential of 364 and 321 mV, respectively.	73
<i>Table 1: Comparison of the electrocatalytic activity of tungsten phosphide electrocatalysts in acidic medium.</i>	75
Fig. 5: LSV curves of (a) WP and (b) α -WP ₂ at different temperatures, (c) Arrhenius curves for WP and α -WP ₂ catalysts.	77
Fig. 6: Band structures and projected density of states of (a) WP and (b) α -WP ₂	79
Fig. S1: X-ray diffraction pattern of as synthesized (a) WP and (b) α -WP ₂	86

Fig. S2: EDX spectra and corresponding atomic % of (a) WP and (b) α -WP ₂ .	87
Fig. S3: The C 1s spectrum of (a) WP and (b) α -WP ₂ .	87
Fig. S4: XRD pattern of long term stored α -WP ₂ .	88
Table S1: Comparison of the electrocatalytic activity of WP and α -WP ₂ catalysts.	88
Table S2: Kinetic parameters of WP and α -WP ₂ catalysts.	88
Fig. S5: Cyclic Voltammetry (CV) curves of (a) WP and (b) α -WP ₂ catalysts measured in a potential window without faradaic processes in 0.5 M H ₂ SO ₄ at scan rate from 20 - 100 mV s ⁻¹ .	89
Fig. S7: Tafel slopes of (a) WP and (b) α -WP ₂ catalysts obtained at different temperatures.	89
Fig. S6: Equivalent circuit for one time constant, where R _s - solution resistant; CPE - constant phase element; R _{ct} – charge transfer resistance.	89
Fig. S8: Calculated hydrogen adsorption energies on (011) and (-201) surfaces for WP and α -WP ₂ , respectively.	90
Fig. 1: XRD patterns of (a) A-MoP and A-WMoP, (b) C-MoP and C-WMoP catalysts; (c) observed XRD peak shift to low 2 θ upon doping of MoP with W; (d) XPS survey spectra of A-WMoP and C-WMoP.	96
Fig. 2: High resolution Mo 3d, P 2p and W 4f spectra of (a-c) A-WMoP and (d-f) C-WMoP catalysts.	97
Fig. 3: TEM images of (a) A-MoP, (b) C-MoP, (c) A-WMoP and (d) C-WMoP catalysts and their corresponding nanoparticle size distribution histograms.	98
Fig. 4: (a) LSV polarization curves of A-MoP, C-MoP, A-WMoP and C-WMoP catalysts; (b) the corresponding Tafel plots of the catalysts in (a); (c) Nyquist plots of A-MoP, C-MoP, A-WMoP and C-WMoP; (d) LSV curves of A-WMoP before and after 1000 potential cycles.	99
Table 1: Performance parameters of the catalysts reported in this study.	100
Table 2: Comparison of metal doped transition-metal phosphide electrocatalysts for HER in 0.5 M H ₂ SO ₄ .	102
Fig. 5: Cyclic Voltammetry curves of (a) A-MoP, (b) C-MoP, (c) A-WMoP and (d) C-WMoP recorded at different scan rates (20-100 mV s ⁻¹) in 0.5 M H ₂ SO ₄ ; (e) Plot of capacitive current vs. scan rate for all the catalysts under study; (f) The polarization curves of the 1 st and 1000 th cycles of durability study.	104
Fig. 1: XRD pattern of (a) α -WP ₂ , Mo(2.5%)/ α -WP ₂ , Mo(5%)/ α -WP ₂ and Mo(10%)/ α -WP ₂ catalysts. (b) Magnified diffraction peak (111) region showing a slight shift to high 2 θ . X-ray photoelectron spectroscopy (XPS) survey spectrum of (c) α -WP ₂ and Mo(10%)/ α -WP ₂ . High-resolution spectra of (d) P 2p, (e) W 4f and (f) Mo 3d in Mo(10%)/ α -WP ₂ .	116

Fig. 2: TEM images of (a) α -WP ₂ , (b) Mo(2.5%)/ α -WP ₂ , (c) Mo(5%)/ α -WP ₂ and (d) Mo(10%)/ α -WP ₂ .	118
Fig. 3: Electrochemical tests: (a) LSV polarization curves of α -WP ₂ , Mo(2.5%)/ α -WP ₂ , Mo(5%)/ α -WP ₂ , Mo(10%)/ α -WP ₂ , Pt/c, vulcan and GCE at a scan rate of 2 mV/s in 0.5 M H ₂ SO ₄ . (b) corresponding Tafel plots, (c) Nyquist plots of α -WP ₂ , Mo(2.5%)/ α -WP ₂ , Mo(5%)/ α -WP ₂ , Mo(10%)/ α -WP ₂ catalysts. (f) LSV curves of Mo(10%)/ α -WP ₂ before and after 1000 potential cycles.	119
<i>Table 1: Summary of the catalytic activity of the various catalysts in acidic media.</i>	121
Fig. 4: (a) Linear fit of the capacitive currents against scan rate for the various catalysts. (b) High resolution XPS spectra of W 4f7/2 with (bottom) and without (top) molybdenum dopant.	122
Fig. 5: (a) XRD pattern of Mo(10%)/ α -WP ₂ before and after annealing at 600, 800 and 950 °C under N ₂ gas. (b) LSV curves of Mo(10%)/ α -WP ₂ heated at various temperatures. The corresponding (c) Tafel and (d) EIS plots.	124
Fig. S2: Energy-dispersive X-ray spectroscopy of (a) α -WP ₂ , (b) Mo(2.5%)/ α -WP ₂ (c) Mo(5%)/ α -WP ₂ and (d) Mo(10%)/ α -WP ₂ catalysts.	130
Fig. S1: XRD patterns of the pristine pure and doped α -WP ₂ catalyst.	130
Fig. S4: XRD pattern of long term stored α -WP ₂ catalyst.	131
Fig. 3: The high resolution (a) P 2p and (b) W f4 spectrum of pristine α -WP ₂ catalyst.	131
<i>Table S1: Catalytic activity comparison of metal doped transition-metal phosphide electrocatalysts for HER in 0.5 M H₂SO₄.</i>	132
Fig. S5: The electrochemical double-layer capacitance for (a) α -WP ₂ , (b) Mo(2.5%)/ α -WP ₂ , (c) Mo(5%)/ α -WP ₂ and (d) Mo(10%)/ α -WP ₂ measured using CV to calculate the ECSA.	134

List of Tables

Chapter 3

Table 1: Comparison of catalytic activity of non-noble metal electrocatalysts in 0.5 M H ₂ SO ₄	53
---	----

Chapter 4

Table 1: Comparison of the electrocatalytic activity of tungsten phosphide electrocatalysts in acidic medium.....	75
Table S1: Comparison of the electrocatalytic activity of WP and α -WP ₂ catalysts.....	88
Table S2: Kinetic parameters of WP and α -WP ₂ catalysts	88

Chapter 5

Table 1: Performance parameters of the catalysts reported in this study	100
Table 2: Comparison of metal doped transition-metal phosphide electrocatalysts for HER in 0.5 M H ₂ SO ₄	102

Chapter 6

Table 1: Summary of the catalytic activity of the various catalysts in acidic media.	121
Table S1: Catalytic activity comparison of metal doped transition-metal phosphide electrocatalysts for HER in 0.5 M H ₂ SO ₄	132

List of abbreviations

1-ODE – 1-octadecene

BE – Binding energy

b – Tafel slope

CB – Conduction band

C_s – Critical supersaturation

C_{dl} – Double-layer capacitance

CV – Cyclic Voltammetry

CASTEP – Cambridge serial energy package

COMPASS – Condensed-phase optimized molecular potentials for atomistic simulation studies

CPE – Constant phase element

D_c – d-band center

DFT – Density Functional Theory

e⁻ – Electron

eV – Electron volts

E_a – Activation energy

E_f – Fermi level

ECSA – Electrochemically active surface area

EIS – Electrochemical impedance spectroscopy

EDS – Energy dispersive X-ray spectroscopy

Eq – Equation

F – Faraday constant

GCE – Glassy carbon electrode

h – Hour

HAADF-STEM – High angular annular dark field scanning transmission electron microscopy

HER – Hydrogen Evolution Reactions

HRTEM – High Resolution Transmission Electron Microscopy

H_{ads} – Adsorbed hydrogen

H⁺ – Hydrogen ion

Hz – Hertz

j – Current density

j₀ – Exchange current density

K – Kelvin

LSV – Linear Sweep Voltammetry

MoP – Molybdenum phosphide

OER – Oxygen evolution reaction

P – Phosphorus

PDOS – Projected density of states

Pt/C – Platinum on carbon

PGM – Platinum group elements

PW19 – Perdew-Wang generalized-gradient approximation functional

SA – Surface area

SEM – Scanning Electron Microscopy

SAED – Selected area electron diffraction

TEM – Transmission electron microscopy

TKD - Tetrakaidekahedral

TMPs – Transition metal phosphides

T. S. – Transition state

TOP – Trioctylphosphine

R - Ideal gas constant

RDS – Rate determining step

R_c – Critical radius

R_{ct} – Charge transfer resistance

RT – Room temperature

RHE – Reversible hydrogen electrode

VASP – Vienna ab initio simulation package (VASP)

WE – Working electrode

WP – Tungsten phosphide

W Tungsten

A-WP₂ – Tungsten diphosphide

XRD – X-ray diffraction

XPS – X-ray photoelectron spectroscopy

Å – Angstrom

η – Overpotential

A – Symmetry coefficient

λ – Wavelength

Ω – Ohm

Θ – Theta

ΔG – Change in Gibbs free energy

ΔG_s – Change in Gibbs free energy at the surface

ΔG_v - bulk free energy change of the crystal

ΔH – Change in Enthalpy

ΔS – Change in Entropy

Δ – Change In

Synopsis

1. Brief description of the thesis

The aim of this study was to employ the colloidal synthesis method to prepare and characterize molybdenum and tungsten phosphide-based nanomaterials for use as electrocatalysts in hydrogen evolution reaction in acidic media. Consequently, the thesis is structured as follows:

Chapter 1: outlines the content discussed in each chapter of the thesis and provides the problem statement addressed in the project. Moreover, the motivation and rationale for the study along with the aims and objectives are elucidated.

Chapter 2: narrates a brief background on the urgent need to find alternative techniques for hydrogen generation and bring forth hydrogen evolution reaction (HER) as a suitable alternative to traditional methods. Background information on transition metal phosphides (TMPs) as electrocatalyst in HER is also provided. Lastly, synthesis methods used to prepare TMPs, vital performance parameters for HER and various potential strategies used to improve the electrocatalytic activity performance of TMPs are explained.

Chapter 3: describes the synthesis and characterization of small and shape controlled amorphous and crystalline molybdenum phosphide (MoP) nanoparticles and their application as electrocatalysts in hydrogen evolution reaction (HER). The rationale behind the difference in the observed catalytic activity between the amorphous and crystalline MoP nanoparticles is explored. This chapter is a published peer reviewed journal article: *New Journal of Chemistry* 44 (2020) 14041-14049.

Chapter 4: outlines the use of colloidal synthesis to prepare two phases of tungsten phosphide (WP and α -WP₂) for use as HER catalysts. Phase-dependant electrocatalytic activity of colloidal synthesized WP and α -WP₂ electrocatalysts for hydrogen evolution reaction. This chapter is a published peer reviewed journal article: *New Journal of Chemistry* 45 (2021) 15594-15606.

Chapter 5: provides a facile route to synthesize amorphous and crystalline W-doped MoP nanoparticles using colloidal synthesis and their use as electrocatalysts in HER. The reported results demonstrate how the introduction of W-dopant into the crystal lattice of MoP

nanoparticles in combination with using an amorphous architecture improves the catalytic properties of the nanoparticles.

Chapter 6: offers a simple route to tailor the electronic properties of α -WP₂ by introducing Mo-dopant atoms into its crystal lattice using colloidal synthesis. A systematic study of the effect of dopant concentration on the catalytic activity of Mo/ α -WP₂ is outlined. Furthermore, structural changes of the most active catalyst (Mo(10%)/ α -WP₂) observed with change in annealing temperature are reported. The catalytic activity of Mo(10%)/ α -WP₂ with varying degrees of crystallinity are explored. This chapter is under peer review in the International Journal of Hydrogen Energy. Manuscript ID: HE-D-21-04366.

Chapter 7: provides general conclusions of the work reported and highlights recommendations for future work.

Chapter 1

General background

1. Problem statement

The availability of reliable sources of energy is important for social and human progress across the globe. To date, humans rely mainly on the burning of fossil fuels in order to sustain the increase in human population, urbanization and industrialization. This has resulted in a rapid depletion of traditional sources of energy overtime, making it important to find alternatives to supplement the high demand.¹⁻² Molecular hydrogen has gained unprecedented momentum as a clean energy source because it produces no greenhouse gases, has a high energy density and is storable. Water electrolysis has emerged as a promising and environmentally friendly method used to generate hydrogen by using electricity in conjunction with an electrocatalyst to decompose water into oxygen and hydrogen. The electricity used to drive electrolysis can be derived from other renewable sources such as solar, wind and hydrothermal energy.³⁻⁵ An electrocatalyst plays an important role in electrolysis as it allows for hydrogen to be produced with the least amount of energy. Up to now, platinum and its alloys are still the most active catalysts in the production of hydrogen from water. But the exorbitant prices associated with it makes it undesirable for large scale application. Recently, transition metal phosphides have opened a new area of research as materials capable of displaying excellent activity in electrolytes of all pH range.⁴⁻⁵ However, there has been drawbacks into their development due to the fact that their preparation requires solid-state reactions which are only possible at high temperature and pressure. These reactions also require the use of the flammable elemental phosphorus (P) as the source of phosphorus. In addition, solid-state reactions offer little room for optimization of the reaction conditions and hence no control over the resulting characteristics of the synthesized nanomaterials. Owing to the drawbacks associated with solid-state reactions, more research needs to be conducted using simple and safe methods of synthesis.⁶

2. Motivation and rationale

Transition metal phosphides (TMPs) have proven to be promising alternative candidate electrocatalysts because they possess the sort after physical properties which resemble those of

borides, nitrides, carbides and silicides. The combination of these properties means that TMPs conduct electricity and heat efficiently, they are rigid and exhibit high chemical and thermal stability. The forementioned parameters play an important role towards the activity and stability of an electrocatalyst. Among other emerging methods of synthesis, colloidal synthesis has materialized as a suitable option for preparing TMPs in such a way that allows for optimization of reaction conditions and hence control over size, morphology, and crystal phase of the nanomaterials. By being able to control the properties of the nanomaterials, their influence on the catalytic activity can be studied and strategies to improve their performance can be devised. TMPs have been proven to be high performance catalysts with high activity, high stability, and nearly 100% Faradic efficiency in not only strong acidic solutions, but also in strong alkaline and neutral media for electrochemical hydrogen evolution. Hence, there is a need for intensive research on TMP's as alternative materials that can be produced easily and at low production cost. The search for this new class of materials is therefore of vital importance in the realization of efficient electrocatalysts in the production of hydrogen gas.

3. Aim and Objectives

The aim of this work was to employ a facile colloidal synthesis method to prepare and characterize molybdenum phosphide, tungsten-doped molybdenum phosphide, tungsten phosphide, and molybdenum-doped tungsten phosphide nanoparticles for application as alternative electrocatalysts to Pt-based materials in hydrogen evolution reaction (HER). To fulfil the forementioned aim, the following objectives were identified.

- ❖ To synthesize and characterize amorphous and crystalline phases of MoP and W-doped MoP nanoparticles.
- ❖ To synthesize and characterize crystalline WP and α -WP₂ nanoparticles.
- ❖ To synthesize and characterize Mo-doped α -WP₂ nanoparticles with varying dopant concentration.
- ❖ Application of the synthesized nanoparticles as electrocatalysts for hydrogen evolution reaction.

4. References

1. S. Chu, A. Majumdar, Opportunities and challenges for a sustainable energy future, *Nature* 488 (2012) 294-303.
2. T.R. Cook, D.K. Dogutan, S.Y. Reece, Y. Surendranath, T.S. Teets, D.G. Nocera, Solar energy supply and storage for the legacy and nonlegacy worlds, *Chemical Reviews* 110 (2010) 6474-6502.
3. X. Peng, C. Pi, X. Zhang, S. Li, K. Huo, P.K. Chu, Recent progress of transition metal nitrides for efficient electrocatalytic water splitting, *Sustain. Energy Fuels* 3 (2019) 366-381.
4. H. Du, R. Kong, X. Guo, F. Qu, J. Li, Recent progress in transition metal phosphides with enhanced electrocatalysis for hydrogen evolution, *Nanoscale* 10 (2018) 21617-21624.
5. P. Xiao, M. A. Sk, L. Thia, X. Ge, R. J. Lim, J.-Y. Wang, K. H. Lim, X. Wang, Molybdenum phosphide as an efficient electrocatalyst for the hydrogen evolution reaction *Energy and Environmental Science* 7 (2014) 2624–2629.
6. S.S. Nkabinde, Z.B. Ndala, N.P. Shumbula, T. Kolokoto, O. Nchoe, G.N. Ngubeni, K.P. Mubiayi, N. Moloto, Delineating the role of crystallinity in the electrocatalytic activity of colloiddally synthesized MoP nanocrystals, *New Journal of Chemistry* 44 (2020) 14041-14049.

Chapter 2

Literature review

1. Colloidal synthesis of nanoparticles

The utilization of the colloidal synthesis method to produce nanoparticles has gained momentum as a promising route for preparation of materials that can be employed in various applications such as catalysis, electronics, biomedicine, magnetism, and optics.¹ Due to the large scale of potential commercial applications, advancements in colloidal synthesis can have beneficial effects both economically and environmentally. Solution phase synthesis methods come with the convenience of having control over the ultimate composition, crystallinity, size, crystal structure and morphology.²⁻⁴ The forementioned characteristics have a significant influence on the resulting physical and chemical properties of the nanoparticles. For instance, by varying the reaction conditions (i.e. time, temperature, type of capping agents, solvents, and precursor concentration), the size, morphology and crystal phase of the nanoparticles can be modified which in turn tunes the optical and magnetic properties.⁵⁻⁸ Systematic optimization of the photoluminescence and absorption properties of these materials has unlocked endless possible applications in biological imaging, active layer in photovoltaics, fluorescent probes and light emitting diodes.⁹⁻¹² Nickel selenide nanocrystals exhibiting phase-dependant catalytic properties have been prepared using colloidal synthesis, and are being used as counter electrodes in the redox reaction of iodide/triiodide electrolyte in dye sensitized solar cells.¹³ Another precedence of employing nanoparticles prepared via colloidal synthesis is their dispersibility in common solvents, which makes them desirable to solution-based drop casting, roll to roll processing, printing and spin coating, which are highly scalable processes.¹⁴⁻¹⁶

As the use of colloidal synthesis continues to grow, promoting the discovery of sort after properties in nanoscale materials, their use in multiple industrial applications becomes possible especially in heterogeneous catalysis. The use of colloidal nanoparticles offers many advantages in heterogeneous catalysis applications, allowing sophisticated surface science techniques to provide a deeper understanding of how chemical reactions occur at the catalyst surface. Catalyst materials in the nanoscale region possess high surface area compared to their bulk counterparts and hence display enhanced catalytic activity due to increased number of exposed active sites. Solid-state reactions rely on the use of high temperatures which routinely

generate crystalline and thermodynamically stable structures, typically with large particle size and poor size uniformity.¹⁷ Alternatively, solution-phase methods not only produce materials with uniform composition but also with a very narrow size distribution. Amorphous materials with uniform size and morphology, for example, are attainable with solution based colloidal methods, as are some non-equilibrium phases.¹⁸⁻²⁰ In an effort to understand the intrinsic properties of a catalyst that leads to enhanced performance, comprehension of the crystallinity, size, shape/facets, composition and structure control is important.

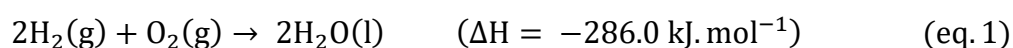
Different materials are made up of different crystal facets which catalyse a specific reaction better than others. Benzene hydrogenation studies done on the surface of a Pt crystal revealed that the (111) surface favours formation of both cyclohexane and cyclohexene whereas the (100) surface generate only cyclohexane. These studies have allowed for colloidal synthesis to be employed to synthesise Pt nanocubes that possess only the (100) active face which selectively yields cyclohexane during the hydrogenation of benzene.²¹ Two different crystal phases of cobalt phosphide, CoP and Co₂P, were compared directly as electrocatalysts for HER. The results demonstrated that even though CoP and Co₂P had nearly the same nanosphere morphology, surface area and size, CoP was more active. The difference in the observed performance was attributed to more exposed (111) facets on CoP surfaces.²² Amorphous and crystalline iron phosphide (FeP) nanoparticles were prepared via colloidal synthesis using temperatures of 180 and 250 °C, respectively. The comparative electrocatalytic activity study between the nanoscaled FeP with different crystallinity revealed that the amorphous nanoparticles were more active in catalysing hydrogen evolution reactions.²³ Different sizes of nickel phosphide nanoparticles were prepared via colloidal synthesis and tested as electrocatalysts for HER. Electrochemical tests indicated that by decreasing the size of the nanoparticles, the electrochemical activity of the nickel phosphide electrocatalyst could be improved.²⁴ Iron, cobalt, manganese, molybdenum metals were systematically introduced into the crystal lattice of NiP to form transition-metal doped NiP nanocrystals using colloidal synthesis. The introduction of the dopant metal did not alter the morphology nor did they result in the formation of new phases. Compared to pristine NiP, the electrocatalytic activity of the metal-doped NiP was significantly improved.²⁵

Previous studies have shown that it is important to have control over reaction parameters as it allows for tailoring of materials properties and potentially improve catalytic activity. The commonly used methods in the synthesis of transition metal phosphides do not offer the flexibility that is possible with colloidal synthesis. Hence, the majority of this thesis will be

expanding on the colloidal synthesis of other transition metal phosphides (MoP, WP, α -WP₂, WMoP, and Mo/ α -WP₂) for application as electrocatalysts in electrochemical water splitting via the hydrogen evolution reaction (HER) route in acidic media.

2. Electrochemical water splitting

For more than a century, the global energy demand has been sustained by non-renewable sources of energy such as coal, oil and natural gas. Non-renewable sources supply around 80% of our energy making it possible to power-up businesses, propel vehicles and keep the lights on in our homes.²⁵⁻²⁹ Nevertheless, the non-renewable energy sources will eventually be depleted and the pollution associated with their expeditious consumption will have long lasting negative effect on mankind and the environment.³⁰⁻³¹ In order to curb a total black out resulting from the depletion of fossil fuels and to minimize global warming, research efforts are being directed into increasing the contribution of renewable sources into the energy grid. Hydrogen, as an energy carrier, has emerged as a viable alternative to fossil fuels. Hydrogen energy is based on the use of molecular hydrogen harvested from hydrogen containing compounds to produce energy that can be utilised in daily practical uses. Hydrogen is considered an optimum alternative due to the fact that it has a very high energy density, non-toxic, most abundant element in nature and generates water as a by-product after it has been utilized (eq. 1).³²⁻³⁴



From eq. 1 it can be seen that 286.0 kJ energy is generated from 1 mol reaction of oxygen with hydrogen. Hence, the mass hydrogen energy density (Energy = 286.0 kJ.mol⁻¹ x 0.5 mol.g⁻¹) works out to be 143.0 kJ.g⁻¹, which is the highest energy density compared to other fuels.³⁵ Large scale production of hydrogen gas is traditionally done through steam methane reforming, and gasification of petroleum coke and coal.³⁶⁻³⁷ These traditional methods require high operating temperatures and generate greenhouse gases as by-products which makes them less desirable as clean technologies are becoming mandatory. Recently, electrochemical water splitting has received a lot of attention as an alternative method for the production of hydrogen. Electrochemical water splitting is a clean and efficient method used in the production of molecular hydrogen and oxygen through the decomposition of water in response to a passage of an electric current.³⁸⁻³⁹ The electrolysis of water can be divided into two half reactions, the hydrogen evolution reaction (HER) and oxygen evolution reaction (OER) as depicted in Fig.

1.⁴⁰ Depending on the pH of the reaction media in which water electrolysis is conducted, it can be described chemically using the following equations:

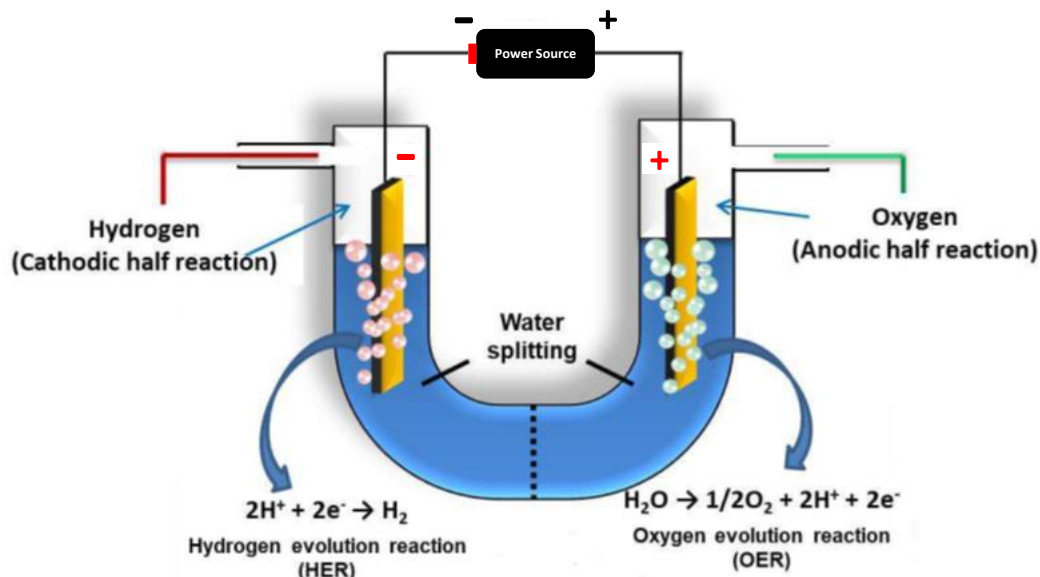
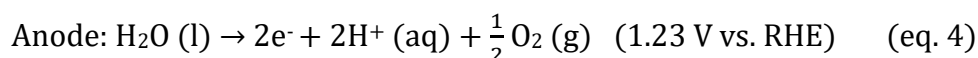
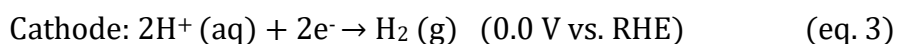


Fig. 1: Graphical representation of hydrogen evolution reaction (HER) and oxygen evolution reaction (OER) via water electrolysis.⁴⁰

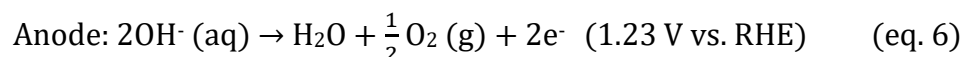
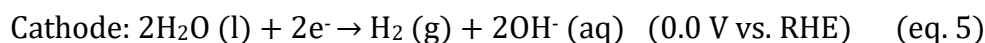
Total reaction:



Acidic media: HER



Alkaline/neutral media: OER



A combination of the cathodic and anodic half reactions shows that a thermodynamic total voltage of 1.23 V (25 °C, 1 atm) is required to drive water splitting. However, voltages higher than the thermodynamic total voltage are required to accomplish electrochemical water splitting. The additional voltage (i.e. overpotential) is used to overcome intrinsic activation barriers, contact and solution resistance.⁴¹⁻⁴² The goal in electrolysis is to produce hydrogen using the least amount of overpotential, and this is achieved through using a highly efficient catalyst.

For HER conducted in an acidic media, there are two possible mechanisms through which hydrogen can be generated, with three possible reactions as illustrated in Fig. 2.⁴³⁻⁴⁶

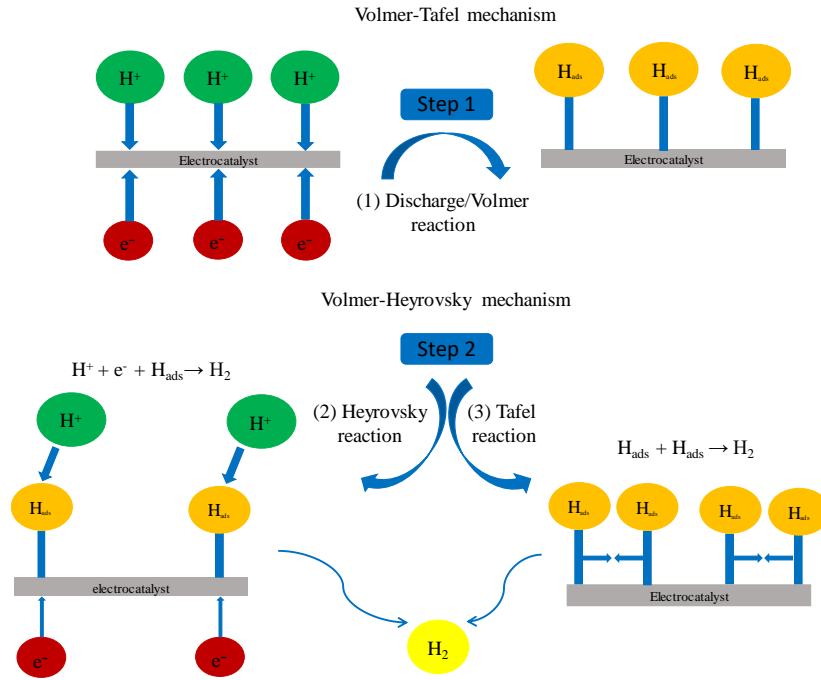
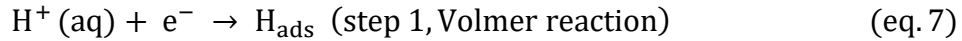


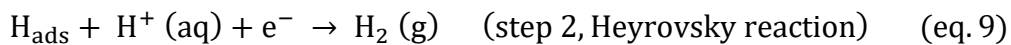
Fig. 2: The two mechanisms of HER on the electrocatalyst surface.

The initial step is the discharge process (Volmer reaction). In this step, an electron migrates to the cathode surface in response to an applied voltage, where it captures a proton (H⁺) in the solution, resulting in an adsorbed atom (i.e. intermediate state) on the active site of the catalytic cathode surface.



$$b_{1,v} = \frac{2.3RT}{\alpha F} \quad (\text{eq. 8})$$

Where $b_{1,v}$ is the Tafel slope, α is the symmetry coefficient with a value of 0.5, F is the Faraday constant, R is the ideal constant, and T is the absolute temperature. The second step can occur via two different pathways to produce H₂ and the first is called the Heyrovsky reaction:



$$b_{2,H} = \frac{2.3RT}{(1 + \alpha)F} \quad (\text{eq. 10})$$

In the case where the coverage of H_{ads} is low, the H_{ads} prefers to react with a new e⁻ and another H⁺ in the solution to produce H₂ in an electrochemical desorption step (eq. 9). However, at high

H_{ads} coverage, the recombination between H_{ads} adjacent to one other is dominant and is called the Tafel reaction or the chemical desorption step.



$$b_{2,T} = \frac{2.3RF}{2F} \quad (\text{eq. 12})$$

Thermodynamically, the overall process as shown by the reactions above could be described as continuous adsorption and desorption of H_{ads} species from the catalytically active sites. An efficient catalyst should find balance between being able to bind strongly to H_{ads} species to allow for formation of $H_{\text{ads}}-H_{\text{ads}}$ bond, but also allow for rapid desorption of the generated H_2 from the surface of the catalyst.⁴⁷⁻⁵⁰ In hydrogen production, the electrocatalytic reduction of protons (H^+) into molecular hydrogen (H_2) is highly dependent on the type of electrocatalyst being used. The main factor currently hindering large scale production of hydrogen gas is the limited number of cheap, readily available and highly active electrocatalysts. To mitigate this drawback, catalysts have to be continuously studied in order to discover new catalysts, improve their activity and understand the intrinsic properties responsible for observed catalytic activity.⁵⁰⁻⁵⁴ In spite of being the most expensive and scarce noble metal, Pt-group metals (Pt⁵⁵, Rh⁵⁶, Pd⁵⁷, Ir⁵⁸, etc.) are still the commonly used and most efficient electrocatalysts for chemical reactions that form the basis of renewable energy sources, such as HER, fuel cells and solar generators.

Pt-group metals are considered exceptional electrocatalysts in HER due to the ability to produce very high current densities at low overpotential.⁵⁹⁻⁶⁰ In acidic solutions, the electrocatalytic reduction of protons (H^+) into molecular hydrogen (H_2) is highly dependent on the type of electrocatalyst being used. Recently, a number of acid-stable HER electrocatalysts have showed potential as inexpensive and readily available non-noble alternatives to Pt such as transition metal oxides, nitrides, carbides and phosphides.⁶¹⁻⁶⁴ Amongst these non-noble catalysts, transition metal phosphides stand out due to the limited work reported on their activity as HER catalysts. Furthermore, they possess an unexpectedly high stability accompanied by high activity emanating from the ability of the metal to act as hydride acceptor sites and the phosphorus acting as proton acceptor sites which both facilitate catalysis of HER.⁶⁵

3. Transition metal phosphides (TMPs)

TMPs are a group of compounds that are formed as a result of a reaction between phosphorus and any other transition metal element in the periodic table. They were first discovered back in the 18th century, however, they remained exotic for scientists as no real application was reported in literature for 200 years.⁶⁶ TMPs have since been gradually applied to lithium ion batteries, hydrodenitrogenation, hydrodesulfurization, photocatalytic degradation, etc.⁶⁷⁻⁷⁰ Given the similarities in the mechanism through which hydrodesulfurization and hydrogen evolution reaction occur, TMPs were hypothesized as potentially active HER electrocatalysts.⁷¹ To date, several different types of TMPs such as Cu₃P, W_xP_y, Mo_xP_y, Co_xP_y, Fe_xP_y and Ni_xP_y have shown promising HER or OER activities. The application and development of TMPs over the years has been hindered by the type of synthesis methods used which required the use of high temperatures/pressures with highly flammable elemental phosphorus as the source of phosphorus which was dangerous and difficult to do.⁷¹⁻⁷² These materials can form different bonds ranging from ionic, metallic and covalent when bonded to alkali/alkaline earth metals, transition metals and main group elements, respectively. Transition metal phosphides (TMPs) are of interest mainly because they possess the well sort after physical properties resembling those of nitrides, carbides, silicides and borides. Apart from abundance and cheapness, the combination of both ceramic properties (i.e. hardness and strength) and transport properties (i.e. electrical and thermal conductivity) have made them an interesting class of compounds in magnetic and electronic applications.⁷³⁻⁷⁶ TMPs have been explored extensively as highly active catalysts in hydrotreating and hydrogenation reactions, with the focus shifting more into their use as electrocatalysts for HER in the last decade.⁷⁷⁻⁸⁰ The high activity of TMPs originates from the ability of the highly electronegative phosphorus atom to draw electrons away from the transition metal. The resulting high electron density on the P atoms act as a base, trapping positively charged protons. Depending on the metal (M_x) to phosphorus (P_y) stoichiometric ratio, TMPs can be classified into metal-rich phosphides (x>y) and phosphorus-rich phosphides (x<y).⁸¹⁻⁸³ The attractive properties displayed by the phosphorus-rich phosphides makes them more sort after than the metal-rich phosphides. Even though TMPs exhibit properties resembling those of nitrides, carbides, silicides and borides, they differ significantly in structure due to the difference in atomic radius of the P atoms relative to N, C, Si and B atoms. The N atoms (0.070 nm) and C atoms (0.077 nm) in nitrides and carbides, respectively, are situated in the interstitial spaces between the host metal atoms to form relatively simple lattices. Contrary, in phosphides, the bigger phosphorus atoms (0.115 nm) do

not fit in octahedral holes formed by closed-packed metal atoms, instead the P atoms are surrounded by metal atoms in the form of a triangular prism (Fig. 3a). A 9-fold tetrakaidekahedral (TKD) coordination is formed in metal-rich phosphides by the addition of metal atoms near the centres of vertical faces of the prism (Fig. 3b).^{75,84-85}

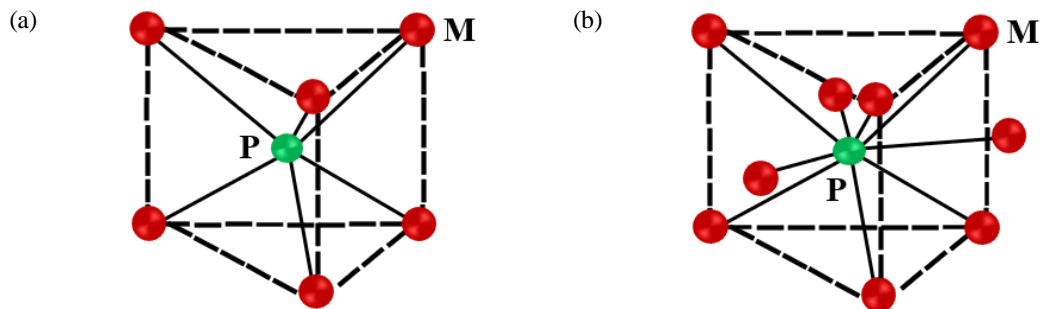


Fig. 3: (a) Triangular prism and (b) tetrakaidekahedral structures of metal phosphides.⁸⁴

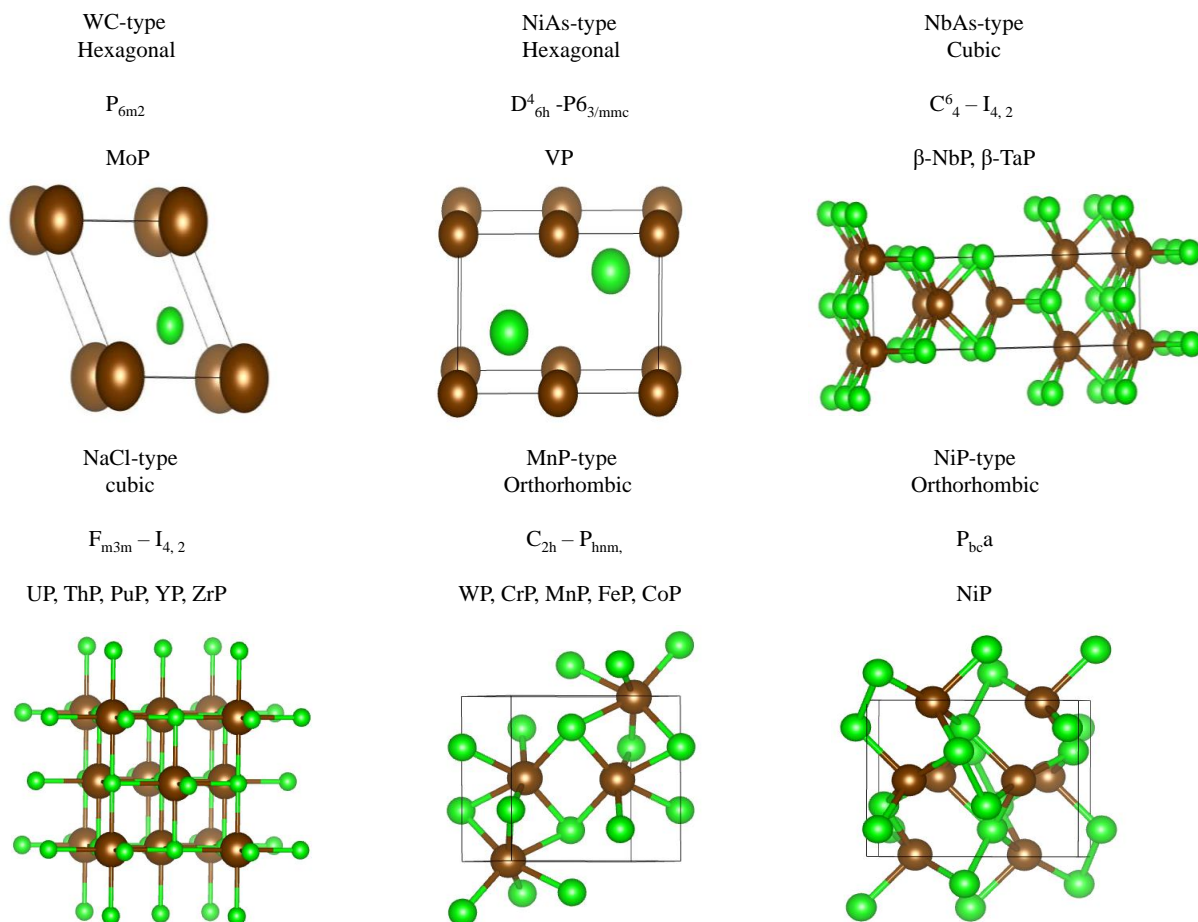


Fig. 4: Various crystal structures of metal-rich phosphides.⁸⁴ (phosphorus = green, metal = brown)

The triangular prism structure adopted by some TMPs resemble those observed in some transition metal sulphides (TMSs). Unlike TMSs which take on a layered structure and are semiconductors or insulators, TMPs display as isotropic morphology and have metallic conducting properties. The surface metal atoms in isotropic crystals are well exposed to fluid phase reactants and hence higher electrocatalytic activity should be observed in TMPs than in TMSs which are less isotropic in composition. Through variation of the M:P precursor ratio during synthesis, a wide range of TMPs structures arise from different arrangements of the triangular prism and tetrakaidekahedral coordination building blocks as shown in Fig. 4.^{75,84-85}

4. Synthesis of transition metal phosphides (TMPs)

Various researchers have concisely reported four main approaches used to successfully prepare TMPs. The methods are (i) gas-solid phase reaction, (ii) solid-state reaction, (iii) electrodeposition and (iv) solution-phase reaction.⁸⁶⁻⁸⁹

4.1. Gas-solid phase reaction

Transition metal phosphides can be produced using gas-solid reactions which entails heating a mixture of the phosphorus and metal sources under the flow of an inert gas or hydrogen, depending on the nature of the phosphorus source being used. The commonly used phosphine (PH₃) in its gaseous state allows for efficient formation of metal phosphides, but the associated high toxicity even at low concentrations (i.e. ppm) hinders its use as a direct suitable phosphorus source. Alternatively, the in-situ formation of PH₃ from compounds such as hypophosphites (NaH₂PO₂ and NH₄H₂PO₂), phosphates (H₂PO₄⁻) and phosphites (H₂PO₃⁻) has opened a less hazardous route in the synthesis of metal phosphides. Phosphates and phosphites require an external hydrogen source to generate PH₃ under inert gas, whereas hypophosphites form the PH₃ through decomposition at ~ 250 °C. The in-situ generated PH₃ (eq. 13) reacts with the metal sources.⁹⁰⁻⁹²



The use of a gaseous source of phosphorus and the absence of a coordinating solvent allows the resulting particles to take on the initial morphology of the metal sources. The mixing, deposition and treatment of the phosphorus and metal sources on a high surface carrier makes this method suitable for preparation of supported metal phosphides. The metal sources

commonly used in gas-phase reactions directly react with metal oxides, metal-organic frameworks (MOFs), metal salts and metal hydroxides. Yu et. al. reported on the synthesis of a Ni₂P nanoarray catalyst embedded on a Ni foam substrate (denoted as Ni₂P/NF). Firstly, Ni(OH)₂/NF was prepared using a two-step hydrothermal method. An ultrasonically cleaned Ni foam plate immersed in a 1 mM transparent aqueous solution of (NH₄)₂HPO₄ (35 mL) was transferred into a sealed autoclave (50 mL) and heated at 180 °C for different times to prepare the precursors. Using deionized water, the resulting green precursors were washed multiple times and dried in air. To form Ni(OH)₂/NF, the green precursors were transferred into 0.1 M KOH aqueous solution (30 mL) contained in a Teflon-lined stainless-steel autoclave. After heating the autoclave for 5 h at 120 °C and allowing it to cool to room temperature, light grey Ni(OH)₂/NF nanoarrays were obtained after washing with deionized water and drying in air. To synthesize Ni₂P/NF, low temperature calcination was used. A 1:10 weight ratio of Ni(OH)₂/NF and Na₂H₂PO₂•H₂O were placed on opposite ends of a ceramic boat with Na₂H₂PO₂•H₂O located at the upstream side. The samples were then heated for 30 min at 300 °C under inert Ar environment, resulting to the formation of black Ni₂P/NF powders.⁹³

4.2. Solid-state reduction

Solid-state reactions involve the direct reaction of a phosphorus source (Na₃P, P, yellow or red phosphorus) and metal precursors (Fig. 5). The successful formation of metal phosphides in this type of reaction depends highly on long reaction time, high temperature and high-pressure systems.

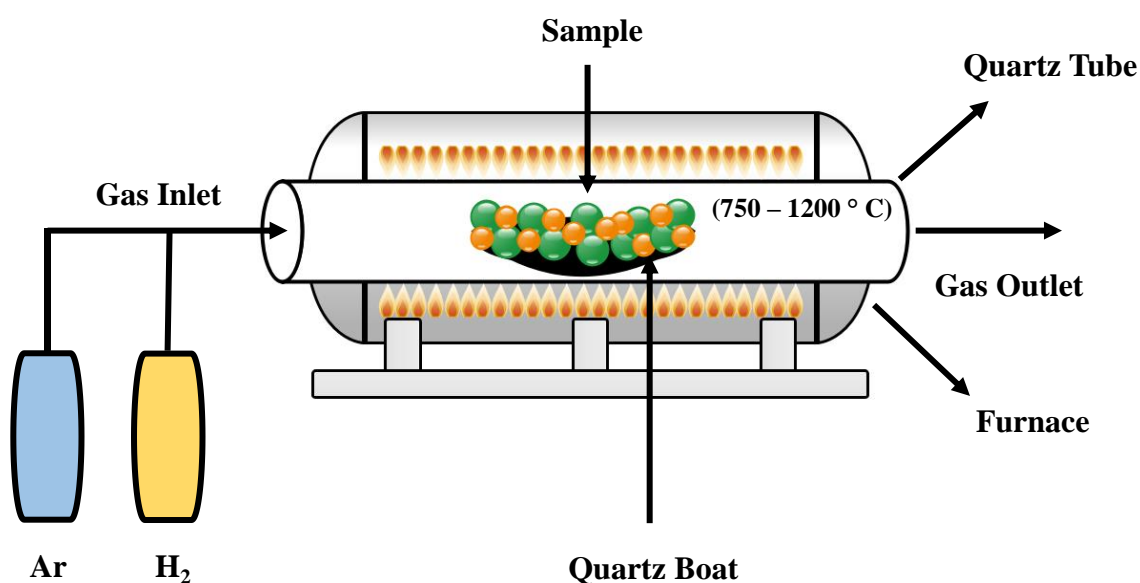


Fig. 5: Schematic illustration of a typical solid-state reduction reaction setup.

In addition to the lack of control of the resulting material characteristics from solid mixtures, the reactions are reported to be highly exothermic. For this reason, they must be performed in inert environment to control the rate of the reaction and reduce the increased reaction temperature. Pi et al. synthesized WP_2 particles with a size of 2-3 micrometres by uniformly mixing and vacuum sealing ($\sim 7 \times 10^{-4}$ Pa) elemental phosphorus and tungsten trioxide (WO_3) in a silica tube. The silica tube was then inserted into a muffle furnace which was heated at a rate of $10\text{ }^\circ\text{C}/\text{min}$ to $950\text{ }^\circ\text{C}$ and maintained for a period of 5 h. After cooling to room temperature and washing multiple times, the black particles were dried under a vacuum oven for 12 h at $60\text{ }^\circ\text{C}$.⁹⁴ Bulk MoP was synthesized by Ge et al. by dissolving $(NH_4)_2HPO_4$ and ammonium molybdate in water while stirring. Following drying at $120\text{ }^\circ\text{C}$ and homogeneous mixing, the obtained powder was placed in a porcelain boat and heated at a rate of $5\text{ }^\circ\text{C}/\text{min}$ to $850\text{ }^\circ\text{C}$ under $H_2(5\%)/Ar$ for 150 min.⁹⁵ Fang et al. employed a solid-state synthesis method to prepare CoP and MoP hybrids via a two-step thermal treatment method. Cobalt nitrate, ammonium molybdate and ammonium dihydrogen phosphate were dissolved in water, ultrasonicated and dried in the oven at $80\text{ }^\circ\text{C}$. The solid mixture was transferred into a quartz tube furnace and heated at a rate of $10\text{ }^\circ\text{C}/\text{min}$ to $350\text{ }^\circ\text{C}$ under Ar flow (100 sccm). After reaching $350\text{ }^\circ\text{C}$, the temperature was reduced to $300\text{ }^\circ\text{C}$ and held for 1 h. The gas flow was subsequently changed to H_2/Ar flow (H_2 , 50 sccm; Ar, 50 sccm) and temperature increased further to $800\text{ }^\circ\text{C}$ ($15\text{ }^\circ\text{C}/\text{min}$) and held for 2 h to produce $Co_{0.5}Mo_{0.5}P$.⁹⁶

4.3. Electrodeposition

Electrodeposition is a well-known facile and mild preparation method capable of producing metal phosphide structures under room temperature without the need for post synthetic treatment. In an electrochemical cell containing phosphorus and metal containing salts as the electrolyte, the ions migrate to the electrode surface (e.g. conducting substrate) in response to an applied external electric field (Fig. 6). Layers of the phosphorus and metal are deposited as a result of the redox reaction at the surface of the working electrode. The absence of a surfactant or capping agent means that the synthesis method can be greatly simplified. Bai et al. reported the preparation of Co/CoP films on Ni foam by galvanostatic electrodeposition at a current density of $0.5\text{ A}\cdot\text{cm}^{-2}$ in a plating bath containing $CoSO_4\cdot 7H_2O$, $NaH_2PO_2\cdot H_2O$ and CH_3COONa . The as prepared Co/CoP films were used as efficient catalysts for hydrogen evolution reactions (HER) in alkaline solution.⁹⁷ Wu et al., employed a facile electrochemical method to prepare a NiP electrode supported on Ni foam by linear sweep voltammetry scans

in the range -0.3 to -0.9 V (vs Ag/AgCl) in an electrolyte containing NiCl_2 and NaH_2PO_4 in water.⁹⁸

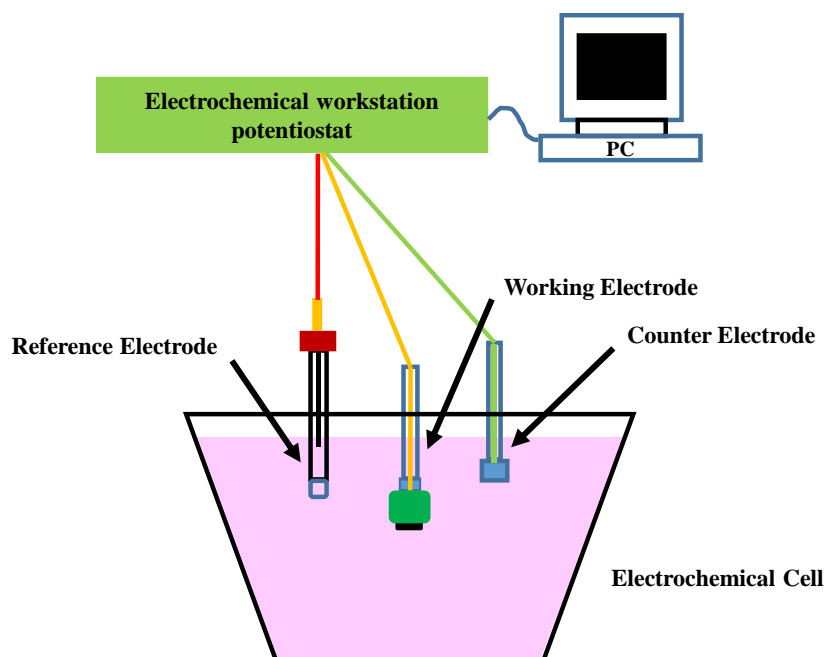


Fig. 6: Illustration of the electrodeposition method conducted using a conventional three-electrode system.

4.4. Colloidal synthesis method

The colloidal synthesis method entails the precipitation of solid nanoparticles from a homogeneous precursor solution. Typically, the precursor solution is made up of solvent, metal/non-metal precursors and organic capping agent. Upon exposure of the mixture to elevated temperature, the precursor dissociates into active molecular or atomic species (monomers) that subsequently react to generate nanoparticles. This method has proven to be an effective route as it allows for tailoring of physical properties such as size, shape and crystal phase by changing precursors, organic capping agent, reaction time, solvent, etc.⁹⁹⁻¹⁰¹ Nanoparticles synthesized using the colloidal method disperse easily in most polar organic solvents to form colloid suspensions that are stable.¹²⁻¹⁶ These suspensions are suitable for use in the production of coatings, nanofluids and thin films. Because of the simplicity of the apparatus required to produce colloidal nanoparticles, there is a huge potential for scaling up to produce quantities large enough for industrial applications.¹⁰² Unlike other traditional synthesis methods, colloidal reactions can be successfully conducted at lower temperatures and atmospheric pressure making them relatively safe. Theoretically, the colloidal synthesis

method involves two main stages: nucleation from initial homogeneous solution and growth of the preformed nuclei. The nucleation and growth processes are typically described by the Lamer and Dinegar mechanism of colloid formation.¹⁰³⁻¹⁰⁴

4.4.1. Nucleation process

Generally, nucleation is described as a process whereby active atomic or molecular species in a reaction medium merge to form nuclei where additional ions, atoms or molecules can be incorporated to facilitate crystal growth.¹⁰⁵ In certain cases, this process can be observed physically during a reaction through formation of a precipitate or colour change of the reaction solution as the reaction progresses. Nucleation can occur either homogeneously or heterogeneously. Homogeneous nucleation takes place where atomic or molecular species coalesce to form nuclei in response to fluctuations in the thermodynamic concentration in the absence of any structural inhomogeneities (dislocations, grain boundaries, container surface, impurities). On the contrary, heterogeneous nucleation occurs on pre-existing nuclei, substrate, surface, ion, particle or dust. In the liquid phase, the presence of a stable nucleation surface allows for heterogeneous nucleation to take place easily.¹⁰⁵⁻¹⁰⁷ The formation of a nucleus in homogeneous nucleation can be delineated thermodynamically by focusing on the nanoparticle's total free energy. The Gibbs free energy (ΔG) is interpreted as the sum of the surface free energy and bulk free energy. In the case of a spherical nanocrystal, the ΔG is defined as:

$$\Delta G = \frac{4}{3}\pi r^3 \Delta G_v + 4\pi r^2 y \quad (\text{eq. 14})$$

$$\Delta G_v = \frac{-k_B T \ln(S)}{v} \quad (\text{eq. 15})$$

Where r is the radius, ΔG_v is the bulk free energy change of the crystal, y is the surface energy. The crystal free energy depends on the Boltzman's constant k_B , temperature (T), supersaturation of solution (S), and its molar volume (v).

Plotting the Gibbs free energy against the radius (Fig. 7) results in a plot that demonstrates the effect of the Gibbs bulk free energy on the negative term and the effect of the surface energy (y) on the positive term.^{106, 108-109} Additionally, the plot shows that at a critical cluster radius (r_c) there is a maximum Gibbs energy. The r_c is then described as the smallest radius of particles in a cluster that are stable in solution. In the case where the cluster radius is smaller than r_c ,

instability dominates in the cluster of particles and will re-dissolve in solution. However, for clusters with a radius that is bigger than r_c , growth is favoured due to the stability of the cluster of particles. By using $d\Delta G/dr = 0$, one can solve for r_c from equation 15 which gives

$$r_c = \frac{2\gamma}{|\Delta G_v|} = \frac{2\gamma v}{k_\beta T \ln(S)} \quad (\text{eq. 16})$$

The nucleation rate for N particles at time t can be expressed using the Arrhenius equation where the energy barrier to nucleation is the activation energy, hence nucleation is considered a statistical process where the nucleation rate dN/dt is expressed as

$$\frac{dN}{dt} = A \left(\frac{-\Delta G_c}{k_\beta T} \right) \quad (\text{eq. 17})$$

$$\frac{dN}{dt} = A e^{\left(\frac{16\pi\gamma^3 v^2}{k_\beta^3 T^3 (\ln(S))^2} \right)} \quad (\text{eq. 18})$$

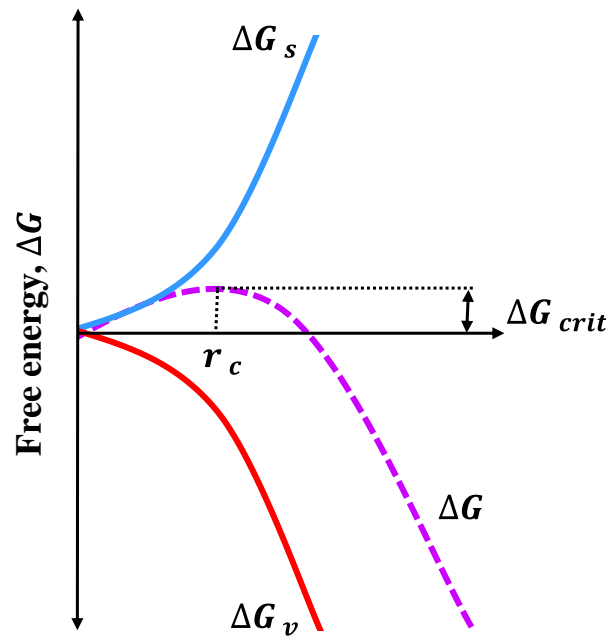


Fig. 7: A graph showing the relationship between the Gibbs free energy versus the radius of the clusters.

LaMer et. al. innovated a theory which explained homogeneous nucleation during the formation of colloidal nanocrystals.^{103, 110} According to LaMer's theory, homogeneous nucleation is described as a process where the formation of many nuclei of the same size occurs when there is a burst of nucleation in response to supersaturation in a solution. Subsequent to nucleation, the pre-formed nuclei grow into crystals without formation of any new nuclei. A

three-step mechanism is used to fully described this process (Fig. 8). The first step describes the formation of monomers from the decomposition of precursors in solution. Monomer formation continues until the solution reaches a critical supersaturation (C_s). In the second step, saturation increase until it reaches a level C_{min} , whereby burst nucleation occurs because the barrier to nucleation has been overcome.

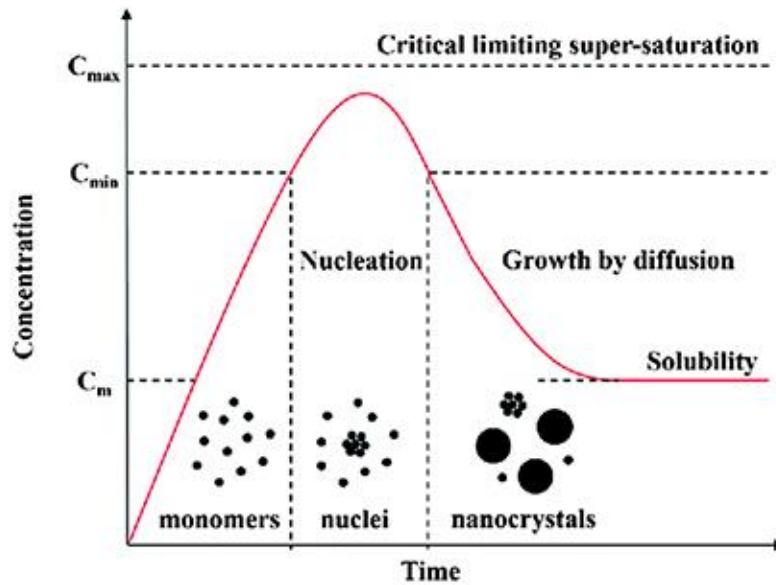


Fig. 8: Graphical representation of the LaMer and Dineger's nucleation mechanism.¹¹¹

Lastly, burst nucleation causes a decrease in monomer concentration which stops nucleation and therefore results in the decrease in supersaturation level. From this point forward, nuclei growth occurs through diffusion of monomers to the sites of nucleation. LaMer and Dinger's mechanism only holds for monodispersed colloidal nanocrystals, it cannot be used to explain cases where formation of nanocrystals with a wide size distribution dominates.¹⁰⁵

4.4.2. Growth process

A decrease in the rate of nucleation results in the accelerated growth of the preformed nuclei. The growth of the nanoparticles is best explained by the Ostwald ripening process.^{105, 112} According to the Ostwald process, larger particles grow at the expense of the smaller particles. The smaller particles in solution are characterized by high surface energy and solubility which makes them unstable. As a result, the monomers making up the smaller particles will segregate and diffuse in the solution to attach to the larger particles which are more stable. Through time,

the number of larger particles will continue to increase, while the number of smaller particles decrease. As this process continues, the average size of particles will become bigger. This phenomenon is undesirable when attempting to synthesize smaller sized particles with a narrow size distribution. Therefore, the burst nucleation step is important in the formation of colloidal nanoparticles. Another possible mechanism is the Finke-Watzky two step mechanism where nucleation and growth occur at the same time. In this mechanism, slow and continuous nucleation is followed by autocatalytic growth of the nanocrystals directly from the precursors. This type of growth is not controlled by monomer diffusion.¹¹³

In the preparation of TMPs, successful formation of the metal-phosphorus bond during colloidal synthesis (Fig. 9) is dependent on the high temperature decomposition ($\geq 300\text{ }^{\circ}\text{C}$) and subsequent reaction between the phosphorus and metal salt precursors in high boiling point solvents (e.g. 1-octadecene, octyl ether, squalene, oleylamine and squalene).

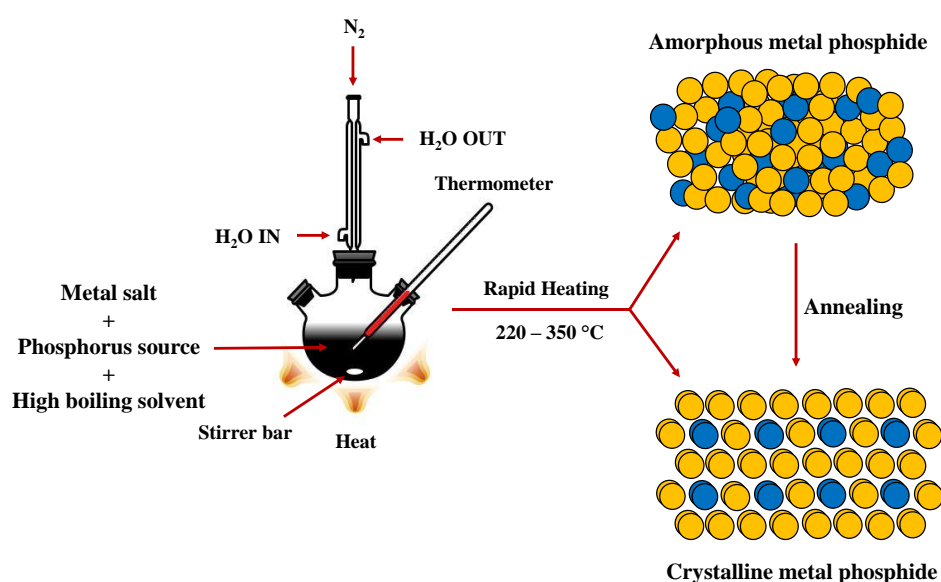


Fig. 9: General schematic representation of the colloidal synthesis method.

Trioctylphosphine (TOP, $\text{P}(\text{C}_8\text{H}_{17})_3$), triphenylphosphine (TPP, $\text{P}(\text{C}_6\text{H}_5)_3$) and tri-n-octylphosphine oxide (TOPO, $\text{PO}[\text{CH}_3(\text{CH}_2)_7]_3$) are the commonly used P sources, with TOP being the most attractive and versatile source.¹¹⁴⁻¹⁷ The catalytic cleavage of the P-C bond in TOP at elevated temperature results in the phosphirization of the metal precursors (e.g. metal oxides, metal chlorides, metal acetate hydrates, metal carbonyls and metal acetylacetonates) to form M-P bonds. The coordinating ability of TOP allows for efficient formation of phosphines and can also facilitate the formation of various sizes and morphologies. McEnaney et. al.

employed a solution-phase synthesis method in which a mixture of squalene, trioctylphosphine and $\text{Mo}(\text{CO})_6$ in a 50 mL three-necked, round-bottom flask was heated for 2 h and 320 °C. The reaction yielded uniform, discrete and amorphous nanoparticles with an average size of 4 nm.¹¹⁸ The same authors reported the synthesis of amorphous WP nanoparticles with an average diameter of 3 nm by heating squalene, trioctylphosphine and $\text{W}(\text{CO})_6$ at 320 °C for 2 h. The WP nanoparticles were deposited on Ti-foil to form a WP/Ti electrode, annealed ($\text{H}_2(5\%)$ Ar(95%)) for 2 h at 450 °C and subsequently used as an electrocatalyst for hydrogen evolution reaction (HER).¹¹⁹ Man et al. synthesized electrocatalytically active spherical NiP nanoparticles (~ 7 nm) by mixing nickel acetate tetrahydrate, oleylamine, trioctylphosphine and tri-n-octylphosphine oxide in a 100 mL three necked round bottom flask. Trace oxygen and moisture were removed under vacuum and the mixture was heated under N_2 flow for 2 h at 300 °C. After cooling the mixture naturally to room temperature, excess ethanol was added to precipitate out the nanoparticles which were collected by centrifugation.¹²⁰ Due to the susceptibility of the phosphines to oxidation, an inert environment is needed for the synthesis of oxygen free metal phosphides. The colloidal synthesis method is sparingly reported in the preparation of TMPs and hence this study aims to close that knowledge gap.

5. Performance parameters for HER

The electrochemical activity of HER electrocatalysts in acidic media can be assessed using a variety of parameters which allow for comparison of different electrocatalysts prepared by various researchers in the field of hydrogen production. The commonly used parameters such as overpotential, Tafel slope, exchange current density and stability are discussed below as they provide valuable information about the catalytic properties of an ideal electrocatalyst.

5.1. Overpotential (η)

Under standard conditions ($T = 298 \text{ K}$, $P_{\text{H}_2} = 1 \text{ atm}$), the electrode potential for HER is defined as zero. However, an additional potential is required to start the HER reaction. The extra potential required to initiate the reaction in the presence of an electrocatalyst is known as the overpotential (η), formerly described as the difference between the equilibrium and applied potential.¹²¹ To allow for unbiased comparison, the overpotential required to produce current density of $10 \text{ mA}\cdot\text{cm}^{-2}$ (Fig. 10) are generally reported for catalysts, and a smaller η indicates more efficient catalytic activity.¹²²

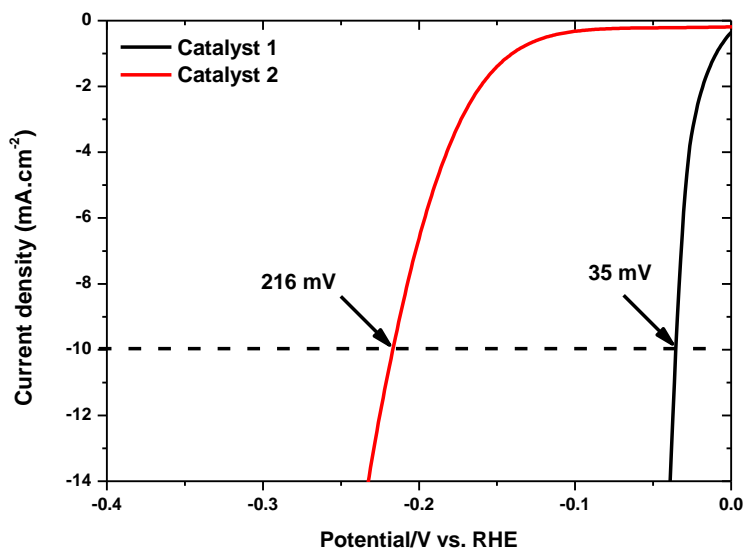


Fig. 10: Linear sweep voltammetry demonstrating catalysts with different catalytic performance based on overpotential required to generate 10 mA.cm⁻².

The value of the overpotential obtained directly from HER is usually higher than the true value as it carries contributions from ohmic drop emanating from the interfaces of the electrocatalyst and the acidic solution. To account for this ohmic drop, IR compensation method is used to get a precise value of the overpotential using the following relationship.

$$E_{\text{corrected}} = IR \quad (\text{eq. 19})$$

$$E_{\text{corrected}} = E_{\text{uncorrected}} - E_{\text{correction}} = E_{\text{uncorrected}} - IR \quad (\text{eq. 20})$$

Where R is the resistance, E is the potential and I is the current through the system. Most electrochemical workstation are capable of determining the value of R directly.¹²³

5.2. Tafel slope and exchange current density

The Tafel slope is another important parameter that is used to evaluate the catalytic activity of an electrocatalyst. The activity of an electrocatalyst is evaluated using linear sweep voltammetry (current density vs overpotential). By replotting the linear sweep voltammetry curve as the Tafel plot (overpotential vs log|current density|) as shown in Fig. 11(a).

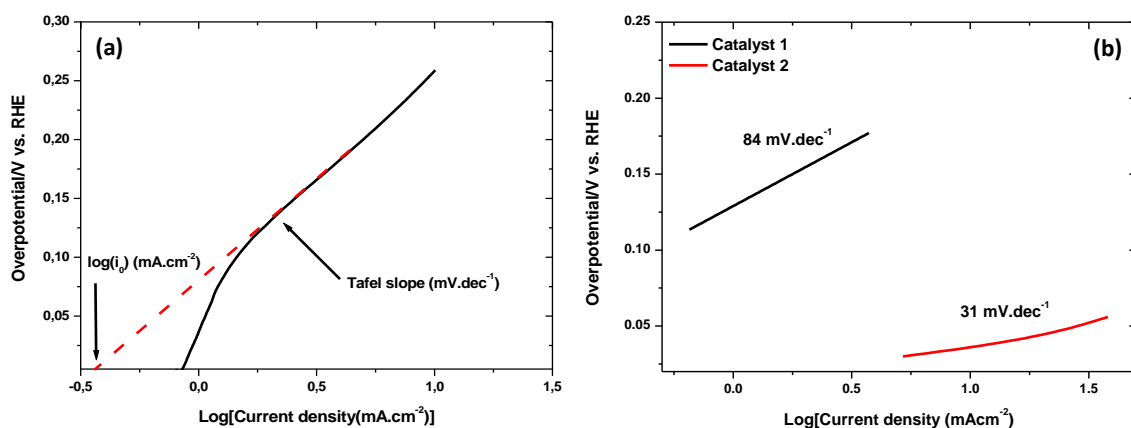


Fig. 11: (a) A plot of overpotential vs log|current density| (b) Tafel slopes of two catalyst exhibiting different activity as extrapolated from the linear region of the overpotential vs log|current density| plot.

The Tafel slope can then be extrapolated from the linear region of the Tafel plot by fitting the Tafel equation (eq. 21).

$$\eta = a + b \log j \quad (\text{eq. 21})$$

Where η is the overpotential, b is the Tafel slope and j is the current density. The extrapolated Tafel slope (Fig. 11(b)) is inversely proportional to the charge transfer coefficient, and catalysts with a small Tafel slope possess a high charge transfer ability.¹²³⁻¹²⁷ In conjunction with Tafel slope, current exchange density (j_0) is another parameter that can be extracted from the Tafel plot. The exchange current density measures the rate of chemical reaction at equilibrium and can be extrapolated from the intercept at zero potential as shown in Fig. 11(b). A catalyst that is able to generate a high exchange current density is considered to be more catalytically active.¹²⁸⁻¹²⁹ A smaller Tafel slope therefore represents a highly active electrocatalyst. Additionally, the Tafel slope is used to understand the reaction pathway and rate determining step (RDS). Theoretically, the calculated Tafel slope of 118.2, 39.4, and 29.6 mV.dec⁻¹ corresponds to the Volmer, Heyrovsky and Tafel reactions, respectively. In the case where the experimentally determined b is closer to 118.2 mV.dec⁻¹, the RDS is the Volmer reaction, and kinetics for adsorption of H-atoms onto the surface of the catalysts is sluggish. The Heyrovsky reaction is the RDS when b is around 39.4 mV.dec⁻¹, and the desorption process controls the generation of H₂. If b is closer to 29.6 mV.dec⁻¹, the rate-limiting step is the combination of adsorbed H atoms and H₂ desorption.¹³⁰⁻¹³³

5.3. Stability

The ability to reuse a catalyst is important in practical applications such as hydrogen evolution reaction. Cyclic voltammetry (CV) and chronopotentiometry or chronoamperometry are the commonly used methods to study the stability of an electrocatalyst. In CV, multiple potential sweeps (e.g. 1000 cycles) are recorded and a comparison is done between the initial and the final cycle (Fig. 12).

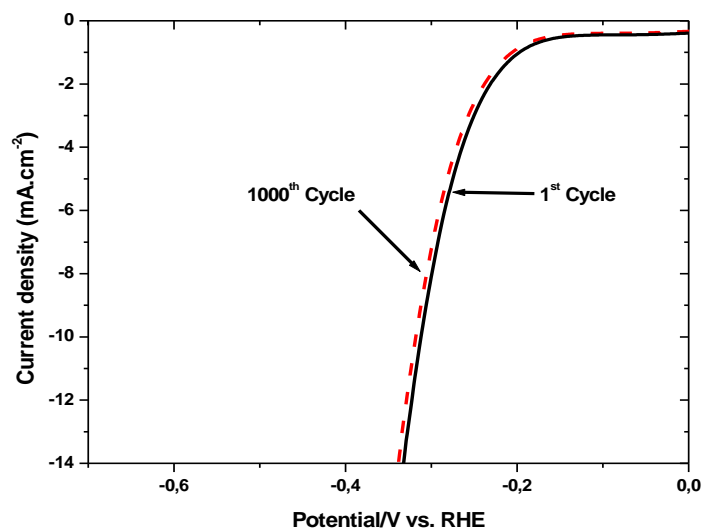


Fig. 12: Linear scan voltammetry curves of a catalyst before and after 1000 potential cycles.

A small change in overpotential or onset overpotential between the 1st and 1000th cycles at constant current density indicates a highly stable electrocatalyst. A larger change in overpotential and onset potential after multiple cycles indicates an easily degradable catalyst. Chronopotentiometry (or chronoamperometry) focuses on the time dependence of the potential (or current density) at a constant current density (or overpotential) of an electrocatalyst. The measurements are conducted over long periods of time (> 12 h) and the durability of the electrocatalyst is determined by the changes in current density and overpotential through time. A catalytically stable electrocatalyst is marked by little variations of the overpotential or current density through time.¹³⁴⁻¹³⁶

6. Enhancing electrocatalytic performance of TMPs

Even though the intrinsic properties of TMPs render them suitable catalysts for HER, their electrocatalytic performance can still be enhanced through structural modification using a variety of strategies. The commonly used strategies to improve catalytic activity such as varying the phosphorus content, doping, crystallinity and incorporation of conducting support are discussed below.

6.1. Tuning M:P stoichiometric ratio

The crystal structure of transition metal phosphides can be visualized as the doping of P atoms onto the metal crystal lattice. Pure metals show poor catalytic activity towards HER due to the high binding energy interaction between the hydrogen ions (H^+) and metal atoms on the surface which inhibit rapid hydrogen dissociation. The incorporation of P atoms therefore plays an important role in the excellent catalytic activity observed in TMPs.¹³⁷⁻¹³⁹ The phosphorus anions create a ligand effect (i.e. ensemble effect) by altering the density of electron around the metal cations which facilitate rapid hydrogen dissociation from the surface of the metal phosphides. Xiao et al. reported a comparative study of the activity of Mo, Mo_3P and MoP as electrocatalyst in HER in both acidic and alkaline solutions. Results indicated that the catalyst with the highest degree of phosphirization (i.e. MoP) possessed the highest catalytic activity and stability over Mo and Mo_3P . The observed catalytic activity order was $MoP > Mo_3P > Mo$. Theoretical calculations from DFT revealed that the phosphirization of Mo to form MoP reduced its hydrogen binding energy to nearly zero and hence the remarkable catalytic performance.⁸¹ Different phases of monodispersed nickel phosphide ($Ni_{12}P_5$, Ni_2P and Ni_5P_4) nanocrystals were prepared by Pan et al. by varying the P:Ni precursor ratio using a thermal decomposition synthesis method. The results showed that the Ni_5P_4 nanocrystals with the highest content of P (44 at %) showed the highest catalytic activity due to the ensemble effect of P.⁸³ Cho et al. successfully transformed Fe nanoparticles through phosphirization into Fe_2P and FeP nanoparticles with well controlled morphology. Similarly, the HER results showed that the FeP nanoparticles displayed superior catalytic activity requiring a small overpotential than Fe_2P to produce current density of 10 mA.cm^{-2} .¹⁴⁰ All the upper-mentioned studies show that the highest catalytic activity is commonly observed in electrocatalysts with high P content.

6.2. Elemental alloying or doping

The introduction of a foreign element (metal or non-metal) in the crystal lattice of TMPs is another way used in the development of highly active HER electrocatalysts. The dopant atoms tune the electronic properties by increasing the electron density of the host catalysts, which in turn allows the positively charged P atoms to efficiently capture protons due to the increased electrostatic affinity, while the positively charged metal atoms act as hydride acceptor sites.^{138, 141-142} Additionally, dopant atoms have been known to introduce defect-sites which exhibit improved hydrogen adsorption properties as determined by DFT calculations. For instance, Kibsgaard and Jaramillo employed a post-sulfidation method to successfully incorporate sulfur (S) onto the surface of molybdenum phosphide (MoP) to produce molybdenum phosphosulfide (MoP/S). A HER comparative study between MoP and MoP/S revealed that overpotentials of 117 and 86 mV, respectively, were required to produce current density of 10 mA.cm⁻². The difference in catalytic activity was attributed to the synergistic effect between the phosphorus and sulfur atoms which promote the formation of a high-surface area mixed anion catalysts with activity higher than those of pure phosphide or sulfide catalysts.¹⁴³ Wang et. al. synthesized a porous Mo-W-P nanostructure through in-situ phosphidation of molybdenum tungsten oxide (Mo-W-O) nanowires grown on carbon cloth (CC). The catalytic activity of pure MoP nanosheets and Mo-W-P were subsequently studied. Mo-W-P displayed the highest catalytic activity compared to MoP, requiring very low overpotential of -138 mV to produce current density of 100 mA.cm⁻² in 0.5 M H₂SO₄. The superior catalytic activity was attributed to strong synergistic effect of W and Mo atoms in the Mo-W-P, porous nanosheet structure and the 3D conductive scaffolds which formed due to the introduction of the W dopant.¹⁴⁴ Yan et. al. illustrated the positive effect of Cu doping on HER activity using density functional density (DFT). Compared to CoP/CP and Cu₃P/CP, Cu_{0.075}Co_{0.925}P/CP had the smallest hydrogen adsorption free energy (ΔG_H), an important property influencing the catalytic activity of an electrocatalyst.¹⁴⁵

6.3. Introduction of conducting carbon support

Electrical conductivity, an important intrinsic property of an electrocatalyst, can be tuned by supporting the catalyst on a high surface area conducting support. Electrocatalysts with poor conductivity require very high overpotentials to generate current densities rendered practical in hydrogen evolution reactions. A support therefore improves the dispersion of the active

phase allowing for optimum exposure of the active sites while contributing to its conductivity. The widely used support for TMPs are carbon-based materials. These materials are chosen because of their inertness in HER enabling researchers to specifically study the catalytic activity of the active phase and because they are commercially available, possess a high surface area and are highly conducting. Du et. al. prepared C₆₀-decorated Ni-Co-P and C₆₀-free Ni-Co-P electrodes for application as catalysts in HER. Electrochemical impedance spectroscopy results revealed that the C₆₀-decorated Ni-Co-P exhibited faster hydrogen-adsorption kinetics and charge-transfer kinetics which promoted its electrocatalytic performance over the C₆₀-free Ni-Co-P catalyst.¹⁴⁶ Tungsten phosphide nanorod arrays grown on carbon cloth (WP NAs/CC) were prepared by Pu et. al. and used as a stable and efficient electrocatalyst at all pH values. The WP NAs/CC cathode displayed superior catalytic activity needing an overpotential of 130 mV to afford current density of 10 mA.cm⁻² and remained active even at the end of 5000 CV cycles. Notably, the WP NAs/CC catalyst was found to be active in neutral, acidic and alkaline solutions. The researchers reported that the efficient activity was only ascertained due to direct immobilization of the active phase on the carbon cloth rather than using polymer binders such as Nafion as film-forming agents during electrode preparation. Polymer binders block active sites resulting to reduced catalytic activity.¹⁴⁷ Yan et al. employed a robust assembly method to uniformly anchor cluster-like MoP nanoparticles on reduced graphene oxide (MoP/rGO) for use as a catalyst in HER. BET surface area measurement of MoP/rGO and MoP were found to be 160.2 and 5.4 m².g⁻¹, respectively. The even distribution of MoP on rGO gave rise to a high surface area catalyst with a high proportion of active sites, which exhibited high catalytic activity compared to the unsupported MoP nanoparticles.¹⁴⁸

6.4. Crystallinity tailoring

The performance of catalysts in HER is highly dependent on the amount of active catalytic sites exposed on its surface. Decreasing the size of the nanoparticles is the most reported strategy that is used to increase the surface area of catalysts which in turn result in more exposed active sites on the surface. Recently, amorphous structures have been reported to possess more active sites than their crystalline counterpart and hence display improved catalytic activity. The surface of amorphous structures is characterized by asymmetrical bonding which consist of a substantial density of unsaturated sites. The high surface energy associated with unsaturated sites (i.e. dangling bonds) favours the adsorption of protons on the

catalyst surface resulting in improved catalytic activity.¹⁴⁹⁻¹⁵⁰ For instance, Zhao et al. conducted a comparative study between amorphous and crystalline NiP catalysts in HER. Hydrophilicity, an important factor affecting catalytic performance, was measured to fully delineate the observed catalytic activity difference. It was found that the amorphous NiP had a smaller contact angle (36.1°) compared to the crystalline phase (44.7°) and hence considered more hydrophilic.¹⁵¹ Hydrophilic surfaces allow for increased interaction between the catalyst surface and electrolyte which promote the desired reaction.¹⁵² Beltran-Suito et al. reported on the preparation of amorphous and crystalline CoP nanoparticles using two different preparation routes. The catalytic performance results revealed that the amorphous phase outperforms the crystalline CoP counterpart. The high catalytic activity of the amorphous CoP was attributed to its susceptibility to dissolution of P from the arbitrarily oriented bonds and structural flexibility which promote formation of an increased number of unsaturated sites. The unsaturated sites accelerated reactant adsorption, as supported by a high electrochemically active surface area.¹⁵³ Xu et al. employed a facile method to prepare amorphous $\text{np}-(\text{Ni}_x\text{Fe}_{1-x})_4\text{P}_5$ catalysts for overall water splitting. Owing to the amorphous nature of the catalysts in conjunction with doping, the amorphous $\text{np}-(\text{Ni}_x\text{Fe}_{1-x})_4\text{P}_5$ catalyst displayed excellent catalytic activity requiring overpotential of only -245 and -120 mV to generate a current density of $10 \text{ mA}\cdot\text{cm}^{-2}$ for OER and HER in 1 M KOH, respectively. The overall water-splitting produced current density of $10 \text{ mA}\cdot\text{cm}^{-2}$ at overpotential of 1.62 V, which was comparable to activity of the highly active Pt/C-Ir/C catalyst.¹⁵⁴

7. References

1. Y. Yin, A.P. Alivisatos, Colloidal nanocrystal synthesis and the organic-inorganic interface, *Nature* 437 (2005) 664-670.
2. B.R. Cuenya, Synthesis and catalytic properties of metal nanoparticles: Size, shape, support, composition, and oxidation state effects, *Thin solid films* 518 (2010) 3127-3150.
3. M. Haruta, Size- and support-dependency in the catalysis of gold, *Catal. Today* 36 (1997) 153-166.
4. R. Xu, D. Wang, J. Zhang, Y. Li, Shape-dependant catalytic activity of silver nanoparticles for the oxidation of styrene, *Chem. Asian J.* 1 (2006) 888-893.

5. X. He, X. Song, W. Qiao, Z. Li, X. Zhang, S. Yan, W. Zhong, Y. Du, Phase- and size-dependant optical and magnetic properties of CoO nanoparticles, *J. Phys. Chem. C* 17 (2015) 9550-9559.
6. S.K. Lee, E.J. McLauran, Recent advances in colloidal indium phosphide quantum dot production, *Curr. Opin. Green Sustain. Chem.* 12 (2018) 76-82.
7. T.S. Ahmadi, Z.L. Wang, T.C. Green, A. Henglein, M.A. El-Sayed, Shape-controlled synthesis of colloidal platinum nanoparticles, *Science* 272 (1996) 1924-1925.
8. J. Chang, E.R. Waclawik, Colloidal semiconductor nanocrystals: controlled synthesis and surface chemistry in organic media, *RSC Adv.* 4 (2014) 23505-23527.
9. R. Singh, H.S. Nalwa, Medical applications of nanoparticles in biological imaging, cell labelling, antimicrobial agents, and anticancer nanodrugs, *J. Biomed Nanotechnol* 7 (2011) 489-503.
10. M.P. Kalenga, S. Govindraju, M. Airo, M.J. Moloto, L.M. Sikhwivhili, N. Moloto, Fabrication of a Schottky device using CuSe nanoparticles: Colloidal versus microwave digestive synthesis, *J. Nanosci. Nanotechnol*, 15 (2015) 4480-4486.
11. O.S. Wolfbeis, An overview of nanoparticles commonly used in fluorescence bioimaging, *Chem. Soc. Rev.* 44 (2015) 4743-4768.
12. H. Chen, P. Yang, Z.H. Khan, J.M. Wu, G. Li, A.R. Kamali, Quantum dots and nanoparticles in light emitting diodes, displays, and optoelectronic devices, *J. Nanomater.* 2015 (2015) 371679.
13. M.A. Airo, F. Otieno, L. Mxakaza, A. Ipadeola, R.S. Kadzutu-Sithole, L.F.E. Machogo-Phao, C. Billing, M. Moloto, N. Moloto, Probing the stoichiometry dependent activity of nickel selenide counter electrodes in the redox reaction of iodide/triiodide electrolyte in dye sensitized solar cells, *RSC Adv.* 10 (2020) 39509-39520.
14. S. Jeong, L. Hu, H.R. Lee, E. Garnett, J.W. Choi, Y. Cui, Fast and scalable printing of large area monolayer nanoparticles for nanotexturing applications, *Nano Lett.* 10 (2010) 2989 -2994.
15. F.C. Krebs, Fabrication and processing of polymer solar cells: A review of printing and coating techniques, *Sol. Energy Mat. Sol. Cells* 93 (2009) 394-412.
16. E. Tekin, P.J. Smith, U.S. Schubert, Inkjet printing as a deposition and patterning tool for polymers and inorganic particles, *Soft Matter.* 4 (2007) 703-713.
17. C. Ye, M.Q. Wang, G. Chen, Y.H. Deng, L.J. Li, H.Q. Luo, N.B. Li, One-step CVD synthesis of carbon framework wrapped Co₂P as a flexible electrocatalyst for efficient hydrogen evolution, *J. Mater. Chem. A.* 5 (2017) 7791-7795.

18. J.M. McEnaney, J.C. Crompton, J.F. Callejas, E.J. Popczun, A.J. Biacchi, N.S. Lewis, R.E. Schaak, Electrocatalytic hydrogen evolution using amorphous tungsten phosphide nanoparticles, *Chem. Commun.* 50 (2014) 11026-11028.
19. S.S. Nkabinde, Z.B. Ndala, N.P. Shumbula, T. Kolokoto, O. Nchoe, G.N. Ngubeni, K.P. Mubiayi, N. Moloto, Delineating the role of crystallinity in the electrocatalytic activity of colloiddally synthesized MoP nanocrystals, *New J. Chem.* 44 (2020) 14041-14049.
20. I.T. Sines, R. Misra, P. Schiffer, R.E. Schaak, Structure-selective nanocrystal cation exchange in the synthesis of metastable zinc blende MnS and CoS, *Angew. Chem. Int. Ed.* 49 (2010) 4638.
21. A.R. Tao, S. Habas, P. Yang, Shape control of colloidal metal nanocrystals, *Small* 3 (2008) 310-325.
22. J.F. Callejas, C.G. Read, E.J. Popczun, J.M. McEnaney, R.E. Schaak, Nanostructured Co₂P electrocatalyst for the hydrogen evolution reaction and direct comparison with morphologically equivalent CoP, *Chem. Mater.* 27 (2015) 3769-3774.
23. F. D'Accriscio, E. Schrader, C. Sassoey, M. Selmare, R.F. Andre, S. Lamaison, D. Wakerley, M. Fontecave, V. Mougel, G. Le Corre, H. Grutzmached, C. Sanchez, S. Carencio, A single molecular stoichiometric P-source for phase-selective synthesis of crystalline and amorphous iron phosphide nanocatalysts, *ChemNanoMat* 6 (2020) 1208-1219.
24. Y. Pan, Y. Lin, Y. Liu, C. Liu, Size-dependent magnetic and electrocatalytic properties of nickel phosphide nanoparticles, *Appl. Surf. Sci.* 366 (2016) 439-447.
25. T. Shan-Shan, W. Xue-Jing, L. Qing-Chuan, H. Xiao-Jun, Progress on electrocatalysts of hydrogen evolution reaction based on carbon fiber materials, *Chin. J. Anal. Chem.* 44 (2016) 1447-1457.
26. J.A. Turner, A realizable renewable energy future, *Science* 285 (1999) 687-689.
27. Z. Chen, X. Duan, W. Wei, S. Wang, B. Ni, Recent advances in transition metal-based electrocatalysts for alkaline hydrogen evolution, *J. Mater. Chem. A*, 7 (2019) 14971-15005.
28. J.E. Payne, A survey of the electricity consumption-growth literature, *Appl. Energy* 87 (2010) 723-731.
29. Z.W. Seh, J. Kibsgaard, C.F. Dickens, I. Chorkendorff, J.K. Nørskov, T.F. Jaramillo, Combining theory and experimental in electrocatalysis: Insights into materials design, *Science* 355 (2017) 6321.

30. T.R. Cook, D.K. Dogutan, S.Y. Reece, Y. Surendranath, T.S. Teets, D.G. Nocera, Solar energy supply and storage for the legacy and nonlegacy worlds, *Chem. Rev.* 110 (2010) 6474-6502.
31. H.B. Gray, Powering the planet with solar fuel, *Nature Chem.* 1 (2009) 7.
32. M. Gong, D.Y. Wang, C.C. Chen, B.J. Hwang, H. Dai, A mini review on nickel-based electrocatalysts for alkaline hydrogen evolution reaction, *Nano Res.* 9 (2016) 28-46.
33. Y.Y. Liang, Y.G. Li, H.L. Wang and H.J. Dai, Strongly coupled inorganic/nanocarbon hybrid materials for advanced electrocatalysis, *J. Am. Chem. Soc.* 135 (2013) 2013-2036.
34. A.J. Byrd, K.K. Pant and R.B. Gupta, Heterogeneous catalysis for energy applications, *Energy Fuels*, 21 (2007) 3541-3547.
35. J. Bard, L. R. Faulkner, *Electrochemical methods: Fundamentals and applications*, Wiley (2000) 2nd Edition.
36. U. Amjad, C.W.M. Quintero, G. Ercolino, C. Italiano, A. Vita, S. Specchia, Methane steam reforming on the Pt/CeO₂ catalysts: Effect of daily start-up and shut-down on long-term stability of the catalyst, *Ind. Eng. Chem. Res.* 58 (2019) 16395-16406.
37. H.F. Abbas, W.M.A. Wan Daud, Hydrogen production by methane decomposition: A review, *Int. J. Hydrogen Energy* 35 (2010) 1160-1190.
38. Y. Yan, B.Y. Xia, B. Zhao, X. Wang, A review on noble-metal-free bifunctional heterogeneous catalysts for overall electrochemical water splitting, *J. Mater. Chem. A* 4 (2016) 17587-17603.
39. J. Wang, X. Yue, Y. Yang, S. Sirisomboonchai, P. Wang, X. Ma, A. Abudula, G. Guan, Earth-abundant transition-metal-based bifunctional catalysts for overall electrochemical water splitting: A review, *J. Alloys Compd.* 819 (2020) 153346.
40. V. Vij, S. Sultan, A.M. Harzandi, A.Meena, J.N. Tiwari, W.G. Lee, T. Yoon, K.S. Kim, nickel-based electrocatalysts for energy related application: Oxygen reduction, oxygen evolution, and hydrogen evolution reactions, *ACS Catal.* 7 (2017) 7196-7225.
41. Y. Shi, B. Zhang, Recent advances in transition metal phosphide nanomaterials: synthesis and applications in hydrogen evolution reaction, *Chem. Soc. Rev.* 45 (2016) 1529-1541.
42. M. Mori, T. Mrzljak, B. Drbnic, M. Sekavcnik, Integral characteristics of hydrogen production in alkaline electrolyzers, *J. Mech. Eng.* 59 (2013) 585-594.
43. Y. Zhang, J. Xiao, L. Qiyang, S. Wang, Self-supported transition metal phosphide-based electrodes as high-efficient water splitting cathodes, *Front. Chem. Sci. Eng.* 12 (2018) 494-508.

44. X. Zou and Y. Zhang, Noble metal-free hydrogen evolution catalysts for water splitting, *Chem. Soc. Rev.* 44 (2015) 5148-5180.
45. B. Huang, N. Zhou, X. Chen, W. Ong, N. Li, Insights into the electrocatalytic hydrogen evolution reaction mechanism on two-dimensional transition-metal carbonitriles (MXene), *Chem. Eur. J.* 24 (2018) 18479-18486.
46. R.A. Fischer, L. Juan, S. Hou, W. Li, A. Bandarenka, Recent approaches to design electrocatalysts based on metal-organic frameworks and their derivatives, *Chem. Asian J.* 14 (2019) 3474-3501.
47. R. Kronberg, M. Hakala, N. Holmberg, K. Laasonen, Hydrogen adsorption on MoS₂-surfaces: a DFT study on preferential sites and the effect of sulfur and hydrogen coverage, *Phys. Chem. Chem. Phys.* 19 (2017) 16231-16241.
48. T. Bligaard, J. Norskov, S. Dahl, J. Matthiesen, C. Christensen, J. Sehested, The Bronsted-Evans-Polanyi relation and the volcano curve in heterogeneous catalysis, *J. Catal.* 224 (2004) 206-217.
49. A.J. Medford, A. Vojvodic, J. Voss, F. Abild-Pedersen, ChemInform Abstract: From the Sabatier principle to a predictive theory of transition-metal heterogeneous catalysis, *J. Catal.* 328 (2015) 36-42.
50. M. Che, Nobel Prize in chemistry 1912 to Sabatier: organic chemistry or catalysis?, *Catal. Today* 218–219 (2013) 162–171.
51. Y. Li, Z. Dong, L. Jiao, multifunctional transition metal-based phosphides in energy-related electrocatalysis, *Adv. Energy Mater.* 10 (2020) 1902104.
52. Z. Chen, X. Duan, W. Wei, S. Wang, B. Ni, Recent advances in transition metal-based electrocatalysts for alkaline hydrogen evolution, *J. Mater. Chem. A* 7 (2019) 14971-15005.
53. J. Peng, W. Dong, Z. Wang, Y. Meng, W. Liu, P. Song, Z. Liu, Recent advances in 2D transition metal compounds for electrocatalytic full water splitting in neutral media, *Mater. Today Adv.* 8 (2020) 100081.
54. C. Weng, J. Ren, Z. Yuan, Transition metal phosphide-based materials for efficient electrochemical hydrogen evolution: A critical review, *ChemSusChem.* 13 (2020) 3357-3375.
55. P.N. Duchesne, Z.Y. Li, C.P. Deming, V. Fung, X. Zhao, J. Yuan, T. Regier, A. Aldabahi, Z. Almarhoon, S. Chen, D. Jiang, N. Zheng, P. Zhang, Golden single-atomic-site platinum electrocatalysts, *Nat. Mater.* 17 (2018) 1033-1039.

56. L. Zhu, H. Lin, Y. Li, F. Liao, Y. Lifshitz, M. Sheng, S. Lee, M. Shao, A rhodium/silicon co-electrocatalyst design concept to surpass platinum hydrogen evolution activity at high overpotentials, *Nat. Commun.* 7 (2016) 12272.
57. S. Sarkar and S.C. Peter, An overview on Pd-based electrocatalysts for the hydrogen evolution reaction, *Inorg. Chem. Front.* 5 (2018) 2060-2080.
58. F. Luo, L. Guo, Y. Xie, J. Xu, K. Qu, Z. Yang, Iridium nanorods as a robust and stable bifunctional electrocatalyst for pH-universal water splitting, *Appl. Catal. B* 279 (2020) 119394.
59. W. Sheng, H.A. Gasteiger, Y. Shao-Horn, Hydrogen oxidation and evaluation reaction kinetics on platinum: Acid vs alkaline electrolytes, *J. Electrochem. Soc.* 157 (2010) B1529-B1536.
60. X. Ren, Q. Lv, L. Liu, B. Liu, Y. Wang, A. Liu, G. Wu, Current progress of Pt and Pt-based electrocatalysts used for fuel cells, *Sustain. Energy Fuels* 4 (2020) 15-30.
61. Y. Zhu, Q. Lin, Y. Zhong, H.A Tahini, Z. Shao, H. Wang, Metal oxide-based materials as an emerging family of hydrogen evolution electrocatalysts, *Energy Environ. Sci.* 13 (2020) 3361-3392.
62. X. Peng, C. Pi, X. Zhang, S. Li, K. Huo, P.K. Chu, Recent progress of transition metal nitrides for efficient electrocatalytic water splitting, *Sustain. Energy Fuels* 3 (2019) 366-381.
63. W. Chen, J.T. Muckerman, E. Fujita, Recent developments in transition metal carbides and nitrides as hydrogen evolution electrocatalysts, *Chem. Commun.* 49 (2013) 8896-8909.
64. H. Du, R. Kong, X. Guo, F. Qu, J. Li, Recent progress in transition metal phosphides with enhanced electrocatalysis for hydrogen evolution, *Nanoscale* 10 (2018) 21617-21624.
65. E.J. Popczun, J. R. McKone, C. G. Read, A. J. Biacchi, A. M. Wiltrout, N. S. Lewis and R. E. Schaak, Nanostructured nickel phosphide as an electrocatalyst for the hydrogen evolution reaction, *J. Am. Chem. Soc.*, 2013, 135, 9267-9270.
66. S. Carenco, D. Portehault, C. Boissiere, N. Mezailles, C. Sanchez, Nanoscaled metal borides and phosphides: Recent developments and perspectives, *Chem. Rev.* 113 (2013) 7981-8065.
67. S. Boyanov, K. Annou, C. Villevieille, M. Pelosi, D. Zitoun, L. Monconduit, Nanostructured transition metal phosphide as negative electrode for lithium-ion batteries, *Ionics* 14 (2008) 183-190.

68. S.T. Oyama, T. Gott, H. Zhao, Y. Lee, Transition metal phosphide hydroprocessing catalysts: A review, *Catal. Today* 143 (2009) 94-107.
69. Y. Pei, Y. Cheng, J. Chen, W. Smith, P. Dong, P.M. Ajayan, M. Ye, J. Shen, Recent developments of transition metal phosphides as catalysts in the energy conversion field, *J. Mater. Chem. A* 6 (2018) 23220-23243.
70. Y. Ni, L. Jin, J. Hong, Phase-controllable synthesis of nanosized nickel phosphides and comparison of photocatalytic degradation ability, *Nanoscale* 3 (2011) 196-200.
71. N. Singh, P.K. Khanna, TOP: An effective source of phosphorus for synthesis of nanosized InP, *J. Nanosci. Nanotechnol.* 37 (2007) 367-371.
72. P. Liu, J.A. Rodriguez, Catalysts for Hydrogen Evolution from the [NiFe] Hydrogenase to the Ni₂P(001) Surface: The Importance of Ensemble Effect, *J. Am. Chem. Soc.* 127 (2005) 14871-14878.
73. H. Li, C. Jia, X. Meng, H. Li, Chemical synthesis and applications of colloidal metal phosphide nanocrystals, *Front. Chem.* 6 (2019) 652.
74. B. Aronsson, T. Lundström, S. Rundqvist, *Borides, Silicides and Phosphides*, Methuen, London and Wiley, New York, 1965.
75. S.T. Oyama, Transition metal carbides, nitrides, and phosphides, in: G. Ertl, H. Knozinger, J. Weitkamp (Eds.), *Handbook of Catalysis*, Springer-Verlag, Weinheim, 2008.
76. Y. Zhong, X. Xia, F. Shi, J. Zhan, J. Tu, H.J. Fan, Transition metal carbides nitrides in energy storage and conversion, *Adv. Sci.* 3 (2016) 1500286.
77. F. Nozaki, M. Tokumi, Hydrogenation activity of metal phosphides and promoting effect of oxygen, *J. Catal.* 79 (1983) 207-210.
78. M.C. Alvarez-Galvan, J.M. Campos-Martin, J.L.G. Fierro, Transition metal phosphides for the catalytic hydrodeoxygenation of waste oils into green diesel, *Catal.* 9 (2019) 293.
79. Y. Wang, B. Kong, D. Zhao, H. Wang, C. Selomulya, Strategies for developing transition metal phosphides as heterogeneous electrocatalysts for water splitting, *Nanotoday* 15 (2017) 26-55.
80. M.I. Jamesh, Recent progress on earth abundant hydrogen evolution reaction and oxygen evolution reaction bifunctional electrocatalyst for overall water splitting in alkaline media, *J. Power Sources* 333 (2016) 213-236.
81. P. Xiao, M.A. Sk, L. Thia, X. Ge, R.J. Lim, J.-Y. Wang, K.H. Lim, X. Wang, Molybdenum phosphide as an efficient electrocatalyst for the hydrogen evolution reaction, *Energy Environ. Sci.* 7 (2014) 2624-2629.

82. D.E. Schipper, Z. Zhao, H. Thirumalai, A.P. Leitner, S.L. Donaldson, A. Kumar, F. Qin, Z. Wang, L.C. Grabow, J. Bao, K.H. Whitmire, Effects of catalyst phase on the hydrogen evolution reaction of water splitting: Preparation of phase-pure films of FeP, Fe₂P, and Fe₃P and their relative catalytic activities, *Chem Mater.* 30 (2018) 3588-3598.
83. Y. Pan, Y. Liu, J. Zhao, K. Yang, J. Liang, D. Liu, W. Hu, D. Liu, Y. Liu, C. Liu, Monodispersed nickel phosphide nanocrystals with different phases: Synthesis, characterization and electrocatalytic properties for hydrogen evolution, *J. Mater. Chem. A* 3 (2015) 1656-1665.
84. S.T. Oyama, T. Gott, H. Zhao, Y. Lee, Transition metal phosphide hydroprocessing catalysts: A review, *Catal. Today* 143 (2009) 94-107.
85. B. Aronsson, T. Lundstrom, S. Rundqvist, *Borides, Silicides and Phosphides*, Methuen, London and Wiley, New York (1965).
86. L.M. Moreau, D. Ha, H. Zhang, R. Hovden, D.A. Muller, R.D. Robinson, Defining crystalline/amorphous phases of nanoparticles through X-ray absorption spectroscopy and X-ray diffraction: The case of nickel phosphide, *Chem. Mater.* 25 (2013) 2394-2403.
87. Berenguer, T.M. Sankaranarayanan, G. Gomez, I. Moreno, J.M. Coronado, P. Pizarro, D.P. Serrano, Evaluating of transition metal phosphides supported on ordered mesoporous materials as catalyst for phenol hydrodeoxygenation, *Green Chem.* 18 (2016) 1938-1951.
88. J. Li, J. Li, X. Zhou, Z. Highly efficient and robust nickel phosphides as bifunctional electrocatalysts for overall water-splitting, *ACS Appl. Mater. Interfaces* 8 (2016) 10826-10834.
89. N. Jiang, B. You, M.L. Sheng, Y. Sun, Electrodeposition cobalt-phosphorous derived films as competent bifunctional catalysts for overall water splitting, *Angew. Chem. Int. Edit.* 54 (2015) 6251-6254.
90. J. Tian, Q. Liu, A.M. Asiri, X. Sun, Self-supported nanoporous cobalt phosphide nanowire arrays: an efficient 3D hydrogen-evolving cathode over the wide range of pH 0-14, *J. Am. Chem. Soc.* 136 (2014) 7587-7590.
91. P. Xiao, M.A. Sk, L. Thia, X. Ge, R.J. Lim, J.Y. Wang, K.H. Lim, X. Wang, Molybdenum phosphide as an efficient electrocatalyst for the hydrogen evolution reaction, *Energy Environ. Sci.* 7 (2014) 2624-2629.
92. S. Yang, G. Chen, A.G. Ricciardulli, P. Zhang, Z. Zhang, H. Shi, J. Ma, J. Zhang, P.W.M. Blom, X. Feng, Topochemical synthesis of two-dimensional transition-metal phosphides using phosphorene templates, *Angew. Chem. Int. Ed.* 59 (2020) 465-470.

93. X. Yu, Z. Yu, X. Zhang, Y. Zheng, Y. Duan, Q. Gao, R. Wu, B. Sun, M. Gao, G. Wang, S. Yu, "Superaerophobic" nickel phosphide nanoarray catalyst for efficient hydrogen evolution at ultrahigh current densities, *J. Am. Chem.* 141 (2019) 7537-7543.
94. M. Pi, T. Wu, D. Zhang, S. Chen, S. Wang, Facile preparation of semimetallic WP_2 as a novel photocatalyst with high photoactivity, *RSC Adv.* 6 (2016) 15724-15730.
95. R. Ge, J. Huo, T. Liao, Y. Liu, M. Zhu, Y. Li, J. Zhang, W. Li, Hierarchical molybdenum phosphide coupled with carbon as a whole pH-range electrocatalyst for hydrogen evolution reaction, *Appl. Catal. Environ. B* 260 (2020) 118196.
96. S. Fang, T. Chou, S. Samireddi, K. Chen, L. Chen, W. Chen, Enhanced hydrogen evolution reaction on hybrids of cobalt phosphide and molybdenum phosphide, *R. Soc. Open Sci.* 4 (2017) 161016.
97. N. Bai, Q. Li, D. Mao, D. Li, H. Dong, One-step electrodeposition of Co/CoP on Ni foam for efficient hydrogen evolution in alkaline solution, *ACS Appl. Mater. Interfaces* 8 (2016) 29400-29407.
98. R. Wu, Y. Dong, P. Jiang, G. Wang, Y. Chen, X. Wu, electrodeposition synthesis of self-supported Ni-P cathode for efficient electrocatalytic hydrogen generation, *Prog. Nat. Sci.* 26 (2016) 303-307.
99. N. Moloto, M.J. Moloto, N.J. Coville, S.S. Ray, Synthesis and characterization of nickel selenide nanoparticles: size and shape determining parameters, *J. cryst. growth* 324 (2011) 41-52.
100. C.B. Murray, D.J. Norris, M.G. Bawendi, Synthesis and characterization of nearly monodispersed CdE (E = sulfur, selenium, tellurium) semiconductor nanocrystallites, *J. Am. Chem. Soc.* 115 (1993) 8706.
101. Y. Pu, F. Cai, D. Wang, J. Wang, J. Chen, Colloidal synthesis of semiconductor quantum dots toward large scale production: A review, *Ind. Eng. Chem. Res.* 57 (2018) 1790-1802).
102. P. Slepicka, N.S. Kasalkova, J. Siegel, Z. Kolska, V. Svorcik, Methods of gold and silver nanoparticle preparation, *Materials* 13 (2020) 1.
103. V.K. LaMer, R.H. Dinegar, Theory, production and mechanism of formation of monodispersed hydrosols, *J. Am. Chem. Soc.* 72 (1950) 4847-4854.
104. J. Polte, Fundamental growth principles of colloidal metal nanoparticles – a new perspective, *CrystEngComm* 17 (2015) 6809-6830.
105. N. T. K. Thanh, N. Maclean, S. Mahiddine, Mechanism of nucleation and growth of nanoparticles in solution, *Chem. Rev.* 114 (2014) 7610-7630.

106. L. Bährig, S.G. Hickey, A. Eychmüller, Mesocrystalline materials and the involvement of oriented attachment – a review, *CrystEngComm* 16 (2014) 9408-9424
107. A.R. Tao, S. Habas, P. Yang, Shape control of colloidal metal nanocrystals, *small* 4 (2008) 310-325.
108. J.W. Gibbs, On the equilibrium of heterogeneous substances, *Am. J. Sci.* 96 (1878) 441-458.
109. E. Groeneveld, Synthesis and optical spectroscopy of (hetero)-nanocrystals: An exciting interplay between Chemistry and Physics, (2012).
110. V.K. LaMer, Kinetics in phase transitions, *Ind. Eng. Chem.* 44 (1952) 1270-1277.
111. J. Chang, E.R. Walcawik, Colloidal semiconductor nanocrystals: controlled synthesis and surface chemistry in organic media, *RSC Adv.* 4 (2014) 23505-23527
112. W. Ostwald, Emancipation from scientific materialism. *Science Progress* (1894-1898) 4 (1896) 419-436.
113. S.R.K. Perala, S. Kumar, On the Two-step mechanism for synthesis of transition-metal nanoparticles, *Langmuir* 30 (2014) 12703-12711.
114. C. Qian, F. Kim, L. Ma, F. Tsui, P. Yang, J. Liu, Solution-phase synthesis of single-crystalline iron phosphide nanorods/nanowires, *J. Am. Chem. Soc.* 126 (2004) 1195-1198.
115. A.E. Henkes, Y. Vasquez, R.E. Schaak, Converting metals into phosphides: A general strategy for the synthesis of metal phosphide nanocrystals, *J. Am. Chem. Soc.* 129 (2007) 1896-1897.
116. H. Zhang, D. Ha, R. Hovden, L.F. Kourkoutis, R.D. Robinson, Controlled synthesis of uniform cobalt phosphide hyperbranched nanocrystals using Tri-n-octylphosphine oxide as a phosphorus source, *Nano Lett.* 11 (2011) 188-197.
117. J. Wang, Q. Yang, Z. Zhang, S. Sun, Phase-controlled synthesis of transition-metal phosphide nanowires by Ullmann-type reactions, *Chem. A Euro. J.* 16 (2010) 7916-7924.
118. J.M. McEnaney, J.C. Cromton, J.F. Callejas, E.J. Popczun, A.J. Biacchi, N.S. Lewis, R.E. Schaak, Amorphous molybdenum phosphide nanoparticles for electrocatalytic hydrogen evolution, *Chem. Mater.* 26 (2014) 4826-4831.
119. J.M. McEnaney, J.C. Crompton, J.F. Callejas, E.J. Popczun, C.G. Read, N.S. Lewis, R.E. Schaak, Electrocatalytic hydrogen evolution using amorphous tungsten phosphide nanoparticles, *Chem. Commun.* 50 (2014) 11026-11028.
120. H. Man, C. Tsang, M.M. Li, J. Mo, B. Huang, L.Y.S. Lee, Y. Leung, K. Wong, S.C.E. Tsang, Transition metal-doped nickel phosphide nanoparticles as electro- and

- photocatalysts for hydrogen generation reactions, *Appl. Catal. Environ.* 242 (2019) 186-193.
121. M. Zeng, Y. Li, Recent advances in heterogeneous electrocatalysts for hydrogen evolution reaction, *J. Mater. Chem. A* 3 (2015) 14942-14962.
 122. F. Yu, H. Zhou, Y. Huang, J. Sun, F. Qin, J. Bao, W.A. GoddardIII, S. Chen, Z. Ren, High-performance bifunctional porous non-noble metal phosphide catalyst for overall water splitting, *Nat. Commun.* 9 (2018) 2551.
 123. Lasia, Mechanism and kinetics of the hydrogen evolution reaction, *Intern. J. Hydrog. Energy* 44 (2019) 19484-19518.
 124. A.P. Murthy, J. Theerthagiri, J. Madhavan, Insights on Tafel constant in the analysis of hydrogen evolution reaction, *J. Phys. Chem. C* 122 (2018) 23943-23949.
 125. A.P. Murthy, J. Theerthagiri, J. Madhavan, Highly water dispersible polymer acid-doped polyanilines as low-cost, Nafion-free ionomers for hydrogen evolution reaction, *ACS Appl. Energy Mater.* 1 (2018) 1512-1521.
 126. F. Zhao, R.C.T. Slade, J.R. Varcoe, Techniques for the study and development of microbial fuel cells: an electrochemical perspective, *Chem. Soc. Rev.* 38 (2009) 1926-1939.
 127. O. Seri, Differentiating approach to the Tafel slope of hydrogen evolution reaction on nickel electrode, *Electrochem. Commun.* 81 (2017) 150-153.
 128. Y. Liu, X. Xu, M. Sadd, O.O. Kapitanova, V.A. Krivchenko, J. Ban, J. Wang, X. Jiao, Z. Song, J. Song, S. Xiong, A. Matic, Insight into the critical role of exchange current density on electrodeposition behavior of lithium metal, *Adv. Sci.* 8 (2021) 2003301.
 129. R.S. Situmorang, O. Seri, H. Kawai, Estimation of exchange current density for hydrogen evolution reaction of copper electrode by using the differentiating polarization method, *Appl. Surf. Sci.* 505 (2020) 144300.
 130. M.T.M. Koper, Analysis of electrocatalytic reaction schemes: distinction between rate-determining and potential-determining steps, *J. Solid State Electr.* 17 (2013) 339-344.
 131. N. Dubouis, A. Grimaud, The hydrogen evolution reaction: from material to interfacial descriptors, *Chem. Sci.* 10 (2019) 9165-9181.
 132. T. Shinagawa, A.T. Garcia-Araez, K. Takanebe, Insight on Tafel slopes from a microkinetic analysis of aqueous electrocatalysis for energy conversion, *Sci. Rep.* 5 (2015) 13801
 133. P.M. Quaino, M.R. Gennero de Chialvo, A.C. Chialvo, Hydrogen diffusion effects on the kinetics of the hydrogen electrode reaction, *Phys. Chem. Chem. Phys.* 6 (2004) 4450-4455.

134. J.D. Costa, J.L. Lado, E. Carbo-Argibay, E. Paz, J. Gallo, M.F. Cerqueira, C. Rodriguez-Abreu, K. Kovnir, Y.V. Kolen'ko, Electrocatalytic performance and stability of nanostructured-Fe-Ni pyrite-type diphosphide catalyst supported on carbon paper, *J. Phys. Chem. C* 120 (2016) 16537-16544.
135. X. Bu, Y. Li, J.C. Ho, Efficient and stable electrocatalysts for water splitting, *MRS Bull.* 45 (2020) 531-538.
136. A.R. Zeradjnin, J. Masa, I. Spanos, R. Schlogl, Activity and stability of oxides during oxygen evolution reaction: From mechanistic controversies toward relevant electrocatalytic descriptors, *Front. Energy Res.* 8 (2021) 613092.
137. Z. Pu, T. Liu, W. Zhao, X. Shi, Y. Liu, G. Zhang, W. Hu, S. Sun, S. Liao, Versatile route to fabricate precious-metal phosphide electrocatalyst for acid-stable hydrogen oxidation and evolution reactions, *ACS Appl. Mater. Interfaces* 12 (2020) 11737-11744.
138. P. Liu, J.A. Rodriguez, Catalysts for hydrogen evolution from the [NiFe] hydrogenase to the Ni₂P(001) surface: The importance of ensemble effect, *J. Am. Chem. Soc.* 127 (2005) 14871-14878.
139. L. Fang, Y. Wang, X. Yang, H. Zhang, Y. Wang, Uniform OsP₂ nanoparticles anchored on N, P-Doped carbon: A new electrocatalyst with enhanced activity for hydrogen generation at all pH values. *J. Catal.* (370) 2019, 404-411.
140. G. Cho, H. Kim, Y.S. Park, Y. Hong, D. Ha, Phase transformation of iron phosphide nanoparticles for hydrogen evolution reaction electrocatalysis, *Int. J. Hydrog. Energy* 43 (2018) 11326-11334.
141. X. Xiao, L. Tao, M. Li, X. Lv, D. Huang, X. Jiang, H. Pan, M. Wang, Y. Shen, Electronic modulation of transition metal phosphide via doping as efficient and pH-universal electrocatalysts for hydrogen evolution reaction, *Chem. Sci.* 9 (2018) 1970-1975.
142. J.J.L. Humprey, R. Kronberg, R. Cai, K. Laasonen, R.E. Palmer, A.J. Wain, Active site manipulation in MoS₂ cluster electrocatalysts by transition metal doping, *Nanoscale* 12 (2020) 4459-4472.
143. J. Kibsgaard, T.F. Jaramillo, Molybdenum phosphosulfide: An active, acid stable, Earth-abundant catalyst for the hydrogen evolution reaction, *Angew. Chem. Int. Ed.* 53 (2014) 1-6.
144. X. Wang, Y. Xu, H. Rao, W. Xu, H. Chen, W. Zhang, D. Kuang, C. Su, Novel porous molybdenum tungsten phosphide hybrid nanosheets on carbon cloth for efficient hydrogen evolution, *Energy Environ. Sci.* 9 (2016) 1468-1475.

145. L. Yan, B. Zhang, J. Zhu, S. Zhao, Y. Li, B. Zhang, J. Jiang, X. Ji, H. Zhang, P.K. Shen, Chestnut-like copper cobalt phosphide catalyst for all-pH hydrogen evolution reaction and alkaline water electrolysis, *J. Mater. Chem. A* 7 (2019) 14271-14279.
146. Z. Du, N. Jannatum, D. Yu, J. Ren, W. Huang, X. Lu, C₆₀-decorated nickel-cobalt phosphide as an efficient and robust electrocatalyst for hydrogen evolution reaction, *Nanoscale* 10 (2018) 23070-23079.
147. Z. Pu, Q. Liu, A.M. Asiri, X. Sun, Tungsten phosphide nanorod arrays directly grown on carbon cloth: A highly efficient and stable hydrogen evolution cathode at all pH values, *ACS Appl. Mater. Interfaces* 6 (2014) 21874-21879.
148. H. Yan, Y. Jiao, A. Wu, C. Tian, X. Zhang, L. Weng, Z. Ren, H. Fu, Cluster-like molybdenum phosphide anchored and reduced graphene oxide for efficient hydrogen evolution over a broad pH range, *Chem. Commun.* 52 (2016) 9530-9533.
149. Y. Ma, R. Wang, H. Wang, V. Linkov, S. Ji, Evolution of nanoscale amorphous, crystalline and phase-segregated PtNiP nanoparticles and their electrocatalytic effect on methanol oxidation, *Phys. Chem. Chem. Phys.* 16 (2014) 3593-3602.
150. W. Cai, R. Chen, H. Yang, H.B. Tao, H. Wang, J. Gao, W. Liu, S. Hung, B. Liu, Amorphous versus crystalline in water oxidation catalysis: A case study of NiFe, *Nano Lett.* 20 (2020) 4278-4285.
151. X. Zhao, X. Chen, Y. Wang, P. Song, Y. Zhang, High-efficiency Ni-P catalysts with amorphous and crystalline states on hydrogen evolution reaction, *Sustain. Energy Fuels* 4 (2020) 4733-4742.
152. G.B. Darband, M. Aliofkhaezrai, S. Shanmugam, Recent advances in methods and technologies for enhancing bubble detachment during electrochemical water splitting, *Renew. Sustain. Energy Rev.* 114 (2019) 109300.
153. R. Beltran-Suito, P.W. Menezes, M. Driess, Amorphous outperforms crystalline nanomaterials: surface modifications of molecularly derived CoP electro(pre)catalysts for efficient water-splitting, *J. Mater. Chem. A* 7 (2019) 15749-15756.
154. W. Xu, S. Zhu, Y. Liang, Z. Cui, X. Yang, A. Inoue, A nanoporous metal phosphide catalyst for bifunctional water splitting, *J. Mater. Chem. A* 6 (2018) 5574-5579.

Chapter 3

Delineating the role of crystallinity in the electrocatalytic activity of colloiddally synthesized MoP nanocrystals

1. Introduction

The human footprint on natural energy resources has become increasingly apparent as the human population and urbanization continue to increase. This rapid increase has resulted in the decline of natural sources of energy which in turn has sparked interest towards the discovery of renewable and eco-friendly energy reservoirs.¹⁻³ Molecular hydrogen has been proposed as one of the alternative energy carriers capable of meeting today's high energy demand due to its high energy density, light molecular weight and non-toxicity.⁴⁻⁵ Unlike oxygen, molecular hydrogen does not exist freely in nature; it occurs mostly as part of other compounds (e.g. H₂O, C₂H₆) and must be harvested from the compounds that contain it.⁶ Lately, electrocatalytic hydrogen evolution reaction (HER) has proven to be a promising method that can be used to generate hydrogen. Hydrogen evolution reaction ($2\text{H}^+ + 2\text{e}^- \rightarrow \text{H}_2$) is an exemplar of water electrolysis which involves the conversion of hydronium ions (H⁺) in acidic solution in the presence of an electrocatalyst to produce hydrogen gas. The electrocatalyst is the most important component in HER as it minimizes the overpotential required for hydrogen generation.⁷⁻¹¹ To date, platinum group metals (PGMs) and its alloys (e.g. Pt¹², Pd¹³, CuPdPt/C¹⁴, Pt-MoS₂¹⁵ and PtCo¹⁶) are still the most efficient catalysts in electrocatalytic hydrogen evolution due to their superior acidic stability and the ability to produce high exchange current densities at low overpotential. Owing to their scarcity and exorbitant market value, the potential for use in commercial scale hydrogen production has been inhibited.

The challenge currently lies in finding abundant and cheaper alternatives to PGM-based materials to enable a tenable hydrogen industry that would allow for practical use of hydrogen gas as an energy carrier.¹⁷ A wide variety of Mo-based HER electrocatalysts such as molybdenum oxides¹⁸, nitrides¹⁹, and chalcogenides²⁰ have been fabricated for use as potential noble-metal free electrocatalysts. Recently, transition metal phosphides (TMPs) such as CoP²¹, NiP²², MoP²³, WP²⁴ and FeP²⁵ have been recognized as promising acid stable HER electrocatalysts. High efficiencies have been obtained with these as they possess an electronic

structure resembling that of Pt and have high hydrogen adsorption capacities. Among the variety of TMPs, molybdenum phosphide (MoP) is particularly interesting due to its cheapness, high electrocatalytic activity and robustness to dissolution in an acidic media.²⁶ The synthesis of MoP is often done using the less desirable gas-solid and solid-state reduction reactions which depend highly on toxic reagents, long reaction time, high temperature and pressure systems²⁷⁻²⁸. Owing to these environmentally unfriendly conditions, the colloidal synthesis method has emerged as a suitable alternative as it uses low temperatures (< 350 °C), cheap equipment and permits scaling up with ease.²⁹ Additionally, reaction parameters (i.e. temperature, time, solvent etc.) can be systematically varied to allow for control of the size and shape of the nanoparticles, which in turn influence catalytic activity.³⁰⁻³¹

For instance, McEnaney et al. reported a solution phase synthesis of highly active amorphous MoP nanocrystals (~ 4 nm) with a small Tafel slope of 45 mV/dec which remained stable for up to 500 cycles in acidic environment.³² Xiaobo et al. did a comparative study of Mo, MoP and Mo₃P, which showed that the high content of phosphorus in MoP was responsible for its superior catalytic activity. Their study showed that the introduction of P in the crystal lattice of Mo created a hydrogen delivery system which facilitates the ease of dissociation of H from the surface of MoP due to low binding energy.³³ Ren et al. rationally prepared MoP nanocrystals embedded on an N, P-codoped carbon support. Their results showed that small crystalline MoP nanocrystals in conjunction with a conductive carbon support displayed excellent activity and remained stable for up to 1000 cycles.³⁴ Ge et al. employed a SiO₂-template-assisted strategy to synthesize highly crystalline 3-dimensional N, P-codoped graphite carbon nanosheets (3D MoP/NPG) for HER. The results showed the 3D MoP/NPG composite had superior catalytic activity due to the synergistic effect between MoP and the N, P-codoped graphite carbon nanosheets. DFT calculations revealed that charge transfer kinetics were facilitated due to the synergistic interaction between MoP and the carbon sheets which resulted in improved catalytic activity.³⁵

Despite these achievements, a more detailed evaluation of the aforementioned studies revealed that their focal point is on the electrocatalytic activity of either amorphous or crystalline MoP, there are no reports centered on the rationalization of the activity differences observed between amorphous and crystalline MoP electrocatalysts. In this work, we report the utilisation of the molybdenum pentachloride (MoCl₅) precursor to prepare small, shape controlled and highly dispersed amorphous MoP nanocrystals using a one pot colloidal synthetic route. The

nanocrystals retained their shape and dispersity even after crystallization through exposure to elevated temperatures (800 °C, N₂). Furthermore, we demonstrate that even though both amorphous and crystalline MoP are active and acid stable HER catalysts, the amorphous phase is more catalytically active due to its low charge transfer resistance facilitated by a high density of unsaturated sites found on its disordered surface.

2. Experimental

2.1 Chemicals and Materials

Molybdenum pentachloride [95%, MoCl₅, Sigma-Aldrich], trioctylphosphine [90%, TOP, Sigma-Aldrich], 1-octadecene [90%, 1-ODE, Sigma-Aldrich], sulfuric acid [Associated Chemical Associate], hexane [95%, Sigma-Aldrich], Nafion (5 wt%, Sigma-Aldrich) commercial Pt/C (Tanaka Kikinzoku Kogyo K.K., 20 wt%) were used as received without further purification. Deionized water used to prepare the 0.5 M H₂SO₄ solution was purified using a Millipore system.

2.2 Synthesis of amorphous molybdenum phosphide nanocrystals

Molybdenum pentachloride (0.5 mmol), trioctylphosphine (11 mmol), and 1-octadecene (7.8 mmol) were mixed in a 100 mL three-neck round bottom flask equipped with a thermometer, condenser, oil bubbler, heating mantle, and magnetic stirrer. To ensure inert conditions and to remove moisture, the mixture was heated to 140 °C while purging N₂ for 15 min. The temperature was then increased to 340 °C and maintained for 6 h. After 6 h, the heating mantle was removed, and the reaction mixture was saturated with hexane to allow for the rapid cooling and precipitation of the nanoparticles. The nanoparticles were then isolated through centrifugation (7000 rpm, 10 min), washed multiple times with hexane and dried overnight at room temperature. The conversion from amorphous to crystalline MoP was done through heat treatment of the resultant black powders at 800 °C under N₂ for 2 h. The amorphous nanocrystals were denoted as A-MoP, the heat-treated as C-MoP.

2.3 Electrochemical measurements and preparation of working electrode

The electrochemical measurements were conducted using an Epsilon E₂ potentiostat. The electrocatalytic activity of the synthesized nanocrystals was tested in 0.5 M H₂SO₄ using a conventional 3-electrode configuration employing linear sweep voltammetry (LSV) at a scan rate of 1 mV.s⁻¹. All measurements were performed using an Ag/AgCl/3 M KCl reference

electrode and Pt wire as the counter electrode. The working electrode was a MoP coated glassy carbon (diameter = 3 mm, SA = 0.07065 cm²). The durability studies were conducted using a sweep scan rate of 50 mV.s⁻¹ for 1000 cycles using cyclic voltammetry. All potentials are presented with respect to the reversible hydrogen electrode (RHE). Measurements were performed under ambient conditions. The current density was normalized to the geometrical area of the working electrode and IR correction was applied for all electrochemical measurements. The working electrode was prepared using previously reported procedures with slight modifications³⁶. The catalyst ink was prepared by dispersing 5 mg of MoP and 0.5 mg (10 %) of carbon black (Vulcan) in a mixture of water (495 μL), ethanol (495 μL) and 10 μL of 5 % Nafion solution. The resultant catalyst ink was sonicated for 30 min at room temperature to achieve homogeneity, then 5 μL aliquot was pipetted onto the glassy carbon electrode and allowed to dry at RT before use. The amount of MoP loaded on the glassy carbon was kept constant at catalyst loading of 0.35 mg.cm⁻². The Ag/AgCl/3M KCl reference electrode was recalculated with respect to the reference hydrogen electrode (RHE) by adding a value of (0.197 + 0.059 pH). The potentials reported in this study are all against RHE. Electrochemical impedance spectroscopy (EIS) measurements were conducted at -0.25 V (vs Ag/AgCl) using 5 mV amplitude AC signal at a frequency range of 10⁵-0.1 Hz. To confirm the resistance of the electrodes, the corresponding semicircles was fitted to a specific equivalent circuit using the EC-Lab software. The Electrochemical Impedance Spectroscopy measurements were conducted using a 3 electrode configuration using the SP-300 Potentiostat-Bio-Logic instrument.

2.4 Materials characterization

Powder X-ray diffraction (PXRD) analysis was conducted using a Bruker D2 phaser (D2-205530) diffractometer with Cu K α_1 radiation ($\lambda = 1.54060 \text{ \AA}$) at 30 kV and 10 mA. Measurements were taken over 2θ angle range 5 – 90° in steps of 0.026° with a step time of 5 s at ambient temperature. X-ray photoelectron spectroscopy (XPS) analysis was conducted using a Physical Electronics PHI 5700 spectrometer. Non-monochromatic MgK α X-rays (300 W, 15 kV, and 1253.6 eV) were used as the excitation source. The spectrometer energy scale was calibrated using Cu 2p_{3/2}, Ag 3d_{5/2}, and Au 4f_{7/2} photoelectron lines at 932.7, 368.3, and 84.0 eV, respectively. Samples were mounted on a sample holder without adhesive tape and kept overnight at high vacuum in the preparation chamber before being transferred to the analysis chamber for testing. The spectra were collected in the constant pass energy mode at

29.35 eV. The residual pressure in the analysis chamber was maintained below 1.33×10^{-7} Pa during the spectra acquisition with a multi-channel hemi-spherical electron analyser. Transmission electron microscopy (TEM) images were collected using a FEI Technai T12 TEM operated at an accelerating voltage of 120 kV with a beam spot size of 2 in TEM mode and an EDX detector, operated at 120 kV. High resolution transmission electron microscopy (HRTEM) images, high angle annular dark field (HAADF) scanning transmission electron microscopy and energy dispersive X-ray (EDX) elemental mapping images were attained using a JEOL JEM 2100 instrument operated at 200 kV. TEM samples were prepared by dispersing the nanoparticles in hexane, sonicated for 30 min, after which they were deposited on a copper grid and allowed to dry at room temperature before analysis.

3. Results and discussion

3.1. Structural and electronic characterization

PXRD was used to evaluate the structural characteristics of the A-MoP and C-MoP nanocrystals as shown in Fig. 1. The XRD pattern of A-MoP displayed a dominant broad peak centred at $42^\circ 2\theta$, indicating the amorphous nature of the nanocrystals. As the nanocrystals were annealed at 800°C for 2 h, more keen-edge peaks appeared indicating complete crystallization of the nanocrystals. The resultant crystalline pattern of C-MoP was matched with those delineated as the hexagonal phase of molybdenum phosphide (PDF 00-024-0771) with the lattice constant $a = 3.2220 \text{ \AA}$, $b = 3.2220 \text{ \AA}$ and $c = 3.1910 \text{ \AA}$.

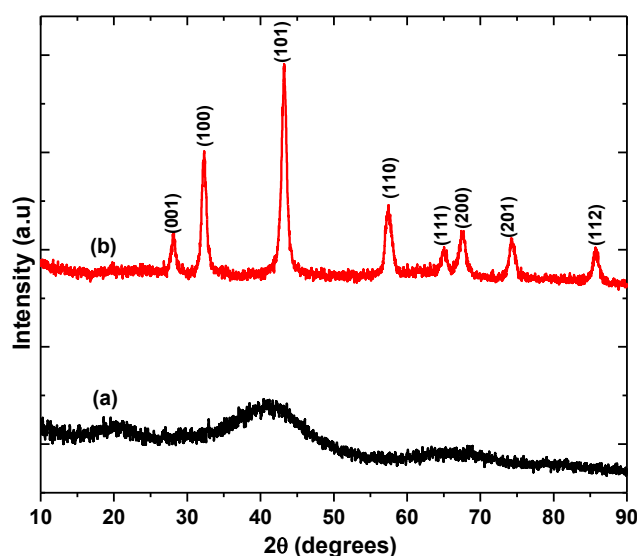


Fig. 1: X-ray diffraction patterns of (a) A-MoP and (b) C-MoP nanocrystals.

The formation of the pure MoP phase upon annealing without any detectable impurities can be used as supportive evidence that the amorphous nanocrystals had a composition close to that of MoP. TEM images of the A-MoP nanocrystals (Fig. 2(a)) showed that they formed small quasi-spherical nanocrystals with an average particles size of 2.17 nm (Fig. S1(a), SI). Consistent with the XRD pattern, the HRTEM of A-MoP showed no observable lattice fringes (Fig. 2(b)) and the corresponding selected-area electron diffraction (insert: Fig. 2(c)) pattern only showed diffuse rings indicating that the nanocrystals lacked long range crystalline ordering.

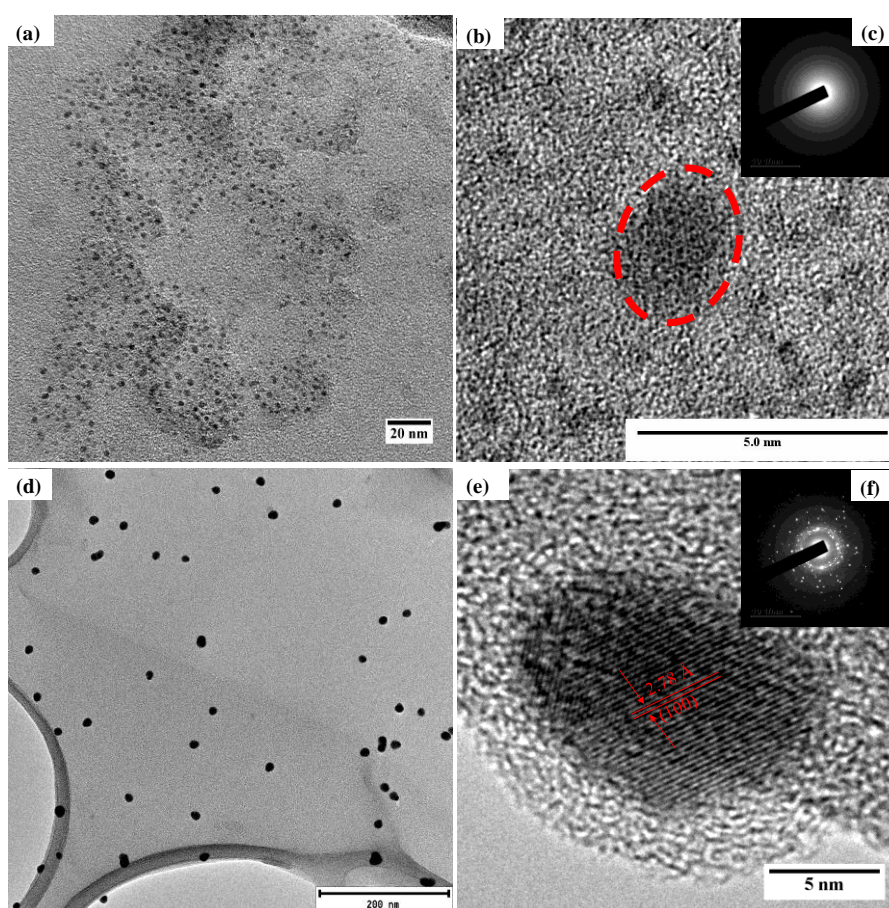


Fig. 2: TEM images of (a) A-MoP, (b) HRTEM image of A-MoP and (insert c) the corresponding SAED pattern, (d) TEM images of C-MoP, (e) HRTEM image of C-MoP and (insert f) corresponding SAED pattern.

Upon heating to aid crystallization, the C-MoP nanocrystals (Fig. 2(d)) grew to an average size of 11.65 nm (Fig. S1(b), SI). The increased nanoparticle size was attributed to the instability of the small (~ 2.1 nm) nanocrystals at high temperature and Ostwald ripening which resulted to the fusion and growth of the already formed amorphous nanocrystals.³⁷ Contrary to the increased nanocrystal size subsequent to annealing; C-MoP nanocrystals underwent no

observable change in their quasi-spherical morphology. HRTEM of C-MoP (Fig. 2(e)) showed well-resolved lattice fringes of the (100) plane with interplanar spacings of 2.8 Å. The presence of spotty diffraction rings in the SAED (insert: Fig. 2(f)) pattern together with the presence of lattice fringes supported the observation of the transformation from amorphous to crystalline MoP nanocrystals as shown in XRD patterns. The high-angle annular dark-field scanning TEM (HAADF-STEM) of the amorphous A-MoP (Fig. 3(a)) and crystalline C-MoP nanocrystals (Fig. 3(b)) showed that Mo, P and O were dispersed homogeneously in the nanocrystals. The O was a result of oxidation on the surface of the nanocrystals and capping agent. EDX spectroscopy (Fig. S2(a) and S2(b), SI) provided further insight on the compositional properties of the amorphous and crystalline nanocrystals. The single spot scans indicated the presence of P and Mo in both the amorphous and crystalline forms of MoP.

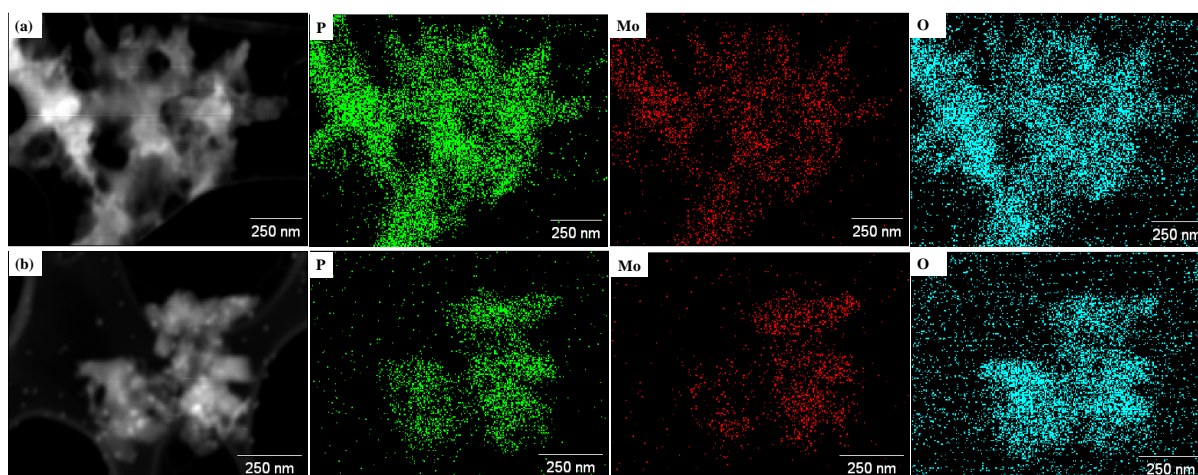


Fig. 3: (a) HAADF-STEM image and elemental mapping of amorphous A-MoP, and (b) HAADF-STEM image and elemental mapping of crystalline C-MoP nanocrystals.

X-ray photoelectron spectroscopy (XPS) was employed to further substantiate the compositional properties and surface electronic information of the amorphous (A-MoP) and highly crystalline (C-MoP) nanocrystals. Shown in Fig. 4(a) is the survey spectrum of A-MoP which manifests clear signals of the elements O, Mo, C and P. The high-resolution P 2p spectrum (Fig. 4(b)) showed a doublet at 128.9 eV (P 2p_{3/2}) and 129.8 eV (P 2p_{1/2}) assigned to P in the P-Mo bond. Additionally, the signal at 133.6 eV (P 2p_{3/2}) corresponded to the P-O bond. The P-O bond emanates from the surface oxidation of the P atoms (PO₄³⁻ or P₂O₅) upon exposure to air.³⁸ The deconvolution of the high-resolution spectrum of Mo 3d resulted in five peaks (Fig. 4(c)), ascribed to Mo⁰ (227.8 eV), Mo³⁺ (228.6 eV), Mo⁶⁺ (230.9 eV) and Mo⁴⁺ (232.7 eV) and Mo⁶⁺ (235.8 eV) species.³⁹ The Mo⁰ peak can be accredited to the presence of Mo-C bonds, which creates the HER active sites.⁴⁰⁻⁴² Mo⁴⁺ and Mo⁶⁺ were assigned to MoO₂

and MoO₃ species resulting from surface oxidation of amorphous MoP upon exposure to air.⁴⁰ PXRD pattern (Fig. S3, SI) of long-term stored A-MoP nanocrystals showed no peaks matching to the oxide species of molybdenum (i.e. MoO₂ and MoO₃) indicating that they only exist on the surface of the nanocrystals. The C 1s spectrum (Fig. S5, SI) was deconvoluted to three signals with binding energies of 284.5, 286.2 and 288.6 eV, corresponding to C-C, C-O and O-C=O⁴³, respectively. The C 1s spectrum confirms presence of carbon that originated from the capping agent and its oxidation.

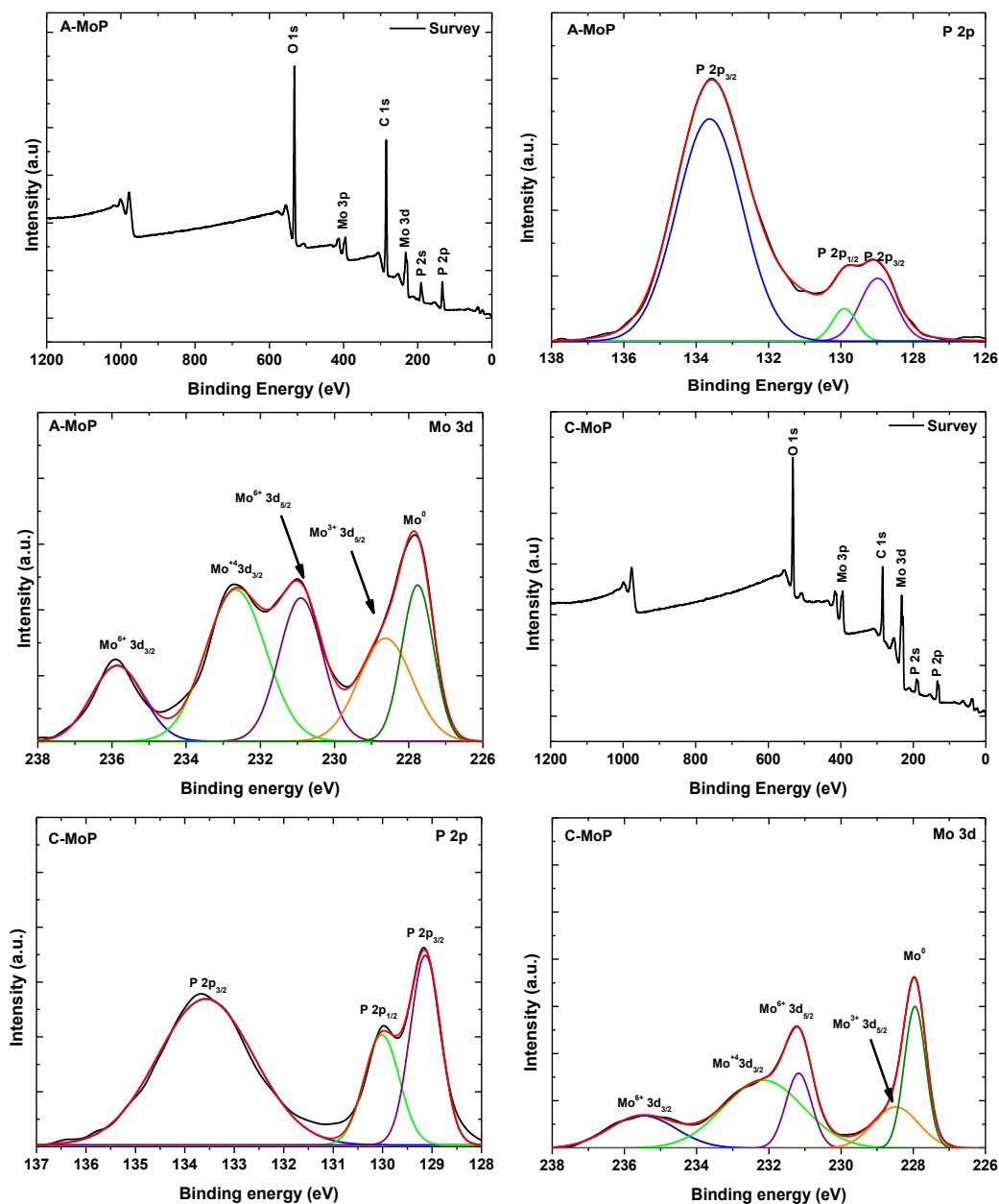


Fig. 4: XPS survey spectrum of (a) A-MoP and corresponding high-resolution spectra: (b) P 2p, (c) Mo 3d; survey spectrum of (d) C-MoP and corresponding high-resolution spectra: (e) P 2p and (f) Mo 3d.

Similarly, the survey spectrum (Fig. 4(d)) of the crystalline (C-MoP) showed signals of the elements O, Mo, C and P. The high-resolution P 2p spectrum (Fig. 4(e)) showed a doublet at 129.2 eV (P 2p_{3/2}) and 130.0 eV (P 2p_{1/2}) that was also attributed to P in the P-Mo bond. Additionally, the signal at 133.6 eV (P 2p_{3/2}) corresponded to the P-O bond. The high-resolution spectrum (Fig. 4(f)) of Mo 3d was deconvoluted into five peaks ascribed to Mo⁰ (227.9 eV), Mo³⁺ (228.5 eV), Mo⁶⁺ (231.2 eV) and Mo⁴⁺ (232.1 eV) and Mo⁶⁺ (235.3 eV) species. Mo⁴⁺ and Mo⁶⁺ can be assigned to MoO₂ and MoO₃ species resulting from surface oxidation of MoP upon exposure to air. PXRD pattern (Fig. S4, SI) of long-term stored C-MoP nanocrystals showed no peaks matching to the oxide species of molybdenum. The C 1s spectrum (Fig. S6, SI) was convoluted to three signals with binding energies of 284.8, 286.2 and 288.3 eV, corresponding to C-C, C-O and O-C=O, again suggesting surface oxidation.

3.2. Hydrogen evolution reaction

The electrochemical HER performance of MoP nanocrystals was assessed using a conventional 3-electrode configuration in a 0.5 M H₂SO₄ solution. The representative nanocrystals were deposited on a 0.07 cm² glassy carbon electrode at mass loadings of 0.35 mg.cm⁻². Fig. 5(a) shows the linear sweep voltammetry curves (current density vs. potential) of the Pt/C, Bare GCE, Vulcan, A-MoP and C-MoP. The polarization curves of bare GCE and Vulcan showed insignificant electrochemical activity, which indicated that they had negligible contribution towards the observed HER activity. As a benchmark, the HER activity of the commercial Pt/C electrocatalyst (Tanaka Kikinokogyo K.K., 20 wt%) was assessed and displayed excellent electrochemical activity, ascertaining current densities of 10 mA.cm⁻² at very low overpotential of -36 mV. The LSV curves clearly showed a difference in the electrochemical performance between the amorphous and crystalline nanocrystals. The A-MoP and C-MoP nanocrystals produced current densities of 10 mA.cm⁻² at overpotentials of -235 and -317 mV, respectively. The catalytic performance of the amorphous A-MoP was relatively higher than that of the crystalline C-MoP. The electrocatalytic activity of an electrocatalyst is known to be highly dependent on its crystallinity. Amorphous nanocrystals lack long range crystalline ordering and hence are dominated by randomly oriented bonds (i.e. dangling bonds) and consist of a substantial density of unsaturated sites on the surface as shown in Fig. 6. The non-symmetrical bonding of the surface atoms results in high surface energy which promotes the adsorption of protons (H⁺) on A-MoP surface enhancing electrocatalytic performance.⁴⁴⁻⁴⁶

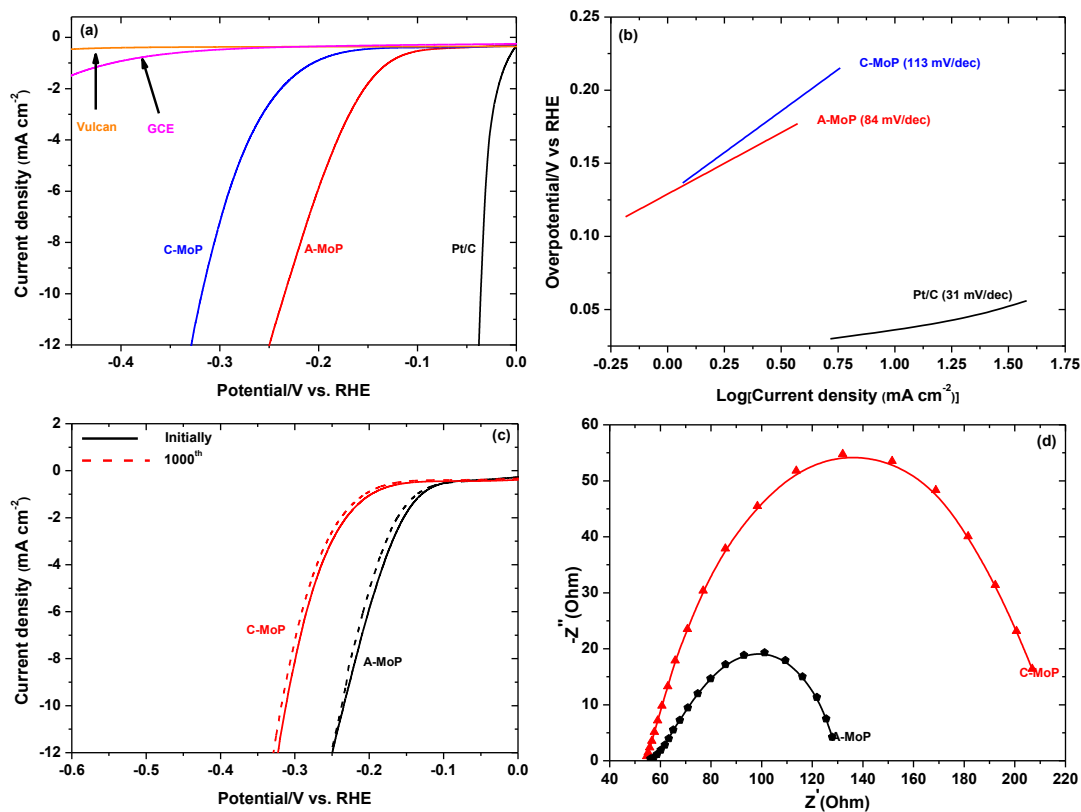


Fig. 5: LSV polarization curves of (a) A-MoP and C-MoP together with Pt/C, bare GCE and Vulcan as controls ($0.5\text{ M H}_2\text{SO}_4$; scan rate 1 mVs^{-1}). (b) Tafel slope plots of A-MoP, C-MoP and Pt/C. (c) LSV curves of A-MoP and C-MoP before and after 1000 potential cycles. (d) Nyquist plots of A-MoP and C-MoP nanocrystals.

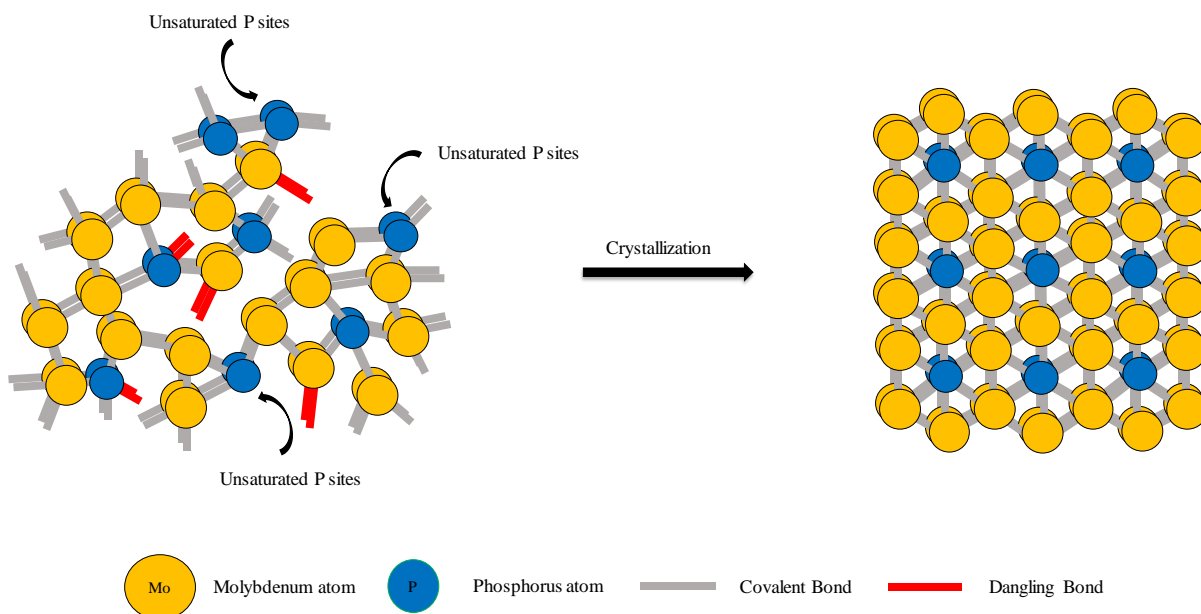
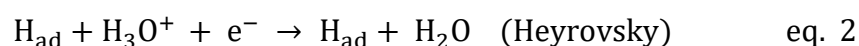


Fig. 6: Schematic diagram illustrating the structural transformation of MoP upon annealing.

Additionally, TEM images indicated an increase in particle size with increase in annealing time. An increase in size insinuates a lower packing density of the nanocrystals per unit volume which result in a small proportion of exposed active sites and hence lower catalytic activity. The small, microscopic interparticle distance (~ 5.210 nm) in A-MoP allowed for efficient particle-particle electron hopping which resulted in better conductivity as opposed to C-MoP which has a large interparticle distance (~ 50.68 nm) that hindered the ease of electron transport.⁴⁷ The Tafel slope is an intrinsic property of an electrocatalyst that is used to comprehend the performance of an electrocatalyst and provide information about the reaction mechanism involved in HER. In general, it is extrapolated from LSV data using the Tafel equation ($\eta = b \log j + a$), where η is the overpotential, a is a constant, b represents the Tafel slope and j corresponds to the current density. The value of the Tafel slope is determined by the rate determining step in HER and a smaller slope indicate a more active electrocatalyst. Fig. 5(b) showed that the Pt/C electrocatalyst gave a very small Tafel slope of 31 mV.dec^{-1} , characteristic of a highly active catalyst. The corresponding extrapolated Tafel slope for A-MoP and C-MoP nanocrystals were 84 and 113 mV.dec^{-1} , respectively. The relatively smaller Tafel slope of A-MoP (84 mV.dec^{-1}) meant it was more catalytically active than the C-MoP nanocrystals. Classical theoretical studies reveal that HER follows a 3-reaction pathway in acidic media. A discharge step (Volmer reaction, eq. 1), followed by a desorption step (Heyrovsky reaction, eq. 2) and lastly the recombination step (Tafel reaction, eq. 3), where H_{ad} represent H atoms adsorbed on active sites on the surface of an electrocatalyst. The corresponding Tafel slopes for the Volmer (eq. 1), Heyrovsky (eq. 2) and Tafel (eq. 3) reactions in acidic solution are 29 , 39 and 118 mV.dec^{-1} , respectively.



Experimentally, the Volmer-Heyrovsky and Volmer-Tafel reactions are the two main pathways commonly observed for HER.⁴⁷⁻⁴⁸ The extrapolated Tafel slopes ($84 - 113 \text{ mV.dec}^{-1}$) in this study suggested a Volmer-Heyrovsky reaction pathway on both the amorphous and crystalline forms of MoP. The overpotentials required to reach 10 mA/cm^2 and corresponding Tafel slopes obtained in this study are comparable to those of other non-noble metal based electrocatalysts (summarized in Table 1).

Table 1: Comparison of catalytic activity of non-noble metal electrocatalysts in 0.5 M H₂SO₄.

HER catalyst	η_{10} (mV)	Tafel slope (mV.dec ⁻¹)	Reference
A-MoP	-235	84	This Work
Ni ₁₂ P ₅	-208	75	49
MoS ₂ 10K	-248	61	50
MoS ₂ Bulk	-471	100	50
3D MoP	-	126	51
Cu ₃ P/CF	-	75.4	52
FeP/C	-157	127	53
Bulk MoP	-	79.2	54
MoP/C	-219	61	55
NFP/C-2	-72	81	53

Long term durability of an electrocatalyst is an important indicator of its potential in large scale applications. The electrochemical stability of A-MoP and C-MoP nanocrystals on GCE was assessed using cyclic voltammetry (CV) sweeps in a potential range from 0 to -0.8V (vs. RHE) using a scan rate of 50 mV.s⁻¹. The excellent stability of the amorphous and crystalline phases of MoP in an acidic medium was confirmed by the small decrease in the electrocatalytic activity after 1000 cycles (Fig. 5(c)). Electrochemical impedance spectroscopy (EIS) was employed to understand the electrical conductivity of the nanocrystal, an important intrinsic property of an electrocatalyst Fig. 5(d). Approximated using a simplified equivalent circuit, the charge transfer resistance (R_{ct}) for A-MoP and C-MoP were 94 and 171 Ω , respectively. The small R_{ct} is an indication of high electron transfer and ion exchange rate at the solution-electrocatalyst interface.

4. Conclusion

Molybdenum pentachloride precursor was adopted to prepare small, highly dispersed and shape controlled amorphous and crystalline molybdenum phosphide nanocrystals through a simple one-pot colloidal synthesis procedure. The nanocrystals demonstrated to be active and stable HER electrocatalysts in acidic media. Amorphous MoP exhibited higher electrocatalytic activity compared to crystalline MoP nanocrystals due to the presence of substantial density of unsaturated sites and low charge transfer resistance (R_{ct}) between the acidic solution and the disordered surface of the amorphous electrocatalyst. The observation that amorphous nanocrystals were more active HER electrocatalyst than their crystalline counterpart provides new insights on a possible strategy that can be followed in the search for highly active non-noble metal alternative electrocatalysts to Pt.

5. References

1. Z. Chen, X. Duan, W. Wei, S. Wang and B.-J Ni, Scalable solid-state synthesis of MoS₂-NiS₂/graphene nanohybrids as bifunctional electrocatalysts for enhanced overall water splitting, *J. mater. Chem. A*, 2019, **7**, 14971
2. Z.W. Seh, J. Kibsgaard, C.F. Dickens, I. Chorkendorff, J.K. Nørskov and T.F. Jaramillo, Combining theory and experiment in electrocatalysis: Insight into materials design *Science*, 2017, **355**, 6321

3. M.G. Walter, E.L. Warren, J.R. McKone, S.W. Boettcher, Q. Mi, E.A. Santori and N.S. Lewis, Solar water splitting cells, *Chem. Rev.*, 2010, **110**, 6446 - 6473
4. M. Gong, D.Y. Wang, C.C. Chen, B.J. Hwang and H. Dai, A mini review on nickel-based electrocatalysts for alkaline hydrogen evolution reaction, *Nano Research*, 2015, 9, 28 - 46
5. Y.Y. Liang, Y.G. Li, H.L. Wang and H.J. Dai, Strongly coupled inorganic/nanocarbon hybrid materials for advanced electrocatalysis, *J. Am. Chem. Soc.*, 2013, **135**, 2013 - 2036
6. A.J. Byrd, K.K. Pant and R.B. Gupta, Hydrogen production from ethanol by reforming in supercritical water using Ru/Al₂O₃, *Energy Fuels*, 2007, **21**, 3541 - 3547
7. W. Zhang, S. Zhu, R. Luque, S. Han, L. Hu and G. Xu, Recent development of carbon electrode materials and their bioanalytic and environmental applications, *Chem. Soc. Rev.*, 2015, **45**, 715 - 752
8. B. Ruqia and S.I. Choi, *energy mater.*, Ultrathin Rh nanosheets as highly efficient bifunctional electrocatalyst for the isopropanol-assisted overall water splitting, 2018, **11**, 2643 - 2653
9. F. Mueller-Langer, E. Tzimas, M. Kaltschmitt and S. Peteves, Symposium on materials in clean power systems, *Int. J. Hydrogen Energy*, 2007, 32, 3797 - 3810
10. Y. Jiao, Y. Zheng, M. Jaroniec and S.Z. Qiao, Design of electrocatalysts for oxygen- and hydrogen-involving energy conversion reactions, *Chem. Soc. Rev.*, 2015, **44**, 2060 - 2086
11. K. Li, Y. Li, Y. Wang, J. Ge, C. Liu and W. Xing, Enhancing electrocatalytic performance for the hydrogen evolution reaction through surface enrichment of platinum nanoclusters alloying with ruthenium in situ embedded in carbon, *Energy Environ. Sci.*, 2018, **11**, 1232 - 1239
12. S. Sarkar and S.C. Peter, An overview on Pd-based electrocatalysts for the hydrogen evolution reaction, *Inorg. Chem. Front.*, 2018, **5**, 2060 - 2080
13. T. Ding, Z. Wang, L. Zhang, C. Wang, Y. Sun and Q. Yang, A highly active and durable CuPdPt/C electrocatalyst for an efficient hydrogen evolution reaction, *J. Mater. Chem. A*, 2016, **4**, 15309 - 15315
14. D. Li, Y. Li, B. Zhang, Y.H. Lui, S. Mooni, R. Chen, S. Hu and H. Ni, Insertion of Platinum Nanoparticles into MoS₂ Nanoflakes for Enhanced Hydrogen Evolution Reaction *Mater.*, 2018, 11, 1520 - 1531
15. Y. Qin, X. Han, S. Gadipelli, J. Guo, S. Wu, L. Kang, J. Callison and Z. Guo, In situ synthesized low-PtCo porous carbon catalyst for highly efficient hydrogen evolution, *J. Mater. Chem. A*, 2019, **7**, 6543 - 6551

16. X. Zou and Y. Zhang, Noble metal-free hydrogen evolution catalysts for water splitting, *Chem. Soc. Rev.*, 2015, **44**, 5148 - 5180
17. G. Zhang, X. Yang, M. Dubois, M. Herraiz, R. Chenitz, M. Lefevre, M. Cherif, F. Vidal, V.P. Glibin, S. Sun and J. Dodelet, Non-PGM electrocatalysts for PEM fuel cells: effect of fluorinated on the activity and stability of a highly active NC_Ar NH₃ catalyst, *Energy Environ. Sci.*, 2019, **12**, 3015-3037
18. Y. Zhu, G. Chen, X. Xu, G. Yang, M. Liu and Z. Shao, Enhancing electrocatalytic activity for hydrogen evolution by strongly coupled molybdenum nitride@nitrogen-doped carbon porous nano-octahedrons, *ACS Catal.* 2017, **7**, 3540 - 3547
19. Y. Chen, X. Wang, M. Lao, K. Rui, X. Zheng, H. Yu, J. Ma, S.X. Dou and W. Sun, Electrocatalytically inactive SnS₂ promotes water adsorption/dissociates sites towards enhanced alkaline hydrogen evolution reaction, *Nano Energy*, 2019, **64**, 103918
20. X. Li, S. Li, A. Yoshida, S. Sirisomboonchai, K. Tang, Z. Zuo, X. Hao, A. Abudula and G. Guan, Mn doped CoP nanoparticles clusters: an efficient electrocatalyst for hydrogen evolution reaction *Catal. Sci. Tech.*, 2018, **8**, 4407 - 4412
21. M. Chen, J. Qi, W. Zhang and R. Cao, *Chem. Comm.*, 2017, **53**, 5507 - 5510
22. Y. Zhang, H. Lei, D. Duan, E. Villota, C. Liu and R. Ruan, Electrosynthesis of NiP_x nanospheres for electrocatalytic hydrogen evolution from a neutral aqueous solution, *ACS Appl. Mater. Interfaces*, 2018, **10**, 20429 - 20439
23. J.M. McEnaney, J.C. Crompton, J.F. Callejas, E.J. Popczun, C.G. Read, N.S. Lewis and R.E. Schaak, Electrocatalytic hydrogen evolution using amorphous tungsten phosphide nanoparticles, *Chem. Comm.*, 2014, **50**, 11026 - 11028
24. D.Y. Chung, S.W. Jun, G. Yoon, H. Kim, J.M. Yoo, K.-S. Lee, T. Kim, H. Shin, A.K. Sinha, S.G. Kwon, K. Kang, T. Hyeon and Y.E. Sung, Large-scale synthesis of carbon-shell-coated FeP nanoparticles for robust hydrogen evolution reaction electrocatalysts, *J. Am. Chem. Soc.*, 2017, **139**, 6669 - 6674
25. Q. Yue, Y. Wan, Z. Sun, X. Wu, Y. Yuand and P. Du, MoP is a novel, noble-metal-free cocatalyst for enhanced photocatalytic hydrogen production from water under visible light, *J. Mat. Chem. A*, 2015, **3**, 16941 -16947
26. M. Pi, T. Wu, D. Zhang, S. Chen and S. Wang, A 3D porous WP₂ nanosheets@carbon cloth flexible electrode for efficient electrocatalytic hydrogen evolution, *RSC Adv.*, 2016, **6**, 15724

27. M.C Alvarez-Galvan, J.M. Campos-Martin and J.L.G. Fierro, Transition metal phosphides for the catalytic hydrodeoxygenation of waste oils into green diesel, *Catalysts*, 2019, **9**, 293
28. M. Nath, A. Govindaraj, C.N.R. Rao, Simple synthesis of MoS₂ and WS₂ nanotubes, *Adv. Mater.*, 2001, **13**, 283
29. N. Moloto, M.J. Moloto, N.J. Coville, S.S. Ray, Optical and structural characterization of nickel selenide nanoparticles synthesized by simple methods, *J. Cryst. Growth*, 2009, **311**, 3924 - 3932
30. N. Moloto, M.J. Moloto, N.J. Coville, S.S. Ray, Synthesis and characterization of nickel selenide nanoparticles: size and shape determining parameters, *J. Cryst. Growth*, 2011, **324**, 41 - 52
31. J.M. McEnaney, J.C. Crompton, J.F. Callejas, E.J. Popczun, A.J. Biacchi, N.S. Lewis and R.E. Schaak, Amorphous Molybdenum Phosphide Nanoparticles for Electrocatalytic Hydrogen Evolution, *Chem. Mater.*, 2014, **26**, 4826 - 4831
32. X. Chen, D. Wang, Z. Wang, P. Zhou, Z. Wu and F. Jiang, Molybdenum phosphide: a new highly efficient catalyst for the electrochemical hydrogen evolution reaction, *Chem. Comm.*, 2014, **50**, 11683
33. J.T. Ren, L. Chen, C.-C. Weng and Z.-Y. Yuan, Self-supported MoP nanocrystals embedded in N,P-codoped carbon nanofibers *via* a polymer-confinement route for electrocatalytic hydrogen production, *Mater. Chem. Front.*, 2019, **3**, 1872 - 1881
34. R. Ge, J. Huo, T. Liao, Y. Liu, M. Zhu, Y. Li, J. Zhang and W. Li, Hierarchical molybdenum phosphide coupled with carbon as a whole pH range electrocatalyst for hydrogen evolution reaction, *Applied Catalysis B: Environmental*, *Appl. Catal. B: Environ.*, 2020, **260**, 118196
35. Z. Xing, Q. Liu, A.M. Asiri and X. Sun, High-Efficiency Electrochemical Hydrogen Evolution Catalyzed by Tungsten Phosphide Submicroparticles, *ACS Catal.*, 2015, **5**, 145 - 149
36. H. Chen, Y. Yu, H.L. Xin, K.A. Newton, M.E. Holtz, D. Wang, D.A. Muller, H.D. Abruna and F.J. DiSalvo, Coalescence in the Thermal Annealing of nanoparticles: An in Situ STEM Study of the Growth Mechanisms of Ordered Pt-Fe Nanoparticles in a KCl Matrix, *Chem. Mater.*, 2013, **25**, 1436 - 1442
37. Y. Huang, J. Ge, J. Hu, J. Zhang, J. Hao and Y. Wei, Nitrogen-doped porous molybdenum carbide and phosphide hybrids on a carbon matrix as highly effective electrocatalysts for the hydrogen evolution reaction, *Adv. Energy Mater.*, 2017, **8**, 1701601

38. M. Hou, X. Teng, J. Wang, Y. Liu, L. Guo, L. Ji, C. Cheng and Z. Chen, Multiscale porous molybdenum phosphide of honeycomb structure for highly efficient hydrogen evolution, *Nanoscale*, 2018, **10**, 14594
39. C. Wan, Y.N. Regmi and B.M. Leonard, Multiple Phases of Molybdenum Carbide as Electrocatalysts for the Hydrogen Evolution Reaction, *Angew. Chem. Int. Ed.*, 2014, **53**, 6407 - 6410
40. C. Tang, H. Zhang, K. Xu, Q. Zhang, J. Liu, C. He, L. Fan and T. Asefa, Unconventional molybdenum carbide phases with high electrocatalytic activity for hydrogen evolution reaction, *J. mater. Chem. A*, 2019, **7**, 18030 - 18038
41. P. Xiao, M.A. Sk, L. Thia, X. Ge, R.J. Lim, J.-Y. Wang, K.H. Lim and X. Wang, Molybdenum phosphide as an efficient electrocatalyst for the hydrogen evolution reaction, *Energy Environ. Sci.*, 2014, **7**, 2624 - 2629.
42. H. Li, F. Ke and J. Zhu, MOF-derived Ultrathin Cobalt Phosphide Nanosheets as Efficient Bifunctional Hydrogen Evolution Reaction and Oxygen Evolution Reaction electrocatalysts, *Nanomaterials*, 2018, **8**, 89
43. Z. Jin, P. Li, X. Huang, G. Zeng, Y. Jin, B. Zheng and D. Xiao, Three-dimensional amorphous tungsten-doped nickel phosphide microsphere as an efficient electrocatalyst for hydrogen evolution, *J. Mater. Chem. A*, 2014, **2**, 18593 - 18599
44. F. Ma and K.-W. Xu, Using dangling bond density to characterize the surface energy of nanomaterials, *Surface and Interface Analysis, Surf. Interface Anal.*, 2007, **39**, 611- 614
45. K.S. Deepa, M.T. Sebastian, and J. James, Effect of interparticle distance and interfacial area on the properties of insulator-conductor composites, *Appl. Phys. Lett.*, 2007, **91**, 202904
46. Y. Li, H. Wang, L. Xie, Y. Liang, G. Hong and H. Dai, MoS₂ nanoparticles grown on graphene: an advanced catalyst for the hydrogen evolution reaction *Journal of American Chemical Society, J. Am. Chem. Soc.*, 2011, **133**, 7296 - 7299
47. B.E. Conway and B.V. Tilak, Interfacial processes involving electrocatalytic evolution and oxidation of H₂, and the role of chemisorbed H, *Electrochimic. Acta*, 2002, **47**, 3571 - 3594.
48. Y. Pan, Y. Liu, J. Zhao, K. Yang, J. Liang, D. Liu, W. Hu, D. Liu, Y. Liu and C. Liu, Monodispersed nickel phosphide nanocrystals with different phases: synthesis, characterization and electrocatalytic properties for hydrogen evolution, *J. Mater. Chem. A*, 2015, **3**, 1656 - 1665

49. J. Benson, M. Li, S. Wang, P. Wang, and P. Papakonstantinou, Electrocatalytic hydrogen evolution reaction on edges of a few layer molybdenum disulfide nanodots, *ASC Appl. Mater. Interfaces*, 2015, **7**, 14113 - 14122
50. Chen Deng, Fei Ding, Xinyuan Li, Yaofang Guo, Wei Ni, Huan Yan, Kening Sun and Yi-Ming Yan, Template-preparation of a three-dimensional molybdenum phosphide sponge as a high performance electrode for hydrogen evolution, *J. Mater. Chem. A*, 2016, **4**, 59 – 66
51. L. Yan, B. Zhang, J. Zhu, S. Zhao, Y. Li, B. Zhang, J. Jiang, X. Ji, H. Zhang and P.K. Shen, Chestnut-like copper cobalt phosphide catalyst for all-pH hydrogen evolution reaction and alkaline water electrolysis, *J. Mater. Chem. A*, 2019, **7**, 14271 - 14279
52. X.F. Lu, L. Yu, X.W. Lou, Highly crystalline Ni-doped FeP/carbon hollow nanorods as all-pH efficient and durable hydrogen evolving electrocatalysts, *Sci. Adv.*, 2019, **5**, 2
53. W. Cui, Q. Liua, Z. Xing, A.M. Asiri, K.A. Alamry, X. Sun, Nanoflower-like metallic conductive MoO₂ as a high-performance non-precious metal electrocatalyst for the hydrogenation, *Appl. Catal. B: Environ.*, 2015, **164**, 144 - 150
54. R. Ge, J. Huo, T. Liao, Y. Liu, M. Zhu, Y. Li, J. Zhang, W. Li, *Appl. Hierarchical molybdenum phosphide coupled with carbon as a whole pH-range electrocatalyst for hydrogen evolution reaction*, *Catal. B: Environ.*, 2020, **260**, 118196

6. Supporting information

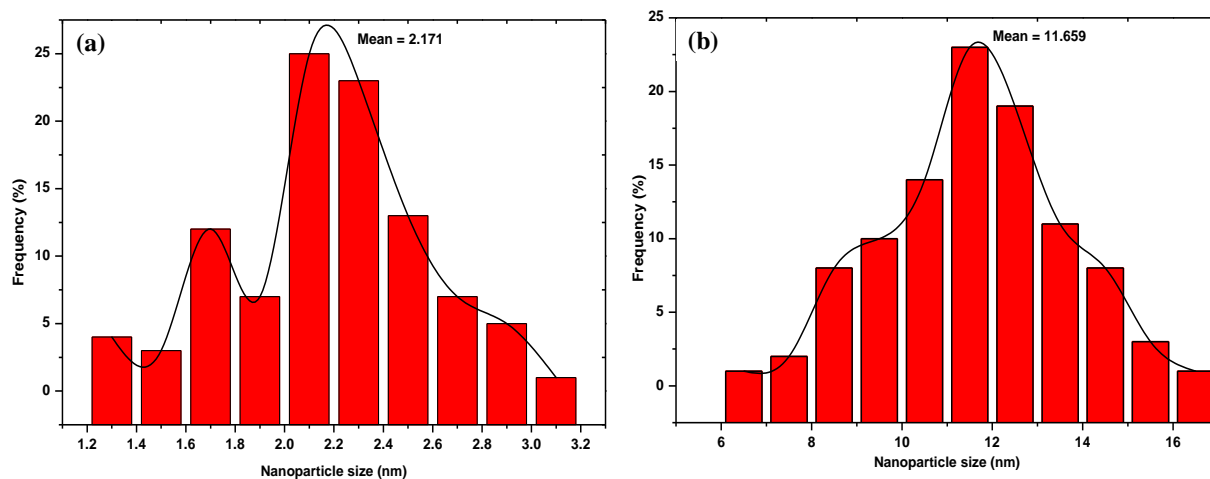


Fig. S1: The size distributions of (a) A-MoP and (b) C-MoP nanocrystals as determined from TEM images (N = 100).

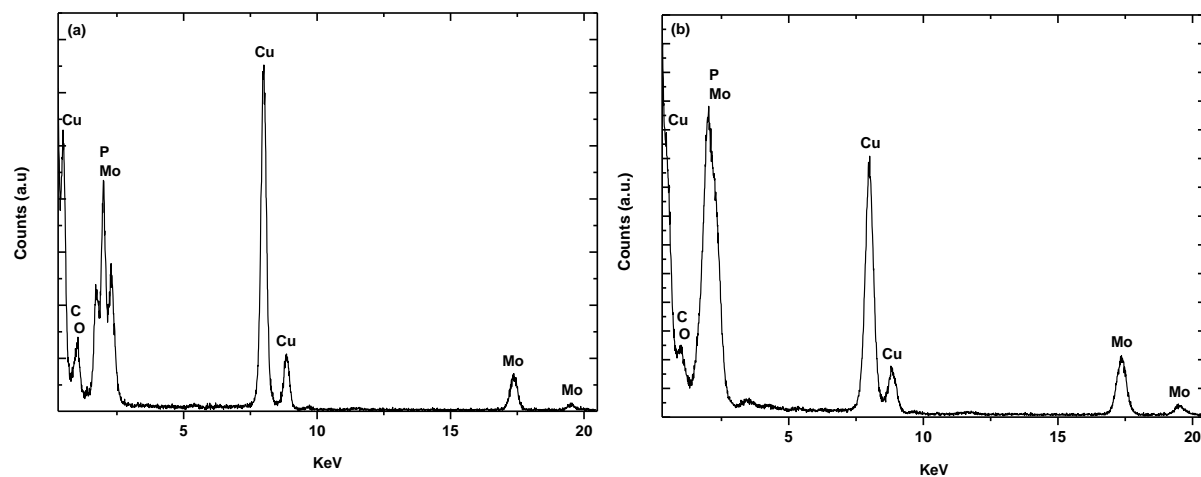


Fig. S2: EDX spectroscopy of (a) amorphous A-MoP and (b) crystalline C-MoP(2 h) nanocrystals.

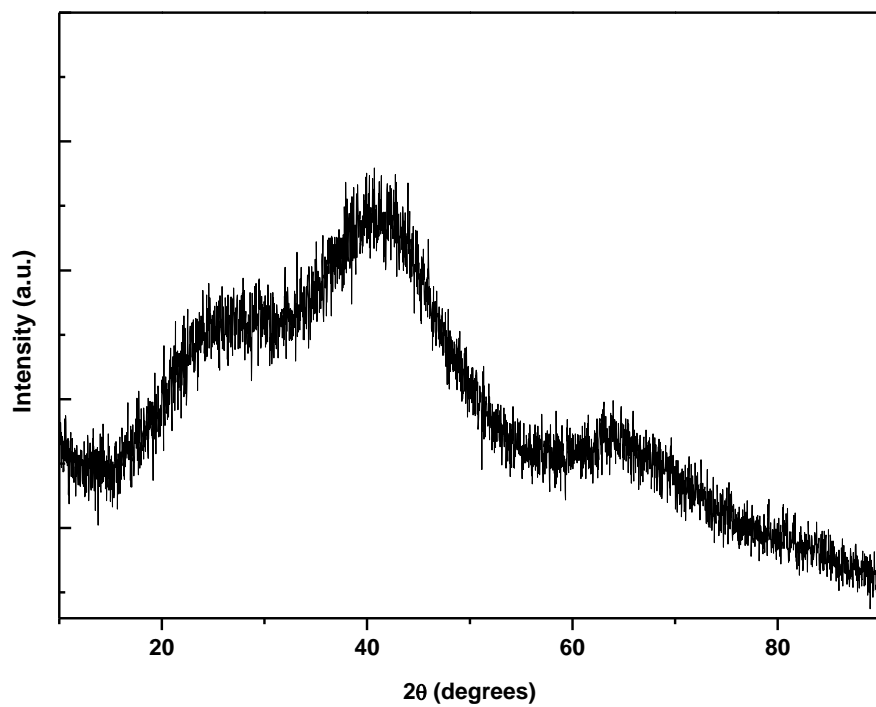


Fig. S3: XRD pattern of long term stored amorphous A-MoP.

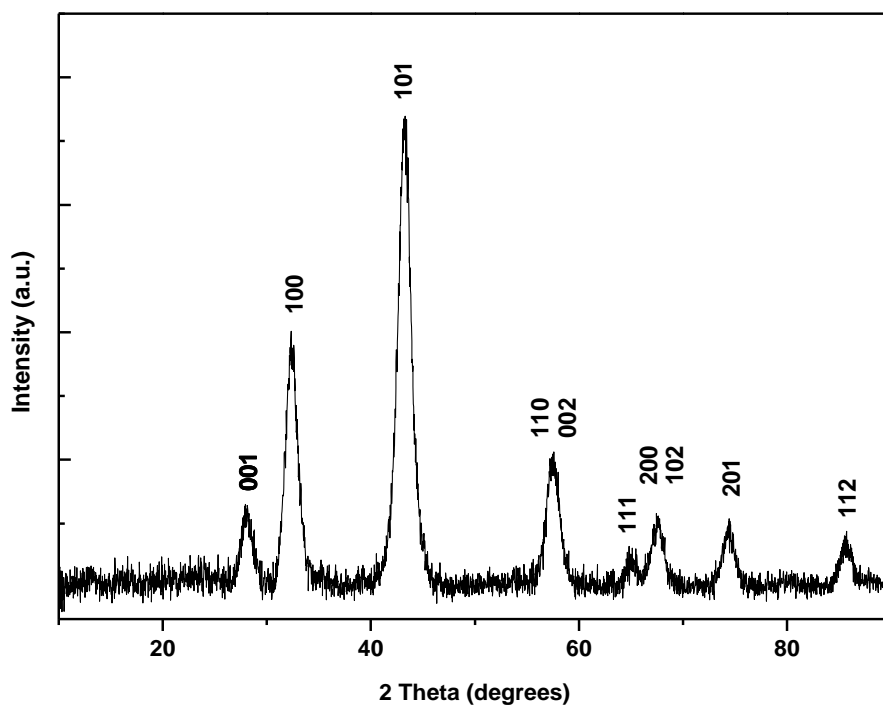


Fig. S4: XRD pattern of long term stored amorphous C-MoP.

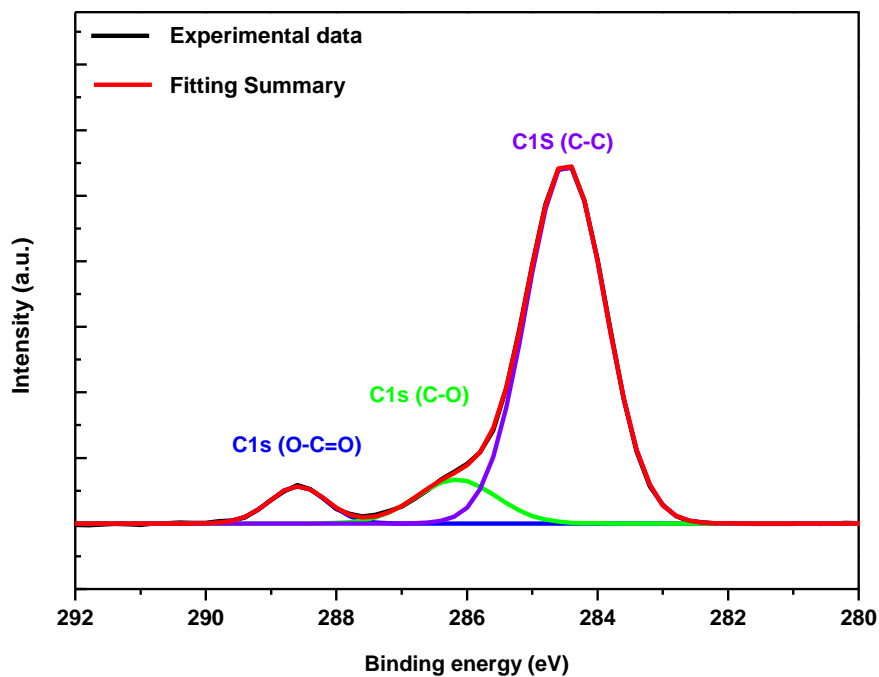


Fig. S5: High resolution spectra of C 1s of A-MoP.

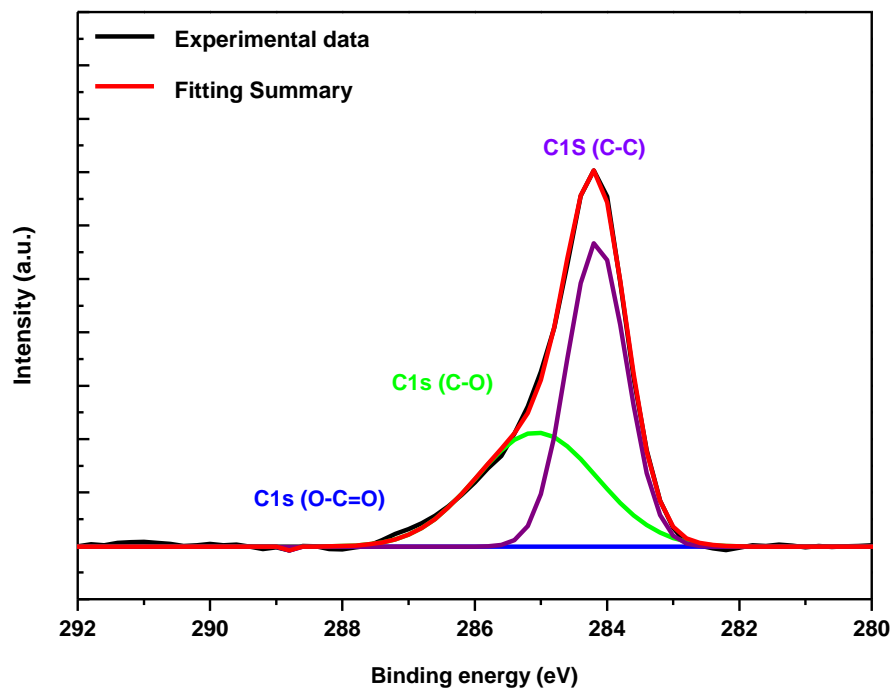


Fig. S6: High resolution spectra of C 1s of C-MoP.

Chapter 4

Phase-dependant electrocatalytic activity of colloiddally synthesized WP and α -WP₂ electrocatalysts in hydrogen evolution reaction

1. Introduction

The current demand for energy across the globe has resulted in potentially an accelerated depletion of fossil fuels that have sustained the energy needs of humans for centuries. As a result, clean and sustainable energy technologies need to be developed to minimize energy shortages and the release of greenhouse gases to the environment in the future.¹⁻³ One promising alternative to fossil fuels is the use of molecular hydrogen, a clean, recyclable, and high energy carrier.⁴⁻⁵ The production of hydrogen through electrochemical water-splitting has been of great interest simply because the electricity required for its operation can be harvested from other renewable energy sources such as solar, wind, turbines, and biomass.⁶ Electrochemical water-splitting leading to hydrogen evolution reaction (HER) requires an electrocatalyst that allows the efficient hydrogen generation at the very low applied potential. Platinum-based materials are still the most active HER electrocatalysts reported to date. However, the high price and scarcity of these Pt-based materials have hindered their use in large scale applications.⁷⁻⁹ For this reason, cheaper and more abundant tungsten-based materials such as tungsten sulphides¹⁰, tungsten nitrides¹¹, tungsten carbides,¹² and tungsten phosphides¹³ were synthesized. Among these less expensive alternatives, tungsten phosphides have emerged as a promising class of non-noble metal materials with high stability and efficiency in both alkaline and acidic media.¹⁴⁻¹⁶

In order to fabricate state-of-the-art tungsten phosphide electrocatalysts; factors influencing their catalytic activity should be fully understood. Recently, it has been established that the crystal phase of an electrocatalyst plays an important role in catalytic activity.¹⁷⁻¹⁹ For example, Pan *et al.* varied the source of the phosphide species to successfully synthesize CoP and Co₂P phases supported on CNTs using a thermal decomposition approach. These results indicated that the different phases exhibited different activities towards the production of hydrogen, with CoP being the most efficient compared to the metal rich Co₂P phase. The Co to P atomic ratios

between CoP and Co₂P were reported to be responsible for the different electrochemical performances.²⁰ Pi *et al.*, fabricated polymorphic tungsten diphosphide (p-WP₂) nanoparticles with mixed orthorhombic (β -) and monoclinic (α -) phases using the phosphidation route via vacuum encapsulation. The hybrid p-WP₂ nanoparticles were found to be more active than the pure β - and α - phases of tungsten diphosphide as a result of improved charge transport (i.e. synergistic effect) and a high number of exposed active sites.²¹ Pan *et al.*, synthesized monodispersed nickel phosphide nanocrystals with different phases (Ni₁₂P₅, Ni₂P and Ni₅P₄) by simply varying the P:Ni precursor ratios using a thermal decomposition route. The results showed that the phosphorus rich Ni₅P₄ was more active than the other two phases because it possessed more proton-acceptor centres and thus, more active catalytic sites.²²

Previous studies have clearly shown that the crystal phase of an electrocatalyst is of vital importance in HER, but limited studies are reported on the synthesis of different phases of tungsten phosphide nanoparticles using solution phase synthesis. As an attempt to close this knowledge gap, this work reports on the colloidal synthesis of two phases of tungsten phosphide (WP and α -WP₂) nanoparticles and their application as electrocatalysts in the HER. The synthesis was conducted using 1-octadecene as a solvent/reductant, tungsten hexachloride as a tungsten source, and trioctylphosphine as the phosphorus source. Phase transformation was achieved by varying the W:P molar ratio of the precursors. The resultant amorphous nanoparticles were exposed to high temperatures to form crystalline phases with compositions that can be readily identified using routine PXRD analysis. The electrocatalytic activities of the two crystalline phases were systematically studied.

2. Experimental

2.1. Chemicals and materials

Tungsten hexachloride [99.9%, WCl₆, Sigma-Aldrich], trioctylphosphine [90%, TOP, Sigma-Aldrich], 1-octadecene [90%, 1-ODE, Sigma-Aldrich], sulfuric acid [H₂SO₄, Associated Chemical Associate], hexane [95%, Sigma-Aldrich], Nafion [5 wt%, Sigma-Aldrich] commercial Pt/C (Tanaka Kikinzoku Kogyo K.K., 20 wt%) and carbon black-Vulcan (XC 72R). Deionized water used to prepare the 0.5 M H₂SO₄ solution was purified using a Millipore system. All chemicals were used as received without further purification.

2.2. Synthesis of WP and WP₂

Trioctylphosphine (11.21 mmol), tungsten hexachloride (0.5546 mmol) and 1-octadecene (15.62 mmol) were mixed in a 100 mL three-neck round bottom flask equipped with a thermometer before refluxing. To ensure inert conditions and to remove moisture, the mixture was heated to 140 °C while purging N₂ for 15 min. The temperature was then increased to 340 °C and maintained for 6 h. After 6 h, the heating mantle was removed, and the reaction mixture was saturated with hexane to allow for rapid cooling and precipitation of the nanoparticles. The nanoparticles were then isolated through centrifugation (7000 rpm, 10 min), washed multiple times with hexane and dried overnight at room temperature. The resultant amorphous nanoparticles were exposed to high temperatures in order to form crystalline phases. Stoichiometric ratios (tungsten hexachloride:trioctylphosphine) of 1:1 and 1:20 were used to obtain the WP and α -WP₂ phases, respectively.

2.3. Materials characterization

Powder X-ray diffraction (PXRD) analysis was conducted using a Bruker D2 phaser (D2-205530) diffractometer with Cu K α radiation ($\lambda = 1.54060 \text{ \AA}$) at 30 kV and 10 mA. Measurements were taken over 2θ angle range of 5 – 90° in steps of 0.0261° with a step time of 5 s at ambient temperature. X-ray photoelectron spectroscopy (XPS) analysis was conducted using a Physical Electronics PHI 5700 spectrometer. Non-monochromatic MgK α X-rays (300 W, 15 kV, and 1253.6 eV) were used as the excitation source. The spectrometer energy scale was calibrated using Cu 2p_{3/2}, Ag 3d_{5/2}, and Au 4f_{7/2} photoelectron lines at 932.7, 368.3, and 84.0 eV, respectively. Samples were mounted on a sample holder without adhesive tape and kept overnight under high vacuum in the preparation chamber before being transferred to the analysis chamber for testing. The spectra were collected in the constant pass energy mode at 29.35 eV. The residual pressure in the analysis chamber was maintained below 1.33×10^{-7} Pa during the spectra acquisition with a multichannel hemi-spherical electron analyser. Transmission electron microscopy (TEM) images were collected using a FEI Technai T12 TEM operated at an accelerating voltage of 120 kV with a beam spot size of 2 in the TEM mode. TEM samples were prepared by dissolving the nanoparticles in hexane, sonicated for 30 min, after which they were deposited on a carbon coated copper grid and allowed to dry at room temperature before analysis. Elemental analysis was performed using an Oxford Instruments energy dispersive X-ray spectroscopy detector fitted in a FEI Technai T12 TEM.

2.4. Electrochemical measurements and preparation of working electrode

The electrochemical measurements were conducted using an Epsilon E₂ potentiostat. The activities of the catalysts were tested in 0.5 M H₂SO₄ using a 3-electrode configuration employing linear sweep voltammetry (LSV) at a scan rate of 2 mV.s⁻¹. All measurements were done using an Ag/AgCl/3M KCl reference electrode and a Pt wire as the counter electrode. The working electrode was a glassy carbon coated with WP or α -WP₂ (diameter = 3 mm, SA = 0.07065 cm²). The stability studies of the catalysts were conducted using a sweep scan rate of 50 mV.s⁻¹ for 1000 cycles using cyclic voltammetry. All potentials were recorded with respect to the reversible hydrogen electrode (RHE). Measurements were performed under ambient conditions. The current density was normalized to the geometrical area of the working electrode and IR correction was applied for all electrochemical measurements. The working electrode was prepared using previously reported methods.²³ The catalyst ink was prepared by dispersing 5 mg of WP/ α -WP₂ and 0.5 mg (10%) of carbon black (Vulcan) in a mixture of water (495 μ L), ethanol (495 μ L) and 10 μ L of 5% Nafion solution. The resultant catalyst ink was sonicated for 30 min at room temperature (RT) to achieve homogeneity, and then a 5 μ L aliquot was pipetted onto the glassy carbon electrode and allowed to dry at RT before use. The amount of WP/ α -WP₂ loaded on the glassy carbon was kept constant at catalyst loading of 0.35 mg.cm⁻². The Ag/AgCl/3M KCl reference electrode was calculated with respect to the reference hydrogen electrode (RHE) by adding a value of (0.197 + 0.059 pH). The potentials reported in this study were all against RHE. Electrochemical impedance spectroscopy (EIS) measurements were conducted at -0.25 V (vs Ag/AgCl) using 5 mV amplitude AC signal at a frequency range of 10⁵-0.1 Hz. To confirm the resistance of the electrodes, the corresponding semicircles was fitted to a specific equivalent circuit using the EC-Lab software. The Electrochemical Impedance Spectroscopy measurements were conducted using a 3 electrode configuration using the SP-300 Potentiostat-Bio-Logic instrument.

2.5. Theoretical calculations

The Density Functional Theory (DFT) as implemented in BIOVIA Materials Studio, was used to complement the experimental results. To achieve this, three BIOVIA Materials Studio modules were employed. These are Cambridge Serial Total Energy Package (CASTEP), DMol³ and Adsorption locator. CASTEP was used for geometrical optimization and determination of the lattice parameters for both WP and WP₂. To study the electronic properties of both structures, DMol³ was used. In both modules, an accuracy threshold was set as 10⁻⁶ eV

and Perdew-Wang generalized-gradient approximation (PW91) functional was employed. This guaranteed considerable increase in the accuracy of predicted energies and structures and minimizing additional computational cost.²⁴ To study H⁺ adsorption on WP and α -WP₂ electrodes, Adsorption locator module was used. Surfaces of 3 x 3 supercells were modelled for WP and α -WP₂ in (011) and (-201) planes, respectively. These plane choices were guided by XRD experimental results. Relaxation was then performed until convergences were achieved, with energy threshold of 10⁻⁶ eV. Hydrogen ion was then modelled for adsorption onto WP and α -WP₂ layers of the electrodes, and 'cleaned' using BIOVIA Materials Studio adsorbate cleaning tool. The maximum adsorption distance was set as 3 Å around the target surface atoms. H⁺ adsorption calculations were then carried out on all the electrodes separately. Energy windows were set at 100 kcal/mol. Condensed-phase Optimized Molecular Potentials for Atomistic Simulation Studies (COMPASS) forcefield was employed. COMPASS is the first ab initio forcefield that has been parameterized and validated using condensed phase properties in addition to various ab initio and empirical data for molecules in isolation.²⁴ Also, COMPASS forcefield enables accurate and simultaneous prediction of structural, conformational, vibrational, and thermophysical properties, that exist for a broad range of molecules in isolation and in condensed phases, and under a wide range of conditions of temperature and pressure.²⁵ The use of this forcefield in this study guaranteed reliable computational results. Low energy configurations and energy distributions were then computed, with accuracy set at 0.0001 kcal/mol.

3. Results and discussion

3.1. Structural and electronic characterisation

The two different phases of tungsten phosphide nanoparticles synthesized by varying the W:P molar ratios of the precursors were determined using XRD. The XRD patterns of the products were characterized by a broad peak at 2 θ of 41°, indicating that the nanoparticles were amorphous (Fig. S1). The amorphous nanoparticles were subsequently heated at 800 °C in N₂ for 1 h, after which complete crystallization was observed resulting in the formation of two phases, namely, tungsten monophosphide (WP) and tungsten diphosphide (α -WP₂) as depicted in Fig. 1. The formation of WP and α -WP₂ nanoparticles was accomplished by using the W:P molar ratios of 1:1 and 1:20, respectively. The WP crystallized in the MnP structure type (space group: Pnma (62)), which coincides with the orthorhombic phase of WP (PDF 00-029-1364) and the lattice constants are a = 5.7310 Å, b = 3.2480 Å, and c = 6.2270 Å. An increase in the phosphorus content to a molar ratio of 1:20 resulted in a phase transformation from WP to α -

WP₂. A high ratio of phosphorous was required to overwhelm the system to force the formation of the less favourable α -WP₂. The α -WP₂ crystallized in the NbAs₂ structure type (space group: C2/m (12)), which corresponds to the monoclinic phase of α -WP₂ (PDF 01-076-2365) and the lattice constants are $a = 8.5000 \text{ \AA}$, $b = 3.1680 \text{ \AA}$, and $c = 7.4660 \text{ \AA}$. The formation of pure tungsten phosphide phases upon annealing without any impurities is supportive evidence that the amorphous nanoparticles had a composition close to that of tungsten phosphide.²⁶

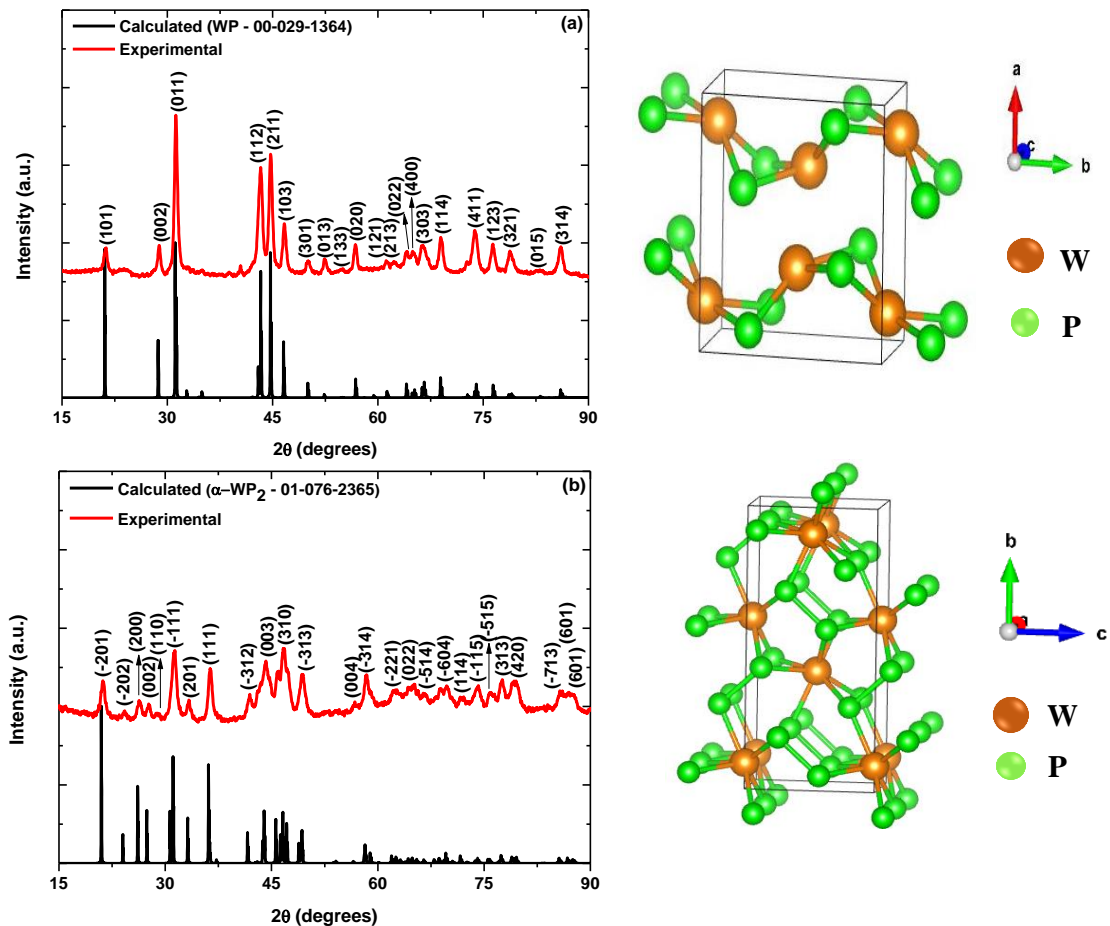


Fig. 1: XRD patterns of (a) tungsten monophosphide (WP, orthorhombic) and (b) tungsten diphosphide (α -WP₂, monoclinic) nanoparticles.

TEM was used to visualize the morphology of the two different phases of tungsten phosphide (Fig. 2). TEM micrograph of WP (Fig. 2a) showed the formation of a continuous sheet-like morphology with small nanoparticles embedded in the sheets. The corresponding HRTEM image (Fig. 2b) revealed well defined lattice fringes with interplanar spacing of 0.307 nm assigned to the (011) plane. Contrary to WP, α -WP₂ (Fig. 2e) formed solely few-layer sheets stacked on top of each other. The corresponding interplanar spacing for α -WP₂ (Fig. 2g) was

0.468 nm which is assignable to the (-201) plane. The interplanar spacing (d_{hkl}) measured from the HRTEM are in good agreement with those calculated from XRD patterns (SI). Furthermore, the SAED patterns of WP (Fig. 2d) and α -WP₂ (Fig. 2h) confirmed the crystalline nature of the catalysts. Energy dispersive X-ray spectroscopy (EDX) was used to confirm the compositional properties of WP and α -WP₂ electrocatalysts. The EDX results (Fig. S2) revealed that the normalized atomic ratio of P/W in WP and α -WP₂ is 1:1.1 and 1:1.5, respectively. This is closer to the empirical chemical formulas of the two catalysts (i.e. WP and α -WP₂).

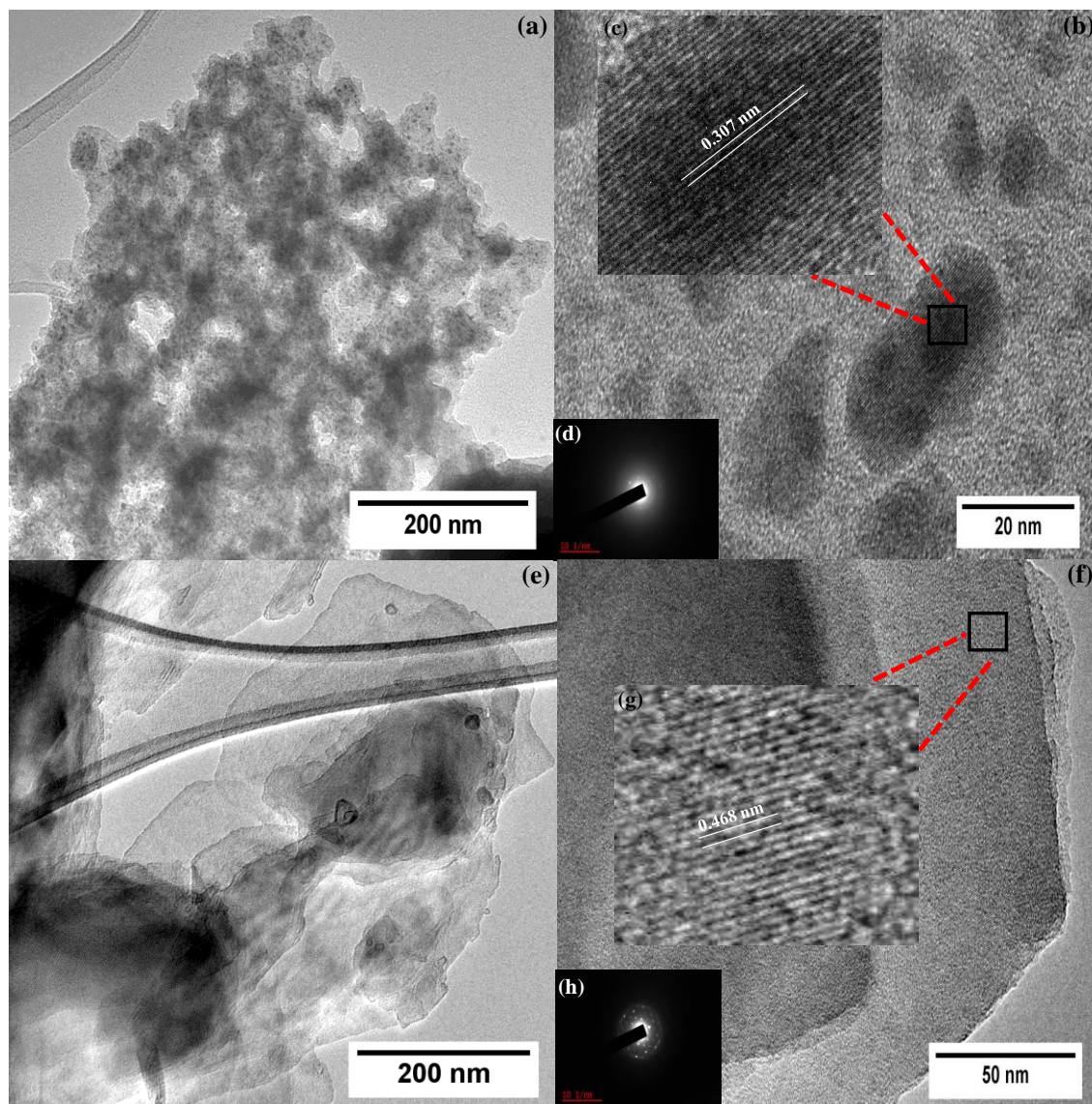


Fig. 2: TEM image of (a) WP, (b) HRTEM image of WP and (inset (c) and (d)) magnified region showing lattice fringes and corresponding SAED pattern for WP. TEM image of (e) α -WP₂, (f) HRTEM image of α -WP₂ and (inset (g) and (h)) magnified region showing lattice fringes and corresponding SAED pattern for α -WP₂.

The compositional properties of WP and α -WP₂ nanoparticles were explored further using X-ray photoelectron spectroscopy (XPS). The survey spectrum of WP (Fig. 3a) revealed the presence of W, P, C, and O elements on its surface, with no signals attributed to any other impurities. The deconvolution of the high-resolution P 2p spectrum (Fig. 3b) resulted in 2 peaks at binding energies (BEs) 129.3 and 130.3 eV, corresponding to P 2p_{3/2} and P 2p_{1/2}, respectively. The P 2p_{3/2} and P 2p_{1/2} peaks were ascribed to P in the P-W bond. The predominant peak located at BE of 133.4 eV (P 2p_{3/2}) was assigned to the P-O bond caused by surface oxidation of the P atoms (PO₄³⁻ and P₂O₅) as they were exposed to air.²⁷ This is not observed in the XRD as such suggests that oxidation only occurs on the surface. The high-resolution W 4f spectrum (Fig. 3c) showed peaks at 31.4 eV (W4f_{7/2}) and 33.5 eV (W4f_{5/2}) that were assigned to W in the P-W bond. Furthermore, two peaks were found at 35.7 eV (W4f_{7/2}) and 37.8 eV (W4f_{5/2}) corresponding to WO₃ formed by partial oxidation (i.e. air) on the nanoparticle's surface.²⁸⁻²⁹ The high-resolution C 1s spectrum (Fig. S3) was deconvoluted to three peaks with BEs of 284.2, 285.0, 285.8 eV, ascribed to C-C, C-O and O-C=O, respectively. The presence of C was attributed to the residual carbon from the starting reagents. The survey spectrum of α -WP₂ (Fig. 3d) revealed the presence of W, P, C, and O elements on its surface, with no signals attributed to any impurities. Contrary to WP, the P 2p spectrum (Fig. 3e) of α -WP₂ displayed a single peak deconvoluted to two at BEs of 133.6 and 134.4 eV, assigned to the P-O bond. The P 2p_{3/2} and P 2p_{1/2} peaks assigned to the P in the P-W bond were not observed in α -WP₂ as expected based on the XRD results. The absence of the P 2p_{3/2} and P 2p_{1/2} peaks in transition metal phosphides (TMP) was previously reported to occur due to their susceptibility to surface oxidation. For example, Chang *et al.* synthesized Ni₅P₄ NPA/CP and S-Ni₅P₄ NPA/CP catalysts for HER. In their study, the P 2p spectrum of Ni₅P₄ NPA/CP showed a single peak assigned to P-O species, with no evidence of P in the Ni-P bond. However, the introduction of the S-dopant to form S-Ni₅P₄ NPA/CP promoted surface passivation and the peak corresponding to P in the phosphide emerged.³⁰ Stern *et al.* reported on the removal of the NiO_x layer on the surface of Ni₂P nanoparticles through Ar ion sputtering. The XPS depth (50 nm) profiling spectrum recorded subsequent to sputtering showed a significant increase in the P/Ni concentration and a decrease in the oxygen content, indicating that the nanoparticles underwent surface oxidation.³¹ The high-resolution W 4f spectrum (Fig. 5f) showed peaks at BEs of 31.1 and 33.4 eV, corresponding to W4f_{7/2} and W4f_{5/2}, respectively. The W4f_{7/2} and W4f_{5/2} were assigned to W in the P-W bond. The two peaks found at 35.8 eV (W4f_{7/2}) and 36.1 eV (W4f_{5/2}) corresponded to WO₃ formed by oxidation (i.e. air) on the nanoparticle's surface. Once more,

it can be noted that the oxide species peak dominates over the W peak in the W-P bond. XRD analysis was then performed on long-term stored α -WP₂ to confirm the bulk composition of the nanoparticles.

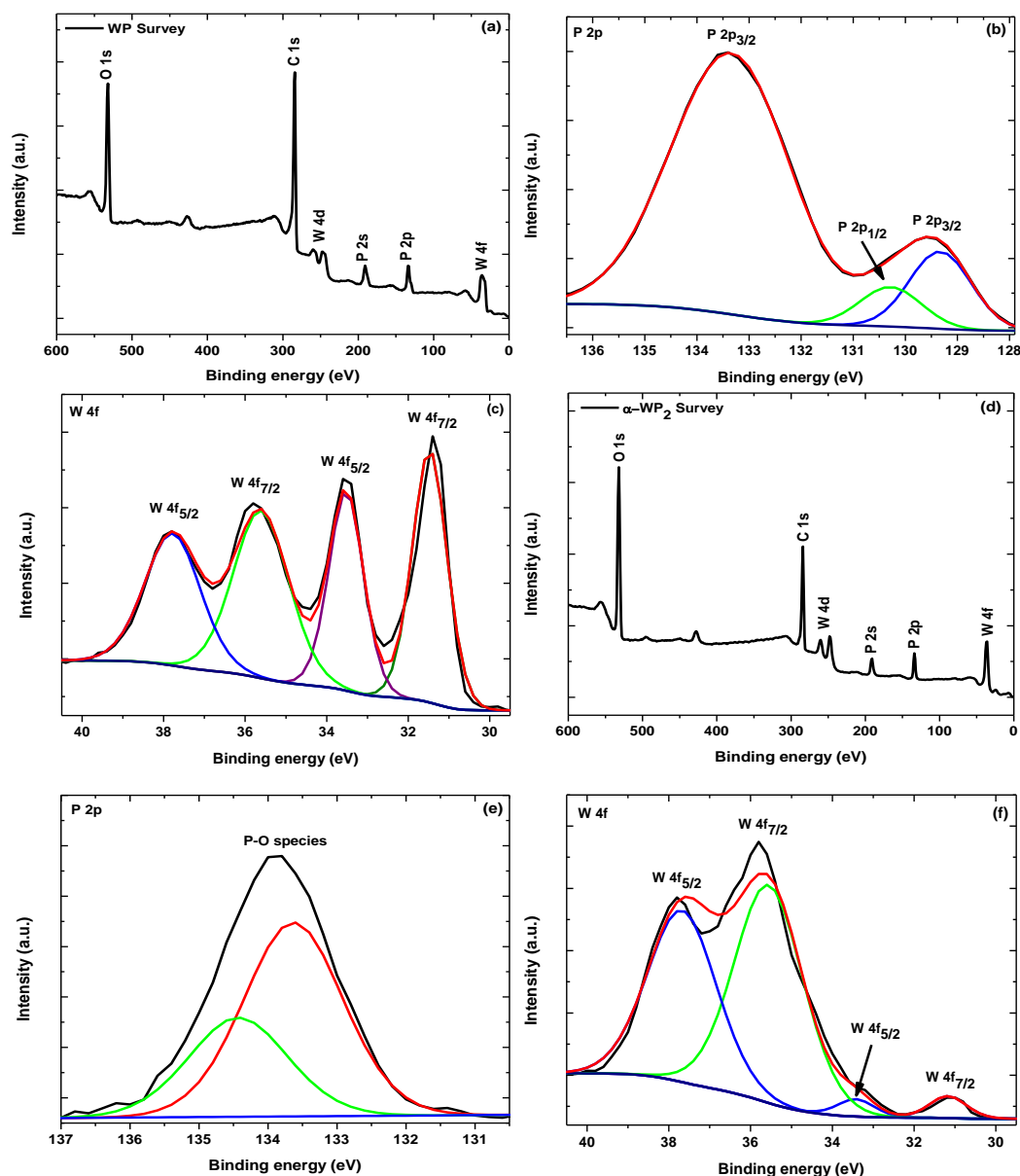


Fig. 3: XPS survey spectrum of (a) WP and corresponding high-resolution spectra: (b) P 2p, (c) W 4f; survey spectrum of (d) α -WP₂ and corresponding high-resolution spectra: (e) P 2p and (f) W 4f.

The resultant XRD pattern (Fig. S4) displayed no peaks that matched to any metaphosphate or oxide species of tungsten (i.e. W(PO₄)₂ or WO₃) proving that they occurred mainly on the surface of the nanoparticles which can only be detected by XPS as it only analyses the surface. The high-resolution C 1s spectrum (Fig. S2), was deconvoluted to three peaks with BEs of 284.2, 285.0, 285.8 eV, ascribed to C-C, C-O and O-C=O, respectively.

3.2. Electrocatalytic HER

The electrocatalytic activity of WP and α -WP₂ towards HER was evaluated using a 3-electrode system in 0.5 M H₂SO₄ at a scan rate of 2 mVs⁻¹. Bare glassy carbon electrode (GCE), carbon black (Vulcan) and Pt/C (20 wt%) were also tested for comparison. The Pt/C benchmark electrocatalyst displayed excellent HER activity characterised by the ~ 0 mV onset overpotential. As expected, the bare GCE and carbon black showed negligible catalytic activity towards HER. The polarization curves revealed that WP and α -WP₂ (Fig. 4a) required overpotentials of -314 and -271 mV to produce a current density of 10 mA.cm⁻², respectively. In an acidic medium, HER is described using three possible reactions, namely, Volmer, Heyrovsky and Tafel reaction.³²⁻³³



At 25 °C, the calculated Tafel slopes for the aforementioned reactions were 118, 39 and 29 mV.dec⁻¹, respectively.³³ The Tafel slope is an important intrinsic property of a catalyst that is used to understand the mechanism and can be used as an indicator of the rate determining step. From first principle calculations, the Volmer reaction is the rate determining step when the Tafel slope is 118 mV.dec⁻¹, while Tafel slopes of 39 and 29 mV.dec⁻¹ indicate that the rate determining step is the Tafel or Heyrovsky reaction, respectively.³³ To study the mechanism, the Tafel slopes were extrapolated from the polarization curves (η vs. $\log j_0$) using the Tafel equation (eq. 4).³⁴⁻³⁵

$$\eta = b \log j + a \quad \text{eq. 4}$$

Where η is the overpotential, b represents the Tafel slope and j corresponds to the current density and 'a' is the intercept and generally assumed to be $\log(j)$ at $\eta = 0$. The Tafel slopes were estimated from the linear region of the Tafel plots (η vs. $\log j$), where the Tafel equation is satisfied.³⁴⁻³⁵ Fig. 4b shows the Tafel slopes of the Pt/C, WP and α -WP₂ catalysts. The Pt/C electrocatalyst gave a very small Tafel slope of 29.79 mV.dec⁻¹, characteristic of the highly active benchmark. The corresponding Tafel slopes for WP and α -WP₂ nanocrystals were 95.71 and 86.83 mV.dec⁻¹, respectively. Experimentally, the two most commonly observed pathways in HER are the Volmer-Heyrovsky and Volmer-Tafel mechanisms. The calculated Tafel slopes for WP and α -WP₂ falls in the range of 39 – 118 mV.dec⁻¹, illustrating the Volmer-Heyrovsky

mechanism on both catalysts where the reaction between H_{ads} , H^+ and e^- to generate hydrogen is the rate determining step.³⁶⁻³⁷

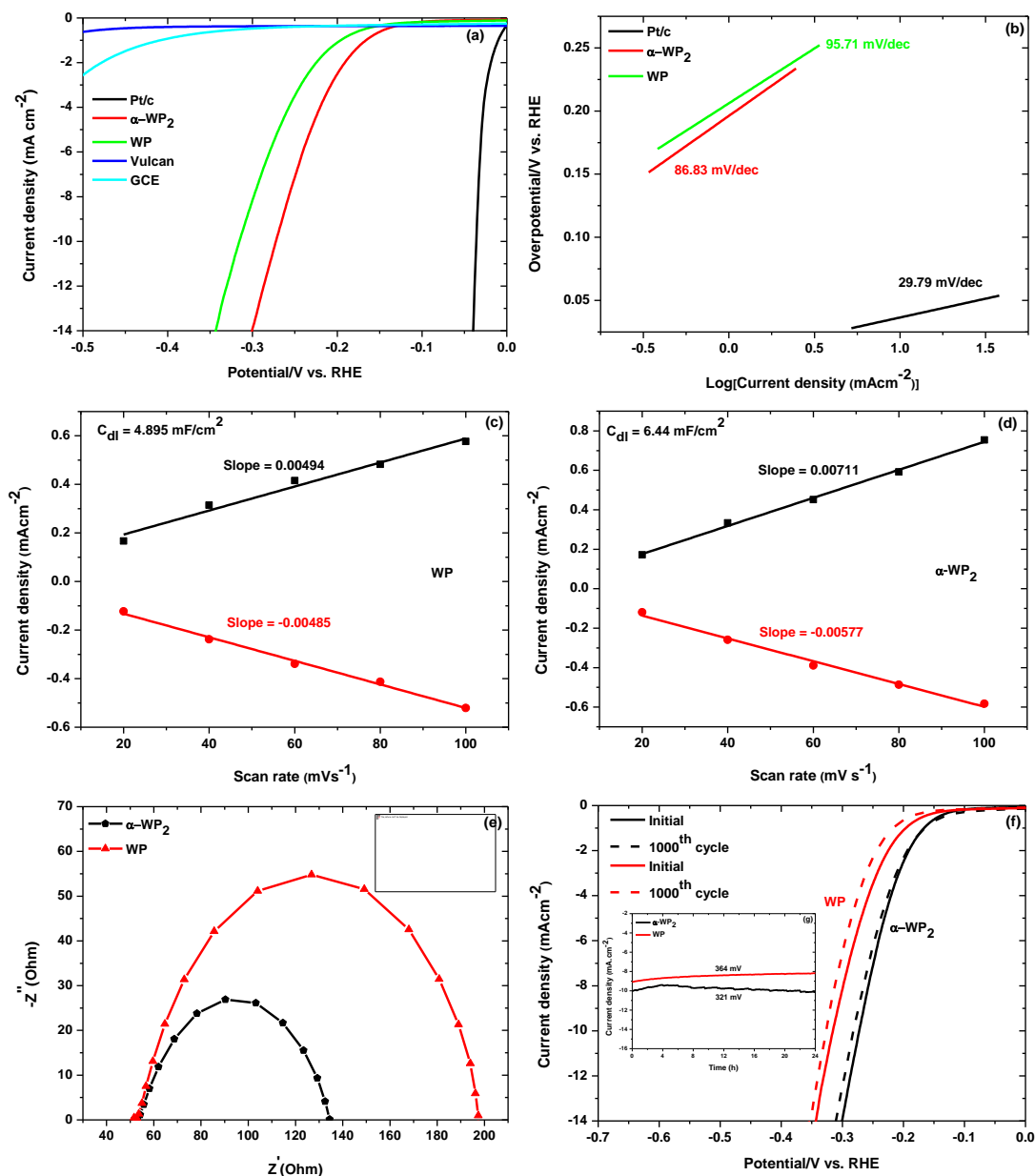


Fig. 4: (a) LSV polarization curves of Pt/c, α -WP₂, WP, Vulcan and GCE at a scan rate of 2 mV/s; (b) corresponding Tafel plots for Pt/c, α -WP₂ and WP; (c) and (d) the C_{dl} of WP and α -WP₂; (e) Nyquist plots of WP and α -WP₂ catalysts; (f) LSV curves of WP and α -WP₂ before and after 1000 potential cycles and (insert (g)) chronoamperometry measurements of WP and α -WP₂ at constant applied potential of -364 and -321 mV, respectively.

The smaller Tafel slope for α -WP₂ indicates faster kinetics, and thus high H₂ generating rates compared to WP. By extrapolating the Tafel plot to 0 V overpotential, the calculated exchange current density (j_0) of α -WP₂ (Table S1) was slightly higher than that of WP, demonstrating an increased reaction rate at the surface of the phosphorus rich α -WP₂. Moreover, the low onset potential of α -WP₂ (-106 mV) over WP (-145 mV) indicates that a small amount of energy is needed to aid the H₂ generation process on its surface. It should be noted that even though α -WP₂ outperformed WP, both catalysts displayed electrocatalytic activity that compared favourably to some of the reported tungsten phosphide HER electrocatalysts (Table 1) even at very low catalyst loading of 0.35 mg.cm⁻².

Table 1: Comparison of the electrocatalytic activity of tungsten phosphide electrocatalysts in acidic medium.

Catalyst	Loading (mg.cm⁻²)	η_{10} (mV)	β (mV.dec⁻¹)	Reference
α -WP ₂	0.35	-271	86.83	This work
WP	0.35	-314	95.71	This work
WP NMPs/CFs	4	-274	98	38
α -WP ₂	2	-201	98	39
β -WP ₂	2	-257	107	39
WP NPs@NC	2	-102	58	40
A-WP	0.213	-254	65	41
WP-600	-	-	90	42
WP-700	-	-	85	42
WP-800	-	-	129	42
WP/KB-700	-	-	60	42
WP ₂ NSs/CC	2	-135	67	43
WP ₂ NPs/CC	2	-201	98	43
WP ₂ NRs	-	-148	52	44
Bulk WP ₂	-	-347	79	44
Bulk WP	2	-501	78	45
WP@NC	2	-306	58	45
WP(nano)	1	-120	54	46

The superior catalytic activity of α -WP₂ over WP can be explained using the electronegativity differences between W and P atoms. The high electronegative P atoms draw electrons away from the W atoms, resulting in the formation of a partial negative charge on the P atoms (i.e. proton-acceptor centres). The partial negative charge allows P atom to act as a base to trap the positively charged H⁺ ion, thus increasing the electrocatalytic performance with the increase in P content.⁴⁷⁻⁴⁹ These results show that a high degree of phosphorization is a key factor in improving the catalytic activity of TMPs. To further elucidate the difference in catalytic activity observed between WP and α -WP₂, the electrochemically active surface area (ECSA) was indirectly determined based on the electrochemical double layer capacitance (C_{dl}, details on calculation of C_{dl} provided in the additional supporting information) using cyclic voltammetry (CV) as shown in Fig. S5. The C_{dl} of WP (Fig. 4c) and α -WP₂ (Fig. 4d) were 4.895 and 6.440 mF.cm⁻², respectively. The slightly higher ECSA of the phosphorus rich α -WP₂ (128.8 cm²) over the WP (122.4 cm²) implied a high proportion of exposed electrochemical active sites which facilitated the observed high HER efficiency. The electrical conductivity properties of the catalysts were studied using electrochemical impedance spectroscopy (EIS) and the corresponding Nyquist plots for WP and α -WP₂ are shown in Fig. 4e. The Nyquist plots for WP and α -WP₂ catalysts exhibit a single semicircle, showing that the corresponding equivalent circuit (Fig. S6) consist of a single time constant. The charge transfer resistance of α -WP₂ (93 Ω) was found to be smaller than that of WP (155 Ω), demonstrating superior electron transport within α -WP₂. Long-term durability is another important property in the development of efficient HER catalysts. Cyclic voltammetry (CV) was used to study the stability by applying 1000 cycles to the WP and α -WP₂ catalysts. Fig. 4f shows that there was a slight decrease in catalytic activity after 1000 cycles for both WP and α -WP₂, indicating that the catalysts were largely stable in acidic media. To corroborate the stability results obtained from subjecting the catalysts to 1000 cycles, fixed potential electrolysis (insert (g)) was conducted for the WP and α -WP₂ catalysts at overpotential of 364 and 321 mV, respectively. Following long period of 24 h, the current density generated by the catalysts at constant potential showed negligible degradation over time, indicating reasonably good long-term stability. Notably for α -WP₂, a decrease is observed for the first 4 h, after which the current density increases and stabilize at 10 mA.cm⁻². The observed increase and stabilization of the current density after 4 h could be attributed to the electrochemical activation of the α -WP₂ catalyst with prolonged exposure to constant potential. In order to get a better understanding of the effect of temperature on the electrocatalytic activity of WP and α -WP₂, LSV polarization

measurements were performed at various temperatures (298, 308, 318 and 328 K). Shown in Fig. 5a and Fig. 5b are the corresponding LSV curves at different temperatures for WP and α -WP₂ catalysts, respectively. For both catalysts, there was a decrease in the overpotential with increasing temperature. This observation can be explained using the Gibbs free energy equation ($\Delta G = \Delta H - T\Delta S$), where ΔH is the reaction enthalpy ($\text{J}\cdot\text{mol}^{-1}$) and ΔS is the change in entropy ($\text{J}\cdot\text{K}^{-1}\cdot\text{mol}^{-1}$). According to the Gibbs free energy equation, an increase in temperature causes a decrease in ΔG , which in turn decreases the potential required to drive the hydrogen evolution process.⁵⁰ The kinetic parameters of the temperature-dependant HER activity of WP and α -WP₂ as estimated from the Tafel plots are summarized in Table S2.

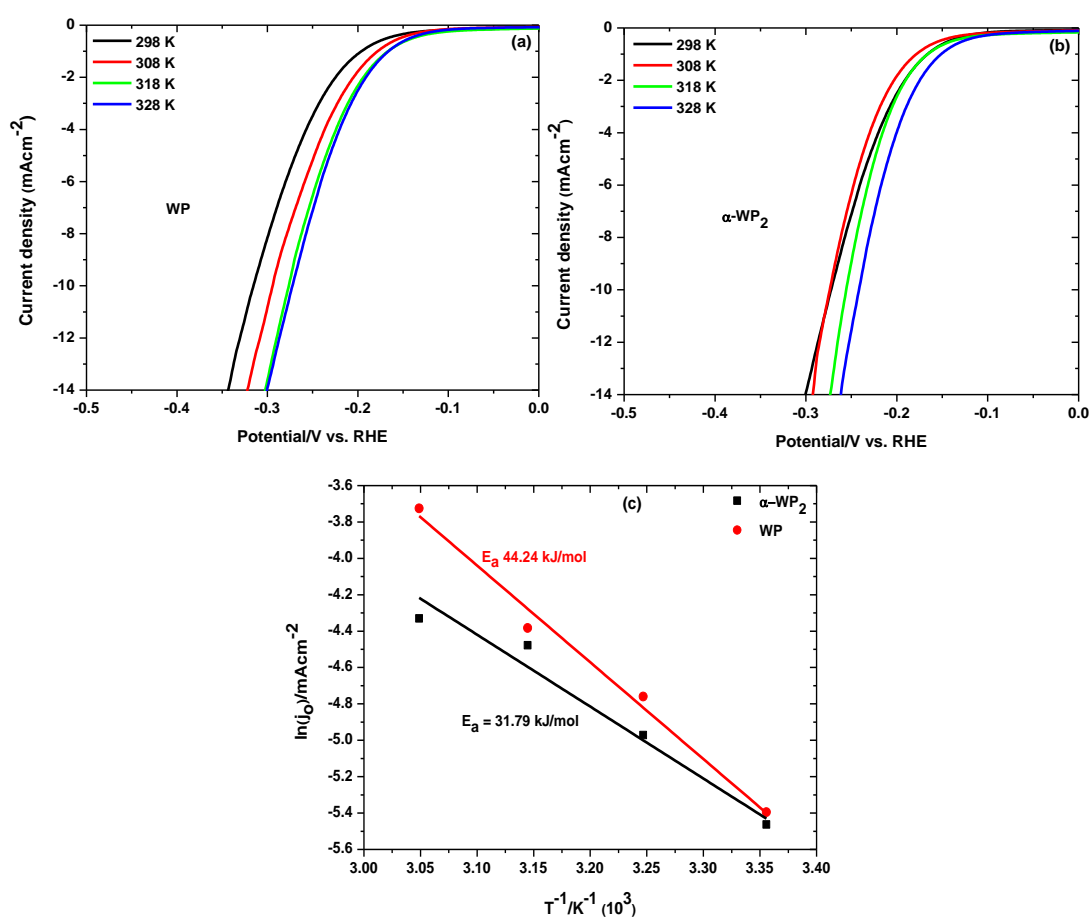


Fig. 5: LSV curves of (a) WP and (b) α -WP₂ at different temperatures, (c) Arrhenius curves for WP and α -WP₂ catalysts.

At all the temperatures studied in this work, an increase in the exchange current density (j_0) and a decrease in the Tafel slope (Fig. S7) was observed as the temperature was increased for both WP and α -WP₂ catalysts. The Arrhenius equation was employed to calculate the minimum amount of energy needed for the generation of hydrogen in an acidic medium. This was done by plotting $\ln(j_0)$ versus $1/T$ (Fig. 5c) where E_a was extrapolated from the slope ($\frac{-E_a}{R}$). The

experimentally determined E_a for WP and α -WP₂ were 44.24 and 31.79 kJ/mol, respectively. The smaller activation energy of α -WP₂ over WP indicated that minimal energy was required to drive hydrogen generation on the surface of the phosphorus rich α -WP₂ catalyst. These results demonstrate that the electrocatalytic activity of non-noble metal electrocatalysts can be improved by increasing the electrolyte temperature.

3.3. DFT calculations

The electronic properties of WP and α -WP₂ were modelled using density functional theory (DFT) calculations in order to further understand the observed catalytic differences between the orthorhombic and monoclinic phases of tungsten phosphide. The conductivity of an electrocatalyst is beneficial in HER as it allows for efficient electron transport. Fig. 6 shows the band structures and projected density of states (PDOS) of WP and α -WP₂. From the band structures, it can be observed that the fermi level (E_f) of WP lies on the edge of the conduction band (CB) whereas in α -WP₂ there is a clear overlap between the E_f and CB. This implies that α -WP₂ is a good conductor material compared to WP, possessing semi-metallic properties typical of transition metal phosphides. The theoretically determined conductivity differences were also observed experimentally using EIS (Fig. 4e). It is well known that the electron configuration of a molecule controls its electronic properties. An efficient HER electrocatalyst shows well-developed d-bands extending across the fermi level, which lower the activation energy by interacting with the hydrogen atoms.⁵¹ From the PDOS diagrams it can be seen that compared to WP, the contribution of the d-electrons is prominent for the energy bands near the fermi level of the α -WP₂. The high d-electrons density plays a vital role in the conductivity of the α -WP₂ catalyst. The calculated bond lengths of WP and α -WP₂ were 2.5165 and 2.5177 Å, respectively. The slightly longer bond length of α -WP₂ enhances the delocalization of electrons on the P-atoms resulting in the reduction of the barrier to proton binding, which is beneficial to catalytic activity.⁵² In HER, the generation of hydrogen in an acidic media involves adsorption, reduction of proton on the catalyst surface and subsequent desorption of molecular hydrogen.⁵³⁻⁵⁴

The ease of adsorption and desorption make a good HER electrocatalyst. Hence, an efficient electrocatalyst must find balance between the two aforementioned processes. The best performing electrocatalyst (i.e. Pt) have hydrogen adsorption energies close to $\Delta G_H = 0$, binding hydrogen neither too strong nor too weak.⁵⁵⁻⁵⁷ The hydrogen adsorption calculations were conducted on the (001) and (-201) surfaces for WP and α -WP₂, respectively, as shown in Fig. S8. The hydrogen adsorption energies of WP and α -WP₂ were found to be -0.709 and -0.665 eV, respectively. The slightly lower adsorption energy (i.e. 6.63% lower) of α -WP₂ indicated that it allowed for better H⁺ adsorption and desorption, thus becoming favourable for HER.

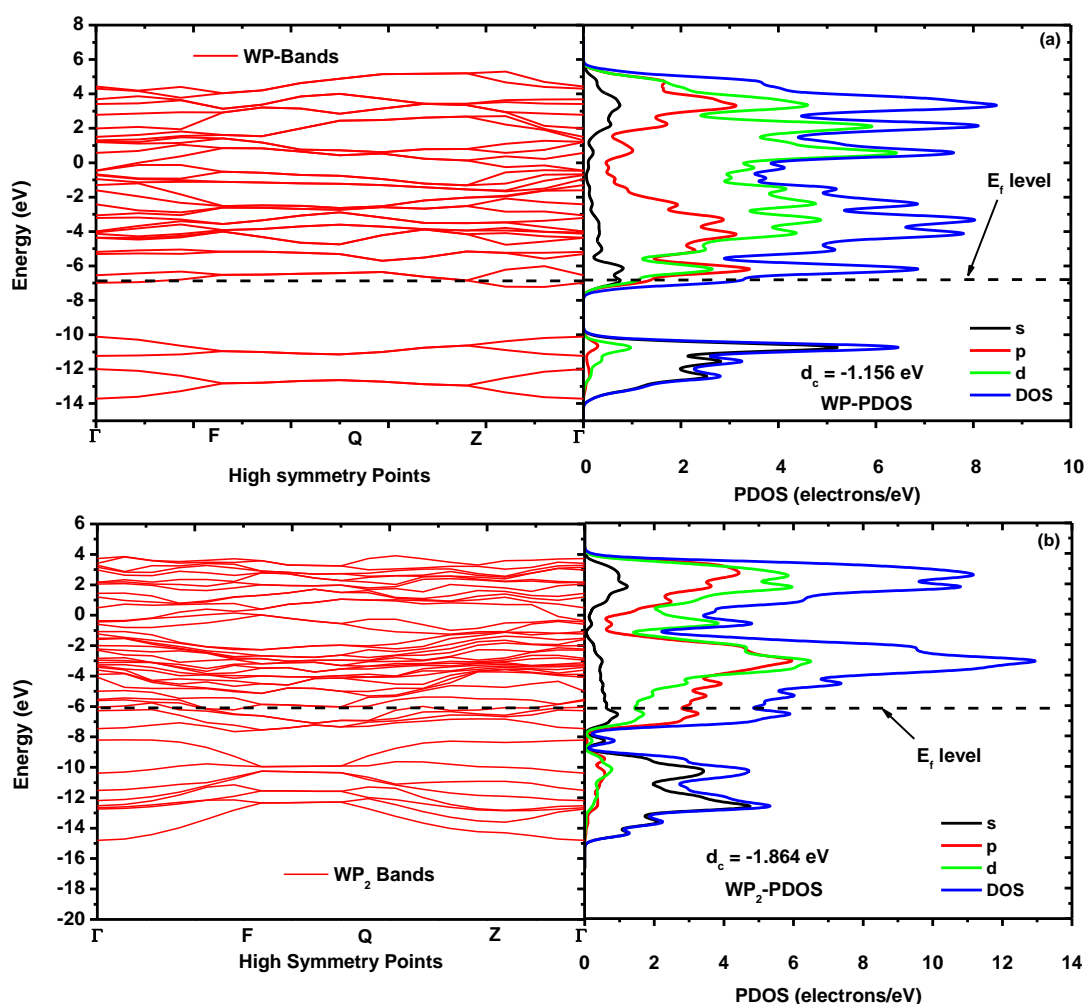


Fig. 6: Band structures and projected density of states of (a) WP and (b) α -WP₂.

Further DFT calculations revealed that the energy barrier for the transition state (T. S.) of H-atom adsorption on α -WP₂ (-0.0084 eV) was less negative than that on WP (-0.019 eV). The formation of H-H bonds is easily achieved at lower energy barrier. In addition to the hydrogen adsorption energies, the position of the d-band center (d_c) can also be used to understand the

catalytic activity of catalysts. The d-band center for the WP and α -WP₂ were determined to be -1.156 and 1.864 eV, respectively. The lower energy of the d-band for α -WP₂ implies a reduced binding strength of the hydrogen protons on the catalyst surface which promotes ideal desorption resulting in improve catalytic activity.⁵⁸⁻⁵⁹

4. Conclusion

The monoclinic (WP) and orthorhombic (α -WP₂) phases of tungsten phosphide were successfully synthesized via a simple one-pot colloidal synthesis method and investigated as potential electrocatalysts for HER. The phase change was ascertained by varying the molar ratio of the precursors, with molar ratios of 1:1 and 1:20 favouring the formation of WP and α -WP₂, respectively. Both phases displayed excellent activity and stability as electrocatalysts in acidic media. The α -WP₂ catalysts required an overpotential of -271 mV at 10 mA.cm⁻² and a Tafel slope of 86.83 mV/dec, whereas WP required -314 mV at 10 mA.cm⁻² and a Tafel slope of 95.71 mV/dec. The superior catalytic activity of α -WP₂ over WP was attributed to, amongst others, high proportion of active sites, ensemble effect of P on phosphorus rich α -WP₂, high electrical conductivity, favourable hydrogen adsorption energy, lower barrier for formation of transition state and low d-band center energy. This work demonstrates that tailoring the crystal phase or phosphorus content of an electrocatalyst is an efficient strategy that can be employed to improve the activity of TMPs catalysts.

5. References

1. J. Mu, J. Xu, C. Zhou, Q. Wang, X. Wang, Z. Liu, X. Zhao, E. Yang, Self-supported oxygen and molybdenum dual-doped cobalt phosphide hierarchical nanomaterials as superior bifunctional electrocatalysts for overall water splitting, *ChemElectroChem*. 8 (2021) 103-111.
2. X. Zou, Y. Zhang, Noble metal-free hydrogen evolution catalysts for water splitting, *Chem. Soc. Rev.* 44 (2015) 5148-5180.
3. J. Wang, Y. Qin, X. Liu, X. Zhang, In situ synthesis of magnetically recyclable graphene-supported Pd@Co core-shell nanoparticles as efficient catalysts for hydrolytic dehydrogenation of ammonia borane, *J. Mat. Chem.* 22 (2012) 12468-12470.

4. S.K. Shiva, V. Himabindu, Hydrogen production by PEM water electrolysis – A review, *Mater. Sci. Energy Technol.* 2 (2019) 442-454.
5. A. Kazim, T.N. Veziroglu, Utilization of solar–hydrogen energy in the UAE to maintain its share in the world energy market for the 21st century, *Renew. Energy* 24 (2001) 259-274.
6. G. Cipriani, V.D. Dio, F. Genduso, D.L. Cascia, R. Liga, R. Miceli, G.R. Galluzzo, Perspective on hydrogen energy carrier and its automotive applications, *Intern. J. Hydrog. Energy* 39 (2014) 8482-8494.
7. P.N. Duchesne, Z.Y. Li, C.P. Deming, V. Fung, X. Zhao, J. Yuan, T. Regier, A. Aldalbahi, Z. Almarhoon, S. Chen, D. Jiang, N. Zheng, P. Zhang, Golden single-atomic-site platinum electrocatalysts, *Nat. Mater.* 17 (2018) 1033-1039.
8. T. Ding, Z. Wang, L. Zhang, C. Wang, Y. Sun, Q. Yang, Highly active and durable CuPdPt/C electrocatalyst for efficient hydrogen evolution reaction, *J. Mater. Chem. A* 4 (2016) 15309-15315.
9. B. Kim, T. Kim, K. Lee, J. Li, Recent advances in transition metal phosphide electrocatalysts for water splitting under neutral pH conditions, *ChemElectroChem*, 7 (2020) 3578-3589.
10. L. Yang, X. Wu, X. Zhu, C. He, M. Meng, Z. Gan, P.K. Chu, Amorphous nickel/cobalt tungsten sulfide electrocatalysts for high-efficiency hydrogen evolution reaction, *Appl. Surf. Sci.* 341 (2015) 149-156.
11. W.F. Chen, J.M. Schneider, K. Sasaki, C.H. Wang, J. Schneider, S. Iyer, S. Iyer, Y. Zhu, J. Muckerman, E. Fujita, Tungsten carbide–nitride on graphene nanoplatelets as a durable hydrogen evolution electrocatalyst, *ChemSusChem commun.* 7 (2014) 2414-2418.
12. A.V. Nikiforov, I.M. Petrushina, E. Christensen, N.V. Alaxeev, A.V. Samokhin, N.J. Bjerrum, WC as a non-platinum hydrogen evolution electrocatalyst for high temperature PEM water electrolyzers, *Intern. J. Hydrog. Energy* 37 (2012) 18591-18597.
13. J.M. McEnaney, J.C. Crompton, J.F. Calleja, E.J. Popczun, C.G. Read, N.S. Lewis, R.E. Schaak, Electrocatalytic hydrogen evolution using amorphous tungsten phosphide nanoparticles, *ChemComm* 50 (2014) 11026-11028.
14. L. Feng, H. Xue, Advances in transition-metal phosphide applications in electrochemical energy storage and catalysis, *ChemElectroChem* 4 (2017) 20-34.
15. Z. Pu, Q. Liu, A.M. Asiri, X. Sun, Tungsten phosphide nanorod arrays directly grown on carbon cloth: A highly efficient and stable hydrogen evolution cathode at all pH values, *ACS Appl. Mater. Interfaces* 6 (2014) 21874-21879.

16. Z. Pu, X. Ya, I.S. Amiin, Z. Tu, X. Liu, W. Li, S. Mu, Ultrasmall tungsten phosphide nanoparticles embedded in nitrogen-doped carbon as a highly active and stable hydrogen evolution electrocatalyst, *J. Mater. Chem. A* 4 (2016) 15327-15332.
17. P. Liu, J.A. Rodriguez, Catalysts for hydrogen evolution from the [NiFe] hydrogenase to the Ni₂P(001) surface: The importance of ensemble effect. *J. Am. Chem. Soc.* 127 (2005) 14871-14878.
18. P. Xiao, M.A. Sk, L. Thia, X. Ge, R.J. Lim, J. Wang, K.H. Lim, X. Wang, Molybdenum phosphide as an efficient electrocatalyst for the hydrogen evolution reaction, *Energy Environ. Sci.* 7 (2014) 2624-2629.
19. Y. Shi, B. Zhang, Recent advances in transition metal phosphide nanomaterials: synthesis and applications in hydrogen evolution reaction, *Chem. Soc. Rev.* 45 (2015) 1529-1541.
20. Y. Pan, Y. Lin, Y. Chen, Y. Liu, C. Liu, Cobalt phosphide-based electrocatalysts: synthesis and phase catalytic activity comparison for hydrogen evolution, *J. Mater. Chem. A* 4 (2016) 4745-4754.
21. M. Pi, T. Wu, W. Guo, X. Wang, D. Zhang, S. Wang, S. Chen, Phase-controlled synthesis of polymorphic tungsten diphosphide with hybridization of monoclinic and orthorhombic phases as a novel electrocatalyst for efficient hydrogen evolution, *J. Power Sources* 349 (2017) 138-143.
22. Y. Pan, Y. Liu, J. Zhao, K. Yang, J. Liang, D. Liu, W. Hu, D. Liu, Y. Liu, C. Liu, Monodispersed nickel phosphide nanocrystals with different phases: synthesis, characterization and electrocatalytic properties for hydrogen evolution, *J. Mater. Chem. A* 3 (2015) 1656-1665.
23. Z. Xing, Q. Liu, A. M. Asiri, X. Sun, High-efficiency electrochemical hydrogen evolution catalyzed by tungsten phosphide submicroparticles, *ACS Catal.* 5 (2015) 145-149.
24. J.P. Perdew, Y. Wang, Accurate and simple analytic representation of the electron-gas correlation energy, *Phys. Rev. B* 45 (1992): 13244-13249.
25. S. Sharma, P. Kumar, R. Chandra, Overview of BIOVIA Materials Studio, LAMMPS, and GROMACS. In *Molecular Dynamics Simulation of Nanocomposites Using BIOVIA Materials Studio, LAMMPS and GROMACS*, Elsevier:2019); Chapter 2, pp 39-100.
26. S.S. Nkabinde, Z.B. Ndala, N.P. Shumbula, T. Kolokoto, O. Nchoe, G.N. Ngubeni, K.P. Mubiayi, N. Moloto, Delineating the role of crystallinity in the electrocatalytic activity of colloiddally synthesized MoP nanocrystals, *New J. Chem.* 44 (2020) 14041-14049.

27. A.P. Grosvenor, S.D. Wik, R.G. Cavell, A. Mar, Examination of the bonding in binary transition-metal phosphides MP (M = Cr, Mn, Fe, Co) by X-ray photoelectron spectroscopy, *Inorg. Chem.* 14 (2005) 8988-8998.
28. X. Zhang, T. Guo, T. Liu, K. Lv, Z. Wu, Tungsten phosphide (WP) nanoparticles with tunable crystallinity, W vacancies, and electronic structures for hydrogen production, *Electrochim. Acta* 323 (2019) 134798.
29. Y. Shen, L. Li, J. Xi, X. Qiu, A facile approach to fabricate free-standing hydrogen evolution electrodes: riveting tungsten carbide nanocrystals to graphite felt fabric by carbon nanosheets, *J. Mater. Chem. A* 4 (2016) 5817-5822.
30. J. Chang, K. Li, Z. Wu, J. Ge, C. Liu, W. Xing, Sulfur-doped nickel phosphide nanoplates arrays: A monolithic electrocatalysts for efficient hydrogen evolution reactions. *ACS Appl. Mater. Interfaces* 10 (2018) 26303-26311.
31. L.A. Stern, L. Feng, F. Song, Ni₂P as a Janus catalyst for water splitting: the oxygen evolution activity of Ni₂P nanoparticles, *Energy Environ. Sci.* 8 (2015) 2347-2351.
32. Y. Shen, L. Li, X. Qiu, A facile approach to fabricate free-standing hydrogen evolution electrodes: riveting tungsten carbide nanocrystals to graphite felt fabrics by carbon nanosheets, *J. Mater. Chem. A* 4 (2016) 5817-5822.
33. Y. Shi, B. Zhang, Recent advances in transition metal phosphide nanomaterials: synthesis and applications in hydrogen evolution reaction, *Chem. Soc. Rev.* 45 (2016) 1529-1541.
34. A.P. Murthy, J. Theerthagiri, J. Madhavan, Insights on Tafel constant in the analysis of hydrogen evolution reaction, *J. Phy. Chem. C*, 122 (2018) 23943 – 23949.
35. T. Shinagawa, A.T. Garcia-Esparza, K. Takanabe, Insight on Tafel slopes from a microkinetic analysis of aqueous electrocatalysis for energy conversion, *Sci. Rep.* 5 (2015) 13801.
36. R. Zhang, X. Wang, S. Yu, T. Wen, X. Zhu, F. Yang, X. Sun, X. Wang, W. Hu, Ternary NiCo₂P_x nanowires as pH-universal electrocatalysts for highly efficient hydrogen evolution reaction, *Adv. Mater.* 29 (2017) 1605502.
37. M.I. Abdullah, A. Hameed, N. Zhang, M. Ma, Nickel nanocrystal assemblies as efficient electrocatalysts for hydrogen evolution from pH-neutral aqueous solution, *ChemElectroChem* 6 (2019) 2100-2106.
38. K. Xu, X. Fu, H. Li, Z. Peng, A novel composite of network-like tungsten phosphide nanostructures grown on carbon fibers with enhanced electrocatalytic hydrogen evolution efficiency, *Appl. Surf. Sci.* 456 (2018) 230 – 237.

39. M. Pi, T. Wu, W. Guo, X. Wang, D. Zhang, S. Wang, S. Chen, Phase-controlled synthesis of polymorphic tungsten diphosphide with hybridization of monoclinic and orthorhombic phases as a novel electrocatalyst for efficient hydrogen evolution, *J. Power Sources* 349 (2017) 138 – 143.
40. Z. Pu, X. Ya, I.S. Amiin, Z. Tu, X. Liu, W. Li, S. Mu, Ultrasmall tungsten phosphide nanoparticles embedded in nitrogen-doped carbon as a highly active and stable hydrogen-evolution electrocatalyst, *J. Mater. Chem. A* 4 (2016) 15327 – 15332.
41. X. Zhang, T. Guo, T. Liu, K. Lv, Z. Wu, D. Wang, Tungsten phosphide (WP) nanoparticles with tunable crystallinity, W vacancies, and electronic structures for hydrogen production, *Electrochim. Acta* 323 (2019) 134798.
42. D. Wang, K. Lv, Z. Wu, facile synthesis of tungsten phosphide/Ketjen black hybrid electrocatalyst for hydrogen production, *Mater. Res. Express* 5 (2018) 065509.
43. M. Pi, X. Wang, D. Zhang, S. Wang, S. Chen, a 3D porous WP₂ nanosheets@carbon cloth flexible electrode for efficient electrocatalytic hydrogen evolution, *Front. Chem. Sci. Eng.* 12 (2018) 425 – 432.
44. H. Du, S. Gu, R. Liu, C.M. Li, Tungsten diphosphide nanorods as an efficient catalyst for electrochemical hydrogen evolution, *J. Power Sources*, 278 (2015) 540 – 545.
45. Z. Pu, X. Ya, I.S. Amiin, Z. Tu, X. Liu, W. Li, S. Mu, Ultrasmall tungsten phosphide nanoparticles embedded in nitrogen-doped carbon as a highly active and stable hydrogen-evolution electrocatalyst, *J. Mater. Chem. A* 4 (2016) 15327 – 15332.
46. J.M. McEnaney, J.C. Crompton, J.F. Callejas, E.J. Popczun, C.G. Read, N.S. Lewis, R.E. Schaak, Electrocatalytic hydrogen evolution using amorphous tungsten phosphide nanoparticles, *Chem. Commun.* 50 (2014) 11026 – 11028.
47. R. Zhou, J. Zhang, Z. Chen, X. Han, C. Zhong, W. Hu, Y. Deng, Phase and composition controllable synthesis of nickel phosphide-based nanoparticles via a low-temperature process for efficient electrocatalytic hydrogen evolution, *Electrochim. Acta* 258 (2017) 866-875.
48. G. Cho, H. Kim, Y.S. Park, Y. Hong, Phase transformation of iron phosphide nanoparticles for hydrogen evolution reaction electrocatalysis, *Intern. J. Hydrog. Energy* 43 (2018) 11326-11334.
49. C.Y. Son, I.H. Kwak, Y.R. Lim, J. Park, FeP and FeP₂ nanowires for efficient electrocatalytic hydrogen evolution reaction, *Chem. Commun.* 52 (2016) 2819-2822.

50. A.K. Ipadeola, K.I. Ozoemena, Alkaline water-splitting reactions over Pd/Co-MOF-derived carbon obtained via microwave-assisted synthesis, *RSC Adv.* 10 (2020) 17359-17368
51. S. Feng, X. Cheng 1, X. Cheng, J. Yue and J. Li, Theoretical study on electronic, optical properties and hardness of technetium phosphides under high pressure, *Crystals* 7 (2017) 176.
52. M. Pi, T. Wu, D. Zhang, S. Chen, S. Wang, Self-supported three-dimensional mesoporous semimetallic WP_2 , nanowire arrays on carbon cloth as a flexible cathode for efficient hydrogen evolution, *Nanoscale* 8 (2016) 19779-19786.
53. N. Dubouis, A. Grimaud, The hydrogen evolution reaction: from material to interfacial descriptors, *Chem. Sci* 10 (2019) 9165-9181.
54. Y. Zheng , Y. Jiao , A. Vasileff and S.Z. Qiao , The hydrogen evolution reaction in alkaline solution: from theory, single crystal models, to practical electrocatalysts, *Angew. Chem. Int. Ed.* 57 (2018) 7568-7579.
55. Z.W. She, J. Kibsgaard, C.F. Dickens, I. Chorkendorff, J. Norskov, T.F. Jaramillo Combining theory and experiment in electrocatalysis: Insights into materials design, *Science* 355 (2017) eaad4998.
56. C. Tsai, K. Chan, J.K. Nørskov, F. Abild-Pedersen, Rational design of MoS_2 catalysts: tuning the structure and activity via transition metal doping, *Catal. Sci. Technol.* 5 (2015) 246-253.
57. Y. Zheng, Y. Jiao, M. Jaroniec, S.Z. Qiao, Advancing the electrochemistry of the hydrogen-evolution reaction through combining experiment and theory, *Angew. Chemie Int. Ed.* 54 (2015) 52-65.
58. Q. Xu, G.Li, Y. Zhang, Q. Yang, Y. Sun, C. Felser, Descriptor for hydrogen evolution catalysts based on the bulk band structure effect, *ACS Catal.* 10 (2020) 5042-5048.
59. Y. Pan, K. Sun, Y. Lin, X. Cao, Y. Cheng, S. Liu, L. Zeng, W. Cheong, D. Zhao, K. Wu, Z. Liu, Y. Liu, D. Wang, Q. Peng, C. Chen, Y. Li, Electronic structure and d-band center control engineering over M-doped CoP (M = Ni, Mn, Fe) hollow polyhedron frames for boosting hydrogen production, *Nano Energy* 56 (2019) 411-419.

6. Supporting Information

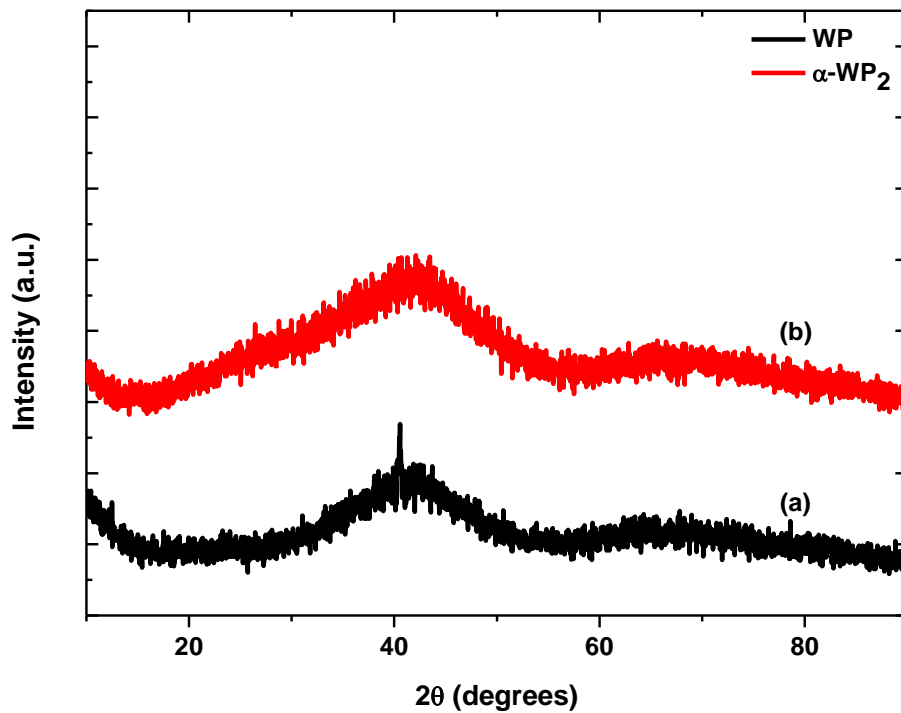


Fig. S1: X-ray diffraction pattern of as synthesized (a) WP and (b) α -WP₂.

Calculations of the interplanar spacing from the XRD results:

WP (011)

$$2\theta = 31.115$$

$$\theta = 15.5575, \lambda = 0.15460 \text{ nm}$$

$$\lambda = 2d\sin\theta$$

$$d = 0.15406 \text{ nm} / 2\sin\theta = 0.2871 \text{ nm}$$

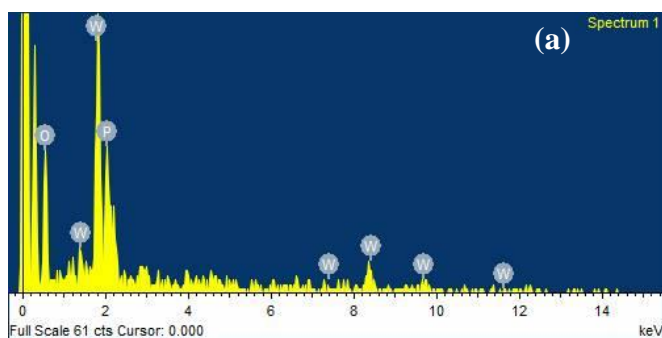
A-WP₂ (-201)

$$2\theta = 20.971$$

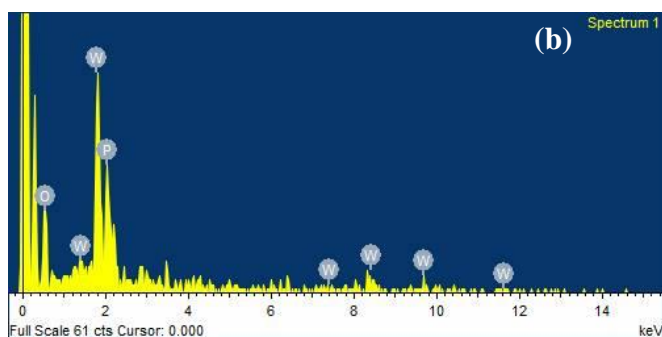
$$\theta = 10.4855, \lambda = 0.15460 \text{ nm}$$

$$\lambda = 2d\sin\theta$$

$$d = 0.15406 \text{ nm} / 2\sin\theta = 0.4231 \text{ nm}$$



Element	Atomic %
O	76.82
P	12.39
W	10.79



Element	Atomic %
O	70.86
P	17.36
W	11.78

Fig. S2: EDX spectra and corresponding atomic % of (a) WP and (b) α -WP₂.

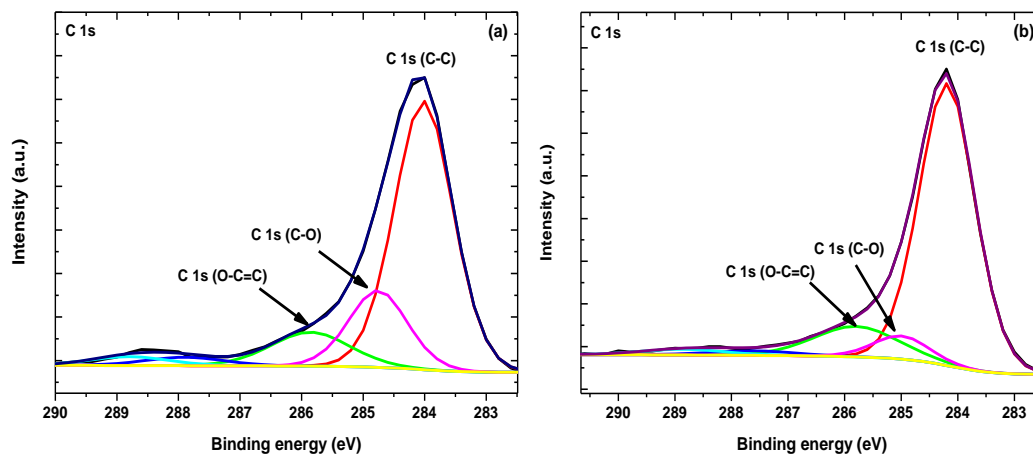


Fig. S3: The C 1s spectrum of (a) WP and (b) α -WP₂.

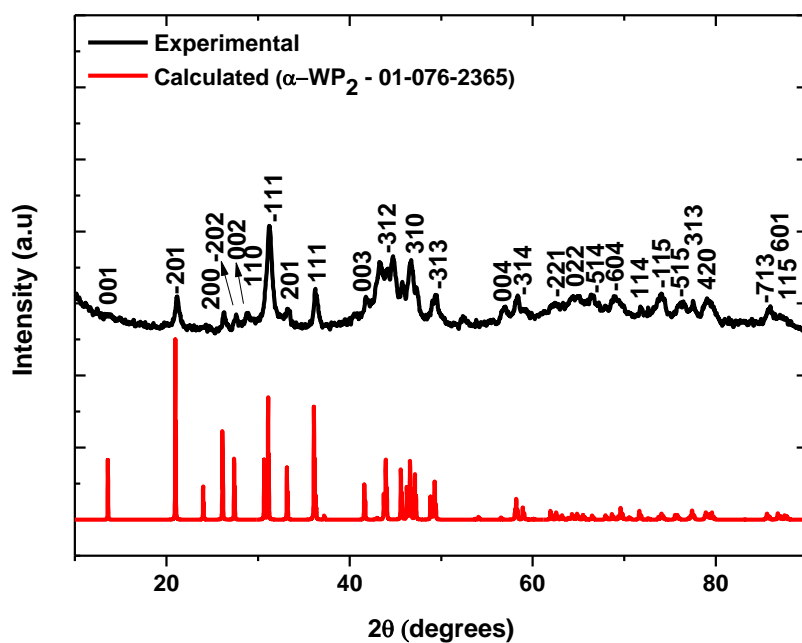


Fig. S4: XRD pattern of long term stored α -WP₂.

Table S1: Comparison of the electrocatalytic activity of WP and α -WP₂ catalysts.

Catalyst	Tafel Slope (mV.dec ⁻¹)	Overpotential (10 mA.cm ⁻²)	Exchange current density (mA.cm ⁻²)	Onset potential (mV)
WP	95.71	-314	0.004239	-145
α -WP ₂	86.83	-271	0.004536	-106

Table S2: Kinetic parameters of WP and α -WP₂ catalysts.

Catalyst	T(K)	β (mV.dec ⁻¹)	J_0 (mA.cm ⁻²)	E_a (kJ.mol ⁻¹)
WP	298	95.71	0.004239	44.24
	308	92.58	0.006973	
	318	87.34	0.001136	
	328	84.59	0.01316	
α -WP ₂	298	86.83	0.004536	31.79
	308	84.86	0.009468	
	318	82.72	0.01023	
	328	80.25	0.02410	

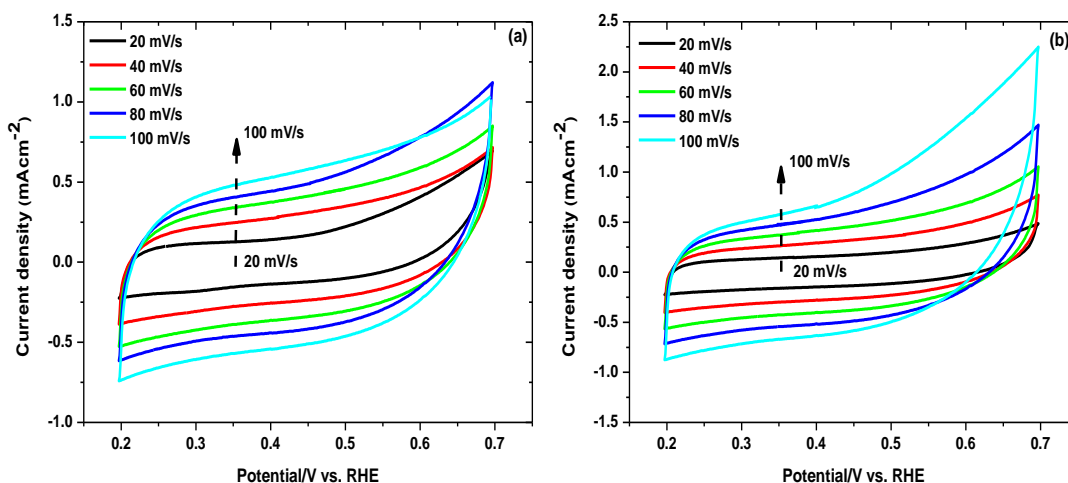


Fig. S5: Cyclic Voltammetry (CV) curves of (a) WP and (b) α -WP₂ catalysts measured in a potential window without faradaic processes in 0.5 M H₂SO₄ at scan rate from 20 - 100 mV.s⁻¹.

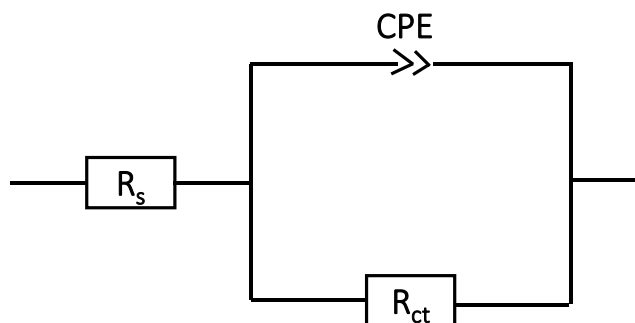


Fig. S6: Equivalent circuit for one time constant, where R_s - solution resistant; CPE - constant phase element; R_{ct} - charge transfer resistance.

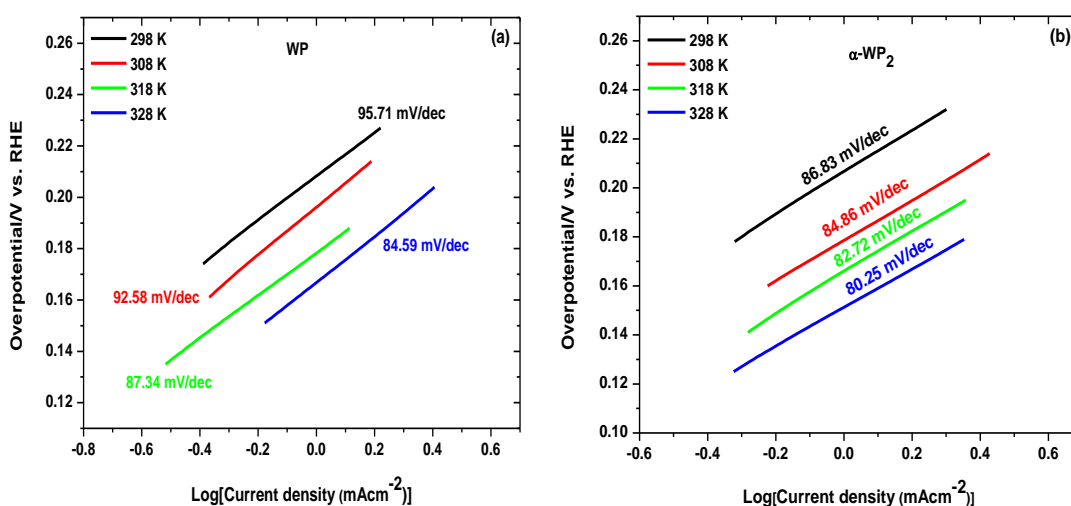


Fig. S7: Tafel slopes of (a) WP and (b) α -WP₂ catalysts obtained at different temperatures.

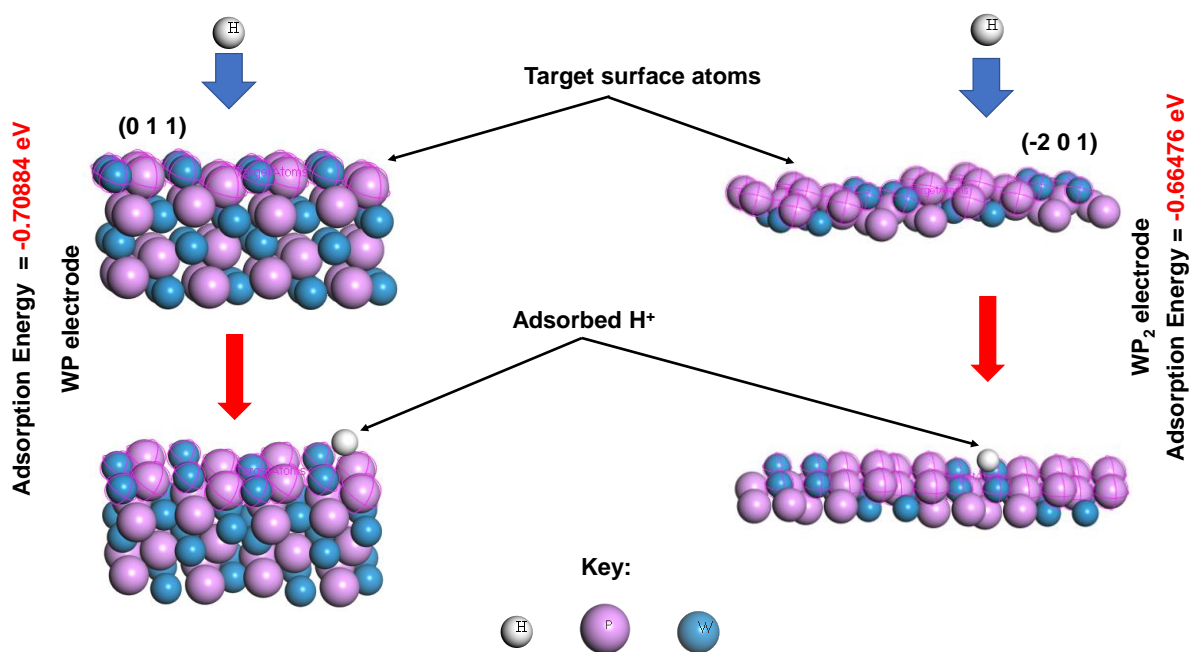


Fig. S8: Calculated hydrogen adsorption energies on (011) and (-201) surfaces for WP and α -WP₂, respectively.

Chapter 5

The synergistic effect of W dopant on colloiddally synthesized molybdenum phosphide electrocatalyst in hydrogen evolution reaction

1. Introduction

In the quest for new energy sources, eco-friendly energy reservoirs that infrequently infringe environmental protection laws have been of great interest. The search for sustainable energy sources emerged in response to the decline in the discovery of non-renewable energy sources in the 21st century.¹ Hydrogen as an energy carrier has captivated a lot of attention from researchers as a suitable alternative owing to its zero emission of greenhouse gases and a high energy density.²⁻³ Currently, large scale production of hydrogen is successfully achieved through a steam reforming process in which natural gas (e.g. methane) is heated in high temperature steam (450-1000 °C) to produce hydrogen. The downfall with steam reforming is its contribution to global greenhouse emissions through the generation of carbon monoxide and carbon dioxide, as well as high temperature and pressure required for operation.⁴⁻⁵ Alternative to steam reforming, electrocatalytic hydrogen evolution reaction (HER) is amongst the promising processes that have the potential to produce hydrogen without burdening the environment.⁶⁻⁸ However, on the account of the high overpotential required to drive the cathodic hydrogen evolution reaction in overall water splitting, an efficient electrocatalyst is required to lower the electrolytic potential.⁹

The most efficient HER electrocatalysts reported to date are Pt-based materials.¹⁰⁻¹² However, large scale application of noble-metal catalysts has been hindered by their scarcity and high market value. Recently, metal-doped transition metal based electrocatalysts (phosphides¹³, carbides¹⁴, nitrides¹⁵ and chalcogenides¹⁶) have shown great promise as suitable alternatives to noble-metal catalysts. Among these materials, doped transition metal phosphides exhibit high catalytic activity for HER. The introduction of dopant atoms on the crystal lattice of the bulk structure has been put forward as an effective way to improve catalytic activity. Doping results in the modification of the Gibbs free energy (ΔG_{H}^0) of hydrogen adsorption, thus enhancing electrochemical kinetics.¹⁷ The dopant may be the foundation for defects in the lattice which

redirects electrons to the P atom for improved activity.¹⁸ Moreover, doping affects the proportion of exposed active sites and allows for tunability of intrinsic electronic properties (i.e. synergistic effect), this result in high activity in hybrids over their single component counterpart.¹⁹

For example, Wang et. al. synthesized undoped WP, Mo-doped WP and Co-doped WP to conduct an experimental and theoretical comparative study of the electrocatalytic activity over a wide pH range. The introduction of the dopants yielded high surface area porous nanostructures. DFT studies revealed that the enhanced electrocatalytic performance was due to the optimization of the water dissociation step and hydrogen generation step upon introduction of dopant atoms.²⁰ Man et. al. systematically substituted Fe, Co, Mn and Mo in a NiP parent lattice while preserving the morphology and metallic structure. They found that the substitution of Ni by atoms with a smaller number of d-electrons enhanced the activity of undoped NiP due to optimal electron filling of the metallic bands of NiCoP.²¹ Z. Jin et. al. employed a seed-mediated co-deposition method to synthesize amorphous tungsten-doped nickel phosphide microspheres for HER. The W-doped Ni_xP displayed superior HER activity requiring an overpotential of -110 mV to generate current density of 20 mA.cm⁻² and a small Tafel slope of 39 mV.dec⁻¹. The enhanced catalytic activity was attributed to the contributions from the amorphous architecture and doping of tungsten.²² Wang et. al. prepared porous MoWP hybrid nanosheets on carbon cloth via in situ phosphidation. The hybrid nanosheets displayed superior activity producing current densities of 100 mA.cm⁻² at low overpotential of -138 mV, with a tafel slope of 52 mV.dec⁻¹.²³ Captivated by the upper mentioned findings, we propose that by combining the positive attributes emanating from doping and the use of amorphous nanoparticles, the catalytic activity of MoP can be significantly improved. Herein, we report on the colloidal synthesis of amorphous molybdenum phosphide (A-MoP) and amorphous tungsten-doped molybdenum phosphide (A-WMoP) nanoparticles and their use as electrocatalysts in HER. Furthermore, we delineate the catalytic activity differences observed between the amorphous and crystalline phases.

2. Experimental

2.1. Chemicals and Materials

Molybdenum pentachloride [99.9%, WCl₆, Sigma-Aldrich], tungsten hexachloride [99.9%, WCl₆, Sigma-Aldrich], trioctylphosphine [90%, TOP, Sigma-Aldrich], 1-octadecene [90%, 1-ODE, Sigma-Aldrich], sulfuric acid [H₂SO₄, Associated Chemical Associate], hexane [92.5%,

Sigma-Aldrich], Nafion [5 wt%, Sigma-Aldrich] commercial Pt/C (Tanaka Kikinzoku Kogyo K.K., 20 wt%) and carbon black-vulcan (XC 72R). Deionized water used to prepare the 0.5 M H₂SO₄ solution was purified using a Millipore system. All chemicals were used as received without further purification.

2.2. Synthesis of pure A-MoP and W-doped MoP (A-WMoP)

Molybdenum pentachloride (0.5 mmol), trioctylphosphine (11 mmol), and 1-octadecene (7.8 mmol) were mixed in a 100 mL three-neck round bottom flask equipped with a thermometer, condenser, oil bubbler, heating mantle, and magnetic stirrer. The nanocrystals were then isolated through centrifugation (7000 rpm, 10 min), washed multiple times with hexane and dried overnight at room temperature. To remove moisture and achieve inert conditions, the mixture was heated to 140 °C while purging N₂ for 15 min. The temperature was then increased to 340 °C and maintained for 6 h. After 6 h, the heating mantle was removed, and the reaction mixture was saturated with hexane to allow for rapid cooling and precipitation of the nanoparticles. Annealing (800 °C under N₂ for 2 h) was subsequently used to convert the as-synthesized amorphous powders to crystalline MoP (C-MoP). The synthesis of A-WMoP was done by adding tungsten pentachloride (10 mol% W) to the forementioned reaction. The resultant amorphous powders were also annealed at 800 °C under N₂ for 2 h to form crystalline C-WMoP catalyst. The 4 samples studied were labelled as A-MoP, C-MoP, A-WMoP and C-WMoP, where A and C stand for amorphous and crystalline, respectively.

2.3. Electrochemical Measurements and Preparation of Working Electrode

The electrochemical measurements were conducted using an Epsilon E₂ potentiostat. The activity of the catalysts was tested in 0.5 M H₂SO₄ using a 3-electrode configuration employing linear sweep voltammetry (LSV) at a scan rate of 2 mV.s⁻¹. All measurements were done using an Ag/AgCl/3M KCl reference electrode and a Pt wire as the counter electrode. The working electrode was a MoP or WMoP decorated glassy carbon (diameter = 3 mm, SA = 0.07065 cm²). The stability studies of the catalysts were conducted using a sweep scan rate of 50 mV.s⁻¹ for 1000 cycles using cyclic voltammetry. All potentials were presented with respect to the reversible hydrogen electrode (RHE). Measurements were performed under ambient conditions. The current density was normalized to the geometrical area of the working electrode and iR compensation was applied for all electrochemical measurements using the in-built iR compensation function in the potentiostat. The working electrode was prepared using

previously reported methods with some modifications.²⁴ The catalyst ink was prepared by dispersing 5 mg of MoP or WMoP and 0.5 mg (10 %) of carbon black (Vulcan) in a mixture of water (495 μL), ethanol (495 μL) and 10 μL of 5 % Nafion solution. The resultant catalyst ink was sonicated for 30 min at room temperature to achieve homogeneity, then 5 μL aliquot was pipetted onto the glassy carbon electrode and allowed to dry at RT before use. The amount loaded on the glassy carbon was kept constant at catalyst loading of 0.35 $\text{mg}\cdot\text{cm}^{-2}$ for all samples. The Ag/AgCl/3M KCl reference electrode was calculated with respect to the reference hydrogen electrode (RHE) by adding a value of (0.197 + 0.059 pH). The potentials reported in this study are all against RHE. The Tafel slopes were extrapolated using the Tafel equation, $\eta = a + b \log j$, where η is the overpotential, a means content, b is the Tafel slope and j is the current density. Electrochemical impedance spectroscopy (EIS) measurements were conducted at -0.25 V (vs Ag/AgCl) using 5 mV amplitude AC signal at a frequency range of 10^5 -0.1 Hz. To confirm the resistance of the electrodes, the corresponding semicircles was fitted to a specific equivalent circuit using the EC-Lab software. The Electrochemical Impedance Spectroscopy measurements were conducted using a 3 electrode configuration using the SP-300 Potentiostat-Bio-Logic instrument.

2.4. Materials Characterization

Powder X-ray diffraction (PXRD) analysis was conducted using a Bruker D2 phaser (D2-205530) diffractometer with Cu Ka1 radiation ($\lambda = 1.54060 \text{ \AA}$) at 30 kV and 10 mA. Measurements were taken over 2θ angle range of 5 – 90° in steps of 0.0261° with a step time of 5 s at ambient temperature. X-ray photoelectron spectroscopy (XPS) analysis was conducted using a Physical Electronics PHI 5700 spectrometer. Non-monochromatic MgKa X-rays (300 W, 15 kV, and 1253.6 eV) were used as the excitation source. The spectrometer energy scale was calibrated using Cu $2p_{3/2}$, Ag $3d_{5/2}$, and Au $4f_{7/2}$ photoelectron lines at 932.7, 368.3, and 84.0 eV, respectively. Samples were mounted on a sample holder without adhesive tape and kept overnight under high vacuum in the preparation chamber before being transferred to the analysis chamber for testing. The spectra were collected in the constant pass energy mode at 29.35 eV. The residual pressure in the analysis chamber was maintained below 1.33×10^{-7} Pa during the spectra acquisition with a multichannel hemi-spherical electron analyser. Transmission electron microscopy (TEM) images were collected using a FEI Technai T12 TEM operated at an accelerating voltage of 120 kV with a beam spot size of 2 in the TEM mode. TEM samples were prepared by dispersing the nanoparticles in hexane, sonicated for 30

min, after which they were deposited on a copper grid and allowed to dry at room temperature before analysis.

3. Results and discussion

3.1. Compositional, morphological and structural characterization

The aim of the investigation was to determine the effect of combining the positive catalytic features exhibited by amorphous catalysts with those that are obtained by doping a foreign element into the host catalyst. In this study, amorphous and crystalline phases of pure molybdenum phosphide and tungsten-doped molybdenum phosphide were prepared as described in the synthesis section. The catalysts investigated were amorphous MoP (A-MoP), crystalline MoP (C-MoP), amorphous tungsten-doped molybdenum phosphide (A-WMoP) and crystalline tungsten-doped molybdenum phosphide (C-WMoP). X-ray diffraction analysis was used to investigate the structural characteristics of the synthesized catalysts. Fig. 1(a) shows the XRD patterns of A-MoP and A-WMoP which exhibit a single broad peak centered at 2θ value of 42° . The absence of sharp diffraction peaks in the patterns of A-MoP and A-WMoP indicated that they were amorphous. To obtain the correspond crystalline phases, the pristine products were annealed at 800°C for 2 h. The resultant XRD patterns (Fig 1(b)) of C-MoP and C-WMoP displayed clear sharp peaks, indicating the successful formation of crystalline phases. The XRD patterns of C-MoP and C-WMoP could both be matched with those delineated as the hexagonal phase of molybdenum phosphide (PDF 00-024-0771) and lattice constant $a = 3.2220 \text{ \AA}$, $b = 3.2220 \text{ \AA}$ and $c = 3.1910 \text{ \AA}$. Subsequent to the incorporation of W into MoP (C-WMoP), a slight shift in peak position (Fig 1(c)) to low 2θ values is observed, showing crystal lattice expansion due to substitution of the smaller Mo atoms (1.90 \AA) by the slightly larger W atoms (1.93 \AA). The absence of new peaks or phases in the XRD pattern of C-MoWP suggest successful substitution of the Mo ions with the W ions.

To further substantiate the compositional properties and surface electronic information of the catalysts, X-ray photoelectron spectroscopy (XPS) analysis of the Mo-doped MoP catalysts was performed. Fig. 1(d) shows the survey spectra of the A-WMoP and C-WMoP catalysts while Fig. 2 shows the corresponding high-resolution spectra of Mo 3d, W 4f and P 2p elements for both catalysts. The survey spectra of A-WMoP and C-WMoP manifest clearly signals of the elements O, Mo, W, C and P, with no signals attributed to any impurities. The high resolution spectra of Mo 3d (Fig. 2(a)) for A-WMoP displays 5 peaks at binding energies (BEs) of 227.59 eV (Mo^0), 228.49 eV (Mo^{3+}), 230.79 eV (Mo^{+6}), 232.56 eV (Mo^{+4}) and 235.67 eV

(Mo⁺⁶). The doublet at low BEs (227.59 and 228.49 eV) can be attributed to the presence of Mo-species in the Mo-P bond.²⁵⁻²⁶ The additional 3 peaks at high BEs (230.79, 232.56 and 235.67 eV) represents the presence of MoO₂ and MoO₃ species, emanating from surface oxidation.²⁵⁻²⁶ The doublet in the corresponding P 2p spectra (Fig. 2(b)) located at BEs of 129.07 eV (P 2p_{3/2}) and 130.16 eV (P 2p_{1/2}) correspond to P in the Mo-P bond.²⁶⁻²⁷ The high intensity peak in the P 2p spectra located at BEs of 133.33 eV corresponded to the P-O bond.²⁷ The W 4f spectra (Fig. 2(c)) displays peaks at BEs of 35.95 and 38.09 eV that can be ascribed to W 4f_{7/2} and W 4f_{5/2}, respectively.²⁸

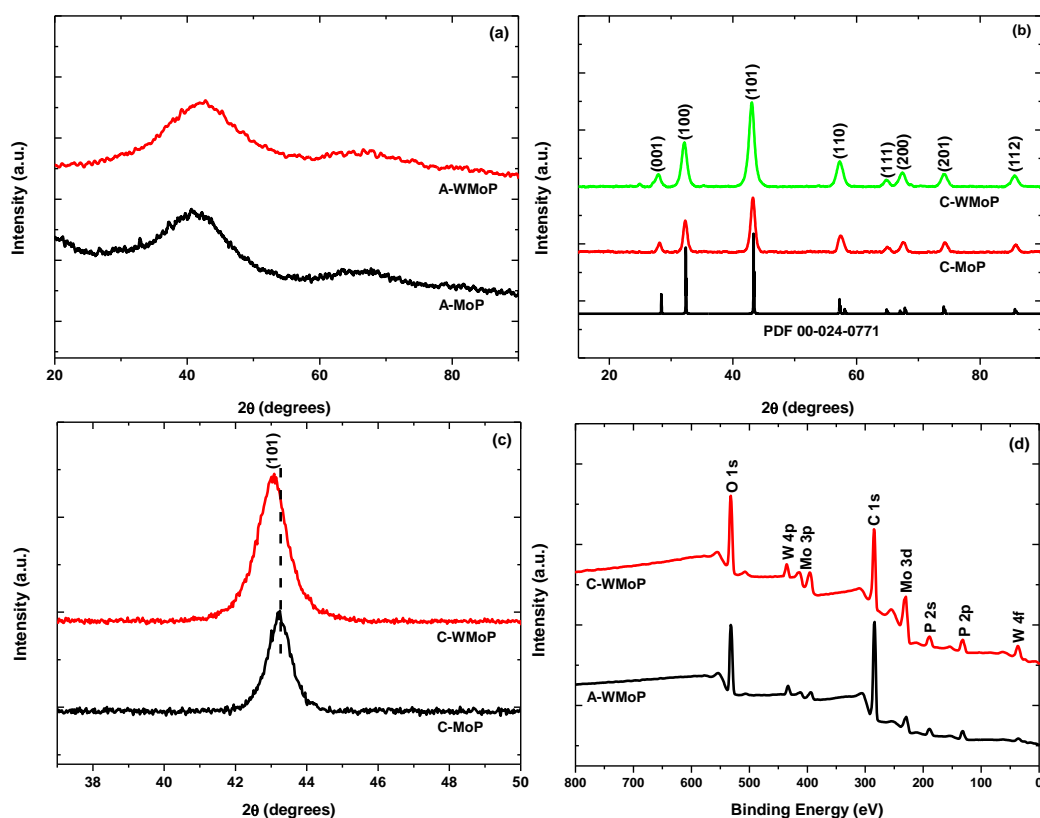


Fig. 1: XRD patterns of (a) A-MoP and A-WMoP, (b) C-MoP and C-WMoP catalysts; (c) observed XRD peak shift to low 2θ upon doping of MoP with W; (d) XPS survey spectra of A-WMoP and C-WMoP.

For C-WMoP, The high resolution spectra of Mo 3d (Fig. 2(d)) also displays 5 peaks at binding energies (BEs) of 228.31 eV (Mo⁰), 229.12 eV (Mo³⁺), 231.61 eV (Mo⁺⁶), 232.51 eV (Mo⁺⁴) and 235.77 eV (Mo⁺⁶). The doublet at low BEs (228.31 and 229.12 eV) can be attributed to the presence of Mo-species in the Mo-P bond. The additional 3 peaks at high BEs (231.61, 232.51 and 235.77 eV) represents the presence of MoO₂ and MoO₃ species, emanating from surface oxidation. The doublet in the corresponding P 2p spectra (Fig. 2(e)) located at BEs of 129.58 eV (P 2p_{3/2}) and 130.41 eV (P 2p_{1/2}) correspond to P in the Mo-P bond. The broad peak in the

P 2p spectra located at BEs of 133.77 eV corresponded to the P-O bond. The W 4f spectra (Fig. 2(f)) displays peaks at BEs of 36.27 and 38.11 eV that can be ascribed to W 4f_{7/2} and W 4f_{5/2}, respectively. The XPS results confirm the presence of W in MoP and confirmed the composition of the amorphous phase.

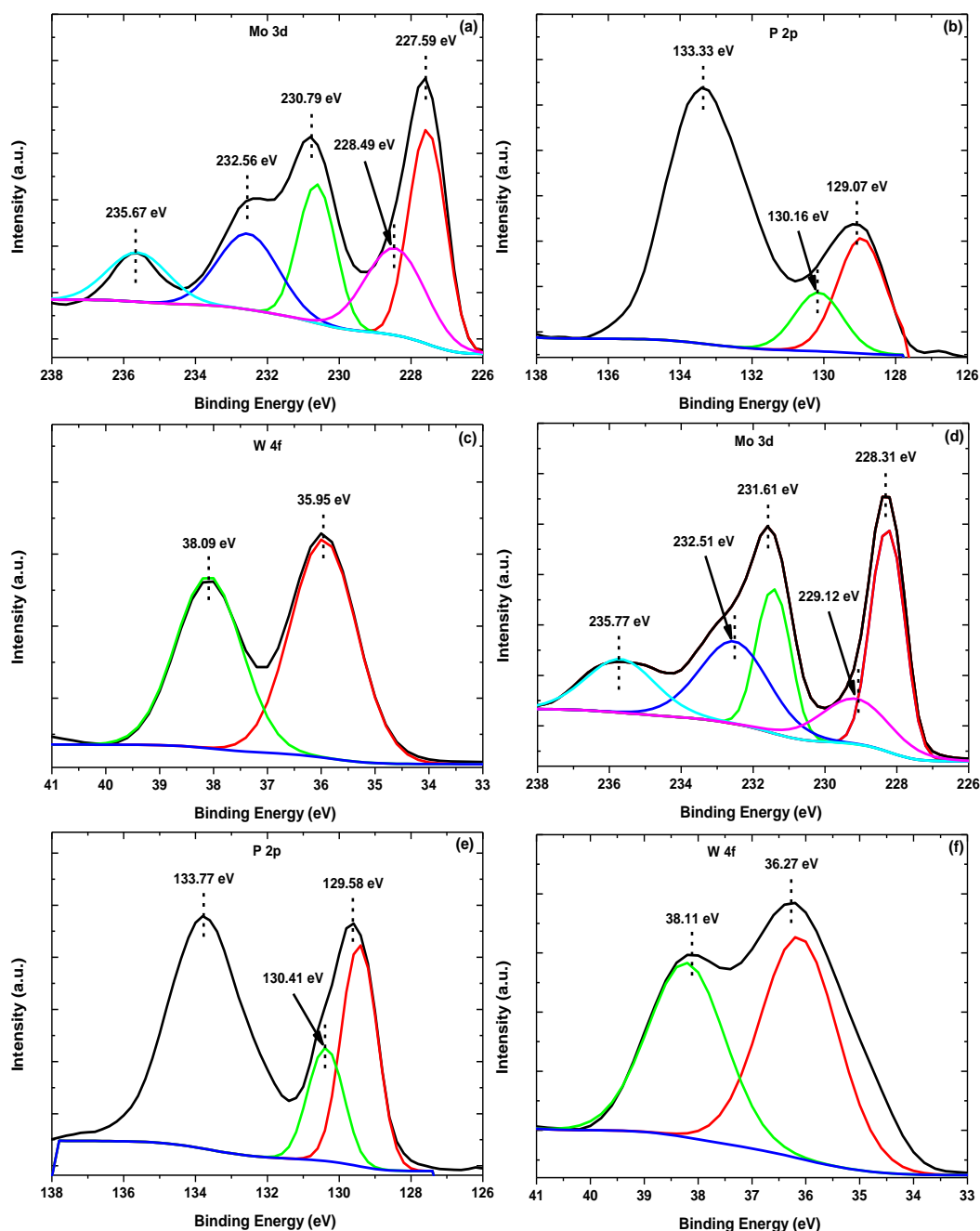


Fig. 2: High resolution Mo 3d, P 2p and W 4f spectra of (a-c) A-WMoP and (d-f) C-WMoP catalysts.

Fig. 3 shows the TEM images of the amorphous and crystalline MoP and WMoP catalysts.

The corresponding histograms were obtained by measuring the size of 100 randomly selected nanoparticles. The A-MoP and A-WMoP took on an ultrasmall, quasi-spherical morphology with an average nanoparticle size of 2.17 and 6.03 nm, respectively. The spherical morphology was also observed in the crystalline C-MoP and C-WMoP catalyst, however, an increase in nanoparticle size to 11.71 and 12.11 nm was observed, respectively. These results reveal that the introduction of W atoms into the crystal structure of both the amorphous and crystalline MoP nanoparticles had minimal influence on the morphology. It can also be seen that even after heat treatment at 800 °C, nanoparticles with a narrow size distribution were still observed. Notably in C-WMoP, there are a few bigger nanoparticles with a maximum particle size of 25 nm. The larger crystalline nanoparticles formed as a result of the adjacent amorphous nanoparticles merging at elevated temperature.

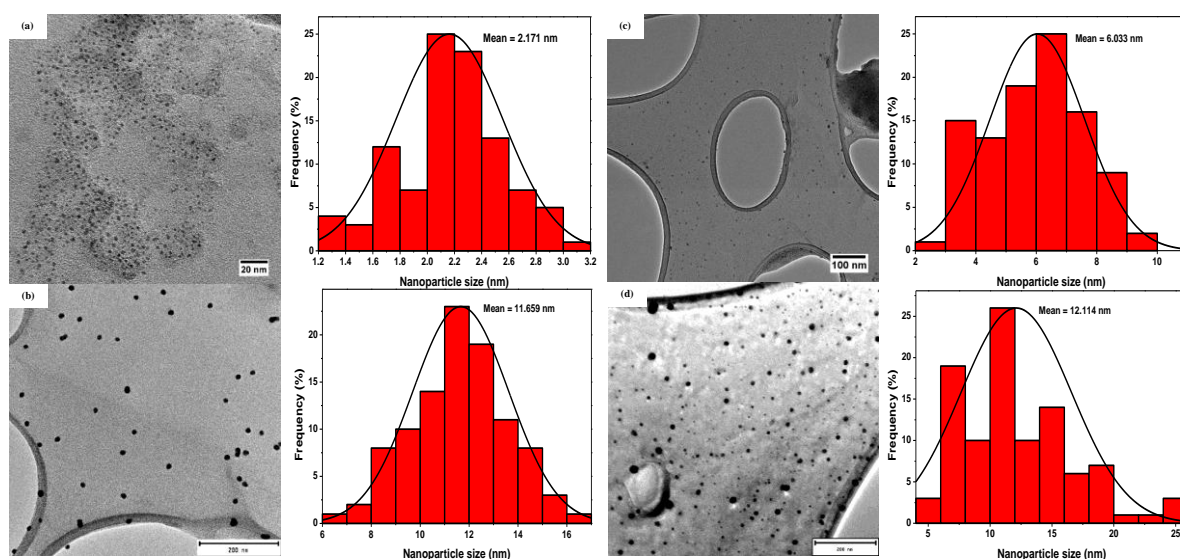


Fig. 3: TEM images of (a) A-MoP, (b) C-MoP, (c) A-WMoP and (d) C-WMoP catalysts and their corresponding nanoparticle size distribution histograms.

3.2. Hydrogen Evolution Reaction (HER)

To evaluate the HER activities of the various catalysts, LSV measurements were conducted using a conventional 3-electrode configuration system in a 0.5 M H₂SO₄ solution at a scan rate of 2 mV.s⁻¹ as shown in Fig. 4(a). The experimentally determined performance parameters are summarized in Table 1. For comparison, the activity of Pt/C, glassy carbon electrode (GCE) and vulcan were also measured. The polarization curves of bare GCE and vulcan are shown in to manifest their negligible HER activity in the investigated potential range. As a benchmark, the HER activity of the commercial Pt/C electrocatalyst displayed excellent electrochemical performance requiring only -35 mV to reach current densities of 10 mA.cm⁻². The A-MoP, C-

MoP, C-WMoP catalysts generated current density of $10 \text{ mA}\cdot\text{cm}^{-2}$ at overpotential of -235, -317, and -160 mV, respectively. Whereas A-WMoP displayed the best HER activity delivering current density of $10 \text{ mA}\cdot\text{cm}^{-2}$ at overpotential of only -145 mV. From the experimentally determined overpotentials, it can be noted that compared to the pure MoP catalysts, the W-doped MoP phases exhibited enhanced catalytic activity and the amorphous phases displayed higher performance than their crystalline counterpart. Notably, the use of W-dopant in conjunction with amorphous phases dramatically improved the catalytic activity. In transition metal phosphides, the phosphorus atoms play an important role in the generation of hydrogen during HER. A closer look at the XPS results (Fig 4 (d)) reveal that compared to the P 2P spectrum of the crystalline WMoP, the P 2P spectrum of the amorphous WMoP is negatively shifted, demonstrating electronic structure modification due to the variance in crystallinity. We therefore stipulate that the enhanced activity observed in A-WMoP was due to the contributions from unsymmetrical bonding and synergistic effect between the W and Mo elements which optimize the electronic properties of the active sites.²⁹⁻³⁰

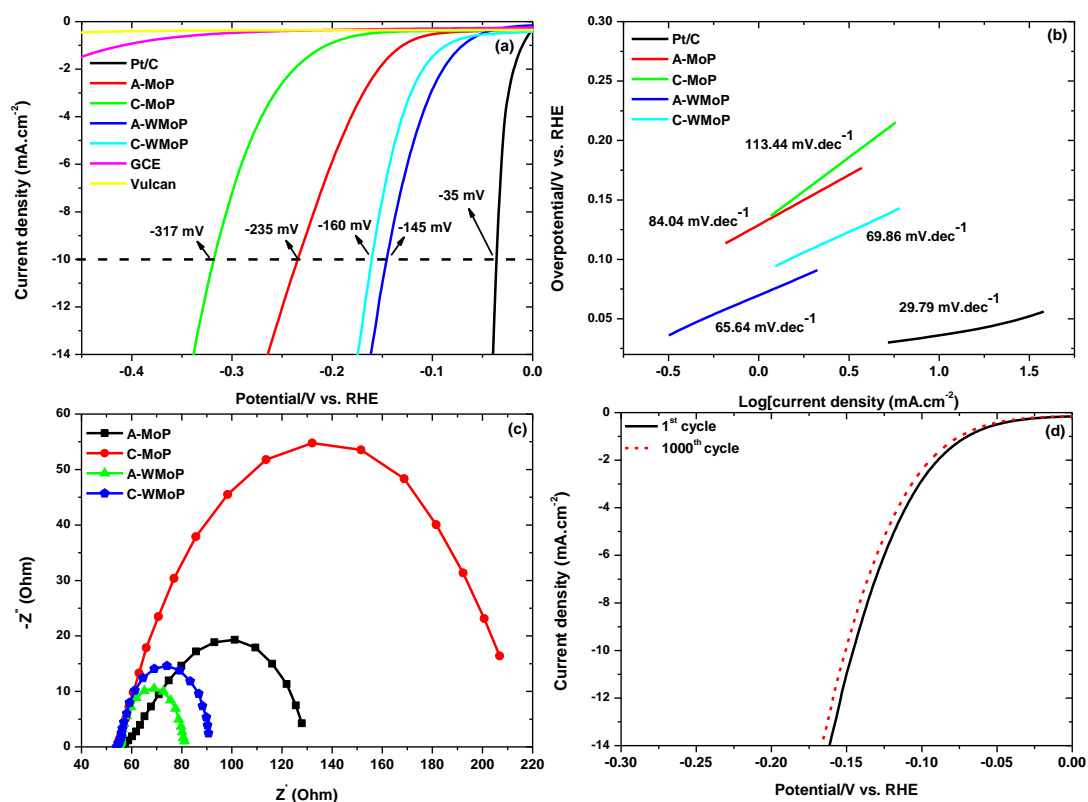


Fig. 4: (a) LSV polarization curves of A-MoP, C-MoP, A-WMoP and C-WMoP catalysts; (b) the corresponding Tafel plots of the catalysts in (a); (c) Nyquist plots of A-MoP, C-MoP, A-WMoP and C-WMoP; (d) LSV curves of A-WMoP before and after 1000 potential cycles.

Table 1: Performance parameters of the catalysts reported in this study.

Catalyst	Tafel Slope (mV.dec ⁻¹)	Overpotential (10 mA.cm ⁻²)	Onset potential (at 1 mA.cm ⁻²)	ECSA (mF.cm ⁻²)	Charge transfer resistance (Ω)
A-MoP	133.4	-317	-207.7	716.25	93
C-MoP	84.04	-235	-131.9	98.00	171
A-WMoP	69.86	-160	-88.31	1180.75	26
C-MoP	65.64	-145	-69.90	818.75	37

Wang et al. reported density functional theory (DFT) calculations which revealed that the introduction of dopant atoms into the parent lattice optimized the hydrogen adsorption free energy, and thus improved the HER process.³¹ Amorphous materials contain a high density of unsaturated sites due to unstructured bonding. These non-symmetrical bonds tend to be characterized by high surface energy, dangling bonds, surface defects and coordinative unsaturated metal sites where rapid hydrogen generation may take place.³²⁻³⁶ To determine the HER kinetics and get a better insight into the intrinsic properties of the catalysts, Tafel slopes were extrapolated from the linear region of the Tafel plot (η vs. $\log(j)$). The Tafel slope for A-WMoP was determined to be 65.85 mV.dec⁻¹, much smaller than that of A-MoP (84.04 mV.dec⁻¹), C-MoP (113.04 mV.dec⁻¹) and C-WMoP (69.86 mV.dec⁻¹), demonstrating that A-WMoP has outstanding HER kinetics (Fig 4b). The slopes of all the catalysts reported in this study fall in the range between 39-118 mV.dec⁻¹, implying that they all follow the Volmer-Heyrovsky mechanism.³⁷ The superior catalytic activity achieved by A-WMoP was comparable and even superior to other doped transition metal phosphide electrocatalysts recently reported in literature (Table 2).

Table 2: Comparison of metal doped transition-metal phosphide electrocatalysts for HER in 0.5 M H₂SO₄.

Catalyst	η_{10} (j, mA.cm⁻²)	Tafel Slope (mV.dec⁻¹)	Reference
NiCoP/CC	-118	114.4	38
5% Ni-WP ₂ NS/CC	-124	71	39
Ni-FeP	-169	86.9	40
CoP-MnP	-193.1	88.2	41
CoP-FeP	-130.9	45.1	41
Mo-WP	-139	65	42
NiCoP	-	80	43
0.1Mn-MoP	-242	60	44
Ni ₂ P/NiCoP@NHCCs	-168	90	45
C-WMoP	-160	69.86	This work
A-WMoP	-145	65.64	This work

To shed light into the observed differences in catalytic activity, electrochemical impedance spectroscopy (EIS) measurements were conducted to understand the electrical conductivity capability of the catalysts. Fig. 4(c) shows that the Nyquist plot of A-WMoP has the smallest semicircle amongst the catalysts. The small semicircle of A-WMoP (27 Ω) demonstrates that it has a small charge transfer resistance (R_{ct}) compared to A-MoP (94 Ω), C-MoP (171 Ω) and C-WMoP (38 Ω). A small R_{ct} is an indication of high electron transfer and ion exchange rate at the solution-electrocatalyst interface which result in high efficiency as demonstrated in the LSV curves (Fig.4a). It is evident that utilizing amorphous architecture and addition of W into MoP reduces the R_{ct} , which promote efficient HER activity. The electrochemically active surface area (ECSA) is another important property that is used to access the catalytic activity of a catalyst and is estimated from the double layer capacitance (C_{dl} , details on calculation of C_{dl} provided in the additional supporting information) calculated from CV scans recorded at various scan rates (20-100 mV s^{-1}) in the double layer region (Fig. 5(a-d)). As shown in Fig. 5(e), the C_{dl} of A-WMoP (47.23 mF.cm^{-2}) was larger compared to those of A-MoP (28.65 mF.cm^{-2}), C-MoP (3.92 mF.cm^{-2}) and C-WMoP (32.75 mF.cm^{-2}). The high ECSA of A-WMoP (1180.75 cm^2) over the A-MoP (716.25 cm^2), C-MoP (98.00 cm^2) and C-WMoP (818.75 cm^2) implied a high proportion of exposed electrochemical active sites which facilitated the observed high HER efficiency. This confirmed that the amorphous Mo-doped catalyst is composed of more catalytically active sites. These results fully demonstrate that amorphous architecture and electronic engineering resulting from presence of W-dopant dramatically enhance HER activity of MoP. Considering potential practical application, the stability of the best performing A-WMoP catalyst was tested by running 1000 continuous cycles using cyclic voltammetry (CV). From Fig. 5(f), it can be seen that the initial and final polarization curves nearly overlap. The negligible difference shows the excellent electrochemical stability of the A-WMoP catalyst.

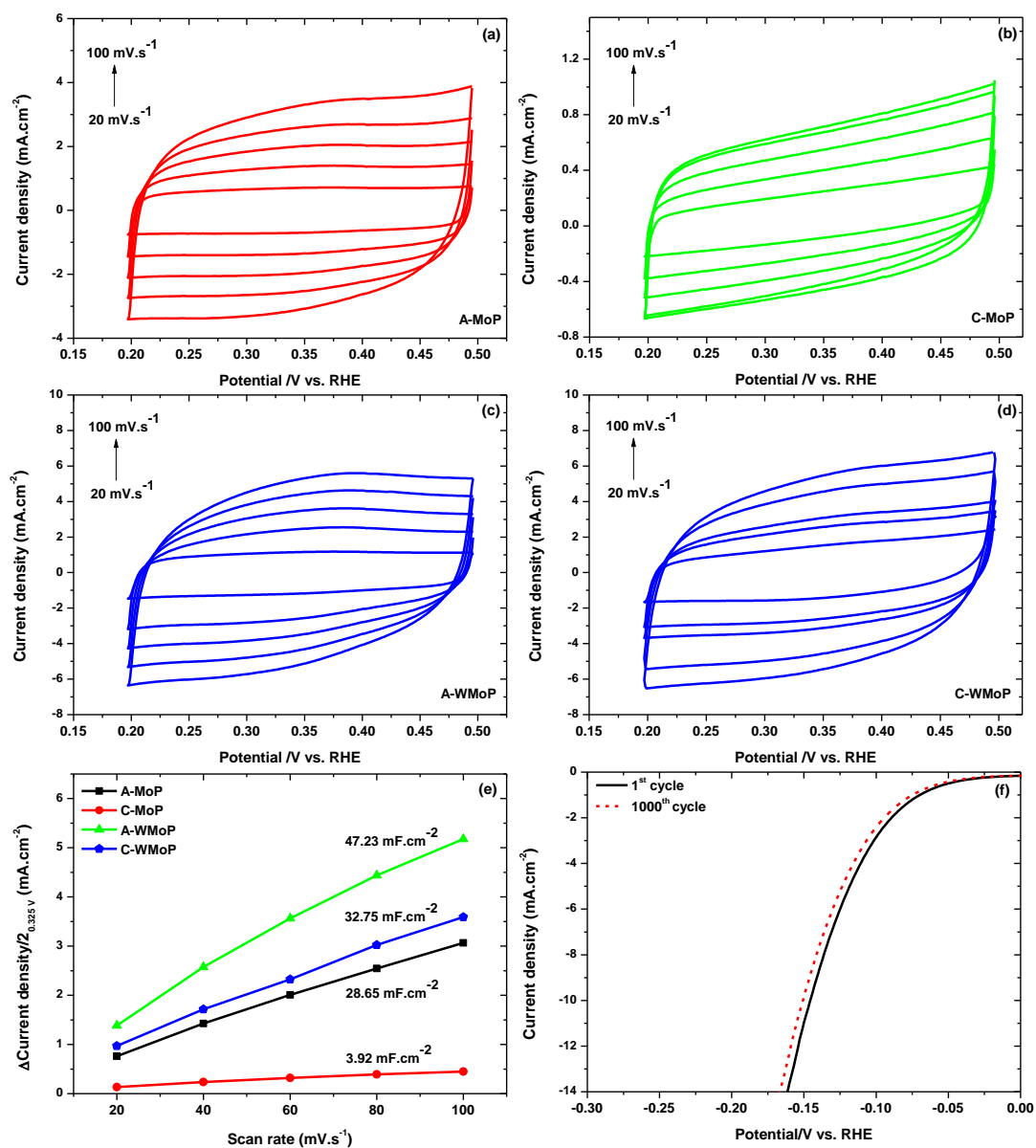


Fig. 5: Cyclic Voltammety curves of (a) A-MoP, (b) C-MoP, (c) A-WMoP and (d) C-WMoP recorded at different scan rates (20-100 mV s^{-1}) in 0.5 M H_2SO_4 ; (e) Plot of capacitive current vs. scan rate for all the catalysts under study; (f) The polarization curves of the 1st and 1000th cycles of durability study.

4. Conclusion

In summary, we have successfully prepared amorphous molybdenum phosphide (A-MoP) and tungsten doped molybdenum phosphide (A-WMoP) electrocatalysts using a one-pot colloidal synthesis method. The corresponding crystalline phases (C-MoP and C-WMoP) were ascertained through subsequent high temperature treatment. Experimental results from the

HER process reveal that amorphous catalysts were more active than their crystalline equivalent. Moreover, the rational of doping W into the amorphous phase of MoP significantly increase the catalytic performance, with only -145 mV required to generate 10 mA.cm⁻², and a Tafel slope of 65.64 mV.dec⁻¹. The high catalytic efficiency of the A-WMoP was attributed to increase density of active sites, electronic property modulation due to the synergistic effect between W and Mo atoms, reduced electrical conductivity of the catalyst and high surface energy emerging from the non-symmetrical bonding that dominate in amorphous catalysts. This work provides a new route of incorporating the sort after inherent properties of amorphous structures with those emanating from doping in order to produce highly active non-noble metal electrocatalysts.

5. References

1. M.S. Faber, S. Jin, Earth-abundant inorganic electrocatalysts and their nanostructures for energy conversion applications, *Energy Environ. Sci.* 7 (2014) 3519-3542.
2. S.K. Shiva, V. Himabindu, Hydrogen production by PEM water electrolysis – A review, *Mater. Sci. Energy Technol.* 2 (2019) 442-454.
3. M. Gong, D.Y. Wang, C.C. Chen, B.J. Hwang, H. Dai, A mini review on nickel-based electrocatalysts for alkaline hydrogen evolution reaction, *Nano Res.* 9 (2015) 28-46.
4. X. Zou, Y. Zhang, Noble metal-free hydrogen evolution catalysts for water splitting. *Chemical Society Reviews* 44 (2015) 5148-5180.
5. M.D. Falco, G. Santoro, M. Capocolli, G. Caputo, A. Giaconia, Hydrogen production by solar steam methane reforming with molten salts as energy carriers: Experimental and modelling analysis, *Int. J. Hydrog. Energy* 46 (2021) 10682-10696.
6. C. Li, J. Baek, Recent advances in noble metal (Pt, Ru, and Ir)-based electrocatalyst for efficient hydrogen evolution reaction, *ACS Omega* 5 (2020) 31-40.
7. R.V Digraskar, V.S. Sapner, S.M. Mali, S.S. Narwade, A.V. Ghule, B.R. Sathe, CZTS decorated on graphene oxide as an efficient electrocatalyst for high-performance hydrogen evolution reaction, *ACS Omega* 4 (2019) 7650-7657.
8. T.F. Jeramillo, K.P. Jorgensen, J. Bonde, J.H. Nielsen, S. Horch, B. Chorkendorff, Identification of active edge sites for electrochemical H₂ evolution from MoS₂ nanocatalysts, *Science* 317 (2007) 100-102.
9. X.X. Zou, Y. Zhang, Noble metal-free hydrogen evolution catalysts for water splitting, *Chem. Soc. Rev.* 44 (2015) 5148-5180.

10. M. Li, K. Duanmu, C. Wan, T. Cheng, L. Zhang, S. Dai, W. Chen, Z. Zhao, P. Li, H. Fei, Y. Zhu, R. Yu, J. Luo, K. Zang, Z. Lin, M. Ding, J. Huang, H. Sun, J. Guo, X. Pan, W.A. Goddard III, P. Sautet, Y. Huang, X. Duan, Single-atom tailoring of platinum nanocatalysts for high-performance multifunctional electrocatalysis, *Nat. Catal.* 2 (2019) 495 – 503.
11. B. Ruqia, S. Choi, Pt and Pt-Ni(OH)₂ electrodes for the hydrogen evolution reaction in alkaline electrolytes and their nanoscaled electrocatalysts, *ChemSusChem* 11 (2018) 2643-2653
12. D.M.F. Santos, C.A.C. Sequeira, D. Maccio, A. Saccone, J.L. Figueredo, Platinum-rare earth electrodes for hydrogen evolution in alkaline water electrolysis, *Int. J. Hydrog. Energy* 38 (2013) 3137-3145
13. C. Zhang, Y. Xie, H. Deng, C. Zhang, J. Su, Y. Dong, J. Lin, Ternary nickel iron phosphide supported on nickel foam as a high-efficiency electrocatalyst for overall water splitting, , *Int. J. Hydrog. Energy* 43 (2018) 7299-7306.
14. C. Wan, B.M. Leonard, Iron-doped molybdenum carbide catalyst with high activity and stability for the hydrogen evolution reaction, *Chem. Mater.* 27 (2015) 4281-4288.
15. Q. Liang, G. Brocks, X. Zhang, A. Bieberle-Hutter, Monolayer nitrides doped with transition metal as efficient catalysts for water oxidation: The singular role of nickel, *J. Phys. Chem. C* 123 (2019) 26289-26298.
16. J. Yin, J. Jin, H. Lin, Z. Yin, J. Li, M. Lu, L. Guo, P. Xi, Y. Tang, C. Yan, Optimized metal chalcogenides for boosting water splitting, *Adv. Sci.* 7 (2020) 1903070.
17. Y. Gao, H. Li, J. Wang, J. Ma, H. Ren, New insight on hydrogen evolution reaction activity of MoP₂ from theoretical perspective, *Nanomaterials* 9 (2019) 1270.
18. X. gao, G. Zhou, H. Wang, J. Yin, L. Zhang, F. Xiao, K. Siddharth, S. Zhu, M. Shao, Defect engineering of molybdenum-based materials for electrocatalysis, *Catalysts* 10 (2020) 1301.
19. Y. Men, P. Li, J. Zhou, S. Chen, W. Luo, Trends in alkaline hydrogen evolution activity on cobalt phosphide electrocatalysts doped with transition metals, *Cell Rep.* 1 (2020) 100136.
20. J. Wang, K. Chang, Z. Sun, J.H. Lee, B.M. Tackett, C. Zhang, J.G. Chen, C. Liu, A combined experimental and theoretical study of the accelerated hydrogen evolution kinetics over wide pH range on porous transition metal doped tungsten phosphide electrocatalysts, *Appl. Catal. B* 251 (2019) 162-167.
21. H. Man, C. Tsang, M.M. Li, J. Mo, B. Huang, L.Y.S. Lee, Y. Leung, K. Wong, S.C.E. Tsang, Transition metal-doped nickel phosphide nanoparticles as electro- and photocatalysts for hydrogen generation reactions, *Appl. Catal. B* 242 (2019) 186-193.

22. Z. Jin, P. Li, X. Huang, G. Zeng, Y. Jin, B. Zheng, D. Xiao, Three-dimensional amorphous tungsten-doped nickel phosphide microsphere as an efficient electrocatalyst for hydrogen evolution, *J. Mater. Chem. A* 2 (2014) 18593-18599.
23. X. Wang, Y. Xu, H. Rao, W. Xu, H. Chen, W. Zhang, D. Kuang, Novel porous molybdenum tungsten phosphide hybrid nanosheets on carbon cloth for efficient hydrogen evolution, *Energy Environ Sci.* 9 (2016) 1468-1475.
24. Z. Xing, Q. Liu, A.M. Asiri and X. Sun, High-efficient electrochemical hydrogen evolution catalyzed by tungsten phosphide submicroparticles, *ACS Catal.* 5 (2015) 145-149.
25. M. Hou, X. Teng, J. Wang, Y. Liu, L. Guo, L. Ji, C. Cheng, Z. Chen, Multiscale porous molybdenum phosphide of honeycomb structure for highly efficient hydrogen evolution, *Nanoscale* 10 (2018) 14594-14599.
26. P. Xiao, M.A. Sk, L. Thia, X. Ge, R.J. Lim, J.-Y. Wang, K.H. Lim and X. Wang, Molybdenum phosphide as an efficient electrocatalyst for the hydrogen evolution reaction, *Energy Environ. Sci.*, 2014, 7, 2624-2629.
27. Z. Zhang, X. Yu, L. Zhang, F. Zhou, Y. Liang, R. Wang, Molybdenum phosphide/carbon hybrids as pH-universal electrocatalysts for hydrogen evolution reaction, *Adv. Funct. Mater.* 28 (2018) 1726523.
28. Z. Pu, X. Ya, I.S. Amiinu, Z. Tu, X. Liu, W. Li, S. Mu, Ultrasmall tungsten phosphide nanoparticles embedded in nitrogen-doped carbon as a highly active and stable hydrogen-evolution electrocatalyst, *J. Mater. Chem. A* 4 (2016) 15327-15332.
29. H. Zheng, X. Huang, H. Gao, G. Lu, A. Li, W. Dong, Cobalt-tuned nickel phosphide nanoparticles for highly efficient electrocatalysts, *Appl. Surf. Sci.* 479 (2019) 1254-1261.
30. S. Ye, J. Feng, G. Li, Pd nanoparticle/CoP nanosheet hybrids: Highly electroactive and durable catalyst for ethanol oxidation, *ACS Catal.* 6 (2016) 7962-7969.
31. J. Wang, K. Chang, Z. Sun, J.H. Lee, B.M. Tackett, C. Zhang, J.G. Chen, C. Liu, A combined experimental and theoretical study of the accelerated hydrogen evolution kinetics over wide pH range on porous transition metal doped tungsten phosphide electrocatalysts, *Appl. Catal. B.* 251 (2010) 162-167.
32. S.S. Nkabinde, Z.B. Ndala, N.P. Shumbula, T. Kolokoto, O. Nchoe, G.N. Ngubeni, K.P. Mubiayi, N. Moloto, Delineating the role of crystallinity in the electrocatalytic activity of colloiddally synthesized MoP nanocrystals, *New J. Chem.* 44 (2020) 14041-14049.
33. D. Merki, H. Vrubel, L. Rovelli, S. Fierro, X. Hu, Fe, Co, and Ni ions promote the catalytic activity of amorphous molybdenum sulfide films for hydrogen evolution, *Chem. Sci.* 3 (2012) 2515-2525.

34. Z. Jin, P. Li, X. Huang, G. Zeng, Y. Jin, B. Zheng, D. Xiao, Three-dimensional amorphous tungsten-doped nickel phosphide microsphere as an efficient electrocatalyst for hydrogen evolution, *J. Mater. Chem.* 2 (2014) 18593-18599.
35. R. Beltran-Suito, P.W. Menezes, M. Driess, Amorphous outperforms crystalline nanomaterials: surface modifications of molecularly derived CoP electro(pre) catalysts for efficient water-splitting, *J. Mater. Chem. A* 7 (2019) 15749-15756.
36. R.D.L. Smith, M.S. Prevot, R.D. Fagan, Z. Zhang, P.A. Sedach, M.K.J. Siu, S. Trudel and C.P. Berlinguette, Photochemical route for accessing amorphous metal oxide materials for water oxidation catalysis, *Science* 340 (2013) 60-63.
37. M.I. Abdullah, A. Hameed, N. Zhang, M. Ma, Nickel nanocrystal assemblies as efficient electrocatalysts for hydrogen evolution from pH-neutral aqueous solution, *ChemElectroChem* 6 (2019) 2100-2106.
38. S. Ma, L. Wang, S. Zhang, H. Jin, M. Wan, Y. Pan, T. Zhang, Y. Wen, M. Zhang, H. Zhu, M. Du, Facile fabrication of a binary NiCo phosphide with hierarchical architecture for efficient hydrogen evolution reactions, *Int. J. Hydro. Energy* 44 (2019) 4188-4196.
39. W. Liu, P. Geng, S. Li, W. Liu, D. Fan, H. Lu, Z. Lu, Y. Liu, Tuning electronic configuration of WP2 nanosheet arrays via nickel doping for high-efficiency hydrogen evolution reaction, *J. Energy Chem.* 55 (2020) 17-24.
40. G. Cho, Y. park, H. Kang, Y. Hong, T. Lee, D. Ha, Transition metal-doped FeP nanoparticles for hydrogen evolution reaction catalysis, *Appl. Surf. Sci.* 510 (2020) 145427.
41. Y. Du, Z. Wang, H. Li, Y. Han, Y. Liu, Y. Yang, Y. Liu, L. Wang, Controllable synthesized CoP-MP (M=Fe, Mn) as efficient and stable electrocatalyst for hydrogen evolution reaction at all pH values, *Int. J. Hydro. Energy* 44 (2019) 19978-19985.
42. J. Wang, K. Chang, Z. Sun, J.H. Lee, B.M. Tackett, C. Zhang, J.G. Chen, C. Liu, A combined experimental and theoretical study of the accelerated hydrogen evolution kinetics over wide pH range on porous transition metal doped tungsten phosphide electrocatalysts, *Appl. Catal. B* 251 (2019) 162-167.
43. L. Zhang, Y. Qi, L. Sun, G. Chen, L. Wang, M. Zhang, D. Zeng, Y. Chen, X. Wang, K. Xu, F. Ma, Facile route of nitrogen doping in nickel cobalt phosphide for highly efficient hydrogen evolution in both acid and alkaline electrolytes, *Appl. Surf. Sci.* 512 (2020) 145715.
44. Z. Mu, T. Guo, H. Fei, Y. Mao, Z. Wu, D. Wang, Mn-doped porous interconnected MoP nanosheets for enhanced hydrogen evolution, *Appl. Surf. Sci.* (2021) 149321

45. L. Han, T. Yu, W. Lei, W. Liu, K. Feng, Y. Ding, G. Jiang, P. Xu, Z. Chen, Nitrogen doped carbon nanocones encapsulating with nickel-cobalt mixed phosphides for enhanced hydrogen evolution reaction, *J. Mater. Chem. A* 5 (2017) 16568-16572.

6. Supporting Information

Calculating the electrochemical active surface area.

From the linear plots of capacitive current against the scan rate (20-100 mV.s⁻¹), the specific capacitance was determined to be 28650, 3920, 47230 and 32750 $\mu\text{F}\cdot\text{cm}^{-2}$ for $\alpha\text{-WP}_2$, Mo(2.5%)/ $\alpha\text{-WP}_2$, Mo(5%)/ $\alpha\text{-WP}_2$ and Mo(10%)/ $\alpha\text{-WP}_2$, respectively. The specific capacitance was then converted into ECSA using the value for a flat standard with an actual SA of 1 cm^2 . Generally, C_s for a flat surface is in the range of 20-60 $\mu\text{F}\cdot\text{cm}^{-2}$. Hence a median value of 40 $\mu\text{F}\cdot\text{cm}^{-2}$ for C_s was assumed for the calculation of ECSA.¹⁻²

$$ECSA = \frac{C_{dl}}{C_s}$$

Where C_{dl} is the double layer capacitance and C_s is the specific capacitance.

A-MoP:

$$ECSA = \frac{28650 \mu F}{40 \mu F \text{ cm}^{-2} \text{ per } \text{cm}^2_{ECSA}} = 716.25 \frac{\text{cm}^2}{ECSA}$$

C-MoP:

$$ECSA = \frac{3920 \mu F}{40 \mu F \text{ cm}^{-2} \text{ per } \text{cm}^2_{ECSA}} = 98 \frac{\text{cm}^2}{ECSA}$$

A-WMoP:

$$ECSA = \frac{47230 \mu F}{40 \mu F \text{ cm}^{-2} \text{ per } \text{cm}^2_{ECSA}} = 1180.75 \frac{\text{cm}^2}{ECSA}$$

C-WMoP:

$$ECSA = \frac{32750 \mu F}{40 \mu F \text{ cm}^{-2} \text{ per } \text{cm}^2_{ECSA}} = 818.75 \frac{\text{cm}^2}{ECSA}$$

References

1. C.C.L. McCrory, S. Jung, J.C. Peters, T.F. Jaramillo, Benchmarking heterogeneous electrocatalysts for the oxygen evolution reaction, *J. Am. Chem. Soc.* 135 (2015) 16977-16987.
2. P. Connor, J. Schuch, B. Kaiser, W. Jaegermann, The determination of electrochemical active surface area and specific capacity revisited for the system MnO_x as an oxygen evolution catalyst, *Z. Phys. Chem.* 234 (2020) 979-994

Chapter 6

Fine-tuning the electronic properties of α -WP₂ electrocatalyst via Mo-doping for efficient hydrogen evolution in acidic media

1. Introduction

The production of hydrogen gas via electrochemical water splitting has become an important technology in the search for environmentally friendly energy sources.¹⁻² Hydrogen is a preferred alternative to traditional fuels due to its high energy density, abundance, and non-toxicity.³ Precious metals such as platinum (Pt) and ruthenium (Ru) have proven to be highly efficient electrocatalysts in the generation of hydrogen gas, requiring nearly zero overpotential in an acidic medium.⁴⁻⁵ Nonetheless, there is an urgent need to develop non-noble metal electrocatalysts that are not only efficient and stable, but also cheap and bountiful in nature. Transition metal nitrides⁶, selenides⁷, sulfides⁸, carbides⁹ and phosphides¹⁰ have been identified as promising alternatives capable of reducing the cost of hydrogen evolution reactions (HER) drastically. Amongst the aforementioned compounds, transition metal phosphides, specifically WP₂, has received an ever-growing interest as one of the promising electrocatalyst in HER.¹¹⁻¹² However, there is still a need to find strategies directed at improving its catalytic activity to ensure that it becomes comparable to that of precious metals. The intrinsic properties of an electrocatalyst control its catalytic activity. One common method used to alter the intrinsic properties is by introducing a metal dopant into the crystal structure of the host catalyst. The foreign atoms tend to modulate the electronic properties of the catalyst resulting to improved activity as a result of optimized hydrogen adsorption free energy and reduced charge transfer resistance.¹³⁻¹⁵ For instance, Lu et. al. fabricated W-NiCoP/NF, NiCoP/NF, W-NiP/NF and NiP/NF electrocatalysts for hydrogen evolution in a basic medium. The results revealed that NiP/NF displayed the lowest catalytic activity requiring an overpotential of -354.1 mV to produce current density of 100 mA.cm⁻². Whereas the W-NiCoP/NF, NiCoP/NF and W-NiP/NF electrocatalysts exhibited improved activity, delivering a current density of 100 mA.cm⁻² with overpotentials of -141.2, -207 and -320.2 mV, respectively. The superior catalytic activity observed in W-NiCoP/NF was attributed to the synergistic effect between the metals and optimization of the electronic structure of the active

sites.¹⁶ Wang et al. conducted an experimental and theoretical study on Mo and Co doped porous tungsten phosphide (i.e. Mo-WP and Co-WP) electrocatalysts in hydrogen evolution. Experimentally, the formation of porous nanostructures with an increased number of active sites and low charge transfer resistance were observed due to the incorporation of the metal dopants. Computation studies performed using density functional theory (DFT) demonstrated that the presence of dopants optimized the hydrogen adsorption free energy resulting in improved catalytic performance.¹⁷

Anjum et al. employed the thiourea-phosphate-assisted strategy to synthesize sulfur and nitrogen dual-doped molybdenum phosphide supported on graphene (MoP/SNG) for hydrogen evolution in acidic and basic media. XPS data confirmed that the highly electronegative N, S and C atoms stabilized the P^{3-} through P-N, P-S and P-C by removing the electron density from P and donating it back to the empty d-orbitals of Mo. The presence of dopant atoms in conjunction with a conducting support resulted in an electrocatalyst with a high number of active sites and high conductivity with catalytic activity which outperforms most MoP-based electrocatalyst reported in literature.¹⁸ Inspired by this positive strategy, we propose that the introduction of dopant atoms into α -WP₂ could alter its electronic properties and result to enhanced catalytic activity. To the best of our knowledge, the synthesis of Mo-doped α -WP₂ using colloidal synthesis in conjunction with high temperature treatment has never been reported. Herein, we demonstrate the systematic introduction of various mol% of Mo-dopant to α -WP₂ using colloidal synthesis and its application as an electrocatalyst for hydrogen evolution reaction. Furthermore, the effect of annealing temperature on the structural and electrocatalytic properties of the best performing Mo(10%)/ α -WP₂ was also reported. The introduction of Mo into the crystal structure of α -WP₂ plays an important role in modifying the intrinsic properties of the electrocatalyst, thus improving the HER catalytic activity.

2. Experimental

2.1. Chemicals and materials

Tungsten hexachloride [99.9%, WCl₆, Sigma-Aldrich], molybdenum pentachloride [99.9%, WCl₆, Sigma-Aldrich] trioctylphosphine [90%, TOP, Sigma-Aldrich], 1-octadecene [90%, 1-ODE, Sigma-Aldrich], sulfuric acid [H₂SO₄, Associated Chemical Associate], hexane [92.5%, Sigma-Aldrich], Nafion [5 wt%, Sigma-Aldrich] commercial Pt/C (Tanaka Kikinzoku Kogyo K.K., 20 wt%) and carbon black-vulcan (XC 72R). Deionized water used to prepare the 0.5 M

H₂SO₄ solution was purified using a Millipore system. All chemicals were used as received without further purification.

2.2. Synthesis of pristine α -WP₂ and Mo-doped α -WP₂ (Mo/ α -WP₂)

Typically, trioctylphosphine (11.21 mmol), tungsten hexachloride (0.5546 mmol), and 1-octadecene (15.62 mmol) were mixed in a 100 mL three-neck round bottom flask equipped with a thermometer, condenser, oil bubbler, heating mantle, and magnetic stirrer. To ensure inert conditions and remove moisture, the mixture was heated to 140 °C while purging N₂ for 15 minutes. The temperature was then increased to 340 °C and maintained for 6 h. After 6 h, the heating mantle was removed, and the reaction mixture was saturated with hexane to allow for rapid cooling and precipitation of the nanoparticles. The nanoparticles were then isolated through centrifugation (7000 rpm, 10 min), washed multiple times with hexane and dried overnight at room temperature. The resultant amorphous nanoparticles were exposed to high temperature (800 °C in N₂ for 1 h) in order to form crystalline phases identified as tungsten diphosphide (α -WP₂). To synthesize Mo-doped tungsten diphosphide (Mo/ α -WP₂), molybdenum pentachloride was added to the aforementioned reaction using mol% Mo of 2.5, 5 and 10%. Similarly to the α -WP₂ sample, 800 °C in N₂ for 1 h was used to aid crystallization. To understand the effect of annealing on the Mo(10%)/ α -WP₂ nanoparticles, temperatures of 600, 800 and 950 °C were studied. The doped nanoparticles were denoted as Mo(2.5%)/ α -WP₂, Mo(5%)/ α -WP₂ and Mo(10%)/ α -WP₂.

2.3. Electrochemical measurements and preparation of working electrode

The electrochemical measurements were conducted using an Epsilon E₂ potentiostat. The activity of the catalysts was tested in 0.5 M H₂SO₄ using a 3-electrode configuration employing linear sweep voltammetry (LSV) at a scan rate of 2 mV.s⁻¹. All measurements were done using an Ag/AgCl/3M KCl reference electrode and a Pt wire as the counter electrode. The working electrode was a α -WP₂ or Mo/ α -WP₂ decorated glassy carbon (diameter = 3 mm, SA = 0.07065 cm²). The stability studies of the catalysts were conducted using a sweep scan rate of 50 mV.s⁻¹ for 1000 cycles using cyclic voltammetry. All potentials were recorded with respect to the reversible hydrogen electrode (RHE). Measurements were performed under ambient conditions. The current density was normalized to the geometrical surface area of the working electrode for all electrochemical measurements. The working electrode was prepared using previously reported methods with some modifications.¹⁹ The catalyst ink was prepared by dispersing 5 mg

of α -WP₂ or Mo/ α -WP₂ and 0.5 mg (10 %) of carbon black (Vulcan) in a mixture of water (495 μ L), ethanol (495 μ L) and 10 μ L of 5 % Nafion solution. The resultant catalyst ink was sonicated for 30 min at room temperature to achieve homogeneity, then 5 μ L aliquot was pipetted onto the glassy carbon electrode and allowed to dry at RT before use. The amount loaded on the glassy carbon was kept constant at catalyst loading of 0.35 mg.cm⁻² for all samples. The Ag/AgCl/3M KCl reference electrode was calibrated with respect to the reference hydrogen electrode (RHE) by adding a value of (0.197 + 0.059 pH). The potentials reported in this study are all against RHE. The Tafel slopes were extrapolated using the Tafel equation, $\eta = a + b \log j$, where η is the overpotential, a means content, b is the Tafel slope and j is the current density. Electrochemical impedance spectroscopy (EIS) measurements were conducted at -0.25 V (vs Ag/AgCl) using 5 mV amplitude AC signal at a frequency range of 10⁵-0.1 Hz. To confirm the resistance of the electrodes, the corresponding semicircles was fitted to a specific equivalent circuit using the EC-Lab software. The Electrochemical Impedance Spectroscopy measurements were conducted using a 3 electrode configuration using the SP-300 Potentiostat-Bio-Logic instrument.

2.4. Materials Characterization

Powder X-ray diffraction (PXRD) analysis was conducted using a Bruker D2 phaser (D2-205530) diffractometer with Cu Ka1 radiation ($\lambda = 1.54060 \text{ \AA}$) at 30 kV and 10 mA. Measurements were taken over 2θ angle range of 5–90° in steps of 0.026° with a step time of 5 s at ambient temperature. X-ray photoelectron spectroscopy (XPS) analysis was conducted using a Physical Electronics PHI 5700 spectrometer. Non-monochromatic MgKa X-rays (300 W, 15 kV, and 1253.6 eV) were used as the excitation source. The spectrometer energy scale was calibrated using Cu 2p_{3/2}, Ag 3d_{5/2}, and Au 4f_{7/2} photoelectron lines at 932.7, 368.3, and 84.0 eV, respectively. Samples were mounted on a sample holder without adhesive tape and kept overnight under high vacuum in the preparation chamber before being transferred to the analysis chamber for testing. The spectra were collected in the constant pass energy mode at 29.35 eV. The residual pressure in the analysis chamber was maintained below 1.33 X 10⁷ Pa during the spectra acquisition with a multichannel hemi-spherical electron analyser. Transmission electron microscopy (TEM) images were collected using a FEI Technai T12 TEM operated at an accelerating voltage of 120 kV with a beam spot size of 2 in the TEM mode. TEM samples were prepared by dispersing the nanoparticles in hexane, sonicated for 30

min, after which they were deposited on a copper grid and allowed to dry at room temperature before analysis.

3. Results and discussion

3.1. Structural characterization

Pure α -WP₂ and Mo-doped α -WP₂ with different molybdenum dopant content were prepared using colloidal synthesis by varying the Mo:W molar ratios of the precursors. X-ray diffraction (XRD) analysis was employed to investigate the crystal phase of the undoped α -WP₂ and doped Mo(2.5%)/ α -WP₂, Mo(5%)/ α -WP₂ and Mo(10%)/ α -WP₂ nanoparticles. The XRD patterns of the pristine products showed no diffraction peaks (Fig. S1). All the patterns exhibited a broad peak centred at 41 °, indicating that the pristine nanoparticles were amorphous. Subsequent to heat treatment at 800 °C in N₂ for 1 h, the nanoparticles crystallized as indicated by the formation of prominent peaks in all samples as shown in Fig. 1(a). The pure and doped nanoparticles all crystallized in the NbAs₂ structure type (space group: C2/m (12)), which corresponds to the monoclinic phase of α -WP₂ (PDF 01-076-2365) and the lattice constants are $a = 8.5000 \text{ \AA}$, $b = 3.1680 \text{ \AA}$ and $c = 7.4660 \text{ \AA}$. The introduction of different Mo-dopant contents did not cause any destruction to the crystal structure of α -WP₂. The absence of any diffraction peaks matching to either Mo_xP or MoWP₂ shows that Mo was incorporated into the lattice of α -WP₂ without forming any new phases during synthesis.²⁰ However, it is worth noting that at higher dopant concentration (10 mol % Mo), a slight shift to the right was observed for Mo(10%)/ α -WP₂ as indicated by the (111) diffraction peak in Fig 1(b). The shift to higher 2θ indicates the contraction of the lattice upon substitution of the relatively larger W atoms (1.93 Å) with smaller Mo atoms (1.90 Å). Energy-dispersive X-ray spectroscopy (Fig. S2) of α -WP₂ shows peaks corresponding to elements W, P, C and O. In addition to the forementioned elements, the Mo element was detected in all the Mo-doped α -WP₂ catalysts. The electronic and compositional properties of the nanoparticles were further examined using X-ray photoelectron spectroscopy (XPS). Displayed in Fig. 1(c) is the XPS survey spectra of pure α -WP₂ and Mo(10%)/ α -WP₂ nanoparticles, with clear peaks attributed to P, W, Mo, C and O chemical elements. The P 2p spectrum of Mo(10%)/ α -WP₂ (Fig 1(d)) displays three distinct peaks located at binding energies of 129.3, 130.3 and 133.4 eV. The peaks at 129.3 and 130.3 eV correspond to P 2p_{3/2} and P 2p_{1/2} in the W-P bond, respectively.²¹ Whereas the peak at 133.4 eV correspond to P 2p_{3/2} in P-O, resulting from the partial surface oxidation due to exposure to air.²² The high-resolution spectrum of W 4f (Fig 1(e)) shows peaks at 31.4, 34.1, 35.7 and 37.8 eV. The peaks at 31.4 and 34.1 eV correspond to W4f_{7/2} and W4f_{5/2} assigned to W in the W-P

bond.²³ The peaks located at binding energy of 35.7 and 37.8 eV are assigned to $W 4f_{5/2}$ in WO_3 , resulting from surface oxidation.²⁴⁻²⁵ It is worth noting that contrary to pristine α - WP_2 , an additional peak attributed to the Mo dopant is observed in the survey spectrum of $Mo(10\%)/\alpha$ - WP_2 (dashed lines) indicating the successful incorporation of Mo into α - WP_2 .

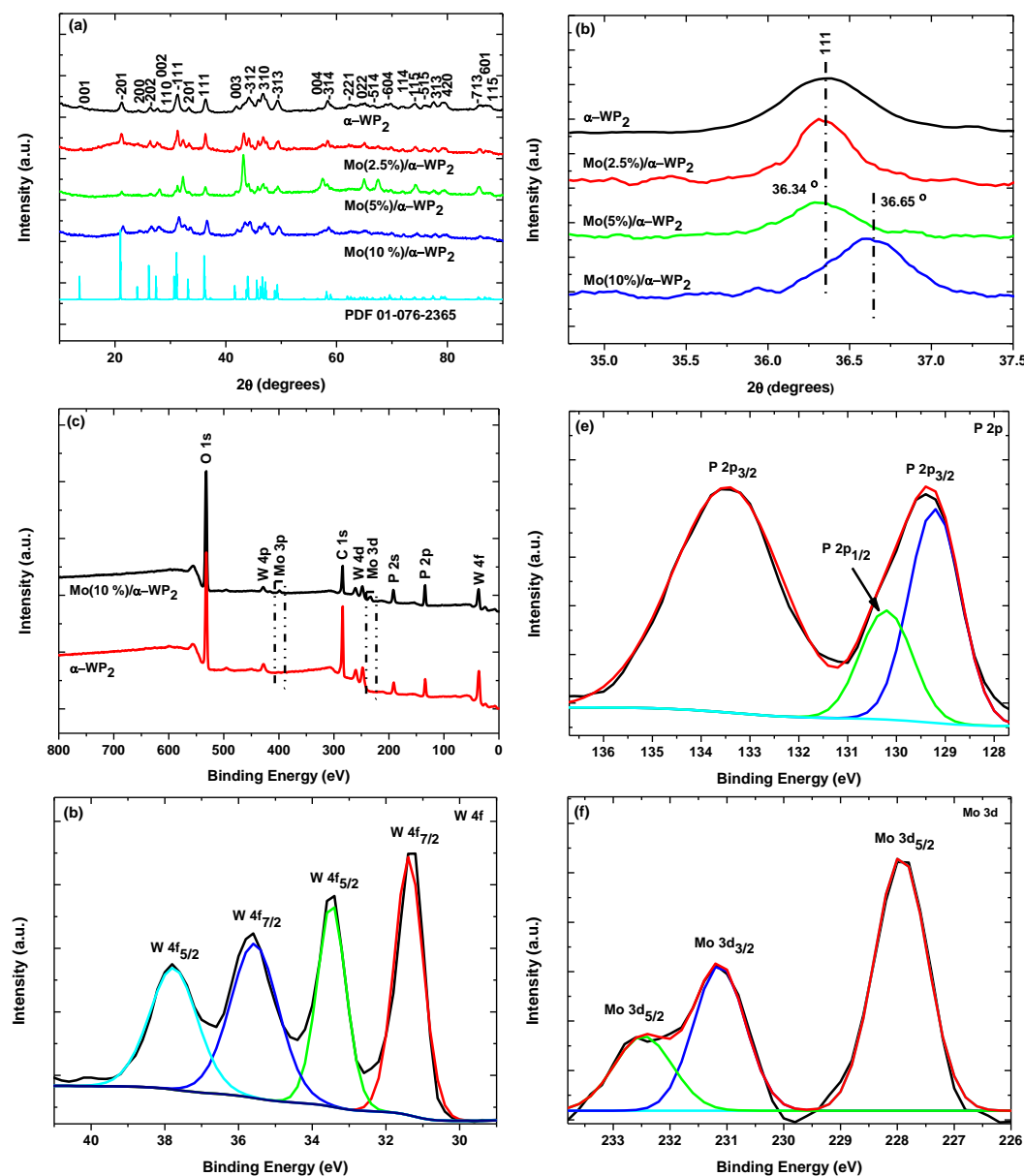


Fig. 1: XRD pattern of (a) α - WP_2 , $Mo(2.5\%)/\alpha$ - WP_2 , $Mo(5\%)/\alpha$ - WP_2 and $Mo(10\%)/\alpha$ - WP_2 catalysts. (b) Magnified diffraction peak (111) region showing a slight shift to high 2θ . X-ray photoelectron spectroscopy (XPS) survey spectrum of (c) α - WP_2 and $Mo(10\%)/\alpha$ - WP_2 . High-resolution spectra of (d) P 2p, (e) W 4f and (f) Mo 3d in $Mo(10\%)/\alpha$ - WP_2 .

The Mo 3d spectra (Fig. 1(f)) was deconvoluted into 3 peaks at 227.9, 231.2 and 232.5 eV corresponding to binding energies of Mo 3d_{5/2}, Mo 3d_{3/2} and Mo 3d_{5/2}, respectively.²⁶ For pristine α -WP₂, the P 2p spectrum (Fig S3(a)) displayed a strong peak at about 134.2 eV corresponding to the binding energy of oxidized P species. The absence of the peaks attributed to P in the P-W bond for α -WP₂ indicates the large extent of surface oxidation commonly observed in TMPs.²⁷⁻²⁹ The high-resolution spectrum of W 4f (Fig S3(b)) was deconvoluted into four peaks located at binding energies of 31.1 eV (W 4f_{7/2}), 33.4 eV (W 4f_{5/2}), 35.8 eV (W 4f_{5/2}) and 36.1 eV (W4f_{5/2}). The peaks at 31.1 and 33.4 eV were attributed to W in the W-P bond. Whereas those at higher binding energies (35.8 and 36.1 eV) were attributed to oxidized tungsten species (i.e., WO₃). The dominant tungsten oxide peaks over those signifying the presence of W in the W-P bond indicate a higher degree of surface oxidation due to exposure of the nanoparticles to air.³⁰⁻³² To further confirm the bulk composition of pure α -WP₂, XRD analysis was performed on long term stored α -WP₂ nanoparticles. The XRD pattern of the long term stored α -WP₂ (Fig. S4) showed no peaks confirming the presence of any tungsten oxide or metaphosphate species. This proved that the oxides were a result of surface oxidation that could only be detected by XPS with an escape depth of the photo-electrons ranging from 2-10 nm. Even though surface oxidation is observed in both α -WP₂ and Mo(10%)/ α -WP₂, it dominates mainly on the pure α -WP₂. We postulate that the lesser extent of surface oxidation in the doped nanoparticles was as a result of surface passivation promoted by the presence of the Mo dopant, which is beneficial for electronic conductivity and electrocatalytic properties.³³⁻
³⁴ The surface morphologies of the catalysts with different dopant percentages were studied using TEM and are shown in Fig. 2. From the TEM images, it can be seen that pure α -WP₂ (Fig. 2(a)) and Mo(2.5%)/ α -WP₂ (Fig. 2(b)) catalysts formed solely sheets stacked on top of one another. On the contrary, Mo(5%)/ α -WP₂ (Fig. 2(c)) and Mo(5%)/ α -WP₂ (Fig. 2(d)) took on a sheet-like morphology with small crumbles observable on the sheets. The alteration of the uniform sheet-like morphology observed in pure α -WP₂ is prominent in the catalyst with the highest Mo-dopant content.

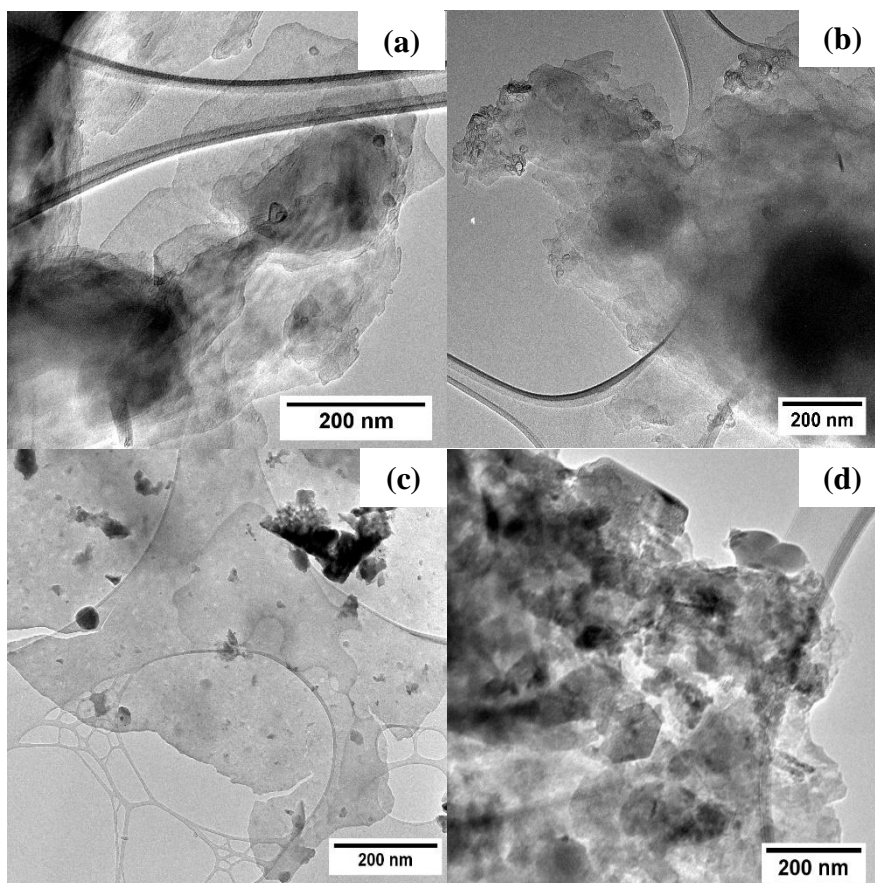


Fig. 2: TEM images of (a) α -WP₂, (b) Mo(2.5%)/ α -WP₂, (c) Mo(5%)/ α -WP₂ and (d) Mo(10%)/ α -WP₂.

3.2. HER Performance Evaluation

Linear sweep voltammetry (LSV) was used to determine the catalytic activity of the various catalysts in 0.5 M H₂SO₄ solution. For comparison, Pt/C, vulcan and glassy carbon were also tested. As expected, Pt/C displayed superior catalytic activity, vulcan and glassy carbon showed negligible activity towards HER (Fig. 3(a)). Fig 3(a) further reveals that the pristine α -WP₂ catalyst exhibited the lowest activity compared to its doped counterparts, with o(10%)/ α -WP₂ being the most active catalyst. The results clearly show that the introduction of the Mo-dopant into the crystal structure of α -WP₂ enhances the catalytic activity in the order Mo(10%)/ α -WP₂ > Mo(5%)/ α -WP₂ > Mo(2.5%)/ α -WP₂ > α -WP₂. To produce a current density of 10 mA.cm⁻², α -WP₂, Mo(2.5%)/ α -WP₂, Mo(5%)/ α -WP₂ and Mo(10%)/ α -WP₂ catalysts required an overpotential of -271, -229, -210 and -165 mV, respectively. There is a clear increase in the performance of the catalysts as the concentration of the Mo-dopant was increased. This enhanced catalytic activity with doping indicates the important effect of the Mo

dopant in optimizing the electronic structure on the catalytic sites and creating the synergistic effect between the W and Mo metals.³⁵ In acidic media, HER can be described using a multistep reaction process, which involves three possible reactions with two different mechanisms. The first step involves the adsorption and subsequent reaction of a proton with an electron on the surface of a catalyst forming an intermediate state of adsorbed hydrogen (H_{ads}) (Volmer reaction, eq. S1).

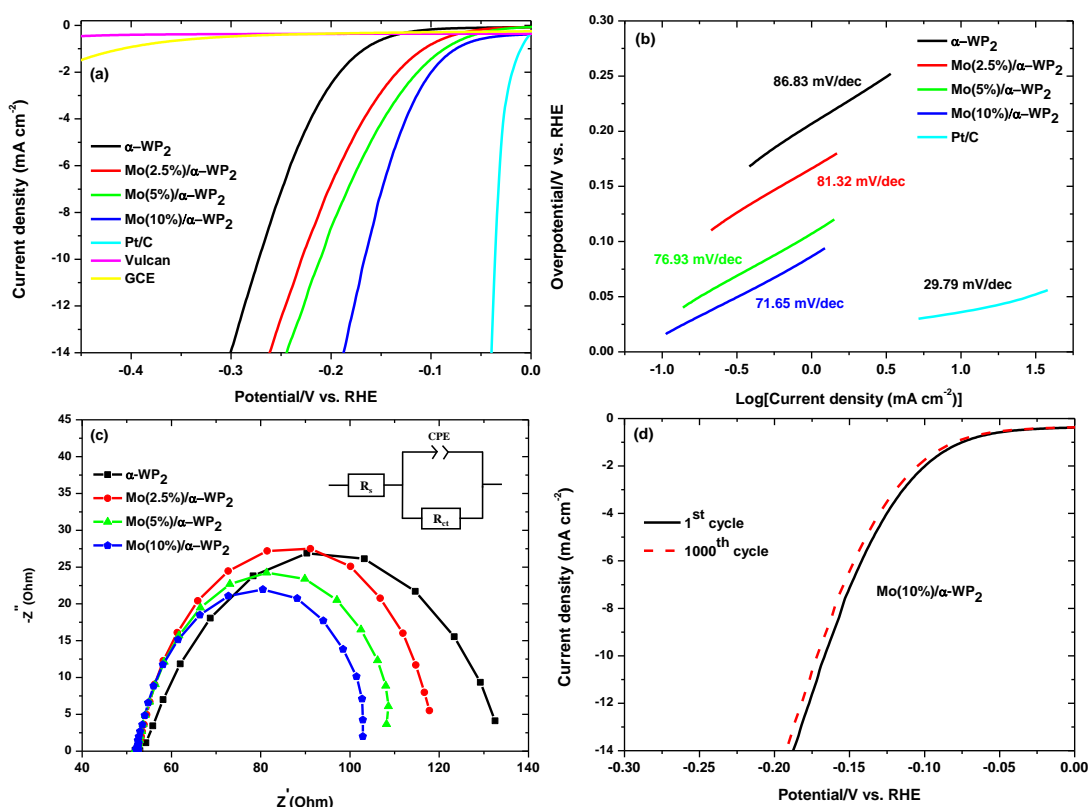


Fig. 3: Electrochemical tests: (a) LSV polarization curves of α -WP₂, Mo(2.5%)/ α -WP₂, Mo(5%)/ α -WP₂, Mo(10%)/ α -WP₂, Pt/c, vulcan and GCE at a scan rate of 2 mV/s in 0.5 M H₂SO₄. (b) corresponding Tafel plots, (c) Nyquist plots of α -WP₂, Mo(2.5%)/ α -WP₂, Mo(5%)/ α -WP₂, Mo(10%)/ α -WP₂ catalysts. (f) LSV curves of Mo(10%)/ α -WP₂ before and after 1000 potential cycles.

The next step may proceed through either the Heyrovsky reaction (Eq. S2) or Tafel reaction (Eq. S3) to form molecular hydrogen (H₂). The Heyrovsky reaction dominates at low H_{ads} coverage, where H₂ is formed by the recombination of the H_{ads} with a new electron and a proton. At high H_{ads} coverage, the Tafel reaction dominates and H₂ is generated from the recombination of adjacent H_{ads} atoms. The forementioned reactions are reported to have tafel slopes of 118, 39 and 29 mV.dec⁻¹, respectively.³⁶ To get a better understanding of the HER mechanism, the reaction kinetics were studied using the Tafel slopes, an intrinsic property of a catalyst. As

shown in Fig 3(b), the Tafel slope for Mo(10%)/ α -WP₂ (71.65 mV.dec⁻¹) is lower than those of Mo(5%)/ α -WP₂ (76.93 mV.dec⁻¹), Mo(2.5%)/ α -WP₂ (81.32 mV.dec⁻¹) and α -WP₂ (86.83 mV.dec⁻¹). A smaller Tafel slope indicates that hydrogen gas is generated more rapidly on the surface of a catalyst. The Tafel slopes of the catalysts under study are in the range between 38 – 118 mV.dec⁻¹, which indicates that they all follow the Volmer-Heyrovsky pathway, where the rate-determining step is the Volmer step during the HER process.³⁷ The Mo(10%)/ α -WP₂ catalyst possesses catalytic activity which compares favourably to some of the recently reported metal doped transition metal phosphides electrocatalysts (Table S1). To gain further insight into the intrinsic properties that influence electrocatalytic performance, electrochemical impedance spectroscopy (EIS) was used to determine the electron transfer ability of the catalysts. The Nyquist plots (Fig 3(c)) of all the catalysts exhibited only one semicircle (charge transfer resistance, R_{ct}), indicating that the corresponding equivalent circuit (insert: Fig 3(c)) is characterized by one time constant.³⁸ The results show that the R_{ct} of Mo(10%)/ α -WP₂ (53.05 Ω) is smaller than that of Mo(5%)/ α -WP₂ (60 Ω), Mo(2.5%)/ α -WP₂ (68 Ω) and α -WP₂ (93 Ω), indicating its rapid charge transfer rate and superior HER kinetics. The catalytic performance parameters of the different catalysts are summarized in Table 1.

Table 1: Summary of the catalytic activity of the various catalysts in acidic media.

Catalyst	Tafel Slope (mV.dec ⁻¹)	Overpotential (mV) (at 10 mA.cm ⁻²)	Charge transfer resistance (Ω)	ECSA (cm ²)	Onset potential (mV) (at 1 mA.cm ²)
α -WP ₂	86.83	-271	93	6.440	-163
Mo(2.5%)/ α WP ₂	81.32	-229	69	8.885	-104
Mo(5 %)/ α -WP ₂	76.93	-210	60	14.76	-86
Mo(10%)/ α -WP ₂	71.65	-165	53	22.97	-73

Long term stability is an important property in catalyst applications. Therefore, the electrochemical durability of Mo(10%)/ α -WP₂ was tested using cyclic voltammetry (CV) sweeps in a potential range from 0 to -0.8 V (vs. RHE) using a scan rate of 50 mV.s⁻¹. The Mo(10%)/ α -WP₂ catalyst exhibited excellent stability in an acidic medium showing only a minor decrease in catalytic activity after 1000 continuous cycles. In addition to electrical conductivity, the density of electrochemically active sites also provides information about the activity of an electrocatalyst.

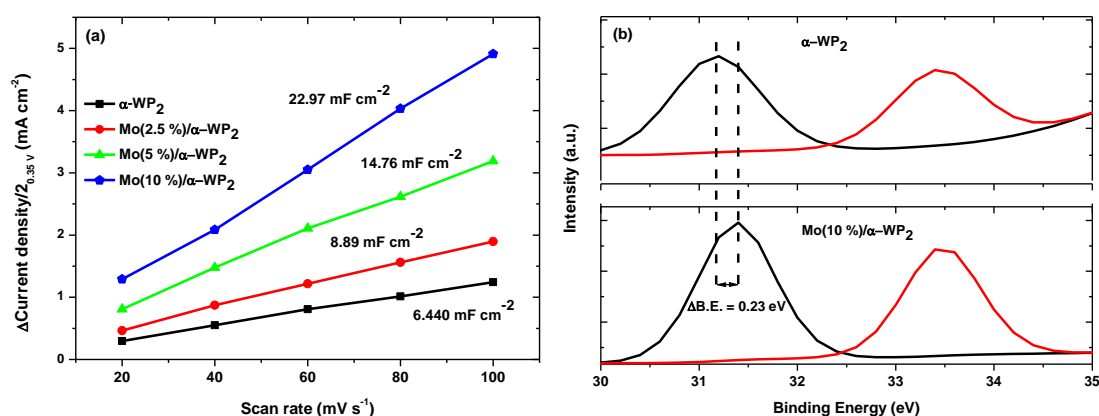


Fig. 4: (a) Linear fit of the capacitive currents against scan rate for the various catalysts. (b) High resolution XPS spectra of W 4f_{7/2} with (bottom) and without (top) molybdenum dopant.

The electrochemical double-layer capacitance (C_{dl} , details on calculation of C_{dl} provided in the additional supporting information) was measured using cyclic voltammetry (Fig. S5) in order to estimate the electrochemically active surface area (ECSA) of the different catalysts (details about calculation of ECSA are shown in the SI).³⁹ The measured capacitive currents were plotted against the scan rate (20–100 mV.s⁻²) as shown in Fig. 4(a). As depicted in Fig. 4(a), the C_{dl} of Mo(10%)/ α -WP₂ (22.965 mF.cm⁻²) was found to be significantly higher than those of Mo(5%)/ α -WP₂ (14.755 mF.cm⁻²), Mo(2.5%)/ α -WP₂ (8.885 mF.cm⁻²) and α -WP₂ (6.440 mF.cm⁻²), showing that it possessed a high number of catalytically active sites. Moreover, a closer look at the W 4f_{7/2} peak (Fig. 4(b)) in the W-P bond for pure α -WP₂ and Mo(10%)/ α -WP₂ reveals a slight shift to high binding energy (Δ = 0.23 eV) due to the presence of the Mo dopant. This positive shift indicates the partial transfer of electron density from Mo to W as a result of the difference in electronegativity (2.16 for Mo vs. 2.36 for W). Metals in transition metal phosphides are catalytically active hydride-acceptor sites.⁴⁰ Therefore, a high electron density around the metal sites result in high activity towards HER.

High temperature treatment is a common procedure used to aid crystallization of amorphous nanoparticles. As mentioned in earlier sections of the study, the as-synthesized nanoparticles were amorphous and crystalline phases were obtained through annealing at 800 °C for 1 h in N₂ gas. Due to this, we were compelled to get a better understanding of the effect of annealing temperature on the catalytic performance of the best performing Mo(10%)/ α -WP₂ catalyst. This was done by comparing the catalytic activity of nanoparticles that are unannealed and those annealed at 600, 800 and 950 °C. Subsequent to heat treatment at various temperatures, the structural properties were recorded using XRD (Fig. 5(a)). The XRD patterns of as-synthesized nanoparticles and those annealed at 600 °C are characterized by broad peaks which indicated that they lacked long range crystalline order. As the temperature was increased to 800 °C, distinct characteristic peaks of α -WP₂ (PDF 01-076-2365) were observed. A further increase in annealing temperature to 950 °C resulted in the formation of a different compound which could be matched to WP (PDF 00-029-1364). However, due to the presence of Mo, the peaks were slightly shifted to higher 2 θ as shown in Fig 5(a). Seemingly, high annealing temperature promotes the loss of excess phosphorus resulting in phase transformation from the phosphorus rich monoclinic tungsten diphosphide (α -WP₂) into the orthorhombic tungsten monophosphide (WP). The catalysts were then tested for activity in 0.5 M H₂SO₄ solution and the corresponding polarization curves are shown in Fig. 5(b). As depicted, to produce current density of 10 mA cm⁻², the Mo(10%)/ α -WP₂-0 °C, Mo(10%)/ α -WP₂-600 °C, Mo(10%)/ α -WP₂-800 °C and Mo(10%)/WP-950 °C catalysts required overpotentials of -205, -267, -165 and -350 mV, respectively. The corresponding Tafel slopes (Fig. 5(c)) for the Mo(10%)/ α -WP₂-0 °C, Mo(10%)/ α -WP₂-600 °C, Mo(10%)/ α -WP₂-800 °C and Mo(10%)/WP-950 °C catalysts were determined to be 75.18, 88.52, 71.65 and 98.10 mV.dec⁻¹, respectively. The catalytic activity of these catalysts follows the order of Mo(10%)/ α -WP₂-800 °C > Mo(10%)/ α -WP₂-0 °C > Mo(10%)/ α -WP₂-600 °C > Mo(10%)/WP-950 °C. Interestingly, even though Mo(10%)/ α -WP₂-800 °C was the best performing catalyst, the as-synthesized catalyst exhibited HER activity which is much higher than those of Mo(10%)/ α -WP₂-600 °C and Mo(10%)/WP-950 °C. Amorphous catalysts lack long range order which promotes formation of dangling bonds that have a substantial density of unsaturated sites. The non-symmetrical bonding aids adsorption of H⁺ ions on the catalyst surface resulting in improved catalytic activity.⁴¹⁻⁴² The Mo(10%)/WP-950 °C catalyst displayed the lowest catalytic activity with η_{10} of -350 mV, which suggests that the phosphorus poor WP structure is less active than the phosphorus rich α -WP₂. To further understand the difference in catalytic activity, EIS was conducted to

determine the electron transfer ability of the catalysts heat treated at different temperatures. As observed from the EIS plots (Fig. 5(d)), the Mo(10%)/ α -WP₂-800 °C catalyst exhibits a charge transfer resistance (R_{ct}) of 53 Ω , which is smaller than those of Mo(10%)/ α -WP₂-600 °C (68 Ω) and Mo(10%)/ α -WP₂-950 °C (152 Ω), signifying better electrical conductivity. The EIS results corroborate with the HER activity trend that was observed in the polarization curve

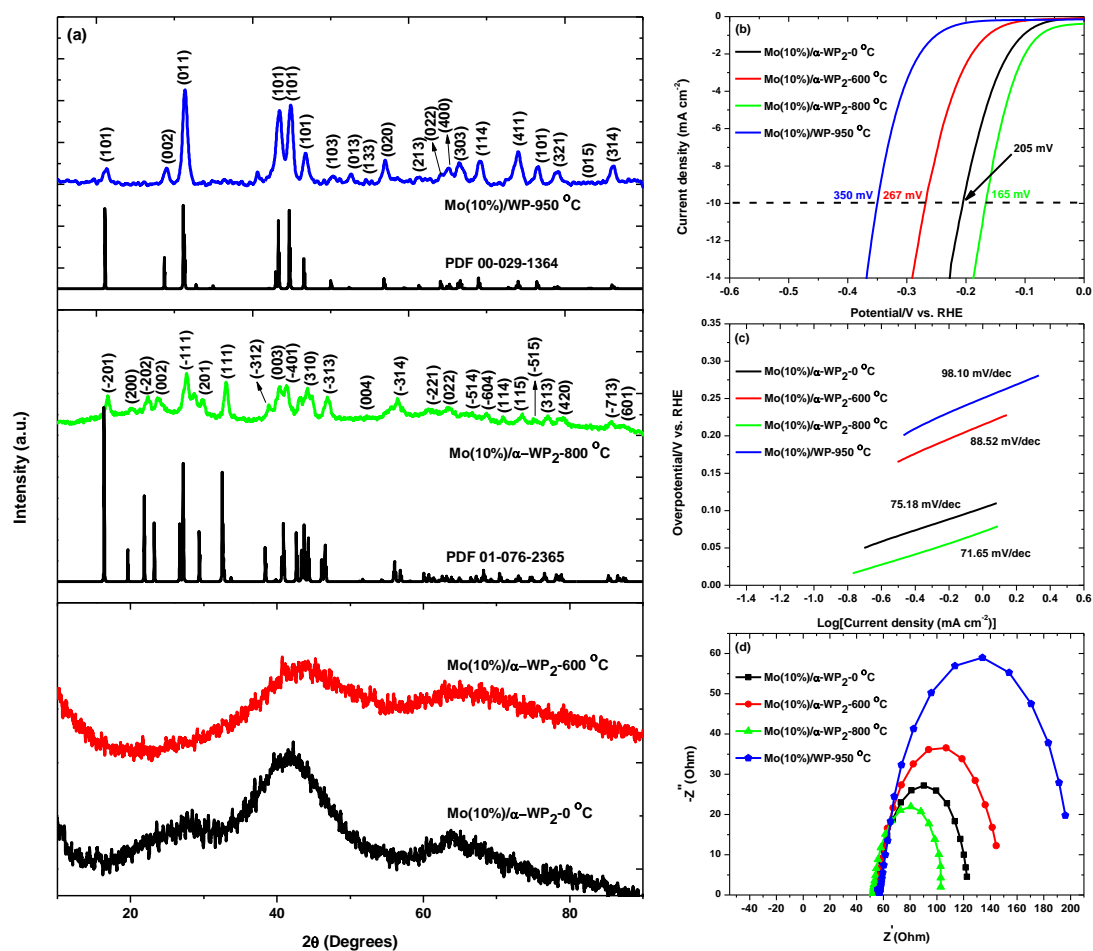


Fig. 5: (a) XRD pattern of Mo(10%)/ α -WP₂ before and after annealing at 600, 800 and 950 °C under N₂ gas. (b) LSV curves of Mo(10%)/ α -WP₂ heated at various temperatures. The corresponding (c) Tafel and (d) EIS plots.

4. Conclusion

Colloidal synthesis was utilized to systematically introduce different concentrations of Mo-dopant (2.5, 5 and 10 mol%) into the crystal structure of α -WP₂. The resultant pure tungsten diphosphide (α -WP₂) and molybdenum tungsten diphosphide (Mo/ α -WP₂) nanoparticles were studied as electrocatalysts for HER in acidic medium. The combination of XRD, EDS and XPS analysis confirmed the successful incorporation of Mo atoms into the crystal structure of α -

WP₂. HER results reveal that the presence of the Mo dopant optimized the electronic structure of the active sites of α -WP₂ resulting in enhanced catalytic performance. A small charge-transport resistance, more exposed electrochemically active sites, high electron density on the W sites and high stability were responsible for the superior activity of the Mo(10%)/ α -WP₂ catalyst. A study on the effect of annealing revealed that heat treatment of Mo(10%)/ α -WP₂ at high temperatures (i.e. 950 °C) result in the formation of a phosphorus poor Mo(10%)/ α -WP-950 °C phase, with inferior catalytic activity. Whereas excellent activity was observed from the as-synthesized catalyst due to unsymmetrical bonding found in amorphous structures. This work provides new insight into the development of TMPs into highly active HER in acidic medium by tuning of electronic properties through doping.

5. References

1. S. Chu and A. Majumdar, Opportunities and challenges for a sustainable energy future, *Nature* 488 (2012) 294-303.
2. T.R. Cook, D.K. Dogutan, S.Y. Reece, Y. Surendranath, T.S. Teets and D.G. Nocera, Solar energy supply and storage for the legacy and nonlegacy worlds, *Chem. Rev.* 110 (2010) 6474-6502.
3. T.S. Teets and D.G. Nocera, Photocatalytic hydrogen production, *Chem. Commun.* 47 (2011) 9268-9274.
4. C. Li and J. Baek, Recent advances in noble metal (Pt, Ru, and Ir)-based electrocatalysts for efficient hydrogen evolution reaction, *ACS Omega*
5. M. Sheng, B. Jiang, B. Wu, F. Liao, X. Fan, H. Ling, Y. Li, Y. Lifshitz, S. Lee and M. Shao, Approaching the volcano top: Iridium/Silicon nanocomposites as efficient electrocatalysts for the hydrogen evolution reaction, *ACS Nano* 13 (2019) 2786-2794.
6. X. Peng, C. Pi, X. Zhang, S. Li, K. Huo, P.K. Chu, Recent progress of transition metal nitrides for efficient electrocatalytic water splitting, *Sustain. Energy Fuels* 3 (2019) 366-381.
7. X. Xia, L. Wang, N. Sui, V.L. Colvin and W.W. Yu, Recent progress in transition metal selenide electrocatalysts for water splitting, *Nanoscale* 12 (2020) 12249-12262).
8. S. Chandrasekaran, L. Yao, L. Deng, C. Bowen, Y. Zhang, S. Chen, Z. Lin, F. Peng and P. Zhang, Recent advances in metal sulfides: from controlled fabrication to electrocatalytic,

- photocatalytic and photoelectrochemical water splitting and beyond, *Chem. Soc. Rev.* 48 (2019) 4178-42-80.
9. M. Kuang, W. Huang, C. Hegde, W. Fang, X. Tan, C. Liu, J. Ma and Q. Yan, Interface engineering in transition metal carbides for electrocatalytic hydrogen generation and nitrogen fixation, *Mater. Horiz.* 7 (2020) 32-53.
 10. H. Du, R. Kong, X. Guo, F. Qu, J. Li, Recent progress in transition metal phosphides with enhanced electrocatalysis for hydrogen evolution, *Nanoscale* 10 (2018) 21617-21624.
 11. Q. Qin, J. Li, Z. Guo, C. Jian and W. Liu, Tungsten phosphide nanosheets seamlessly grown on tungsten foils toward efficient hydrogen evolution reaction in basic and acidic media, *Int. J. Hydrog. Energy* 44 (2019) 27483-2749.
 12. H. Du, S. Gu, R. Liu and C.M. Li, Tungsten diphosphide nanorods as an efficient catalyst for electrochemical hydrogen evolution, *J. Power sources* 278 (2015) 540-545.
 13. Y. Li, F. Li, Y. Zhao, S. Li J. Zeng, H. Yao and Y. Chen, Iron doped cobalt phosphide ultrathin nanosheets on nickel foam for overall water splitting, *J. Mater. Chem. A* 7 (2019) 20658-20666.
 14. X. Xiao, L. tao, M. Li, X. Lv, D. Huang, X. Jiang, H. Pan, M. Wang, Y. Shen, Electronic modulation of transition metal phosphide via doping as efficient and pH-universal electrocatalysts for hydrogen evolution reaction, *Chem. Sci.* 9 (2018) 1970-1975.
 15. P. Li and H.C. Zeng, Promoting electrocatalytic oxygen evolution over transition-metal phosphide-based nanocomposites via architectural and electronic engineering, *ACS Appl. Mater. Interfaces* 11 (2019) 46825-46838.
 16. S. Lu, L. Zhang, Y. Dong, J. Zhang, X. Tong, D. Sun, X. Shang, J. Chi, Y. Cha and B. Dong, Tungsten-doped Ni-Co phosphides with multiple catalytic sites as efficient electrocatalysts for overall water splitting 7 (2019) 16859-16866.
 17. J. Wang, K. Chang, Z. Sun, J.H. Lee, B.M. Tackett, C. Zhang, J.G. Chen and C. Liu, A combined experimental and theoretical study of the accelerated hydrogen evolution kinetics over wide pH range on porous transition metal doped tungsten phosphide electrocatalysts, *Appl. Catal. B* 251 (2019) 162-167.

18. M.A.R. Anjum and J.S. Lee, Sulfur and nitrogen dual-doped molybdenum phosphide nanocrystallites as an active and stable hydrogen evolution reaction electrocatalyst in acidic and alkaline media, *ACS Catal.* 7 (2017) 3030-3038.

19. Z. Xing, Q. Liu, A. M. Asiri, X. Sun, High-efficiency electrochemical hydrogen evolution catalysed by tungsten phosphide submicroparticles, *ACS Catal.* 5 (2015) 145-149.

XRD

20. C. Guan, W. Xiao, H. Wu, X. Liu, W. Zang, H. Zhang, J. Ding, Y.P. Feng, S.J. Pennycook, J. Wang, Hollow Mo-doped CoP nanoarrays for efficient overall water splitting, *Nano Energy* 48 (2018) 73-80.

21. Z. Pu, X. Ya, I.S. Amiinu, Z. Tu, X. Liu, W. Li and S. Mu, ultrasmall tungsten phosphide nanoparticles embedded in nitrogen-doped carbon as a highly active and stable hydrogen-evolution electrocatalyst, *J. Mater. Chem. A* 4 (2016) 15327-15332

22. A.P. Grosvenor, S.D. Wik, R.G. Cavell, A. Mar, Examination of the bonding in binary transition-metal phosphides MP (M = Cr, Mn, Fe, Co) by X-ray photoelectron spectroscopy, *Inorg. Chem.* 14 (2005) 8988-8998.

23. X. Zhang, T. Guo, T. Liu, K. Lv, Z. Wu, Tungsten phosphide (WP) nanoparticles with tunable crystallinity, W vacancies, and electronic structures for hydrogen production, *Electrochim. Acta* 323 (2019) 134798.

24. Y. Shen, L. Li, J. Xi, X. Qiu, A facile approach to fabricate free-standing hydrogen evolution electrodes: riveting tungsten carbide nanocrystals to graphite felt fabric by carbon nanosheets, *J. Mater. Chem. A* 4 (2016) 5817-5822.

25. Q. Qin, J. Li, Z. Guo, C. Jian, W. Liu, Tungsten phosphide nanosheets seamlessly grown on tungsten foils toward efficient hydrogen evolution reaction in basic and acidic media, *Int. J. Hydro. Energy* 44 (2019) 27483-27491.

26. A. Wang, X. Chen, L. Cheng, X. Shen, W. Zhu, L. Li, J. Pang, Insight into the synergistic effect of multi-walled carbon nanotube decorated Mo-doped CoP₂ hybrid electrocatalysts toward efficient and durable overall water splitting, *J. Mater. Chem. A* 8 (2020) 17621-17633.

27. J. Chang, K. Li, Z. Wu, J. Ge, C. Liu, W. Xing, Sulfur-doped nickel phosphide nanoplates arrays: A monolithic electrocatalysts for efficient hydrogen evolution reactions. *ACS Appl. Mater. Interfaces* 10 (2018) 26303-26311.

28. L.A. Stern, L. Feng, F. Song, Ni₂P as a Janus catalyst for water splitting: the oxygen evolution activity of Ni₂P nanoparticles, *Energy Environ. Sci.* 8 (2015) 2347-2351.

29. K. Xu, X. Fu, H. Li, Z. Peng, A novel composite of network-like tungsten phosphide nanostructures grown on carbon fibers with enhanced electrocatalytic hydrogen evolution efficiency, *Appl. Surf. Sci.* 456 (2018) 230-237.
30. J. Pan, C. Zhen, L. Wang, G. Liu, H. Cheng, WB crystals with oxidized surface as counter electrode in dye-sensitized solar cells, *Sci. Bul.* 62 (2017) 114-118.
31. W. Liu, P. Geng, S. Li, R. Zhu, W. Lu, H. Lu, S. Chandrasekaran, Y. Pang, D. Fan, Y. Liu, Self-supported three-dimensional WP₂ (WP) nanosheet arrays for efficient electrocatalytic hydrogen evolution, *Int. J. Hydro. Energy* 45 (2020) 28576-28585.
32. D. Wang, K. Lv, Z. Wu, Facile synthesis of tungsten phosphide/ketjen black hybrid electrocatalyst for hydrogen production, *Mater. Res. Express* 5 (2018) 065509.
33. S. Yang, C. Li, Y. Wang, S. Chen, M. Cui, X. Bai, C. Zhi, H. Li, Suppressing surface passivation of bimetallic phosphide by sulfur for long-life aqueous zinc batteries, *Energy Storage Mater.* 33 (2020) 230-238.
34. J.A. Cecilia, A. Infantes-Molina, J. Sanmartin-Donoso, E. Rodriguez-Aguado, D. Ballesteros-Plata, E. Rodrigues -Castellon, Enhanced HDO activity of Ni₂P promoted with noble metals, *Catal. Sci. Technol.* 6 (2016) 7323-7333.
35. J. Wang, K. Chang, Z. Sun, J.H. Lee, B.M. Tackett, C. Zhang, J.G. Chen, C. Liu, A combined experimental and theoretical study of the accelerated hydrogen evolution kinetics over wide pH range on porous transition metal doped tungsten phosphide electrocatalysts, *Appl. Catal. B.* 251 (2010) 162-167.
36. Y. Shi, B. Zhang, Recent advances in transition metal phosphide nanomaterials: synthesis and applications in hydrogen evolution reaction, *Chem. Soc. Rev.* 45 (2016) 1529-1541.
37. M.I. Abdullah, A. Hameed, N. Zhang, M. Ma, Nickel nanocrystal assemblies as efficient electrocatalysts for hydrogen evolution from pH-neutral aqueous solution, *ChemElectroChem* 6 (2019) 2100-2106.
38. S. Anantharaj, S. Noda, Appropriate use of electrochemical impedance spectroscopy in water splitting electrocatalysis, *ChemElectroChem* 7 (2020) 2297-2308.
39. Z. Pu, Q. Liu, A.M. Asiri, X. Sun, Tungsten phosphide nanorod array directly grown on carbon cloth: A highly efficient and stable hydrogen evolution cathode at all pH values, *ACS Appl. Mater. Interfaces* 6 (2014) 24.
40. C.Y. Son, I.H. Kwak, Y.R. Lim, J. park, FeP and FeP₂ nanowires for efficient electrocatalytic hydrogen evolution reaction, *ChemComm* 52 (2016) 2819-2822.

41. S.S. Nkabinde, Z.B. Ndala, N.P. Shumbula, T. Kolokoto, O. Nchoe, G.N. Ngubeni, K.P. Mubiayi, N. Moloto, Delineating the role of crystallinity in the electrocatalytic activity of colloiddally synthesized MoP nanocrystals, *New J. Chem.* 44 (2020) 14041-14049.
42. Z. Jin, P. Li, X. Huang, G. Zeng, Y. Jin, B. Zheng, D. Xiao, Three-dimensional amorphous tungsten-doped nickel phosphide microsphere as an efficient electrocatalyst for hydrogen evolution, *J. Mater. Chem. A* 2 (2014) 18593-18599.

6. Supporting Information

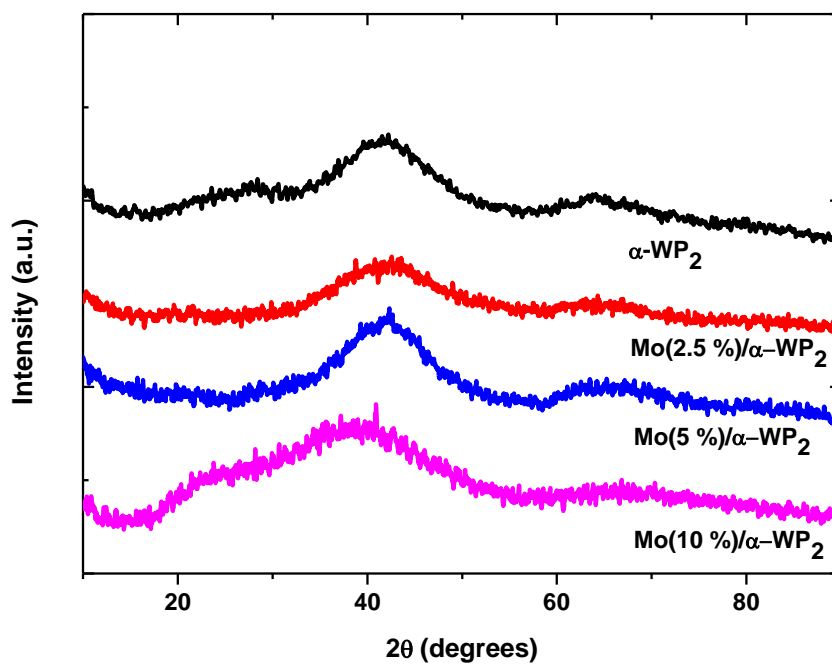


Fig. S1: XRD patterns of the pristine pure and doped α -WP₂ catalyst.

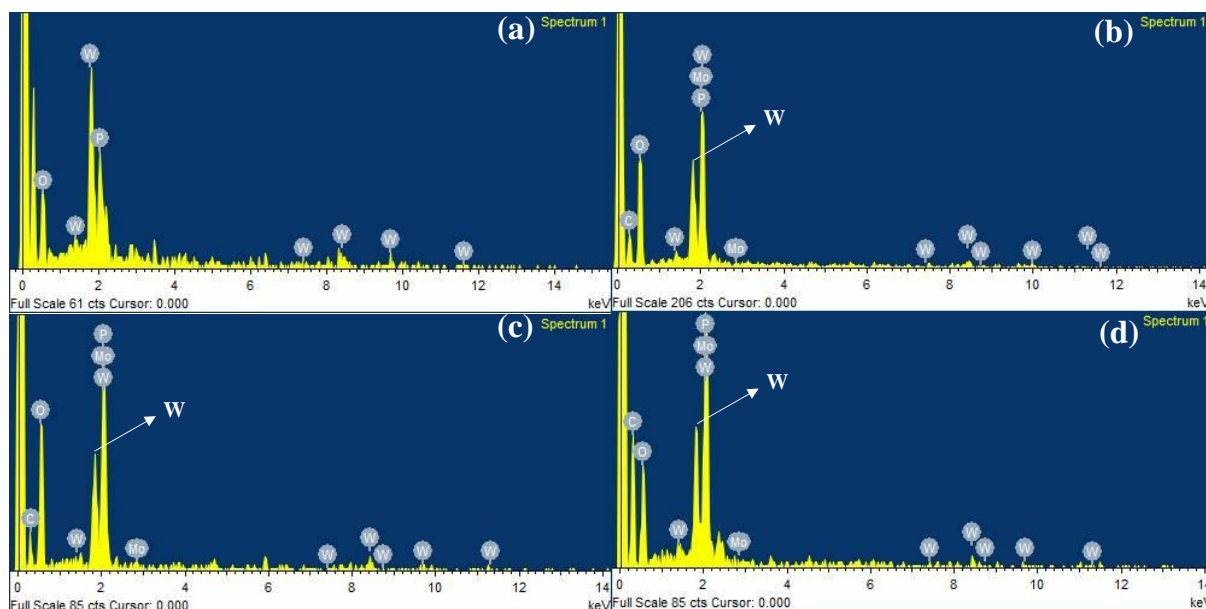


Fig. S2: Energy-dispersive X-ray spectroscopy of (a) α -WP₂, (b) Mo(2.5%)/ α -WP₂ (c) Mo(5%)/ α -WP₂ and (d) Mo(10%)/ α -WP₂ catalysts.

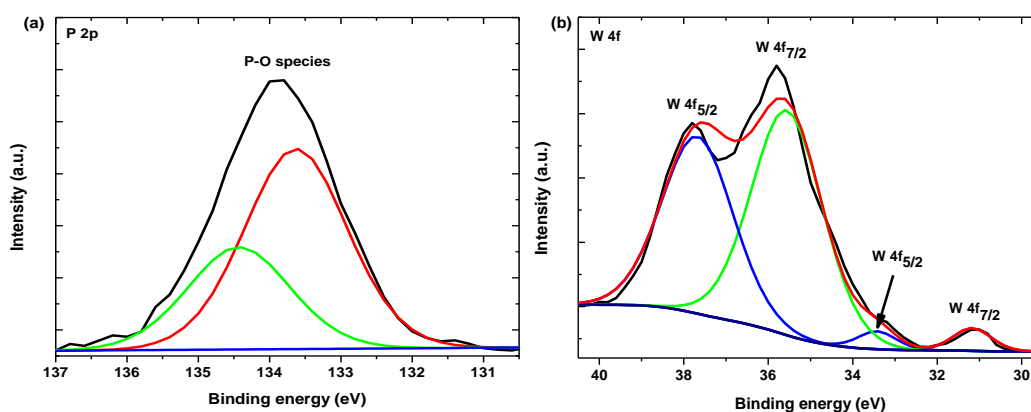


Fig. 3: The high resolution (a) P 2p and (b) W f4 spectrum of pristine α -WP₂ catalyst.

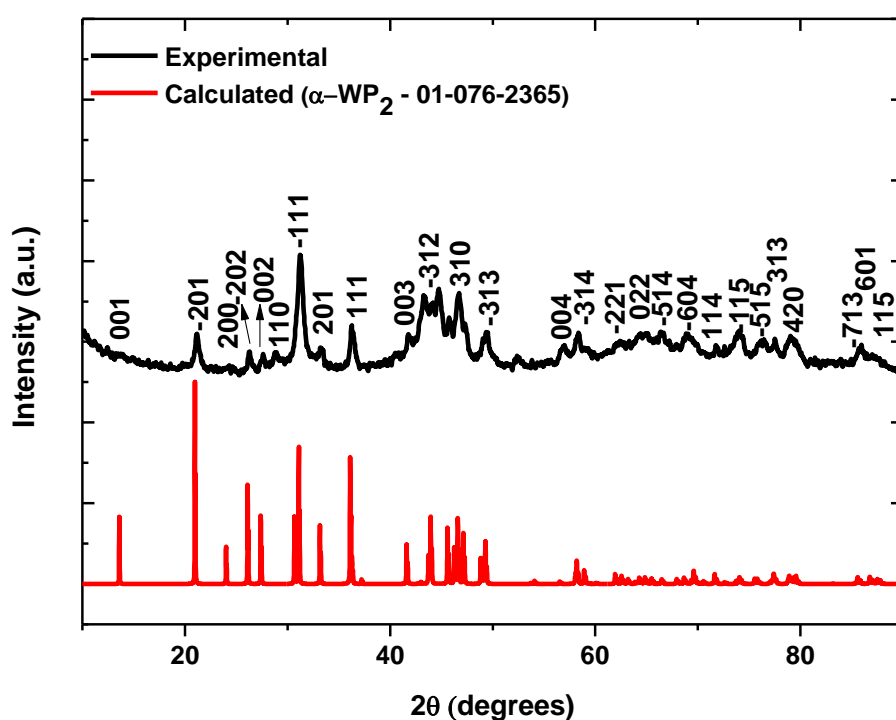


Fig. S4: XRD pattern of long term stored α -WP₂ catalyst.

The three possible reactions undergone by a catalyst in acidic medium

1. $H^+(aq) + e^- \rightarrow H_{ads}$ (Volmer reaction) Eq. S1
2. $H_{ads} + H^+(aq) + e^- \rightarrow H_2$ (Heyrovsky reaction) Eq. S2
3. $H_{ads} + H_{ads} \rightarrow H_2 (g)$ (Tafel reaction) Eq. S

Table S1: Catalytic activity comparison of metal doped transition-metal phosphide electrocatalysts for HER in 0.5 M H₂SO₄.

Catalyst	Catalyst loading (mg.cm ⁻²)	Current density (j, mA.cm ⁻²)	Overpotential (mV) (at 10 mA.cm ⁻²)	Tafel slope (mV.dec ⁻¹)	Ref
Mo(10%)/α-WP ₂	0.35	10	-165	71.65	This work
NiCoP HA/CC	-	10	-74	77.2	1
NiCoP/CC	-	10	-118	114.4	1
Mo-WP	0.2	10	-139	65	2
CoP-FeP	-	10	-130.9	45.1	3
CoP-MnP	-	10	-193.1	88.2	3
Co-FeP	0.04	10	-126	63.6	4
Ni-FeP	0.04	10	-169	86.9	4
Mn-FeP	0.04	10	-175	63.6	4
0.1Mn-MoP	0.213	10	-242	60	5
NiCoP/Ni Foam	5.6	10	-118	68	6
NiCoP	1	10	-	80	7
N-NiCoP NWs	1	10	-97.5	40.1	7
W-CoP/CC	1.9	10	-32	57	8
0.5% Ni-WP ₂	-	10	-129	73	9
NS/CC	-	10	-122	65	9
1% Ni-WP ₂ NS/CC	-	10	-128	69	9
3% Ni-WP ₂ NS/CC	-	10	-124	71	9
5% Ni-WP ₂ NS/CC	0.5	10	-168	90	10
Ni ₂ P/NiCoP@NHC	0.5	10	-116	90	10
Cs	0.071	10	-	72	11
Ni ₂ P/NiCoP@NCCs	0.071	10	-	69	11
FeMoP-0.14					
FeMoP-0.12					

References

1. S. Ma, L. Wang, S. Zhang, H. Jin, M. Wan, Y. Pan, T. Zhang, Y. Wen, M. Zhang, H. Zhu, M. Du, Facile fabrication of a binary NiCo phosphide with hierarchical architecture for efficient hydrogen evolution reactions, *Int. J. Hydro. Energy* 44 (2019) 4188-4196.
2. J. Wang, K. Chang, Z. Sun, J.H. Lee, B.M. Tackett, C. Zhang, J.G. Chen, C. Liu, A combined experimental and theoretical study of the accelerated hydrogen evolution kinetics over wide pH range on porous transition metal doped tungsten phosphide electrocatalysts, *Appl. Catal. B* 251 (2019) 162-167.
3. Y. Du, Z. Wang, H. Li, Y. Han, Y. Liu, Y. Yang, Y. Liu, L. Wang, Controllable synthesized CoP-MP (M=Fe, Mn) as efficient and stable electrocatalyst for hydrogen evolution reaction at all pH values, *Int. J. Hydro. Energy* 44 (2019) 19978-19985.
4. G. Cho, Y. park, H. Kang, Y. Hong, T. Lee, D. Ha, Transition metal-doped FeP nanoparticles for hydrogen evolution reaction catalysis, *Appl. Surf. Sci.* 510 (2020) 145427.
5. Z. Mu, T. Guo, H. Fei, Y. Mao, Z. Wu, D. Wang, Mn-doped porous interconnected MoP nanosheets for enhanced hydrogen evolution, *Appl. Surf. Sci.* (2021) 149321
6. Nickel-Cobalt phosphide nanowires supported on Ni foam as a highly efficient catalyst for electrochemical hydrogen evolution reaction, T. Liu, X. Yan, P. Xi, J. Chen, D. Qin, D. Shan, S. Devaramani, X. Lu, *Int. J. Hydro. Energy* 42 (2017) 14124-14132.
7. L. Zhang, Y. Qi, L. Sun, G. Chen, L. Wang, M. Zhang, D. Zeng, Y. Chen, X. Wang, K. Xu, F. Ma, Facile route of nitrogen doping in nickel cobalt phosphide for highly efficient hydrogen evolution in both acid and alkaline electrolytes, *Appl. Surf. Sci.* 512 (2020) 145715.
8. Z. Ren, X. Ren, L. Zhang, C. Fu, X. Li, Y. Zhang, B. Hao, L. Yang, P.K Chu, K. Huo, Tungsten-doped CoP nanoneedle arrays grown on carbon cloth as efficient bifunctional electrocatalysts for overall water splitting, *ChemElectroChem* 6 (2019) 5229-5236.
9. W. Liu, P. Geng, S. Li, W. Liu, D. Fan, H. Lu, Z. Lu, Y. Liu, Tuning electronic configuration of WP2 nanosheet arrays via nickel doping for high-efficiency hydrogen evolution reaction, *J. Energy Chem.* 55 (2020) 17-24.
10. L. Han, T. Yu, W. Lei, W. Liu, K. Feng, Y. Ding, G. Jiang, P. Xu, Z. Chen, Nitrogen doped carbon nanocones encapsulating with nickel-cobalt mixed phosphides for enhanced hydrogen evolution reaction, *J. Mater. Chem. A* 5 (2017) 16568-16572.
11. X. Liang, D. Zhang, Z. Wu, D. Wang, The Fe-promoted MoP catalyst with high activity for water splitting, *Appl. Catal. A Gen.* 524 (2016) 134-138

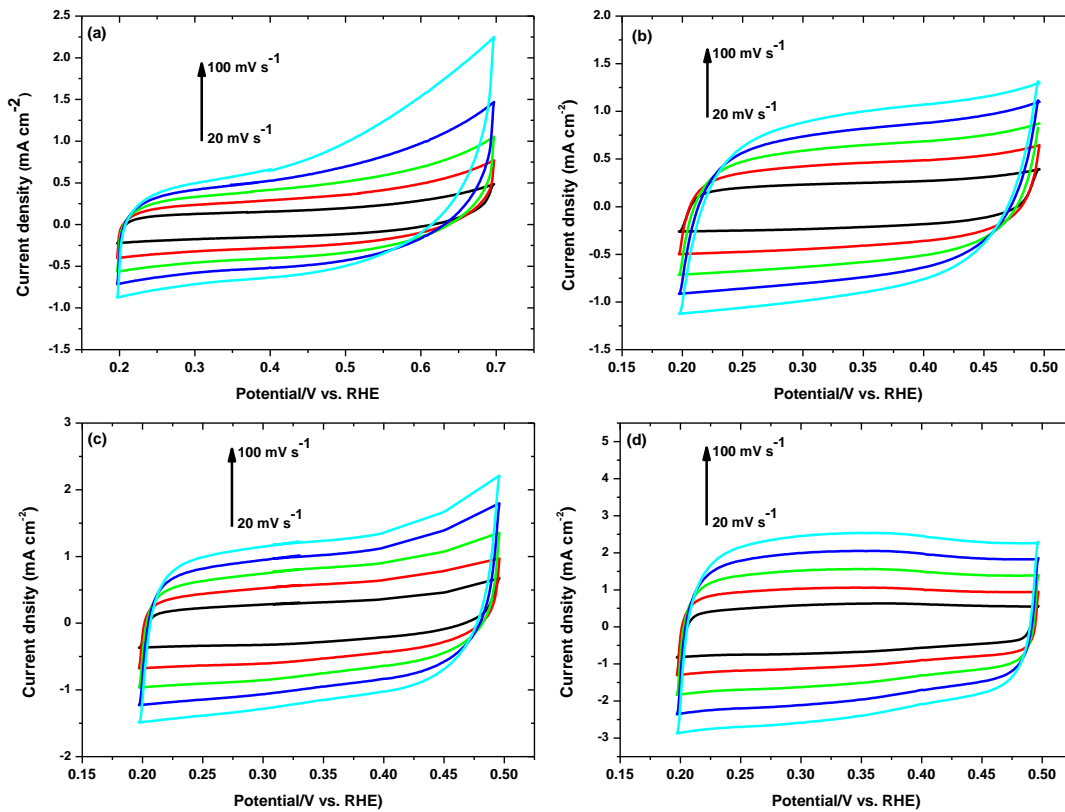


Fig. S5: The electrochemical double-layer capacitance for (a) α -WP₂, (b) Mo(2.5%)/ α -WP₂, (c) Mo(5%)/ α -WP₂ and (d) Mo(10%)/ α -WP₂ measured using CV to calculate the ECSA.

Calculating the electrochemical active surface area.

From the slopes of the linear plots of capacitive current against the scan rate (20-100 mV s⁻¹), the specific capacitance was determined to be 6440, 8890, 14760 and 22970 $\mu\text{F cm}^{-2}$ for α -WP₂, Mo(2.5%)/ α -WP₂, Mo(5%)/ α -WP₂ and Mo(10%)/ α -WP₂, respectively. The specific capacitance was then converted into ECSA using the value for a flat standard with an actual SA of 1 cm². Generally, C_s for a flat surface is in the range of 20-60 $\mu\text{F cm}^{-2}$. Hence a median value of 40 $\mu\text{F cm}^{-2}$ for C_s was assumed for the calculation of ECSA.¹⁻²

$$ECSA = \frac{C_{dl}}{C_s}$$

Where C_{dl} is the double layer capacitance and C_s is the specific capacitance.

α -WP₂:

$$ECSA = \frac{6440 \mu F}{40 \mu F \text{ cm}^{-2} \text{ per cm}^2_{ECSA}} = 161 \text{ cm}^2_{ECSA}$$

Mo(2.5 %)/ α -WP₂:

$$ECSA = \frac{8890 \mu F}{40 \mu F \text{ cm}^{-2} \text{ per cm}^2_{ECSA}} = 222 \text{ cm}^2_{ECSA}$$

Mo(5 %)/ α -WP₂:

$$ECSA = \frac{14760 \mu F}{40 \mu F \text{ cm}^{-2} \text{ per cm}^2_{ECSA}} = 369 \text{ cm}^2_{ECSA}$$

Mo(10 %)/ α -WP₂:

$$ECSA = \frac{22970 \mu F}{40 \mu F \text{ cm}^{-2} \text{ per cm}^2_{ECSA}} = 574 \text{ cm}^2_{ECSA}$$

References

1. C.C.L. McCrory, S. Jung, J.C. Peters, T.F. Jaramillo, Benchmarking heterogeneous electrocatalysts for the oxygen evolution reaction, *J. Am. Chem. Soc.* 135 (2015) 16977-16987.
2. P. Connor, J. Schuch, B. Kaiser, W. Jaegermann, The determination of electrochemical active surface area and specific capacity revisited for the system MnO_x as an oxygen evolution catalyst, *Z. Phys. Chem.* 234 (2020) 979-994

Chapter 7

General conclusions and future work

1. Conclusions

In this thesis, we report on the utilization of the colloidal synthesis method to prepare transition-metal phosphides as alternative electrocatalysts to platinum (Pt) in hydrogen evolution reaction in acidic media. Within the different chapters (3-6), the effect of size, crystallinity, crystal phase, and doping on the electrocatalytic performance was investigated.

In Chapter 3, we employed the colloidal synthesis method to prepare amorphous, small and quasi-spherical MoP nanoparticles using MoCl_5 , TOP and 1-ODE. Through heat treatment, the corresponding crystalline phase of MoP was ascertained. A comparative study of the electrocatalytic performance showed that the amorphous MoP phase was more active than the crystalline phase requiring an overpotential of only -235 mV to generate current density of $10 \text{ mA}\cdot\text{cm}^{-2}$ with a Tafel slope of $84 \text{ mV}\cdot\text{dec}^{-1}$. The enhanced catalytic performance of the amorphous phase was attributed to high conductivity and high density of active sites, characteristic of amorphous structures. In Chapter 4, we investigated the effect of introducing W atoms into crystal structure of the amorphous and crystalline MoP phases on the catalytic activity. HER results revealed that combining the sort after properties found in amorphous structures with those emanating from doping significantly improves activity. The amorphous tungsten-doped MoP exhibited efficient catalytic activity, requiring an overpotential of only -145 mV to generate current density of $10 \text{ mA}\cdot\text{cm}^{-2}$ and a small Tafel slope of $65.64 \text{ mV}\cdot\text{dec}^{-1}$.

In Chapter 5, we synthesized tungsten monophosphide (WP) and tungsten diphosphide (α -WP₂) by varying the molar ratios of the tungsten and phosphorus precursors using colloidal synthesis. The phosphorus-rich α -WP₂ displayed enhanced activity compared to WP, generating a current density of $10 \text{ mA}\cdot\text{cm}^{-2}$ at an overpotential of -271 mV and a Tafel slope of $86.83 \text{ mV}\cdot\text{dec}^{-1}$. In addition to high electrical conductivity and high density of electrochemically active sites, DFT studies revealed that the improved activity displayed by α -WP₂ was also due to favourable hydrogen adsorption energy, lower barrier for formation of transition state and low d-band center energy. In Chapter 6, the electrocatalytic activity of molybdenum-doped α -WP₂ catalysts with different dopant concentrations (α -WP₂, Mo(2.5%)/ α -WP₂, Mo(4%)/ α -WP₂, Mo(10%)/ α -

WP₂) were explored. The combination of XRD, XPS and EDS confirmed the successful incorporation of the Mo-atoms into the crystal lattice of α -WP₂. XPS results showed that the presence of Mo optimised the electronic properties of the α -WP₂ catalysts and enhanced its performance. Amongst the catalysts studied, Mo(10%)/ α -WP₂ exhibited superior activity, requiring an overpotential of -165 mV to produce current density of 10 mA.cm⁻² and a Tafel slope of 71.65 mV.dec⁻¹. It was also found that annealing the Mo(10%)/ α -WP₂ catalyst at elevated temperature result to liberation of phosphorus atom to form a less active Mo(10%)/ α -WP phase. The amorphous phase of WP₂ displayed enhanced catalytic activity which was slightly less active than the crystalline Mo(10%)/C.

In summary, metal chloride salts were used to successfully synthesis molybdenum and tungsten-based electrocatalysts using the infrequently reported colloidal synthesis method in the preparation of transition metal phosphide. It was possible to control the size, crystallinity, dopant concentration and crystal phase of the catalysts. The influence of the forementioned parameters in hydrogen evolution reaction were addressed.

2. Future work

Despite the great progress made in studying the influence of physical properties of the molybdenum and tungsten-based catalysts in hydrogen evolution reaction in this work, there are still several questions, amongst others, that need be addressed in the future:

- 1) Expand on the phase dependant study of tungsten phosphide by synthesizing metal rich phases (e.g. W₃P) to fully understand the effect of the degree of phosphirization (P:W) on electrochemical performance.
- 2) Study the electrocatalytic activity of the amorphous WP and α -WP₂.
- 3) Employ gas chromatography (GC) to identify and quantify the H₂ gas generated as a function of time.
- 4) Determine the actual doping molar concentration using inductively coupled plasma mass spectrometry (ICP-OES).
- 5) Conduct DFT calculations to study the Gibbs free energy of adsorption of hydrogen (ΔG_{H^*}) of the pure and doped catalysts to understand the improved HER performance.